Characterization of a developmental oscillator in *C. elegans*

Inauguraldissertation
zur
Erlangung der Würde eines Doktors der Philosophie
vorgelegt der
Philosophisch-Naturwissenschaftlichen Fakultät
der Universität Basel

von

Yannick Patrick Hauser

aus Zürich, Schweiz

Basel, 2021

Summary

Genehmigt von der Philosophisch-Naturwissenschaftlichen Fakultät auf Antrag von

Prof. Dr. Anne Spang

Prof. Dr. Helge Grosshans

Dr. Alexander Aulehla

Basel, den 21.04.2020

_____

Unterschrift des Fakultätsverantwortlichen (nur in einem Exemplar)

Prof. Dr. Martin Spiess

(Dekan)

1 Summary

Gene expression oscillations can act as fundamental time-keeping mechanisms to instruct developmental events temporally and spatially. The present work investigates such a developmental oscillator in *C. elegans* that encompasses thousands of oscillating transcripts. The regulation of these transcript oscillations and their functional relevance for development remained elusive. In this thesis, I present insights into the general oscillator characteristics, the regulation of oscillating genes and the contribution of oscillatory gene expression to physiological outcomes.

Using a temporally highly resolved RNA sequencing time course covering all *C. elegans* larval stages (L1-L4) and early adulthood in combination with single worm microscopy studies, we characterize oscillatory gene expression in detail and provide evidence that oscillations peak once per larval stage and are synchronized with the molting cycle. Consequently, we propose oscillatory gene expression and larval development to be coupled. Furthermore, oscillations are arrested (i.e. absent) temporarily in freshly hatched L1 larvae and worms released from dauer arrest, and permanently in adults. The particular oscillator phase at which we observe the arrested oscillator corresponds to the oscillator phase detected around the molt exit. Given that developmental checkpoints have been reported around the time of molt exit we propose the *C. elegans* oscillator to constitute a developmental clock supporting a checkpoint function.

Investigations on the mechanisms leading to rhythmic transcript abundance by RNA polymerase II ChIP-sequencing and transcriptional reporter studies revealed that transcription is mainly responsible for oscillating transcript levels. Together with the fact that oscillatory gene expression is coupled to development, transcription factors were of particular interest in this thesis. We characterize BLMP-1, an oscillating transcription factor that was shown to alter developmental timing. We provide evidence that BLMP-1 acts to regulate the duration of molts, is required for cuticle integrity and acts as a coupling factor to synchronize a group of oscillating genes with the remaining oscillating genes and development. Furthermore, we could show epistatic behavior of *blmp-1* with *dre-1*, an oscillating E3 ubiquitin ligase that degrades BLMP-1 protein. These observations shed light on the regulatory network underlying the *C. elegans* developmental oscillator and are important to understand its architecture and physiological impact.

Table of Contents

Summary

1 Introduction

1.1 Biological Oscillators

Oscillating systems are characterized by one or multiple variables periodically fluctuating away from an equilibrium state in time. The oscillation of a variable can be defined by (i) the amplitude, which indicates the maximum value away from the equilibrium over time, (ii) the period, indicating how much time it takes to complete one full oscillation and (iii) the peak phase which describes the time at which the variable is at its maximum value. The oscillation can be characterized at each time point within one period by its phase, ranging from 0 to 2π or from 0° to 360° equivalently, depending on the definition (Fig 1.1).

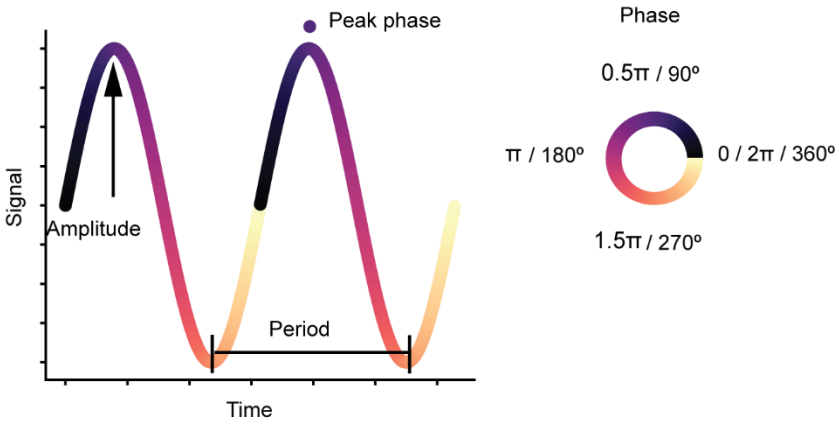

Fig 1.1: Mathematical description of an oscillation

An oscillation can be described by its amplitude, its period and its phase. The phase is displayed in color ranging from 0 to 2π. The peak phase is indicated specifically at the peak of the oscillation.

Oscillations are a common feature in biology and serve many different purposes (Kruse and Jülicher, 2005). The following examples serve to illustrate the diversity of oscillator functions. Sound (the vibration of air pressure) perception is possible through specific hair cells in the inner ear which transduce the vibrations from sound into nerve impulses (Dobie and Van Hemel, 2004). Circadian rhythms that are found in almost all species on earth are the output of circadian clocks that serve to synchronize the behavior of organisms with the periodically changing external environment. In the bacterium *Escherichia coli*, oscillations of the Min proteins perpendicularly

to its long axis lead to the formation of the Z-ring in the middle of the bacterium, which thus initiates the cell division in the middle of the bacterium (Raskin and De Boer, 1999). Furthermore, oscillations of signaling molecules can be used to encode or decode biological information (Purvis and Lahav, 2013). A change in dynamics, e.g switching between continuous and oscillating, can lead to a different response in cellular behavior, as observed for p53. Two different stimuli, γ-irradiation and UV radiation, lead to p53 pulses and prolonged signaling respectively. Upon p53 pulses, cells arrest the cell cycle, whereas prolonged p53 signaling leads to apoptosis (Purvis et al., 2012).

Developmental timing needs to be tightly controlled spatially as well as temporally, which represents a regulatory challenge for organisms. Oscillating systems have been proven to be useful to provide such tight control, thus nature has taken advantage of these systems to orchestrate developmental timing. For example, the lateral root branching in *Arabidopsis* is instructed by oscillating gene expression at the root tip (McCleery et al., 2017). One of the most studied developmental timers is called the segmentation clock which ensures the proper timing of somite formation during embryogenesis in vertebrates.

The mechanisms of oscillatory signal generation are of great interest to research but still not fully understood. In general, oscillating systems consist of an input, the oscillator, and an output. Three oscillating systems will be discussed in further detail below: the well-characterized circadian clock and the segmentation clock, as well as the *Arabidopsis* root branching clock.

1.1.1 Circadian rhythm

The roughly 24 hour circadian ("circa diem" = about one day) rhythms represent autonomous oscillators that are the output of the circadian clock and regulate the adaptation and anticipation of an organism to the periodically changing environment such as the day-night cycle. These rhythms have been studied since the first indication for a "programmed" biological clock in 1729 when the astronomer Jean-Jacques d'Ortous de Mairan discovered that the plant *Mimosa pudica* rhythmically folded and unfolded its leaflets even without a periodic light trigger. Hence d'Ortous de Mairan proposed an active regulation of leaflet folding rather than a mere passive response to light ("De Mairan, JJ. D'Ortous. Observation botanique, 1729" as reviewed in Vitaterna, Takahashi, and Turek 2001). Since then, circadian rhythms have been heavily investigated and researchers have agreed on a number of features that generalize circadian systems. Some of the

most important features include: 1) the period of the rhythm is approximately the length of one day on earth, 2) the rhythm is usually cell-autonomous, 3) the rhythm is temperature-compensated, meaning its period is not dependent on the temperature in the environment, 4) the rhythm can be entrained by a limited range of input frequencies (reviewed in Pittendrigh 1960). External rhythmic inputs such as light, food or temperature can influence and (re-)set the peak phase of the rhythm to match the local time, which is why they are also called "Zeitgeber" ("time-giver") (Aschoff, 1960; Hattar et al., 2002; Lucas et al., 2003; Menaker, 2003). Thus they synchronize the internal clock with the rhythmic environment. An unsynchronized clock can lead to physiological impairments such as cardiovascular issues (reviewed in Crnko et al. 2019), sleep disorders (Kim et al., 2013b), psychiatric disorders (Lamont et al., 2007) and affect metabolic health (Li et al., 2012).

In mammals, the mechanism generating circadian rhythms consists of auto-regulatory transcription-translation feedback loops with the core clock genes *BMAL1* and *CLOCK* (activators), and *PER1/2/3*, *CRY1/2* (repressors). This rhythm is cell-autonomous and runs in all major organ systems and tissues. Nevertheless, the individual peripheral rhythms are synchronized through a specialized hypothalamic structure, the suprachiasmatic nucleus (SCN) which represents the master circadian pacemaker (Welsh et al., 2010).

In order to generate circadian oscillations, post-transcriptional steps, such as splicing (reviewed in Cui, Xu, and Wang 2014; Foley et al. 2019; Bélanger, Picard, and Cermakian 2006), transcriptional termination (Padmanabhan et al., 2012), RNA degradation (So, 1997; Woo et al., 2009), translation (Jouffe et al., 2013; Kojima and Green, 2015; Reddy et al., 2006), and protein degradation (D'Alessandro et al., 2017; Hirano et al., 2017) contribute to circadian rhythms in the peripheral tissues (reviewed in Lim and Allada 2013; Kojima and Green 2015). Interestingly, the oscillating transcriptome and the peak phase distributions can vary drastically between peripheral tissues (Mavroudis et al., 2018), suggesting a tissue-specific aspect contributing to the rhythmic output of the circadian clock (Yeung et al., 2018). For the purpose of this thesis, I will focus on the transcriptional core mechanism as reviewed in Takahashi 2017; Panda, Hogenesch, and Kay 2002, where BMAL1 and CLOCK form a heterodimeric complex and activate clock output genes as well as REV-ERBs (α and β) and PER1/2 and CRY1/2 expression through binding to specific promoter sequences called E-boxes (CACGTG). After translation, formation of heterodimers and

post-translational phosphorylation by the casein kinase 1 (CK1), PER1/2 and CRY1/2 translocate to the nucleus where the PER/CRY complex represses the transcription of clock output genes, *rev-erb* and its own genes, *per1/2/3* and *cry1/2*, by interacting with the BMAL1/CLOCK complex (Fig 1.2A). Thus, transcript levels of *per1/2/3* and *cry1/2* decline rapidly and as the degradation rate of PER1/2 and CRY1/2 are relatively high due to ubiquitination by an E3 ubiquitin ligase, repression is relieved. This results in a new start of transcription of BMAL1 and CLOCK controlled genes. This represents a classic example of a negative feedback loop with a delay. As described above, the REV-ERBs are also activated by BMAL1 and CLOCK and repress the transcription of BMAL1 by competing with the transcription factor retinoic acid-related orphan receptor (ROR). Due to the rhythmic activation of *rev-erb* transcription, a rhythm of BMAL1 expression is generated that is antiphase of CRY and PER. Together, these activators and repressors form a positive-feedback and negative feedback gene network motif, ultimately leading to the rhythmic output of clock-controlled genes and thus controlling circadian behavior of the organism.

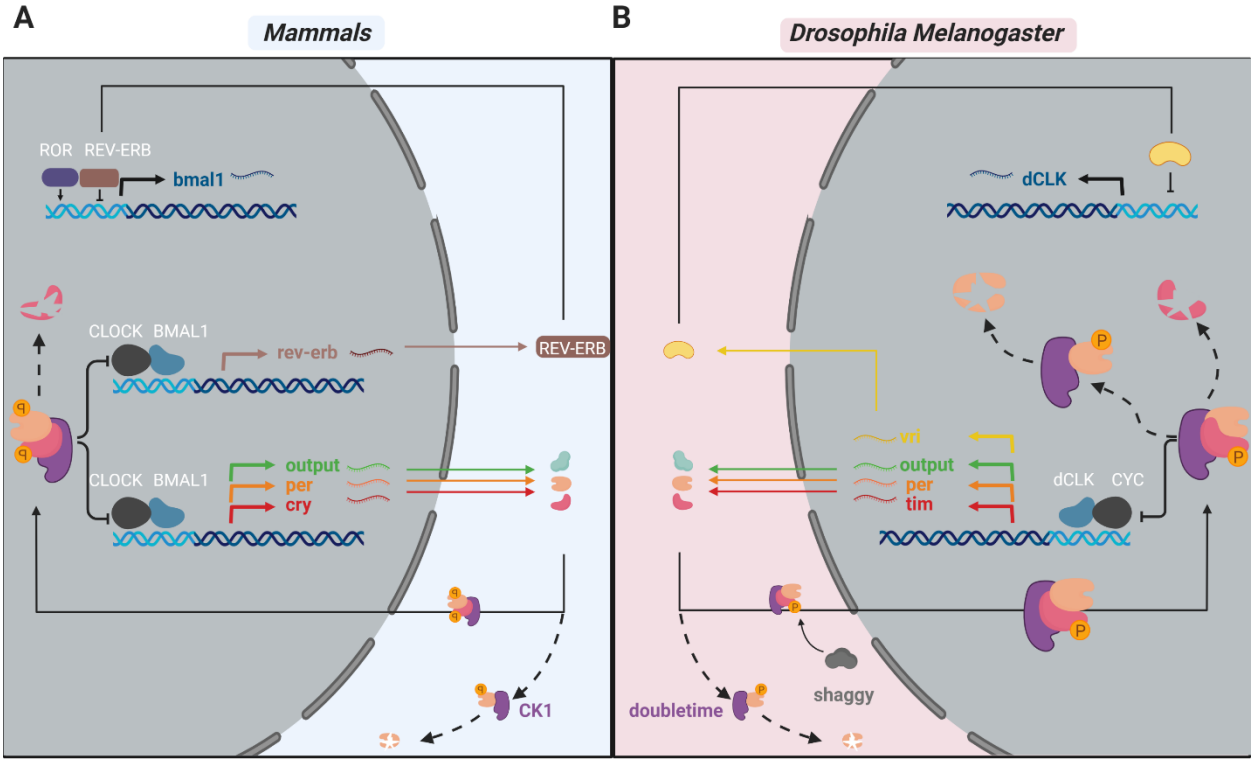

Fig 1.2: Schematic representation of the circadian rhythm in mammals and flies

A, Mammalian representation of circadian rhythm where the heterodimer CLOCK/BMAL1 activates clock output genes as well as *per* and *cry* together with *rev-erb*, forming negative feedback loops important for generating the rhythmic behavior of the system.

B, In flies, dCLK/CYC form a heterodimer that activates clock output genes as well as *per, tim* and *vri* to form negative feedbacks.

The repressing factors (PER, CRY, and TIMELESS) are degraded which is illustrated as splintered proteins. Inspired from Panda et al., 2002; Patke et al., 2020; Takahashi, 2017. Figure created with Biorender.com

In *Drosophila melanogaster*, circadian rhythms are established using very similar regulatory mechanisms as in mammals (Fig 1.2B). At the core of the feedback loop, *period (per)* and *timeless (tim)* form a negative feedback loop, repressing their own transcription. After translation, PER and TIM form a dimer which is also bound by the casein kinase I DOUBLETIME (DBT). As long as TIM levels are not high enough, unbound PER is actively degraded by DBT. After dimerization though, TIM is phosphorylated by the kinase SHAGGY (SGG), enabling and timing nuclear translocation of the PER/TIM/DBT complex. The nuclear PER/DBT complex represses the activity of the transcription factor heterodimer consisting of dCLOCK (dCLK) and CYCLE (CYC), which bind E-box promoter sequences present in the promoters of per, tim and output genes. DBT however can now, in the absence of TIM, phosphorylate PER further which leads to PER degradation. The absence of PER in the nucleus de-represses dCLK and CYC, which then activate transcription again and thus start a new cycle. The fact that TIM is degraded in response to light allows synchronizing (entrain) the rhythm to the light-dark cycle (Zeng et al., 1996). Similarly to the mammalian clock, a second feedback loop is present, consisting of Vrille (*vri*), which is transcriptionally activated by the heterodimer dCLK and CYC. VRI then transcriptionally represses *dclk* (Cyran et al., 2003; Patke et al., 2020).

1.1.2 Segmentation Clock

During vertebrate embryonic development, the anterior-posterior axis undergoes a segmentation process which leads to the formation of so-called somites. The somites give rise to multiple structures including muscles, nerves, blood vessels and vertebrae. Somites are bilaterally paired blocks of paraxial mesoderm that are formed rhythmically within the presomitic mesoderm (PSM) during somitogenesis. The number of somites as well as the time interval at which new somites

are formed can vary between species but is invariant within one individual species. Initial observation of the high regularity of somite formation suggested that this process is tightly regulated by an oscillating mechanism, which became known as the segmentation clock. The first discovery into the molecular architecture of the segmentation in chick embryo (Palmeirim et al., 1997) led to a series of investigations concluding in the characterization of the key features of this rhythm which are reviewed in Hubaud and Pourquié 2014 and Webb and Oates 2016 and summarized here. First, gene expression starts in the tailbud and the PSM, second, a wave of gene expression travels through the PSM from posterior to anterior, third, the wave slows down towards the anterior of the PSM where the wave arrests, and fourth, new waves are initiated in the tailbud, starting consecutive rhythms. The *Clock and Wavefront* model (Cooke and Zeeman, 1976) has been the dominant model to explain the mechanism of rhythmic somite formation. The model states that the molecular clock located in the posterior PSM leads to rhythmic activation of several signaling pathways, including Notch, WNT and FGF (fibroblast growth factor). A signaling gradient called the wavefront travels from anterior to posterior along the PSM and converts the periodic signaling from the segmentation clock into the formation of somites as the periodic signal hits the wavefront. It was suggested that the interplay between the wavefront and the clock leads to a periodic abrupt change in cellular identity, also called "catastrophe", initializing differentiation of these cells. However, this catastrophic event only happens when the wavefront hits oscillating cells in the PSM that are in the correct phase of the oscillation.

This model implies that the segment length is determined by both the period of the oscillations and the speed of the wavefront. In mathematical terms, it can be summarized that

$$S = v * T,$$

where S is the segment length, v the velocity of the wavefront and T the period of the oscillation. Furthermore, the total number of segments is determined by the duration of the segmentation process and the period of the oscillation, such that

$$n = \frac{d}{T},$$

where n is the number of segments, d the duration of the segmentation process and T the period of the oscillation.

Detailed investigations on the molecular oscillator of the segmentation clock further provided support for the clock and wavefront model, when oscillatory expression of the Notch effector gene HAIRY, a member of the HER transcription factor family, was detected in chicken embryos (Palmeirim et al., 1997). Importantly, the 90 minute period of HAIRY oscillation matches the time interval at which somites are formed in chicken. Oscillations of HES / HER family members have been detected in many other species, implying that these transcription factors are important factors in the segmentation clock. The HES / HER transcription factors encode a bHLH (basic helix-loop-helix) DNA binding domain and can act as transcriptional repressors, repressing their own transcription. This negative feedback loop is responsible for the cyclic expression of HES / HER genes (Lewis, 2003) and it is believed that Notch and FGF signaling oscillations in the PSM depend on and are coupled with HES / HER transcriptional repressors (Imayoshi et al., 2013; Niwa et al., 2007). This rhythmic activation then leads to a wave of signaling activity traveling from the posterior to the anterior PSM until it clashes with the wavefront. The wavefront consists of FGF and WNT gradients with high levels in the posterior PSM and low levels in the anterior PSM together with a retinoic acid (RA) gradient in opposite direction (Niederreither et al., 1997; Rossant et al., 1991), forming a determination front. High levels of WNT and FGF render the cells insensitive to the segmentation clock thus only the very anterior cells with low FGF and WNT levels and increased RA levels can respond to signaling from the segmentation clock (Fig 1.3). High levels of RA together with the signaling from the segmentation clock then promote the formation of a new somite boundary through the induction of MESP gene expression. Further evidence for the biological relevance of the gradient stems from experiments where the gradient was shifted which resulted in abnormal somite sizes.

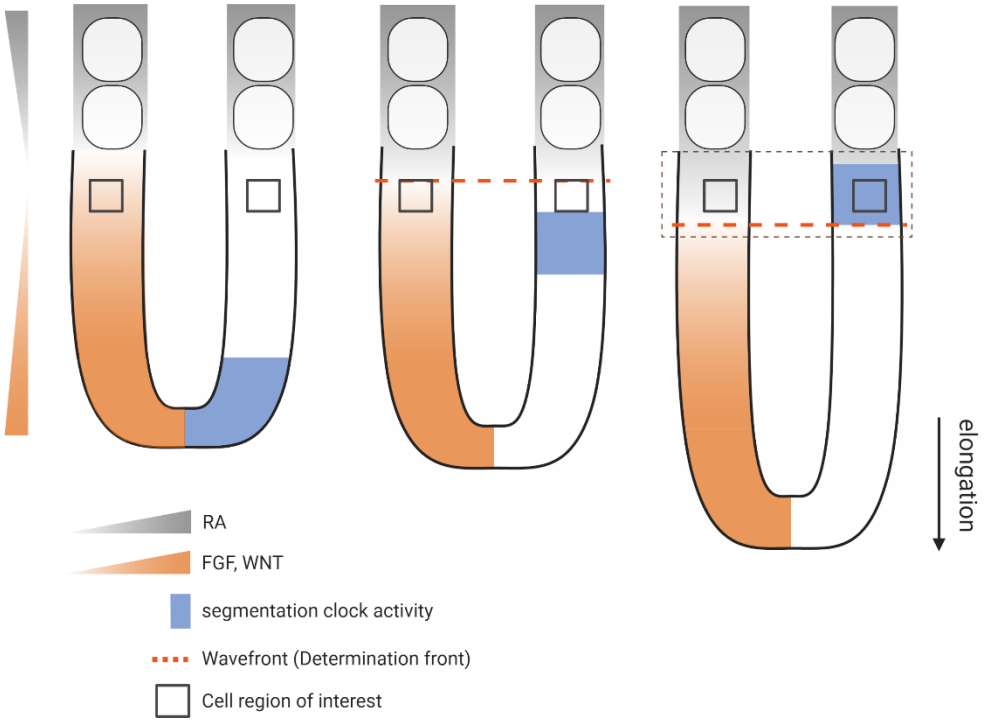

Fig 1.3: Schematic representation of the segmentation clock

FGF, WNT and retinoic acid (RA) form gradients and specify the wavefront in the presomitic mesoderm which together with oscillatory signal from the segmentation clock (blue) initiates the formation of new segments. Inspired by Hubaud and Pourquié 2014. Figure created with Biorender.com

1.2 Requirements for oscillations

Certain features, such as negative autoregulation, time delays, non-linearity and balanced kinetic reaction rates favor sustained oscillations. In the following, I will summarize the importance of these features as described in Novák and Tyson 2008 in regard to oscillating system behavior by mostly introducing the concepts based on a system with one gene present.

1.2.1 Negative autoregulation

As illustrated in 1.2 with the examples of oscillating systems in biology, **negative feedback loops,** also called **negative autoregulation (NAR)** are a general building block in oscillating systems. A

negative feedback loop is characterized by the fact that the rate of production of a molecule is negatively influenced by the molecule itself or its downstream products (Fig 1.4A). Interestingly, all biochemical oscillators include NAR (Novák and Tyson, 2008), yet negative feedback alone is not sufficient to induce sustained oscillations. Before we explore the necessary requirements to generate oscillations from NAR, we take a closer look at the general system properties of a negative feedback loop regulation. The simplest form of NAR is a system with one component, called X, which induces repression of its own production. This mechanism is accompanied by two important features: a faster response time upon activation and lower sensitivity to noise in comparison to simple regulation (linear production, Fig 1.4A). These characteristics can be visualized in a plot where the (production and degradation) rate of X is plotted on the vertical axis and the concentration of X on the horizontal axis (Fig 1.4B).

The formula for NAR, where we define the time derivative of the change of X as

$$\frac{dX}{dt} = f(X) - \alpha X,$$

consists of a non-linear function $f(X)$ for the production and a linear function αX for the degradation. A simple and often used function for $f(X)$ would for example be

$$f(X) = \frac{\beta}{1+\left(\frac{X}{K}\right)^n}$$

where K is the repression coefficient, β the maximal production rate and n, the Hill coefficient, representing non-linearity in the regulation which is further discussed in section 1.2.3. We can analyze NAR by plotting the rate of protein X production and degradation in the same plot as in Fig 1.4B. As we can see from the formula, the degradation and production both depend on the concentration of X. A simple thought experiment reveals that for a negative feedback loops, the production rate is high whenever we have low amounts of X and it is low if high amounts of X are present (salmon line in Fig 1.4B). The opposite is true for the degradation rate, where we have high degradation rates for high amounts of X and vice versa. Fig 1.4B shows both production rate and degradation rate in the same plot and reveals that whenever we see the production rate being higher than the degradation rate, the net rate of X is positive and vice versa. Hence, if we start at low values, X will increase to eventually approach a point where $\frac{\mathrm{dX}}{\mathrm{dt}} = 0$. The opposite is true for initial high levels, where X decreases and thus also approaches the same point. We thus consider

this special value of **X** a **stable fixpoint** because the net rate of X is zero ($\frac{\mathrm{dX}}{\mathrm{dt}} = 0$) and the system approaches the fixpoint from both sides (Fig 1.4B).

In contrast, the mathematical formula for **simple regulation (SR)** is defined by

$$\frac{dX}{dt} = \beta - \alpha X$$

with β representing the production rate and α being the degradation rate. It becomes obvious from the comparison of SR and NAR in the plot for any $X < X_{fixpoint}$, the difference between production and degradation rate is bigger for NAR than SR. This means that NAR progresses faster to the fixpoint compared to SR (Fig 1.4B) (Becskel and Serrano, 2000).

Accordingly, the NAR is less sensitive to noise as we see in Fig 1.4C. Any perturbation away from the fixpoint will move towards the fixpoint again very quickly in the case of NAR. This process happens much slower in SR, which results in a broader distribution at a given time point in a population (Fig 1.4C). Variations in the degradation rate α also lead to a big variation in the fixpoint level of SR whereas, in NAR, this variation is much smaller (Fig 1.4D, E).

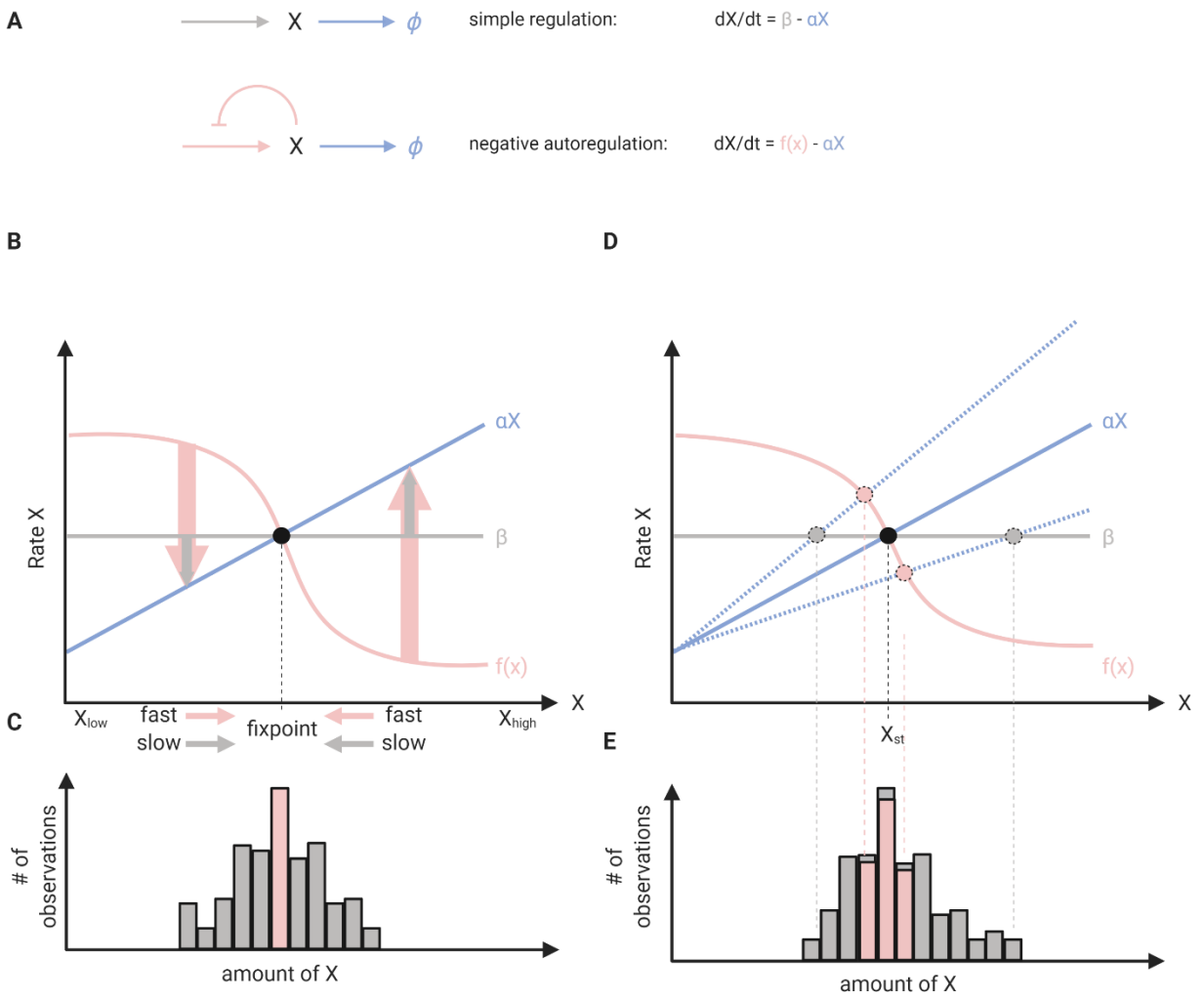

Fig 1.4: Negative feedback reaches fixpoint levels fast and is less sensitive to noise compared to simple regulation

A, Simple regulation (SR) and negative autoregulation (NAR) graphs with their mathematical description on the right.

B, Schematic rate plot of NAR in salmon and SR in grey. The arrows indicate the difference between production and degradation rate. For any value of X, the arrows are bigger for NAR as compared to SR, indicating that the NAR approaches the fixpoint faster than SR. The fixpoint occurs where the rate of production equals the rate of degradation and is indicated as a dot.

C, Any perturbation away from the fixpoint will be reversed faster for the NAR than SR, thus the variation of observed instantaneous levels of X will be lower for NAR than SR.

D, E, Variations in degradation rates (D) cause a much bigger variation in observable levels of X in the case of SR as compared to NAR (E).

Based on Becskel and Serrano 2000; Alon 2007. Figure created with Biorender.com

As already mentioned, the negative autoregulation system is well suited to obtain a level of component X with a fast response time upon gene activation (Alon, 2007) and it is required, but not sufficient to generate oscillations (Alon, 2007; Novák and Tyson, 2008). In order to oscillate, additional features need to be incorporated into the system, which I will discuss below.

1.2.2 Time delay

In order to generate oscillations in a system with negative autoregulation, time delays have to be incorporated in the system, e.g. the repression of X depends on the amount of X that was present at a certain time ($t - \tau$) before the present (Mackey and Glass, 1977). As a consequence, overshoots and undershoots in the production rate of X occur, causing rhythmic dynamics. It is to note, however, that the amount of time delay is critical, with values below a given threshold being insufficient to generate oscillations (Ferrell et al., 2011; Stricker et al., 2008). To visualize this example more intuitively we imagine a freezer that needs to cool down inside temperatures. To fulfill this task, a built-in sensor measures temperature with a certain time interval to signal the freezer to cool down in case of temperatures above the desired one. In such a situation, the freezer will start lowering the temperature to go below the desired threshold (undershooting), but since the sensor measures only after a certain interval (time delay) again, the freezer keeps lowering the temperature until the new measurement which now indicates that the temperature is low enough and the freezer can stop cooling. After a while temperature increases again, overshooting the threshold due to the same time delay as for the undershooting of measurement and thus the cycle starts anew.

One way of introducing time delays in a biochemical system is by adding an additional component in the feedback loop (Alon, 2007; Griffith, 1968; Lewis, 2003). As an example of a simple biological example with one gene, we can consider a system with 4 components: nuclear mRNA, cytoplasmic mRNA, cytoplasmic protein and nuclear protein. In this example, transcription, splicing, transport, translation, nuclear export and import of the various components lead to time delays that are sufficient for generating sustained oscillations. As these time delays are usually small, they lead to periods of around 30 minutes which is in agreement with the observed zebrafish somite oscillations (Lewis, 2003). However, the achievement of longer periods of around 90 – 120

minutes as observed in mouse and chick somitogenesis requires adaptations of the model (Lewis, 2003). Even longer periods as in the case of circadian oscillations require additional time delay which is achieved through post-translational modifications such as phosphorylation (Gallego and Virshup, 2007).

Furthermore, an additional strategy to obtain a delay in the system is by adding a positive feedback loop on the first component in the system, which is known to slow down its response time compared to simple and negative regulation (Alon, 2007). This particular example is known as relaxation oscillator and characterized by sustained robust oscillations and tunable frequencies with stable amplitudes over a large frequency range (Fig 1.5E) (Tsai et al., 2008). Furthermore, this oscillator is characterized by bi-stability or hysteresis, where the levels of system components switch between high and low but intermediate levels are not observed.

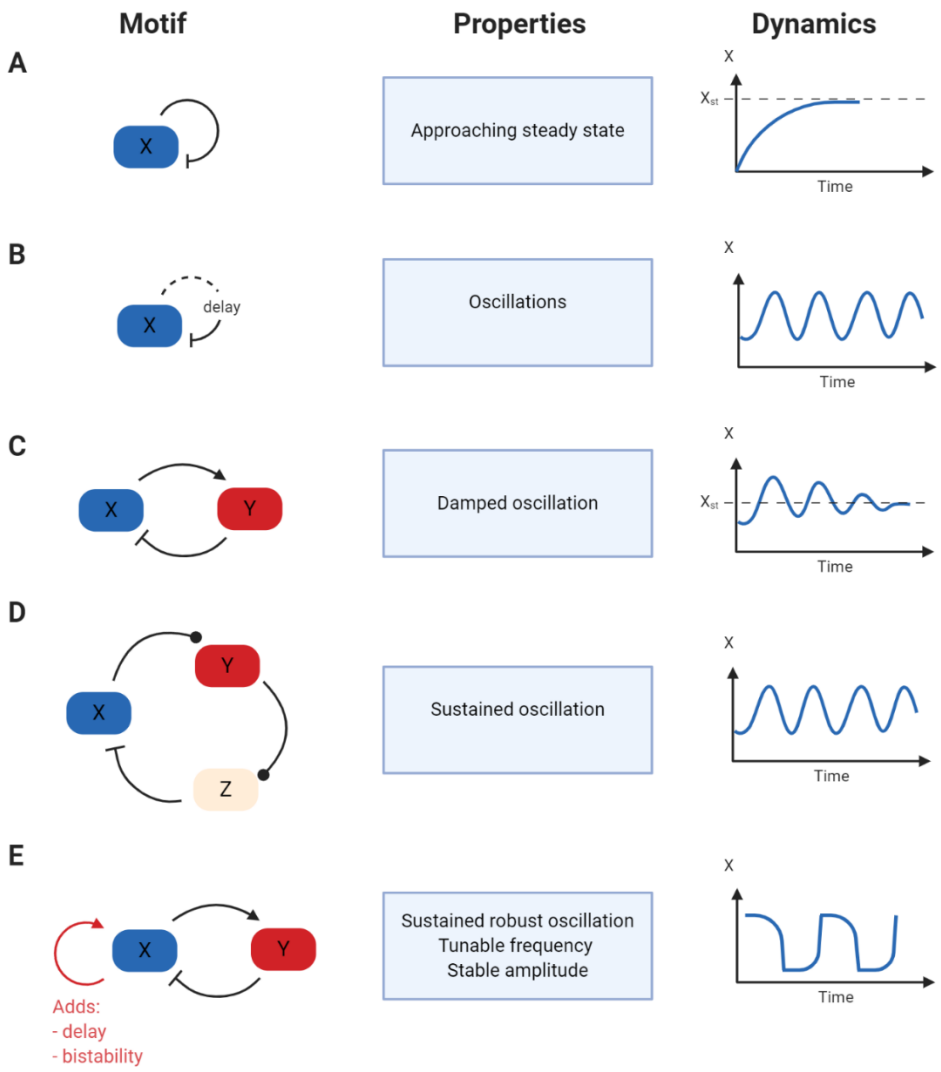

Fig 1.5: Network motifs and their dynamics

Different network topologies are represented on the left with a short description of the properties in the middle and the resulting dynamics on the right. The arrows represent activation, T ending lines represent repression and lines with a dot represent either activation or repression. Adapted from (Novák and Tyson, 2008). Figure created with Biorender.com

A, One component negative feedback without time delay reaches the fixpoint quickly.

B, One component negative feedback including explicit time delay can result in oscillations over time.

C, Two-component negative feedback with insufficient time delay leads to damped oscillations.

D, Multiple component negative feedback generating sufficiently long time delays can result in sustained oscillations.

E, The relaxation oscillator. Adding positive feedback in a two-component negative feedback loop leads to additional time delay and bi-stability behavior which results in sustained robust oscillations with tunable frequencies and stable amplitudes.

1.2.3 Non-linearity

The third important feature favoring oscillations is the non-linearity of the kinetic laws. To obtain an intuitive understanding of this feature we imagine the freezer example from 1.4.2 again. Strong non-linearity in this system would arise if the freezer could respond to the measured inside temperature only by either cooling with maximum power or not at all, depending on whether the inside temperature is above or below the desired temperature, respectively. Together with time delays, non-linearity favors over- and undershoots of the system and thus oscillations in general. Indeed, mathematically, it was shown that increasing non-linearity in the systems favors oscillations (Novák and Tyson, 2008). Biochemically, non-linearity can arise via multiple means (Novák and Tyson, 2008) such as 1) the necessity of transcription factor oligomers to either activate or repress gene expression, 2) cooperativity and allostery, 3) multistep phosphorylation of transcription factors only activating transcription after all phosphorylation sites are phosphorylated and 4) stoichiometric inhibition of the transcription factor where the transcription factor increases in response to a signal. As soon as the transcription factor reaches a higher concentration than the inhibitor, free and uninhibited transcription factor proteins can accumulate, resulting in a sigmoidal non-linear curve of "free" (active) transcription factor in response to the signal (Novák and Tyson, 2008).

1.2.4 Balanced reaction rates

The last feature to enable sustained oscillations is that the rates of involved processes need to be balanced. For example, in the case of the repressing component showing too high degradation rates in comparison to production rates, it might not be able to accumulate enough to fulfill its repressing role, and thus oscillations would be impossible.

Another example is that the time scale of degradation of the repressing component must be appropriately balanced with the time delay as with too slow or too fast degradation, repression could either not be released properly or would not emerge at all, respectively.

In summary, oscillating biochemical systems are characterized by four important features: they are composed of negative feedback loops with sufficient time delay. The kinetic laws of the interactions need to show sufficient non-linear behavior and the production and degradation need to occur on appropriate time scales.

1.3 Bifurcations and their analyses

We have seen how oscillations are generated on the molecular level. However, apart from oscillations, there are many other dynamic behaviors, such as stable expression over time or decline of mRNA or protein over time. Upon system parameter changes, a system can undergo a qualitative change from one behavior to another. This transition is referred to as "bifurcation" of the system and bifurcation theory provides useful tools to investigate these qualitative changes. Depending on the network and how the parameter influences it, there are different bifurcations possible. In order to investigate bifurcations, we use the same visual representation as shown in Fig 1.6, where we plot the rate of X depending on the amount of X present.

Covering all possible bifurcations in detail would be beyond the scope of this thesis which is why I will focus on a one-dimensional example to introduce the reader to the topic and then discuss the system properties of (higher dimensional) bifurcations that are relevant for this work.

In order to facilitate calculations, many problems of the same type can be written in a simplified version, which is called the normal form. For example, a system where

$$\frac{dX}{dt} = e^{-x} - (r - x)$$

with the degradation rate of X described by $r - x$ and the production rate by e^{-x} can be simplified to the normal form

$$\frac{dX}{dt} = r + X^2.$$

This equation is the normal form for **saddle node** bifurcations, in which the so-called bifurcation parameter r allows to change the system's behavior and in the case of saddle node bifurcation leads to *creation* and *destruction* of fixpoints. As represented in Fig 1.6, for $r > 0$, there is no fixpoint present as the production rate never reaches 0. If $r < 0$ we can observe two different fixpoints, one of which is a stable and the other an unstable fixpoint. $r = 0$ results in an intermediate situation

with a half stable fixpoint, which is characterized by the system approaching the half stable fixpoint from one side but being repelled on the other side of the fixpoint (Strogatz 2015, chapter 2).

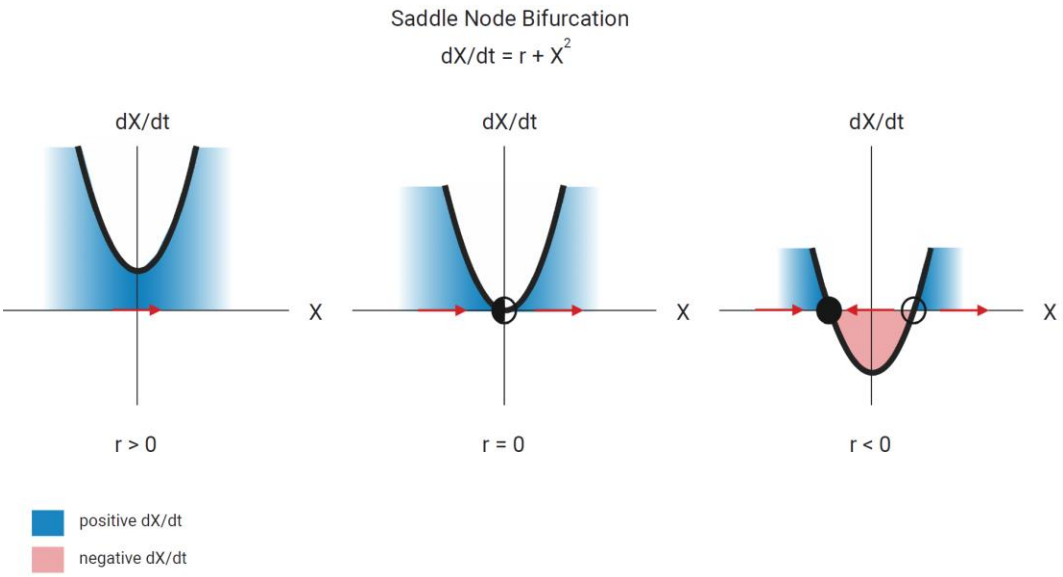

Fig 1.6: Saddle node bifurcation is characterized by the appearance or annihilation of fixpoints

In the example of $dx/dt = r + X^2$, changing the bifurcation parameter r from positive to negative values leads to the appearance of two fixpoints, one of which is stable (black dot) and the other unstable (white dot). The special case where r = 0, results in one half-stable fixpoint, indicated with a half-filled point. The rate of change in X is either positive (blue areas) or negative (red area) which leads to either an increase or a decrease in X as illustrated in red arrows. Inspired by Strogatz 2015. Figure created with Biorender.com

As we can see in the saddle node example, fixpoints can either emerge or they annihilate each other by changing the parameter r. Apart from the saddle node bifurcation, pitchfork and transcritical bifurcations exist in one-dimensional systems. Pitchfork bifurcations are characterized by a fixpoint that changes its stability while two new fixpoints emerge at the same time, while in a transcritical bifurcation, two fixpoints change their stability (Strogatz 2015, chapter 3).

With increasing numbers of dimensions to at least 2 or higher, the possible system behaviors and bifurcations increase. To visualize the system behavior of a two-dimensional system in the way we did above for the one-dimensional case, we now plot the amounts of the individual components, X and Y on the x and y axis. The rates of change are then visualized as arrows that start from any point $P1(X_1, Y_1)$ and extend depending on the rates of X and Y as shown in Fig 1.7A towards

P2(X_2, Y_2). Interestingly this already implies that additional behaviors such as sustained oscillations can exist (Fig 1.7 B). In this special case, the arrows form a circle representing a so-called closed orbit, which is characteristic of systems that show oscillatory behavior. In the special case where neighboring trajectories spiral towards or away from the closed orbit, we refer to the closed orbit as a stable or unstable limit cycle respectively (Strogatz 2015, chapter 7).

For our purposes, the two most important bifurcations form stationary to oscillatory and vice versa in two dimensions are the supercritical Hopf (supH) bifurcation and the saddle node on invariant cycle (SNIC) bifurcation. Both bifurcations allow a system to switch between oscillatory and stationary behavior upon changing a bifurcation parameter. In the case of a supH, a stable fixpoint attracting all trajectories changes stability in response to changes in the bifurcation parameter. After the change in stability, the trajectories approach a newly formed limit cycle around an unstable fixpoint (Fig 1.7C). The SNIC however, similar to its one-dimensional equivalent, bifurcates by annihilation or emergence of a stable and an unstable fixpoint via the formation of a temporary half-stable point at the threshold of the bifurcation parameter (Fig 1.7D). Importantly, the unstable and stable fixpoints appear or disappear on a closed orbit, thus the removal initiates sustained oscillations on a limit cycle whereas the creation of these fixpoints leads to an arrest of the oscillations.

The specific characteristics of how oscillations start and end in proximity to the bifurcation point depends on the type of bifurcation. In particular, during a supH bifurcation oscillations emerge and disappear with a non-zero, constant period and an amplitude increase or decrease respectively, depending on the distance from the bifurcation point (Fig 1.7E). In contrast, the SNIC bifurcation displays constant amplitudes with increasing periods closer to the bifurcation point (Fig 1.7F) (Izhikevich, 2000; Luisa et al., 2017). An additional important feature distinguishing the two above mentioned bifurcations is that supH acts as a resonator, responding to certain input frequencies whereas the SNIC acts as an integrator, responding to the sum of the input signal (Conrad et al., 2008).

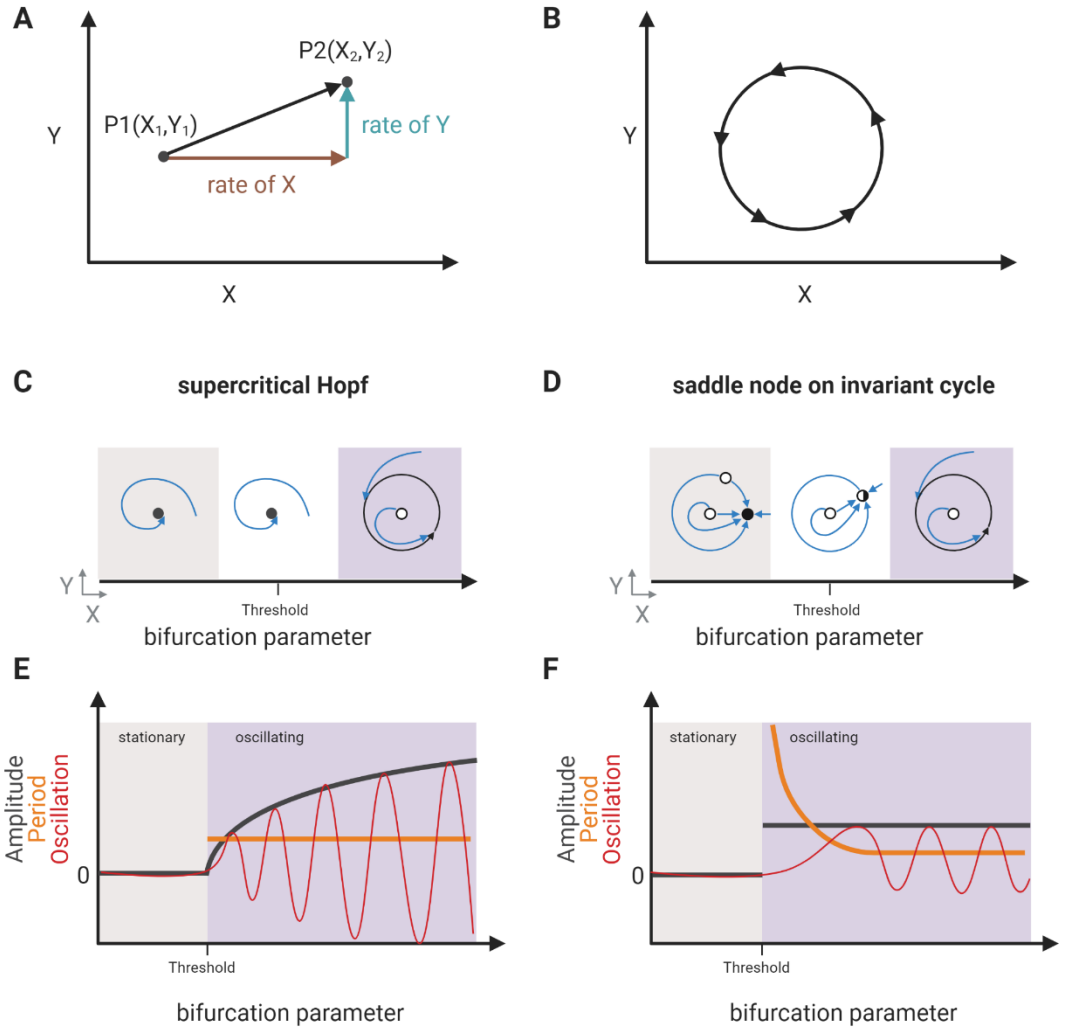

Fig 1.7: System behavior in two dimensions

Figure created with Biorender.com

A, Both components X and Y can change in time in a two-dimensional system. This can be visualized on a plot displaying the levels of X and Y in a two-dimensional coordinate system together with arrows pointing into the direction of the rate of and Y, forming a trajectory from the point P(X_1, Y_1) to the point P(X_2, Y_2).

B, Sustained oscillations can emerge when the trajectories form a closed orbit. In the case where all neighboring trajectories spiral away or towards the closed orbit, we call the closed orbit a limit cycle.

C, The supercritical Hopf (supH) bifurcation is characterized by a change of stability in the fixpoint and the emergence or disappearance of a limit cycle upon a bifurcation parameter change.

D, In the saddle node on invariant cycle (SNIC) bifurcation, two fixpoints are either annihilated or emerge and a limit cycle forms or is destroyed, depending on a bifurcation parameter.

E, Oscillations emerge or disappear with increasing or decreasing amplitudes respectively and a stable period in a supH bifurcation.

F, The SNIC bifurcation is characterized by stable amplitudes but changing period length during bifurcation from the stationary to the oscillating state and vice versa.

As discussed above, the knowledge of amplitudes, periods and phases over time are essential for bifurcation analyses. Acquiring this information requires a more sophisticated analysis than just a normal fit of the data to an oscillating signal such as a cosine or a sine. Different techniques have been used in the past to analyze these so-called instantaneous amplitudes, periods and phases, the best known are the Hilbert transform (Gabor, 1946) and the Wavelet transform (Mallat, 1999). These methods allow the calculation of the instantaneous amplitude, period and phase of an oscillation at each observed time point and hence, changes of these features can be captured quantitatively. While these methods represent at least in mathematical terms equivalent approaches (Bruns, 2004), the facts that we already obtained data using the Hilbert transform and that we could detect a slightly better time resolution using Hilbert transform in comparison to the Wavelet transform, led us to settle on Hilbert transform for this thesis. One drawback of the Hilbert transform, however, is its sensitivity to noise (Huang et al., 1998). This is why in all our signal analyses we filter the signal first by using a butterworth filter (Stephen Butterworth, 1930) to reduce high-frequency noise such that the following analysis via Hilbert transform is more robust (see also Meeuse et al., 2019).

1.4 Perturbations of oscillating systems

Even though we can simulate the behavior of oscillatory systems in isolation, this situation is barely reflecting the natural environment these systems face in the real world. In nature, systems from the molecular up to organism scales interact with each other or are subjected to perturbations that occur in the environment. The effect of a perturbation on an oscillating system can depend on the oscillator phase at which the perturbation is applied. Experimentally, a typical procedure would consist of assessing the phase of the oscillator, perturb the system at a desired oscillator phase followed by reassessing the oscillator phase after the perturbation. Assessment of the effect for the full range of oscillator phases will lead to so-called phase response curves where the effect size (e.g. phase shift) is shown for all the different oscillator phases at which the perturbation was

applied. Normally, the phase shift resulting from a perturbation is measured after several cycles as the system might need time to fully recover from the perturbation.

Generally, a simple phase-only model in which the full complexity of the oscillation is reduced to a single instantaneous phase variable that describes the progression through the cycle, responds to a perturbation with a certain phase shift independently of when the perturbation is applied. However, the more frequent behavior seen in phase response curves is that the phase shift varies depending on the oscillator phase. An excellent example can be given by the circadian rhythm entrainment by light, which can be interpreted as a periodic perturbation that feeds into the system. The normal light impulse during the day is mainly responsible to fine-tune the circadian rhythm and to synchronize it with the duration of one earth rotation around its axis. However, a strong phase shift to the light impulse happens when light is perceived during the nights, as it occurs when we fly to a different time zone, resulting in the adjustment of the circadian rhythm to the shifted day and night cycle by progressively either delaying or advancing the phase over a certain time period until the circadian rhythm is again synchronized with the day-night cycle (Vitaterna et al., 2001).

1.5 Synchronization of coupled oscillators

Instead of an input like the light pulse from the sun during the day, we can also imagine two oscillators influencing each other by triggering phase responses in each other. Considering both oscillators are oscillating with appropriate frequencies within a certain range to affect each other, they can synchronize their rhythm by adjusting their individual angular speed according to one another. This, however, can only occur if these oscillators can “sense” each other, e.g. they are coupled. The coupling can, for example, be mechanical as in the case of oscillating masses connected by a spring or by signaling in genetic oscillators. In general, it leads to a reduction of the phase difference of the two oscillators over time until their periodic behavior is in synchrony. The first investigation of synchronization was by the physicist Cristiaan Huyens, who described the synchronization of a pair of pendulum clocks that were hanging on a common support. Arthur Winfree was one of the first to describe this phenomenon using a reductionist approach in which he described each oscillator in the system by a single phase variable only, allowing to draw general conclusions for the synchronization of oscillator behavior (Winfree, 1967). Each oscillator in the system could emit a pulse and thus perturb the phase velocity of all other oscillators. To

mathematically investigate synchronization, it is necessary to know both the phase response curves and the shape of the pulses, and Winfree could show that a completely disordered system of oscillators is able to synchronize oscillatory behavior (Winfree, 1967, 1980).

Synchronization of cellular oscillators is important and unsynchronized oscillators can lead to detrimental consequences on the phenotype. In the zebrafish segmentation clock, autonomous oscillators of neighboring cells are coupled via intercellular Delta-Notch signaling (Jiang et al., 2000) and reduced coupling has been shown to lead to unsynchronized cell oscillations (Riedel-Kruse et al., 2007), increased period and misregulated segment length (Herrgen et al., 2010). In order to shed light on the molecular design principles on how the coupling of individual oscillators is achieved, Kim et al. 2010 investigated multiple architectures and found that the coupling of biological oscillators is usually achieved through positive feedback. This positive feedback can occur via either double-positive or double-negative interactions of the coupling agent with the two oscillator it needs to synchronize (Kim et al., 2010), with double-positive interaction being advantageous for stable periods and amplitudes of coupled oscillators with a short time delay while double-negative interactions are less sensitive to differences in the coupling strengths (Kim et al., 2010).

1.6 The model organism *Caenorhabditis elegans*

Oscillating systems have been studied in a variety of organisms. In this work, we investigate a developmental oscillator that acts in the larval development of the nematode *Caenorhabditis elegans (C. elegans)*. I will first introduce the model organism *C. elegans*, its development and the timing thereof, followed by a general introduction on transcription and transcriptional regulation in order to prepare the reader for the *C. elegans* developmental oscillator.

1.6.1 *C. elegans*

The nematode *C. elegans* is a small roundworm that feeds on bacteria that grow on rotting organic material. In the lab, *C. elegans* is cultured on agar petri dishes containing *Escherichia coli* bacteria (OP50). Its small size ranging from 0.25mm as newly hatched larvae up to 1mm long adult worms, the relatively fast life cycle and the existence of self-fertilizing hermaphrodites make it an attractive organism in multiple fields of studies (Corsi et al., 2015). Additionally, *C. elegans* is transparent, a characteristic that has been exploited extensively by the pioneer John Sulston to

investigate cell ancestries in *C. elegans*, finally culminating in the exhaustive description of the invariant cell lineage during *C. elegans* development (Sulston and Horvitz, 1977; Sulston et al., 1983). After embryonic development, *C. elegans* develops through four larval stages (L1, L2, L3 and L4) until it reaches adulthood after roughly 2.5 days at 25°C. An adult hermaphrodite consists of 959 somatic nuclei, each contributing to a defined tissue such as epidermis, muscle, digestive system, nervous system and reproductive tissues.

Worms facing unfavorable conditions during larval development such as limited food, crowding or high temperature have the ability to form so-called dauer stage larvae, an optional L3 stage that exists parallel to the normal development (Cassada and Russell, 1975; Golden and Riddle, 1984). Worms respond differently to starvation depending on the developmental stage at which they experience starvation. Starvation right after hatching results in L1 worms that arrest development and manage to survive as such for a limited time period (Johnson et al., 1984; Muñoz and Riddle, 2003). Starvation as well as crowding in L1 results in the formation of dauer diapause animals, an alternative L3 stage in which worms are resistant to starvation up to months (Cassada and Russell, 1975; Golden and Riddle, 1984). If food becomes available during the dauer diapause, worms are able to resume development and molt into an L4 stage. Besides these two dramatic forms of starvation responses, it has been shown that if worms experience starvation after the first larval stage, they are able to arrest at specific developmental "checkpoints" (Schindler et al., 2014). *C. elegans* might need to induce a specific gene expression to arrest at such checkpoints and survive the starvation period. The identity of such a specific gene expression state and to which extent oscillatory gene expression is involved in the regulation of these checkpoints remains to be determined however.

1.6.2 *C. elegans* larval development and its timing

At the end of each of the four larval stages, worms undergo molting, characterized by a sleep-like period of inactivity, called lethargus.

The repetitive molting process in which worms synthesize a new exoskeleton (termed the cuticle) and shed the old one is summarized in the following section 1.6.2.1. Importantly, the repetitive production and shedding of the cuticle have to be precisely regulated in a rhythmic manner and coordinated in time with the linear development of the worms, which is regulated by the heterochronic pathway. The heterochronic pathway consists of a cascade of miRNAs and mRNAs

responsible for consecutive induction of stage-specific gene expression programs that lead to the progression of development through successive larval stages (Ambros and Horvitz, 1984). This pathway and its components were elucidated by mutation experiments where the heterochronic genes mutants showed aberrant timing, with either precocious or retarded development, meaning these mutants executed developmental events either too early or too late relative to wild-type worms (Ambros and Horvitz, 1984). It is likely that *C. elegans* larval development requires a controlled interaction between rhythmic and linear regulatory processes to ensure synchronized molting in regard to the linear development. I will introduce molting in *C. elegans*, followed by its temporal regulation and its interaction with the linear development.

1.6.2.1 Molting in *C. elegans*

The molt and lethargus

As mentioned above, molting refers to the process during which *C. elegans* replaces an existing flexible collagenous cuticle with a new and bigger one. Interestingly, all nematode species undergo four larval molts. Molts can be characterized by a sequence of events starting with the lethargus, characterized by a reduction of feeding behavior and locomotion (Raizen et al., 2008). Lethargic behavior is thought to be mediated by high activity of the RIS neuron at the beginning of lethargus (Bringmann, 2011; Turek et al., 2015) and secretion of the neuropeptide FLP-11. Additionally, the RIA neuron is also involved in regulating both lethargus induction via the neuropeptide NLP-22 and resumption of locomotion after lethargus by a yet unknown mechanism (Nelson et al., 2013). Even though we refer to lethargus as a quiescent state, worms do show bouts of activity during lethargus which last from 2 to 100 seconds (Iwanir et al., 2013). During lethargus, the old cuticle is cleaved off the epidermis in a process termed apolysis followed by synthesis of the new cuticle. Finally, worms exit lethargus and escape from the cuticle, a process known as ecdysis (Singh, 1978).

Apolysis and ecdysis

As the cuticle is attached to the underlying epidermis, it needs to be released before a new cuticle can be built. This process is known as apolysis. Reductases such as TRXR-1 and GSR-1 presumably play a specific role in apolysis by reducing the disulfide bonds between collagens in the cuticle, thus promoting the removal of the old cuticle (Stenvall et al., 2011). Additionally,

putative protease inhibitors such as the MLT-11 are also involved in the regulation of apolysis and they are specifically expressed in the intermolts, preventing precocious cleavage of the cuticle by proteases (Frand et al., 2005). Following apolysis, the new cuticle is synthesized after which the old cuticle is released in a process called ecdysis. The molecular process of ecdysis is still under investigation but two metalloproteases, NAS-36 and NAS-37, as well as the Z-like cysteine protease CPZ-1, are known to be required to degrade the old cuticle (Davis et al., 2004; Hashmi et al., 2004).

1.6.2.2 *The cuticle and its structural components*

The cuticle is an exoskeletal structure that is mainly responsible for the protection of the worm from environmental and mechanical stress. The synthesis of the new cuticle is achieved by the secretion of cuticular components from the apical membranes of the hypodermis and the old cuticle is partially recycled by endocytic processes. The hypodermal cells have a high transcriptional potential due to endoreplication of their DNA content, thus allowing them to quickly provide components for the new cuticle. The cuticle consists mainly of collagens, Glycine-X-Y tripeptide repeat proteins, where X is frequently represented by proline and Y by hydroxyproline. Over 170 collagen genes have been identified, of which 21 result in specific phenotypes when mutated such as DumPY (*Dpy*), ROLler (*Rol*), BLIster (*Bli*), SQuaT (*Sqt*), Ray AbnorMal (*Ram*) and LONg (*Lon*) (Page and Johnstone, 2007). In addition to collagen, other components of the cuticle are cuticlins as well as lipids which are located in the epicuticle. The composition of the cuticle is similar across larval stages, however, L1, dauer diapause and adult worms contain a specialized structure termed alae along the anterior-posterior axis (Cox et al., 1981; Johnstone, 2000). Additionally, the cuticle is attached to muscles via dense bodies to transmit force onto the cuticle which allows worms to move forward. Movement is achieved by the friction of the cuticle with the surface on which the worms are moving and it is hypothesized that specialized circumferential ridges on the cuticle termed annuli allow for flexibility of the cuticle during movement (Shaw et al., 2018).

In addition to the external cuticle, internal cuticular structures can be found in the buccal cavity, the pharynx, rectum, vulva, excretory duct and excretory pore in *C. elegans* (Lažetić and Fay, 2017). These internal cuticles consist mainly of collagens with the exception of the pharyngeal cuticle which contains chitin, resulting in a more rigid structure. This fact prevents the pharynx

from growing continuously, hence it grows periodically by reconstitution of a new, bigger pharynx during the molts when the old cuticle is released (Knight et al., 2002).

1.6.2.3 Timing of the molt

Proper timing of cuticular components and signaling molecules are necessary for molting, and multiple pathways are implicated in their regulation. Hence it is not surprising that a genome-wide RNAi screen has identified 159 genes involved in the molting process (Frand et al., 2005). Two important regulators of molting are the nuclear hormone receptors NHR-23 and NHR-25 (Gissendanner and Sluder, 2000; Kostrouchova et al., 1998). Interestingly, these genes encode homologs of DHR-3 and FTZ-F1 in drosophila and RORα and SF1 in humans respectively. DHR-3 and FTZ-F1 are both implicated in the ecdysone response in *Drosophila melanogaster* to induce stage-specific responses such as pre-pupal to pupal transition or larval metamorphosis ((Broadus et al., 1999; Lam et al., 1999; Lavorgna et al., 1993; Thummel, 2001). Finally, RORα is known for many functions, including its role in the circadian rhythm as we have already seen above. Activation of nuclear receptors usually happens via steroid hormones that are derivatives of cholesterol. However, since *C. elegans* is not able to synthesize de novo cholesterol, it has to obtain cholesterol from food sources. If food does not contain cholesterol, worms are unable to develop normally and develop molting phenotypes, suggesting an important role of cholesterol (and its derivatives) in regulating molting. Nevertheless, many questions are still open, especially since out of the 284 nuclear hormone receptors, the functions of only a few are well understood and their ligands known.

As mentioned earlier, the heterochronic pathway regulates linear development and has to be synchronized with the repetitive developmental events. In fact, both precocious (*lin-14*, *lin-28*, *lin-41* and *hbl-1*) and retarded (*lin-4*, *lin-29* and *let-7*) heterochronic loss of function mutants display either fewer or supernumerary molts respectively (Lažetić and Fay, 2017), demonstrating a (direct) link between these pathways. Importantly, a potential connection between the linear heterochronic timing and the timing of molts was reported by Ruaud and Besserau (Ruaud, 2006) to be important, as they showed larval lethality in the case of unsynchronized timing.

1.6.3 Additional rhythmic processes during larval development

Besides molting, an additional rhythmic process during the *C. elegans* larval development is the proliferation of seam cells, stem cell-like cells that are symmetrically aligned along the anterior-posterior axis of the worm and that produce the lateral ridges in the cuticle in L1 larvae and adults called alae. At the end of the first three larval stages, most of these cells undergo asymmetric cell divisions, resulting in one seam cell and one hypodermal daughter cell. The hypodermal cell endoreplicates its DNA and then fuses with the hyp7 syncytium (Hedgecock and White, 1985) which constitutes the main skin cell in *C. elegans*. During the L4-to-adult transition, the seam cells do not divide anymore but instead terminally differentiate and fuse to form a seam cell syncytium which contributes to the adult cuticle synthesis. The timing of these coordinated cell divisions and terminal differentiation is altered in heterochronic pathway mutants (Ambros and Horvitz, 1984). Precocious heterochronic mutants skip cell divisions whereas, in retarded heterochronic mutants, cell divisions are reiterated. Interestingly, molting is affected similarly to the cell divisions in these mutants and is either skipped or reiterated in precocious or retarded heterochronic mutants, respectively. This indicates a potential coupling between these two processes, which is further supported by the observation that uncoupling of the molting timer and the cell cycle is possible in L2 using the small molecule DMPP, activating nicotinic receptors (Ruaud, 2006)which delays the cell cycle in L2 larvae but leaves the timing of the molts unaffected.

1.7 Gene expression and transcriptional regulation

Despite the vast variability in cell types found in organisms, these cells share the same genetic information stored in the form of DNA. Nevertheless, cells can develop into distinct entities called cell types to fulfill their specific function. This development is achieved by cell-type-specific regulation of the strength and dynamics of gene expression. Gene expression can be regulated on many different scales such as transcription (production of mRNA), alternative splicing, nuclear export of the mRNA, cytosolic localization of the mRNA, degradation of mRNA, translation efficiency and speed as well as protein degradation and localization to ultimately lead to the necessary amount of gene products necessary for differentiation of cells into their specific cell types (Alberts et al., 2011). The steps of gene expression regulation relevant for this thesis will be discussed in further detail below.

1.7.1 Transcription

Transcription is the first step in converting genetic information into expressed information. In eukaryotes, DNA dependent RNA polymerases I, II and III (Pol I, II and III) produce RNA copies from the genetic information stored in the form of DNA. Pol II transcribes messenger RNAs (mRNAs) of protein-coding genes to transfer the genetic information for protein synthesis, microRNAs (miRNAs) and most small nuclear RNAs (snRNAs). I will focus on Pol II specifically, due to its role in transcribing protein-coding genes. Transcription starts with the recognition of the promoter region upstream of a gene by general transcription initiation factors (GTF) and the formation of the pre-initiation complex (PIC). Contrasting with mammals, promoters are less well characterized in *C. elegans*, as roughly 70% of all genes undergo trans-splicing, a process in which the 5' end of the nascent transcript is trimmed off and replaced with a spliced leader consisting of 22 nucleotides (Allen et al., 2011; Blumenthal, 2005; Hastings, 2005). After recruitment of the PIC to the promoters, the PIC is initially paused at the promoter as the C-terminal domain (CTD) of Pol II is in an unphosphorylated state (reviewed in Cramer 2019; Sainsbury, Bernecky, and Cramer 2015). Upon multiple steps of phosphorylation at the CTD, Pol II is released from the paused state and elongates the nascent mRNA transcript. Additional processing factors are recruited that ensure capping, splicing and poly-A tailing of the nascent mRNA molecule. At the end of mRNA synthesis, when Pol II reaches the 3' untranslated region (3' UTR), Pol II is dephosporylated, the nascent transcript is cleaved and poly-adenylated at the poly-A site (Cramer, 2019).

1.7.2 Transcriptional regulation

Even though transcription is probably the most highly regulated step, many additional steps such as specific transcript turnover rates or regulation of mRNA processing in the life of a transcript are precisely regulated and influence the transcript abundance (Sperling, 2007). Most relevant for this thesis, however, is the transcriptional regulation with particular focus on the regulation by transcription factors. Apart from the GTFs mentioned above many gene regulatory transcription factors exist which encode DNA binding proteins characterized by structurally conserved motifs that allow regulating transcription. Depending on the DNA sequence, they display different binding affinity. A single transcription factor usually binds multiple slightly different sequences

with different affinities. Hence the preferred binding sequence is usually represented by a so-called binding motif, summarizing the preferred nucleotide sequence with every nucleotide in the motif accompanied by a certain percentage of occurrence for each position in the motif. Some transcription factors have the capacity to even bind multiple DNA motifs (Siggers and Gordân, 2014). Furthermore, the transcriptional activity can be influenced through cis-regulatory DNA elements, so-called enhancers that activate transcription either locally or distant (Peng and Zhang, 2018). Many of the regulatory transcription factors can homo- or heterodimerize with other transcription factors or additional non-DNA binding co-factors which alters binding affinities and thus adds another layer of complexity (Reiter et al., 2017; Siggers et al., 2011; Slattery et al., 2011). In summary, regulation of gene expression is a highly complex process and understanding the involved transcription factors with their impact on gene expression will help us to gain insights into the regulation of cell fate choices and development in general.

1.8 mRNA oscillations during *C. elegans* larval development

As we have seen, oscillations in gene expression are a widespread phenomenon in biology and can serve multiple purposes, as for example synchronization to the environment or the timing of developmental events. Recently, another occurrence of an oscillating system has been discovered by Hendriks et al. and others (Grün et al., 2014; Hendriks et al., 2014; Kim et al., 2013a). Hendriks et al. identified oscillations on the mRNA level by analyzing an RNA sequencing time course of synchronously developing L3 until early adult worms cultured at 25°C and sampled in 1hr intervals. The identified transcript oscillations were characterized by a shared 8-hr period and were selected based on a somewhat arbitrary fold change of at least >2.1-fold. Compared to other oscillating systems where typically observed changes are about 2-fold (Duffield, 2003; Hughes et al., 2009), the fold changes in *C. elegans* are extremely high with many exceeding 10-fold which led to the hypothesis that they are biologically relevant and functional. Remarkably, such oscillations were detected in 2,718 transcripts, comprising around 20% of the transcriptome during larval development. Detailed analysis revealed that the peak phases of these transcript oscillations can vary extensively, spanning the full phase range from 0° - 360° with high amplitudes observable for every peak phase. Specific investigation of similar components of the cuticle revealed that these shared similar peak phases as exemplified by the *sqt/rol* genes that peaked around 125° or the collagens which peaked mostly between 150 and 250°. This suggested a physiological

importance of the oscillations as they could serve to timely deliver the proteins needed for building the cuticle.

To determine if transcription might be responsible for the rhythmic abundance of mRNA molecules, Hendriks et al. 2014 investigated intronic vs exonic reads in their total RNA sequencing time course. The idea was that intronic reads serve as a proxy for transcription by representing pre-mRNA levels. Indeed for cases where they could see sufficient levels for both exonic and intronic reads, the intronic reads were also rhythmically abundant, however, preceding the exonic reads in terms of peak occurrence by roughly 15min. This is an expected result under the assumption that mature mRNA is more stable than pre-mRNA and given that the processing from pre-mRNA to mRNA takes time even though it happens co-transcriptionally. Hence Hendriks et al. 2014 reasoned that transcription is responsible for the rhythmic mRNA production. However, intronic read counts have to be interpreted with caution as they could also represent spliced out introns and do not necessarily reflect pre-mRNA abundance. It further remained possible that mechanisms such as rhythmic splicing or additional post-transcriptional regulation are needed to ultimately lead to oscillating mature mRNA levels. In particular, if mRNA molecules were to be stable enough, their dynamics would not reveal oscillations but rather show a step-like increase. Hence, increasing the degradation rate on the post-transcriptional level by miRNAs would aid to generate oscillating patterns of abundance. On the other hand, oscillating miRNAs could also be used to modulate mRNA oscillations to either increase or dampen the amplitude of the oscillation depending on whether the miRNA oscillates in phase or out of phase with the mRNA. In fact, damping of oscillations was shown for the *lin-14* mRNA oscillation as a result of its regulation by the miRNA *lin-4* (Kim et al., 2013).

RT-qPCR results from the oscillations of selected transcripts revealed that the oscillation period scales inversely with temperature, e.g. lower temperatures lead to a longer period. This behavior is comparable to the segmentation clock but is in stark contrast to the circadian clock, where periods are constant despite temperature changes within a physiological range, thus these findings argued against the existence of temperature compensation (see section 1.1.1) in the *C. elegans* oscillator.

An additional important aspect of the oscillations in *C. elegans* was observed when worms were released from dauer as they resumed oscillations in a highly similar manner as in continuous

development, suggesting that the ability to induce oscillations does not depend on the life history of worms.

Despite the characterization of mRNA oscillations that our group and others provided, many open questions still remained such as the identity of involved transcription factors, the functional outputs of the oscillations and whether there is one oscillator regulating all oscillating genes or multiple oscillators acting in concert and synchronized with one another. In the case of multiple oscillators at work, it would be interesting to investigate the molecular components responsible for the interaction and synchronization between these oscillators and between oscillators and developmental events. Even though the studies by Kim et al. 2010 (see section 1.5) to investigate coupling mainly revolved around synchronization between oscillators of different cells, we might then uncover common principles in the synchronization of the *C. elegans* oscillators.

1.8.1 BLMP-1: A candidate clock component

In order to find components of the *C. elegans* oscillator and since transcription was likely to be a key driver for oscillatory transcript abundance in the worm, our initial investigations for this thesis revolved around oscillating transcription factors and their importance in the rhythmic larval development.

Based on previously identified core clock genes in the circadian rhythm, we focused on empirically determined phenotypic profiles characteristic for core clock components such as an altered period length by at least 15% (Takahashi, 2004) or a complete loss of the rhythm (Bunger et al., 2000). It should be noted that null mutations of some clock components such as *Per1*/*Per2* or *Cry1/Cry2* reveal less severe phenotypes and only cause strong phenotypes if mutated together. Additionally, another class of non-essential clock components exists composed of genes that are clearly involved in the clock mechanism yet not essential for generating the rhythm (Bae et al., 2001; Van Der Horst et al., 1999; Vitaterna et al., 1999; Zheng et al., 2001).

Despite the challenges of finding components with subtle phenotypes, we aimed to identify core factors of the oscillator resulting in strong developmental phenotypes and focused on the 92 oscillating transcription factors previously identified (Hendriks et al., 2014). Among these, NHR-23, NHR-25, BED-3, GRH-1, MYRF-1 and BLMP-1 showed disrupted larval development in a luciferase assay RNAi screen (Meeuse et al., unpublished) in which RNAi of *nhr-23, bed-3, myrf-*

1 and *grh-1* each led to larval arrest / lethality whereas *nhr-25* and *blmp-1* RNAi resulted in aberrant larval stage durations compared to mock conditions. In particular, *blmp-1* RNAi shortened the intermolts but lengthened the molts, suggesting that reduction of *blmp-1* levels might internally affect the regulation of rhythmically occurring processes, e.g. entry and exit of molts without changing the overall duration of the larval stage (Meeuse et al., unpublished). Hence *blmp-1* might belong to the class of non-essential genes but nevertheless still execute important regulations of the oscillator(s).

BLMP-1 is a transcription factor containing an N-terminal SET domain and five zinc fingers at the C-terminus and is expressed in hypodermal, vulval, and intestinal cells, as well as DTCs (Huang et al., 2014). BLMP-1 shares 27% identity to mouse B lymphocyte-induced maturation protein 1 (Blimp-1) and 26% identity to PRDI-BF1, the human positive regulatory domain I-binding factor (Huang et al., 2014). More specifically, the conservation in the SET domain and the zinc finger domains is at 43% and 70% respectively (Tunyaplin, 2000). The transcription factor was reported to be involved in the terminal differentiation epidermal cells (Magnúsdóttir et al., 2007) as well as B and T cells and act mainly as a repressor (Nutt et al., 2007; Turner et al., 1994). Furthermore, it has been previously implicated in developmental timing and maturation (Agawa et al., 2007; Horn et al., 2014; Huang et al., 2014), which I will illustrate using the following examples.

In Drosophila, the homolog of BLMP-1, *dBlimp-1,* was shown to be induced by 20-hydroxyecdysone and is suspected to control the timing of βFTZ-F1 expression to ensure developmental timing in the ecdysone induced pathway (Agawa et al., 2007). *dBlimp-1* RNAi leads to prepupal lethality and precocious expression of βFTZ-F1 suggesting it negatively regulates βFTZ-F1 to ensure proper timing of its peak. Interestingly, in *dBlimp-1* RNAi conditions, βFTZ-F1 decreases earlier as compared to the mock condition. The shift in βFTZ-F1 expression is accompanied by the fact that Drosophila flies fail to pupate (Agawa et al., 2007).

In *C. elegans,* Horn et al. 2014 identified *blmp-1* as a heterochronic gene that suppresses the epidermal heterochrony of *dre-1* hypomorph mutants (*dh99*). In particular, *blmp-1(tm548); dre-1(dh99)* double mutants rescued the precocious seam cell fusion of *dre-1* mutants in L3 (Horn et al., 2014). Close observation of *blmp-1(tm548)* mutants revealed that these worms displayed heterochronic phenotypes as well, as they did not produce complete alae of the adult cuticle.

However, seam cell division as well as fusion happened correctly. Due to the fact that the incomplete alae were still observed in the double mutant *blmp-1; dre-1*, it was suggested that *blmp-1* acts downstream of *dre-1*. Another timing defect of *blmp-1* mutants was observed for the gonadal turn which normally occurs roughly at 31 hours of development. *Blmp-1* mutants executed the gonadal turn precociously and also often failed to complete the turn, resulting in gonadal growth towards head and tail instead of returning towards the body center (Horn et al., 2014; Huang et al., 2014). This regulation seemed to be dependent on *unc-5* which is normally repressed by BLMP-1 in the dorsal tip cell (DTC) until BLMP-1 disappears and *unc-5* expression initiates the dorsal turn (Huang et al., 2014). The downregulation of BLMP-1 in the DTC seems to depend redundantly on *daf-12*, *lin-29* and *dre-1* (Huang et al., 2014), which act on both the transcriptional and post-transcriptional level to downregulate *blmp-1*. Furthermore, *blmp-1* mutants were observed to be dauer defective (Daf-d) as they could not form dauer worms, in contrast to *dre-1* mutants which showed an increased dauer formation (Horn et al., 2014). Opposite effects could be seen in *blmp-1* overexpression worms which were characterized by a retarded gonadal turn (Huang et al., 2014), enhanced *dre-1* molting phenotypes and synthetic lethality with *dre-1 (dh99)*.

Apart from this specific role in DTC migration, little is known about BLMP-1's function in timing development. It has been shown that BLMP-1 regulates the transcription factor *bed-3* which is involved in vulva cell division and molting (Yang et al., 2015).

As *blmp-1* is expressed in multiple tissues and shows oscillation in our previous RNA sequencing data, an attractive idea is that BLMP-1 orchestrates rhythmic processes and might synchronize gene expression oscillations with other rhythmic or stage-specific processes like molts or DTC migration respectively. In order to do so, BLMP-1 protein either has to show oscillations as well or at the BLMP-1 transcription factor activity needs to be rhythmic.

1.9 Aims of this thesis

While the discovery of extensive oscillatory gene expression during C. *elegans* larval development provided means to study a developmental oscillator in a multicellular organism, many open questions were still to be addressed. Apart from an initial characterization of the oscillations in late larval stages (Hendriks et al., 2014), little was known about the oscillator behavior at the

beginning and the end of larval development, not to mention the molecular architecture of the oscillator or how the oscillator and larval development are related.

In order to address these open questions, we planned to sequence worms for all larval stages and into adulthood and expected to see a developmental oscillator at work, starting and ceasing oscillations at the beginning and the end of larval development respectively. Provided we obtain highly time-resolved RNA sequencing time courses from the beginning until the end of larval development and that oscillations emerge and cease together with development, we aimed to further characterize oscillator behavior at the beginning and the end of oscillations. Inspired by bifurcation theory, we aimed to characterize the possible underlying network(s) by at least rejecting some molecular architectures depending on the behaviors we observe. In parallel, we planned to investigate the link between larval development and oscillatory gene expression by measuring larval stage durations in combination with transcriptional reporter studies using time-lapse microscopy. An important open question was whether oscillatory gene expression and developmental events such as molting are indeed (directly) coupled or if they are independently regulated but precisely timed to occur at the same time.

Despite an initial characterization by (Hendriks et al., 2014), little was known about the transcriptional regulation of oscillatory gene expression. Although transcription by Pol II was suspected to be a key driver for oscillatory transcript abundance, intronic read counts serving as a proxy for transcription were the only observation supporting this hypothesis. Thus we aimed to provide further evidence with the investigation of transcriptional reporters by RT-qPCR time course experiments during larval development.

Additionally, identification of potential transcription factors involved in the regulation of the developmental oscillator was important to further explore the regulatory network underlying the *C. elegans* oscillator. Based on the hypothesis that oscillatory gene expression and rhythmic larval development are linked, we decided to follow up on the transcription factor BLMP-1 based on the initial results obtained in an RNAi screen for developmental phenotypes. Thus, one important part of this thesis included the characterization of the effects arising from BLMP-1 loss of function, both in terms of developmental progression and gene expression oscillations.

State-of-the-art single worm methods and new analysis strategies had to be developed in our lab and were used in combination with genetic tools to address the above-mentioned questions.

2 Results

2.1 Manuscript: State transitions of a developmental oscillator

Gert-Jan Hendriks and Yannick Hauser performed RNA sequencing time courses. Milou Meeuse and Yannick Hauser analyzed RNA sequencing data. Milou Meeuse performed and analyzed luciferase assays. Guy Bogaarts developed the graphical user interface for the luciferase data. Yannick Hauser acquired and analyzed single worm imaging data. Jan Eglinger wrote the KNIME workflow for the single worm imaging. Charisios Tsiairis conceived parts of the analysis. Helge Großhans, Milou Meeuse and Yannick Hauser conceived the project and wrote the manuscript.

Developmental function and state transitions of a gene expression oscillator in *C. elegans*

Milou W.M. Meeuse[1,2]*, Yannick P. Hauser[1,2]*, Gert-Jan Hendriks[1,2], Jan Eglinger[1], Guy Bogaarts[3], Charisios Tsiairis[1], Helge Großhans[1,2,4]

[1] Friedrich Miescher Institute for Biomedical Research (FMI), Maulbeerstrasse 66, CH-4058 Basel.

[2] University of Basel, Petersplatz 1, CH-4001 Basel.

[3] University Hospital, Spitalstrasse 21, CH-4031 Basel.

[4] Corresponding Author and Lead Contact: helge.grosshans@fmi.ch.

* equal contribution.

Abstract

Gene expression oscillators can structure biological events temporally and spatially. Different biological functions benefit from distinct oscillator properties. Thus, finite developmental processes rely on oscillators that start and stop at specific times; a poorly understood behavior. Here, we have characterized a massive gene expression oscillator comprising >3,700 genes in *C. elegans* larvae. We report that oscillations initiate in embryos, arrest transiently after hatching and in response to perturbation, and cease in adults. Experimental observation of the transitions between oscillatory and non-oscillatory states at a resolution where we can identify bifurcation points reveals an oscillator operating near a Saddle Node on Invariant Cycle (SNIC) bifurcation. These findings constrain the architecture and mathematical models that can represent this oscillator. They also reveal that oscillator arrests occur reproducibly in a specific phase. Since we find oscillations to be coupled to developmental processes, including molting, this characteristic of SNIC bifurcations thus endows the oscillator with the potential to halt larval development at defined intervals, and thereby execute a developmental checkpoint function.

Introduction

Gene expression oscillations occur in many biological systems as exemplified by circadian rhythms in metabolism and behavior (Panda et al., 2002), vertebrate somitogenesis (Oates et al., 2012), plant lateral root branching (Moreno-Risueno et al., 2010), and *C. elegans* larval development (Hendriks et al., 2014). They are well-suited for time-keeping, acting as molecular clocks that can provide a temporal, and thereby also spatial, structure for biological events (Uriu, 2016). This structure may represent external time, as illustrated by circadian clocks, or provide a temporal organization of internal processes without direct reference to external time, as illustrated by somitogenesis clocks (Rensing et al., 2001).

Depending on these distinct functions, oscillators require different properties. Thus, robust representation of external time requires a stable period, i.e., the oscillator has to be compensated for variations in temperature and other environmental factors. It also benefits from a phase-resetting mechanism to permit moderate realignments, if needed, to external time. Intuitively, either feature seems unlikely to benefit developmental oscillators. By contrast, because developmental processes are finite, e.g., an organism has a characteristic number of somites, developmental oscillators need a start and an end. How such changes in oscillator activity occur *in vivo*, and which oscillator features enable them, is largely unknown (Riedel-Kruse et al., 2007; Shih et al., 2015).

Here, we characterize the recently discovered '*C. elegans* oscillator' (Hendriks et al., 2014; Kim et al., 2013) at high temporal resolution and across the entire period of *C. elegans* development, from embryo to adult. The system is marked by a massive scale where ~3,700 genes exhibit transcript level oscillations that are detectable, with large, stable amplitudes and widely dispersed expression peak times (i.e., peak phases), in lysates of whole animals. For the

purpose of this study, and because insufficient information exists on the identities of core oscillator versus output genes, we define the entire system of oscillating genes as ‘the oscillator’. We demonstrate that the oscillations are coupled to molting, i.e., the cyclical process of new cuticle synthesis and old cuticle shedding that occurs at the end of each larval stage. We observe and characterize onset and offset of oscillations both during continuous development and upon perturbation, and find that these changes in the state of the oscillator system (or bifurcations) occur with a sudden change in amplitude. They also occur in a characteristic oscillator phase and thus at specific, recurring intervals. Because of the phase-locking of the oscillator and molting, arrests thus always occur at the same time during larval stages, around molt exit. This time coincides with the recurring windows of activity of a checkpoint that can halt larval development in response to nutritionally poor conditions. Hence, our results indicate that the *C. elegans* oscillator functions as a developmental clock whose architecture supports a developmental checkpoint function. Indeed, the features of the bifurcations constrain oscillator architecture, excluding a simple negative-loop design, and possible parameters of mathematical models.

Results

Thousands of genes with oscillatory expression during the four larval stages

Although previous reports agreed on the wide-spread occurrence of oscillatory gene expression in *C. elegans* larvae (Grün et al., 2014; Hendriks et al., 2014; Kim et al., 2013), the published data sets were either insufficiently temporally resolved or too short to characterize oscillations across *C. elegans* larval development. Hence, to understand the extent and features of these oscillations better, including their continuity throughout development, we performed two extended time course experiments to cover the entire period of post-embryonic development plus early adulthood at hourly resolution. We extracted total RNA from populations of animals synchronized by hatching in the absence of food. The first time course (designated TC1) covered the first 15 hours of development on food at 25°C, the second time course (TC2) covered the span of 5 hours through 48 hours after plating at 25°C. [Fig. S1A provides a summary of all sequencing time courses analyzed in this study.] The extensive overlap facilitated fusion of these two time courses into one long time course (TC3) (Fig. S1B), and a pairwise-correlation plot of gene expression over time showed periodic similarity that was repeated four times (Fig. 1A, light-gray off-diagonals), presumably reflecting progression through the four larval stages.

The larger dataset enabled us to improve on the previous identification of genes with oscillatory expression (Hendriks et al., 2014). Using cosine wave fitting, and an amplitude cut-off of $2^{0.5}$, we classified 3,739 genes (24 % of total expressed genes) as ‘oscillating’ (i.e., rhythmically expressed) from TC2 (Fig. 1B, S1C and Table S1; Methods). Relative to the previous result of 2,718 oscillating genes (18.9% of total expressed genes) in mRNA expression data of L3 and L4 animals (Hendriks et al., 2014), this adds 1,240 new genes and excludes 219 of the previously annotated oscillating genes. We consider this latter group to be most likely

false positives from the earlier analysis, resulting from the fact that some genes behave substantially different during L4 compared to the preceding stages as shown below.

Visual inspection of a gene expression heatmap of the fused time course (TC3; Fig. 1C) revealed four cycles of gene expression for the oscillating genes. Oscillations were absent during the first few hours of larval development as well as in adulthood, from ~37 hours on, and both their onset and offset appeared to occur abruptly. We will analyze these and additional features of the system and their implications in more detail in the following sections.

'Oscillating' genes are expressed in several tissues with dispersed peak phases

An examination of the calculated peak phases confirmed the visual impression that individual transcripts peaked at a wide variety of time points, irrespective of expression amplitude (Fig. 1D). In circadian rhythms, peak phase distributions are typically clustered into three or fewer groups when examined in a specific tissue (Koike et al., 2012; Korenčič et al., 2014). However, the identity of oscillating genes differs across cell types and tissues, and for those genes that oscillate in multiple tissues, phases can differ among tissues (Zhang et al., 2014). Hence, we wondered whether the broad peak phase distribution was a consequence of our analysis of RNA from whole animals, whereas individual tissues might exhibit a more defined phase distribution.

To understand in which tissues oscillations occur, we utilized a previous annotation of tissue-specifically expressed genes (Cao et al., 2017). 1,298, and thus a substantial minority (~35%) of oscillating genes, fell in this category for seven different tissues. They were strongly (~2.5-fold) enriched in the hypodermis (epidermis) and pharynx, and more modestly (≤1.5-fold) in glia and intestine (Fig. 1E). By contrast, oscillating genes were greatly depleted from body wall muscle, neurons, and gonad. Hence, oscillatory gene expression occurs indeed in multiple

tissues. However, although peak phase distributions deviated for each tissue to some degree from that seen for all oscillating genes, they were still widely distributed for each individual tissue (Fig. 1F).

We conclude that a wide dispersion of peak phases appears to be an inherent oscillator feature rather than the result of a convoluted output of multiple, tissue-specific oscillators with distinct phase preferences.

Oscillations initiate with a time lag in L1

The observation that oscillations were undetectable during the first few hours of larval development and started only after > 5 hours into L1 (Fig. 1A, C) surprised us. Hence, we performed a separate experiment that covered the first 24 hours of larval development (TC4). This confirmed our initial finding of a lack of oscillations during the first few hours of larval development (Fig. 2A, B).

To understand how oscillations initiate after the initial quiescence, we looked at individual genes and observed that the start of detectable oscillations differed for individual genes (Fig. 2A, C). Nonetheless, the occurrence of first peaks was globally well correlated to the peak phases calculated from data in Fig. 1 (Fig. 2D, E). Moreover, the transcript levels of many genes with a late-occurring (11 – 13 hours) first peak proceeded through a trough before reaching their first peak as exemplified in Fig. 2C for *F11E6.3*. We conclude that initiation of larval development after hatching is accompanied by a time lag prior to transition into an oscillatory state and that oscillations exhibit a structure of phase-locked gene expressing patterns as soon as they become detectable.

Results

L1 larvae undergo an extended intermolt

Although the gene expression oscillations occur in the context of larval development, functional connections have been lacking. However, genes encoding cuticular components were reported to be enriched among previously identified oscillating genes (Hendriks et al., 2014; Kim et al., 2013), and Gene Ontology (GO-) term analysis of the new extended set of oscillating genes confirms that the top 12 enriched terms all linked to cuticle formation and molting, or protease activity (Fig. 3A). These findings, and the fact that molting is itself a rhythmic process, repeated at the end of each larval stage, suggest the possibility of a functional link between molting and gene expression oscillations.

If such a link were true, we would predict that the initial period of quiescence in the early L1 stage be accompanied by a lengthened stage, and, specifically, intermolt duration. Indeed, using a luciferase-based assay that reveals the period of behavioral quiescence, or lethargus, that is associated with the molt (Fig. S2A-C), others had previously reported an extended L1 relative to other larval stages (Olmedo et al., 2015). However, they reported an extension of both molt and intermolt.

As the previously used luciferase-expressing transgenic strains developed relatively slowly and with limited synchrony across animals, presumably due to their specific genetic make-up, we repeated the experiment with a newly generated a strain that expressed luciferase from a single copy integrated transgene and that developed with improved synchrony and speed (Fig. S2D-J, Methods). Our results confirmed that L1 was greatly extended relative to the other larval stages (Fig. S2I). However, in contrast to the previous findings (Olmedo et al., 2015), but consistent with our hypothesis, the differences appeared largely attributable to an extended

intermolt (Fig. S2G). The duration of the first molt (M1) was instead comparable to that of M2 and M3 (Fig. S2H).

Thus, an extended first intermolt coincides with the fact that no oscillator activity can be detected by RNA sequencing during the first five hours of this larval stage. Moreover, because we performed the experiment by hatching embryos directly into food, we can conclude that the extended L1 stage is an inherent feature of *C. elegans* larval development, rather than a consequence of starvation-induced synchronization.

Development is coupled to oscillatory gene expression

The luciferase assay revealed that also the L4 stage took significantly longer than the two preceding stages, though not as long as L1 (Fig. S2I). In this case, both the fourth intermolt and the fourth molt were extended (Fig. S2G, H). As apparent from the gene expression heatmap, and quantified below, the oscillation period during L4 was also extended. Hence, grossly similar trends appeared to occur in larval stage durations and oscillation periods, determined by the luciferase assay and RNA sequencing, respectively. We considered this as further evidence for a coupling of the two processes.

To test this hypothesis explicitly, we sought to quantify the synchrony of oscillatory gene expression and developmental progression in individual animals at the same time. To this end, we established a microchamber-based time-lapse microscopy assay by adapting a previous protocol (Turek et al., 2015). In this assay, animals are hatched and grown individually in small chambers where they can be tracked and imaged while moving freely, enabling their progression through molts. Using Mos1-mediated single-copy transgene integration (MosSCI) (Frøkjær-

Jensen et al., 2012), we generated transgenic animals that expressed destabilized *gfp* from the promoter of *qua-1*, a highly expressed gene with a large mRNA level amplitude.

Consistent with the RNA sequencing data, we detected oscillations of the reporter with four expression peaks (Fig. 3B). Moreover, we observed similar rates of development as in the luciferase assays when we curated the molts (Fig. 3C, Table S2, Methods). The stage durations were in good agreement with the averaged oscillation period times for each cycle, obtained through a Hilbert transform of GFP intensities, for all three larval stages, L2 through L4, for which oscillations period lengths could be reliably determined (Fig. 3D).

Single animal imaging enabled us to ask when molts occurred relative to oscillatory gene expression, and we observed a very uniform behavior across animals (Fig. 3B). To quantify this relationship, we determined the gene expression phases at molt entries and exits. We obtained highly similar values across worms within one larval stage (Fig. 3E), and only a minor drift when comparing phases across larval stages. Two additional reporter transgenes, based on the promoters of *dpy-9* and *F11E6.3*, which differ in peak expression phases from *qua-1* and one another, yielded similar results (Fig. S3).

We considered two possible interpretations of the narrow distributions of oscillation phases at molt entry and exit: first, both oscillations and development could be under independent, but precise temporal control. In this model, certain developmental events would merely coincide with specific phases of oscillations rather than being coupled to them. Therefore, variations in the periods of oscillation and development would add up, non-linearly, to the experimentally observed phase variations. Second, phase-locking of oscillatory gene expression and developmental events might result from the two processes being truly coupled and/or from one driving the other. In this case, the variations in the two periods would partially

explain each other, causing a reduction in the expected phase variation relative to the first scenario (Fig. 3F).

To distinguish between these scenarios, we used error-propagation to calculate the expected error for two independent processes (Methods). Focusing on L2 and L3 stages to exclude any edge effects on the period calculation by Hilbert transform, we found that this calculated error consistently exceeded the experimentally observed error (Fig. 3G), for all three reporter genes, for both molt entry and molt exit, and for both larval stages. Thus, our observations agree with the notion that development and oscillatory gene expression are functionally coupled (Fig. 3H), and potentially causally connected.

Quantification of amplitude and period behavior over time reveal characteristic systems properties

Consistent with the coupling between oscillations and development, both the last larval stage and the period of the last oscillation cycle appeared to increase (Fig. 3D) before oscillations ceased. The characteristics of such a transition from oscillatory to non-oscillatory state, or bifurcation, can be examined in the light of bifurcation theory. Bifurcation, that is, a qualitative change in system behavior, occurs in response to a change in one or more control parameters. Depending on the system's topology, characteristic changes of amplitude and period occur during bifurcation (Fig. 4A) (Izhikevich, 2000; Salvi et al., 2016; Strogatz, 2015). Thus, transition into a quiescent state through a supercritical Hopf (supH) bifurcation involves a declining, and ultimately undetectable, amplitude and a constant period. By contrast, a Saddle Node on Invariant Cycle (SNIC) bifurcation results in a declining frequency (and thus increasing period) but a stable amplitude.

Hence, to gain a better understanding of the oscillator's bifurcation, we quantified oscillation amplitudes and periods over time. To minimize variations from differences between experiments, we did this for the contiguous 5 – 48 hour time course (TC2). This enabled reliable quantification of these features for the last three oscillation cycles, C2 through C4, which begin at 14 h (C2), 20 h (C3) and 27 h (C4), respectively (Fig. 4C). Excluding a small set of 291 genes that exhibited unusual expression trends during the fourth larval stage, i.e., a major change in mean expression levels (Fig. S4) this analysis revealed a good agreement of amplitudes across stages, and in particular no indication of damping during the last cycle, C4 (Fig. 4B).

We used a Hilbert transform (Pikovsky et al., 2001) to quantify the period over time with a high temporal resolution, i.e., at every hour of development. The mean oscillation period thus calculated was approximately seven hours during the first cycles but increased during the fourth cycle (Fig. 4C). This change was also apparent when we reconstructed an oscillation from the mean observed oscillation period and compared it to an oscillation with a constant period of seven hours (Fig. 4D).

In summary, these analyses reveal a sudden loss of oscillation upon transition to adulthood without prior amplitude damping and an oscillator that can maintain a stable amplitude in the presence of period changes. These are features of an oscillator operating near a SNIC rather than a supH bifurcation (Fig. 4A) (Izhikevich, 2000; Salvi et al., 2016; Strogatz, 2015).

Arrest of the oscillator in a specific phase upon transition to adulthood

SNIC and supH bifurcations differ not only in amplitude and period behavior, but also in the stable state, or fixpoint, that the system adopts. In a supH bifurcation, the system spirals from a

limit cycle onto a fixpoint, whereas in a SNIC bifurcation, the fixpoint emerges on the limit cycle (Fig. 5A) (Saggio et al., 2017). In other words, a quiescent oscillator near a SNIC bifurcation adopts a state similar to that of a specific phase of the oscillator; the oscillator has become 'arrested'. By contrast, following a supH bifurcation, the oscillator adopts a stable state that is distinct from any phase of the oscillator. Hence, if the *C. elegans* oscillator entered an arrested state through a SNIC bifurcation, the overall expression profile of the oscillating genes in the adult stage should resemble that seen at some other time point during larval development.

To test this prediction, we analyzed the correlation of oscillating gene expression for adult time points (TP ≥ 37 h) to all other time points of the fused time course (TC3). (In the following, we will use "TPx" to refer to any time point 'x', in hours, after hatching. Technically, this is defined in our experiment as the time after plating synchronized, first larval stage animals on food.) For this analysis (illustrated in Fig. S5), we used the pairwise correlation matrix resulting from the oscillating gene set without the previously excluded genes that changed in expression in the L4 stage (Fig 5B). This provided two insights. First, correlation coefficients among adult time points all exceeded 0.8 with little change over time, confirming the high similarity of samples TP37 – 48 to one another and thus an absence of detectable oscillations. Second, in addition to one another, TP37 – 48 are particularly highly correlated to a specific time – and thus phase – of the oscillatory regime, namely TP13 and the 'repetitive' TP19 and TP26/27 (Fig. 5C, arrows). In other words, expression levels of oscillating genes in the adult resembled a specific larval oscillator phase, providing further support for a SNIC bifurcation.

Results

Phase-specific arrest of the oscillator after hatching

We noticed that the gene expression states of TP37 – 48 also correlated well to each of TP1 – 5; i.e., the early L1 larval stage (Fig. 5B). To examine this further, we performed the same correlation analysis as described above, but now for TP1 – 5. Mirroring the adult situation, correlation coefficients among all these five time points were high and exhibited little change over time, and TP1 – 5 exhibited particularly high levels of correlation to TP13 and the 'repetitive' TP19 and TP27 (Fig. 5D). These are the same larval time points to which the adult time points exhibit maximum similarity. We confirmed these two key observations when fusing the independent time course TC4 to TC2 (generating TC5; Fig. S6).

We conclude that also during the first five hours after plating, oscillating genes adopt a stable expression profile that resembles a specific phase of the oscillator. In other words, both the transition into the oscillatory state during L1 and out of it during L4 occur through a SNIC bifurcation. This finding indeed explains our observation (Fig. 2) that in L1 stage larvae, oscillations exhibit a structure of phase-locked gene expressing patterns as soon as they become detectable: the oscillator initiates from an arrested phase.

Initiation of oscillation soon after gastrulation

We wondered how the oscillator entered the arrested state observed in early larvae, i.e., what dynamics the class of larval oscillating genes exhibited in embryos. Hence, we examined single embryo gene expression data from a published time series (Hashimshony et al., 2015). When plotting the embryonic expression patterns of oscillating genes sorted by their peak phase defined in larvae, we observed a dynamic expression pattern with a striking phase signature (Fig. 6A). To investigate this further, we performed a correlation analysis between embryonic and

larval time points (TC3) for the oscillating genes (Fig. S7A). When we plotted the correlation coefficients for each embryonic time point over larval time we observed two distinct behaviors (Fig. 6B, C), which separated at ~380 min (95%-CI: 317.6 minutes – 444.2 minutes) (Fig. 6D; Fig. S7B): First, from the start of embryogenesis until ~380 min, the peak of correlation occurred always for the same larval time point, but the extent of correlation increased rapidly (Fig. 6B, D). Second, past ~380 min of embryonic development, the peaks of correlation moved progressively from TP14 (which we define as 0°/360° because it demarcates the end of the first and the beginning of the second oscillation cycle in the fused time course, Fig. 1C); towards TP19 (accordingly defined as 300°), but the extent of correlation increased only modestly (Fig 6C, D).

We conclude that the system adopts two distinct states during embryogenesis (Fig. 6E): Initially, it approaches the oscillatory regime through increasing similarity to the oscillator phase TP14/0°. After completion of gastrulation and around the beginning of morphogenesis/organogenesis (Hall et al., 2017), it transitions into the oscillatory state and reaches, at hatching, a phase corresponding to larval ~TP19/300°, where oscillations arrest until resumption later in L1.

A shared oscillator phase for experimentally induced and naturally occurring bifurcations

The arrested states of the oscillator in both early L1 stage larvae and in adults are highly similar and resemble the oscillator state at TP19/300°. Therefore, we wondered whether this oscillator phase was particularly conducive to state transitions of the system in response to changes in the developmental trajectory. To test this, we examined animals that exited from dauer arrest, a diapause stage that animals enter during larval development under conditions of environmental stress such as heat, crowding, or food shortage. Using a published time course of animals

released from dauer arrest after starvation (Hendriks et al., 2014), we found that their expression patterns of oscillating genes correlated highly with those of animals initiating oscillations (TC3) in the L1 stage (Fig. 7A, B). Additionally, gene expression patterns at 1 hour through 5 hours and at 13 hours post-dauer were highly correlated to those of the repetitive TP13, TP19 and TP26/27 during continuous development. Hence, the system state during a period of quiescence during the first five hours after placing animals on food corresponds to an arrest of the oscillation in a phase seen at TP19/300° of the continuous development time course.

We conclude that the system bifurcates in the same manner during continuous, unperturbed development, after hatching, and in response to a perturbation, namely starvation-induced dauer arrest.

Discussion

In this study, we have characterized the biological function and behavior of the *C. elegans* larval oscillator. Our results from the single animal- and population-based analyses reveal a close coupling to development, and specifically molting, and imply that processes essential for molting may not be restricted to lethargus. We have observed that oscillations are highly similar during the four cycles (Fig. 7C, Fig. S8). Yet, oscillations cease and (re-) initiate several times during physiological development, and similar state transitions, or bifurcations, of the system can be induced through an external perturbation (Fig. 7C). In particular, all non-oscillatory states correspond to an arrest of the oscillator in one specific phase. Hence, the observed bifurcations provide a conceptual model of how a developmental checkpoint can operate to halt larval development at a particular, repetitive point of development. Moreover, they constrain possible

system architectures and properties as well as the choice and parametrization of mathematical models that can represent the system.

Oscillatory expression of thousands of genes

Our previous work (Hendriks et al., 2014) identified ~2,700 oscillating (i.e., rhythmically expressing) genes, a number that we now increase to 3,739 genes (24% of total expressed genes). We attribute this improved identification of oscillating genes to the fact that our present analysis focused on the L1, L2 and L3 stages, where a constant oscillation period of ~7 hours facilitates cosine wave fitting. This contrasts with the situation in the previous experiment, which used data from the L3 and L4 stages and thus, as we reveal here, a time of changing period.

Even our current estimate is conservative, i.e., the 'non-oscillating' genes contain genes that exhibit oscillatory expression with low amplitude or, potentially, strongly non-sinusoidal shapes. It is possible that such dynamics may play important roles for specific genes and processes and our data provide a resource to identify these in the future. However, here we focused on genes with robust and extensive oscillations to facilitate functional dissection of the oscillator.

A developmental oscillator with functions in and beyond molting and lethargus

The physiological function of the *C. elegans* oscillator has remained unclear. Here, we have tested a possible connection with molting. By quantifying the periods of both molting and gene expression oscillations simultaneously, in the same individual animals, we revealed their high degree of similarity and showed that the two processes are more closely phase-locked than expected from mere coincidence, i.e., they are coupled. We propose that a function of the

oscillator as a developmental clock provides a parsimonious explanation for the coupling, but other models remain possible, e.g., the oscillator may facilitate an efficient molting process by anticipating the time of peak demand for cuticular building blocks and other factors.

Conventionally, molting is subdivided into three distinct steps, namely apolysis (severing of connections between the cuticle and the underlying epidermis), new cuticle synthesis, and ecdysis (cuticle shedding) (Lažetić and Fay, 2017). The first two occur during, and the latter terminates, lethargus, a period of behavioral quiescence. However, we find that the temporal structure imposed by the *C. elegans* oscillator extends beyond lethargus. Our data reveal two probable causes: occurrence of processes required for molting before lethargus and a temporal organization that extends to processes unrelated to molting.

Specifically, we observed initiation of oscillations in embryos, which execute cuticle synthesis but neither apolysis nor ecdysis, at ~380 min into embryo development and thus long before the first signs of cuticle synthesis at ~600 min (Sulston et al., 1983). Instead, this time coincides with formation of an apical extracellular matrix (ECM). Although termed embryonic sheath, we find genes encoding components of this ECM, namely *sym-1; fbn-1; noah-1; noah-2* (Vuong-Brender et al., 2017), also detectably expressed in larvae, and all four are required for larval molting or proper cuticle formation (Frand et al., 2005; Niwa et al., 2009). Moreover, their mRNA levels oscillate with high amplitudes, and as predicted from the embryonic data, their expression peaks long before lethargus, and in fact shortly after ecdysis, i.e., <u>after</u> a molt has been completed. Hence, to account for all these facts, we propose that molting involve processes that are executed long before the onset of lethargus and that include ECM remodeling.

However, even a substantially more complex molting process may fail to account for the fact that a majority of oscillating genes is phase-locked with the molt but exhibits peak

expression outside the molt and lacks any obvious link to molting. We consider it plausible that robust larval development may benefit from a coordination of molting with other physiological or developmental processes, as previously postulated for skin cell proliferation (Ruaud and Bessereau, 2006). Similarly, as lethargus involves cessation of food-uptake, oscillatory gene expression may serve to anticipate this event, consistent with a large number of intestinally expressed oscillating genes. Nonetheless, even for this class, a broad dispersion of peak expression phases may suggest additional functions, yet to be uncovered. Whatever the benefit, it is evident that the oscillator imposes a temporal structure of gene expression that extends far beyond lethargus.

Oscillatory state transitions and developmental checkpoints

We have observed a loss of oscillations under three distinct conditions, in early L1 stage larvae, dauer arrested animals, and adults. The similarity of the oscillator states under all three conditions is striking and involves an arrest in the same specific phase.

Formally, for the L1 arrest, we cannot distinguish between perturbation-induced or naturally occurring arrest, as the sequencing experiments required animal synchronization by hatching animals in the absence of food, causing a transient arrest of development. However, the fact that the L1 stage is extended also in animals hatched into food suggests that they may adopt a similar arrested state even in the presence of food, perhaps because the nutritional resources in the egg (i.e., egg yolk) have become depleted by the time that hatching occurs. In other words, synchronization of L1 animals by hatching them in the absence of food may propagate a pre-existing transient developmental and oscillator arrest.

Irrespective of this interpretation, a key feature of the arrests that we observe under different conditions is that they always occur in the same phase. This is a behavior one would predict for a repetitive developmental checkpoint. Such a checkpoint has indeed been found to operate shortly after each larval molt exit, arresting development in response to a lack of food (Schindler et al., 2014). Importantly, developmental arrest does not result from an acute shortage of resources. Rather, it is a genetically encoded, presumably adaptive, response to nutritionally poor conditions, as demonstrated by the fact that mutations in the *daf-2*/IGFR signaling pathway causes animals to continue development under the same food-depleted conditions (Baugh, 2013; Schindler et al., 2014).

Within the limits of our resolution, the phase of the arrested oscillator corresponds to the phase seen around ecdysis. Hence, oscillations and development are synchronously arrested, and we propose that signals related to food sensing, metabolism, or nutritional state of the animal help to control the state of the oscillatory system and thereby developmental progression. An oscillator operating near a SNIC bifurcation appears ideally suited to processing such information, because it acts as a signal integrator, i.e., it becomes active when a signal threshold is surpassed (Forger, 2017; Izhikevich, 2000). This contrasts with the behavior of oscillators operating near a supH bifurcation, which function as resonators, i.e., they respond most strongly to an incoming signal of a preferred frequency. Hence, both the phase-specific arrest and the integrator function as characteristics of an oscillator operating in the vicinity of a SNIC bifurcation are physiologically relevant features of this *C. elegans* oscillator.

Insights into oscillator architecture and constraints for mathematical modelling

What mechanisms determine the type and behavior of the *C. elegans* oscillator? Although the nature and wiring of the 'core oscillator', i.e., the machinery that drives the pervasive gene expression oscillation, remains to be established, the behavior of the oscillator that we characterized here provides clear constraints. Thus, a change in period without a noticeable change in amplitude, as seen in L4 stage larvae, is a feature of rigid oscillators (Abraham et al., 2010) that is considered incompatible with the function of a simple negative feedback loop but compatible with the operation of interlinked positive and negative feedback loops (Mönke et al., 2017; Tsai et al., 2008). This conclusion is supported by evidence from synthetic biology, where most synthetic genetic oscillators appear to operate near a supH bifurcation (Purcell et al., 2010). An exception are so-called amplified negative feedback oscillators, which operate near a SNIC bifurcation and rely on interlinked negative and positive feedback loops.

Beyond constraining possible oscillator architectures, our experimental observations will help to guide mathematical modelling of the *C. elegans* oscillator. Modelling is needed because the nonlinear dynamic behaviors of oscillators are difficult to grasp intuitively. However, it is usually difficult to ensure the relevance of a given model, because both its formulation and its parametrization determine whether oscillations occur and which behaviors the resulting oscillator model displays. Amplified negative feedback oscillators are a case in point as they can also operate near a supH bifurcation; operation near a SNIC bifurcation occurs only in a certain parameter space (Conrad et al., 2008; Guantes and Poyatos, 2006). The experimental characterization of the system's bifurcation that we have achieved here will therefore provide crucial constraints to exclude invalid mathematical models.

We do note that mathematical models of somitogenesis clocks, inspired by mechanistic knowledge about the identity of individual oscillator components and their wiring, tend to

represent oscillators operating near a supH bifurcation (Jensen et al., 2010; Webb et al., 2016). This appears consistent with observations on isolated cells *in vitro* (Webb et al., 2016). At the same time it contrasts with changes in both amplitude and period that were shown to occur in zebrafish embryos during somite formation and prior to cessation of oscillation (Shih et al., 2015). Thus, and because an analysis of bifurcation behavior of somitogenesis clocks *in vivo* is challenging due to a complex space-dependence of oscillation features (Soroldoni et al., 2014), it remains to be answered whether and to what extent the *C. elegans* oscillator and the somitogenesis clocks share specific properties. However, whatever the answer, a comparison of the similarities and differences in behaviors, architectures and topologies will help to reveal whether and to what extent diverse developmental oscillators follow common design principles.

References:

Abraham, U., Granada, A.E., Westermark, P.O., Heine, M., Kramer, A., Herzel, H., 2010. Coupling governs entrainment range of circadian clocks. Mol Syst Biol 6, 438. https://doi.org/10.1038/msb.2010.92

Au, K.F., Jiang, H., Lin, L., Xing, Y., Wong, W.H., 2010. Detection of splice junctions from paired-end RNA-seq data by SpliceMap. Nucleic Acids Res 38, 4570–4578. https://doi.org/10.1093/nar/gkq211

Bates, D., Maechler, M., 2018. Matrix: Sparse and Dense Matrix Classes and Methods.

Baugh, L.R., 2013. To grow or not to grow: nutritional control of development during Caenorhabditis elegans L1 arrest. Genetics 194, 539–555. https://doi.org/10.1534/genetics.113.150847

Cao, J., Packer, J.S., Ramani, V., Cusanovich, D.A., Huynh, C., Daza, R., Qiu, X., Lee, C., Furlan, S.N., Steemers, F.J., Adey, A., Waterston, R.H., Trapnell, C., Shendure, J., 2017. Comprehensive single-cell transcriptional profiling of a multicellular organism. Science 357, 661–667. https://doi.org/10.1126/science.aam8940

Conrad, E., Mayo, A.E., Ninfa, A.J., Forger, D.B., 2008. Rate constants rather than biochemical mechanism determine behaviour of genetic clocks. J R Soc Interface 5, S9–S15. https://doi.org/10.1098/rsif.2008.0046.focus

Edgar, R., Domrachev, M., Lash, A.E., 2002. Gene Expression Omnibus: NCBI gene expression and hybridization array data repository. Nucleic Acids Res 30, 207–210. https://doi.org/10.1093/nar/30.1.207

Forger, D.B., 2017. Biological Clocks, Rhythms, and Oscillations: The Theory of Biological Timekeeping. The MIT Press, Cambridge, Massachusetts.

Frand, A.R., Russel, S., Ruvkun, G., 2005. Functional Genomic Analysis of C. elegans Molting. PLOS Biology 3, e312. https://doi.org/10.1371/journal.pbio.0030312

Frøkjær-Jensen, C., Davis, M.W., Ailion, M., Jorgensen, E.M., 2012. Improved Mos1-mediated transgenesis in C. elegans. Nat. Methods 9, 117–118. https://doi.org/10.1038/nmeth.1865

Frøkjaer-Jensen, C., Davis, M.W., Hopkins, C.E., Newman, B.J., Thummel, J.M., Olesen, S.-P., Grunnet, M., Jorgensen, E.M., 2008. Single-copy insertion of transgenes in Caenorhabditis elegans. Nat. Genet. 40, 1375–1383. https://doi.org/10.1038/ng.248

Gaidatzis, D., Lerch, A., Hahne, F., Stadler, M.B., 2015. QuasR: quantification and annotation of short reads in R. Bioinformatics 31, 1130–1132. https://doi.org/10.1093/bioinformatics/btu781

Gaujoux, R., Seoighe, C., 2010. A flexible R package for nonnegative matrix factorization. BMC Bioinformatics 11, 367. https://doi.org/10.1186/1471-2105-11-367

Gibson, D.G., Young, L., Chuang, R.-Y., Venter, J.C., Hutchison, C.A., Smith, H.O., 2009. Enzymatic assembly of DNA molecules up to several hundred kilobases. Nat. Methods 6, 343–345. https://doi.org/10.1038/nmeth.1318

Gritti, N., Kienle, S., Filina, O., van Zon, J.S., 2016. Long-term time-lapse microscopy of *C. elegans* post-embryonic development. Nature Communications 7, 12500. https://doi.org/10.1038/ncomms12500

Grün, D., Kirchner, M., Thierfelder, N., Stoeckius, M., Selbach, M., Rajewsky, N., 2014. Conservation of mRNA and protein expression during development of C. elegans. Cell Rep 6, 565–577. https://doi.org/10.1016/j.celrep.2014.01.001

Guantes, R., Poyatos, J.F., 2006. Dynamical principles of two-component genetic oscillators. PLoS Comput. Biol. 2, e30. https://doi.org/10.1371/journal.pcbi.0020030

Hall, D.H., Herndon, L.A., Altun, Z., 2017. Introduction to C. elegans Embryo Anatomy. In WormAtlas.

Hashimshony, T., Feder, M., Levin, M., Hall, B.K., Yanai, I., 2015. Spatiotemporal transcriptomics reveals the evolutionary history of the endoderm germ layer. Nature 519, 219–222. https://doi.org/10.1038/nature13996

Hendriks, G.-J., Gaidatzis, D., Aeschimann, F., Großhans, H., 2014. Extensive oscillatory gene expression during C. elegans larval development. Mol. Cell 53, 380–392. https://doi.org/10.1016/j.molcel.2013.12.013

Izhikevich, E.M., 2000. Neural excitability, spiking and bursting. Int. J. Bifurcation Chaos 10, 1171–1266. https://doi.org/10.1142/S0218127400000840

Jensen, P.B., Pedersen, L., Krishna, S., Jensen, M.H., 2010. A Wnt Oscillator Model for Somitogenesis. Biophys J 98, 943–950. https://doi.org/10.1016/j.bpj.2009.11.039

Jones, E., Oliphant, T., Peterson, P., 2001. SciPy: Open Source Scientific Tools for Python.

Kim, D., Oh, H.-S., 2018. EMD: Empirical Mode Decomposition and Hilbert Spectral Analysis.

Kim, D. hyun, Grün, D., van Oudenaarden, A., 2013. Dampening of expression oscillations by synchronous regulation of a microRNA and its target. Nat. Genet. 45, 1337–1344. https://doi.org/10.1038/ng.2763

Koike, N., Yoo, S.-H., Huang, H.-C., Kumar, V., Lee, C., Kim, T.-K., Takahashi, J.S., 2012. Transcriptional Architecture and Chromatin Landscape of the Core Circadian Clock in Mammals. Science 338, 349–354. https://doi.org/10.1126/science.1226339

Korenčič, A., Košir, R., Bordyugov, G., Lehmann, R., Rozman, D., Herzel, H., 2014. Timing of circadian genes in mammalian tissues. Sci Rep 4, 1–9. https://doi.org/10.1038/srep05782

Lagido, C., Pettitt, J., Flett, A., Glover, L.A., 2008. Bridging the phenotypic gap: Real-time assessment of mitochondrial function and metabolism of the nematode Caenorhabditis elegans. BMC Physiology 8, 7. https://doi.org/10.1186/1472-6793-8-7

Lažetić, V., Fay, D.S., 2017. Molting in C. elegans. Worm 6, e1330246. https://doi.org/10.1080/21624054.2017.1330246

Lebigot, E.O., n.d. Uncertainties: a Python package for calculations with uncertainties.

McKinney, W., 2010. Data Structures for Statistical Computing in Python, in: Proceedings of the 9th Python in Science Conference. pp. 51–56.

Mönke, G., Cristiano, E., Finzel, A., Friedrich, D., Herzel, H., Falcke, M., Loewer, A., 2017. Excitability in the p53 network mediates robust signaling with tunable activation thresholds in single cells. Scientific Reports 7, 46571. https://doi.org/10.1038/srep46571

Moreno-Risueno, M.A., Van Norman, J.M., Moreno, A., Zhang, J., Ahnert, S.E., Benfey, P.N., 2010. Oscillating gene expression determines competence for periodic Arabidopsis root branching. Science 329, 1306–1311. https://doi.org/10.1126/science.1191937

Niwa, R., Hada, K., Moliyama, K., Ohniwa, R.L., Tan, Y.-M., Olsson-Carter, K., Chi, W., Reinke, V., Slack, F.J., 2009. C. elegans sym-1 is a downstream target of the hunchback-like-1 developmental timing transcription factor. Cell Cycle 8, 4147–4154. https://doi.org/10.4161/cc.8.24.10292

Oates, A.C., Morelli, L.G., Ares, S., 2012. Patterning embryos with oscillations: structure, function and dynamics of the vertebrate segmentation clock. Development 139, 625–639. https://doi.org/10.1242/dev.063735

Olmedo, M., Geibel, M., Artal-Sanz, M., Merrow, M., 2015. A High-Throughput Method for the Analysis of Larval Developmental Phenotypes in Caenorhabditis elegans. Genetics 201, 443–448. https://doi.org/10.1534/genetics.115.179242

Panda, S., Hogenesch, J.B., Kay, S.A., 2002. Circadian rhythms from flies to human. Nature 417, 329–335. https://doi.org/10.1038/417329a

PANTHER Classification System, n.d.

Pikovsky, A., Rosenblum, M., Kurths, J., 2001. Synchronization: A universal concept in nonlinear sciences. Cambridge University Press, Cambridge. https://doi.org/10.1017/CBO9780511755743

Purcell, O., Savery, N.J., Grierson, C.S., di Bernardo, M., 2010. A comparative analysis of synthetic genetic oscillators. J R Soc Interface 7, 1503–1524. https://doi.org/10.1098/rsif.2010.0183

R Core Team, n.d. R: A language and environment for statistical computing.

Rensing, L., Meyer-Grahle, U., Ruoff, P., 2001. Biological timing and the clock metaphor: oscillatory and hourglass mechanisms. Chronobiol. Int. 18, 329–369.

Riedel-Kruse, I.H., Müller, C., Oates, A.C., 2007. Synchrony dynamics during initiation, failure, and rescue of the segmentation clock. Science 317, 1911–1915. https://doi.org/10.1126/science.1142538

Ruaud, A.-F., Bessereau, J.-L., 2006. Activation of nicotinic receptors uncouples a developmental timer from the molting timer in C. elegans. Development 133, 2211–2222. https://doi.org/10.1242/dev.02392

Saggio, M.L., Spiegler, A., Bernard, C., Jirsa, V.K., 2017. Fast–Slow Bursters in the Unfolding of a High Codimension Singularity and the Ultra-slow Transitions of Classes. J Math Neurosci 7. https://doi.org/10.1186/s13408-017-0050-8

Salvi, J.D., Ó Maoiléidigh, D., Hudspeth, A.J., 2016. Identification of Bifurcations from Observations of Noisy Biological Oscillators. Biophys. J. 111, 798–812. https://doi.org/10.1016/j.bpj.2016.07.027

Schindler, A.J., Baugh, L.R., Sherwood, D.R., 2014. Identification of late larval stage developmental checkpoints in Caenorhabditis elegans regulated by insulin/IGF and steroid hormone signaling pathways. PLoS Genet. 10, e1004426. https://doi.org/10.1371/journal.pgen.1004426

Shih, N.P., François, P., Delaune, E.A., Amacher, S.L., 2015. Dynamics of the slowing segmentation clock reveal alternating two-segment periodicity. Development 142, 1785–1793. https://doi.org/10.1242/dev.119057

Soetaert, K., 2017. plot3D: Plotting Multi-Dimensional Data.

Soroldoni, D., Jörg, D.J., Morelli, L.G., Richmond, D.L., Schindelin, J., Jülicher, F., Oates, A.C., 2014. Genetic oscillations. A Doppler effect in embryonic pattern formation. Science 345, 222–225. https://doi.org/10.1126/science.1253089

Spiess, A.-N., 2018. propagate: Propagation of Uncertainty.

Stiernagle, Theresa, n.d. Maintenance of C. elegans (February 11, 2006), WormBook, ed. The C. elegans Research Community, WormBook, doi/10.1895/wormbook.1.101.1, http://www.wormbook.org.

Strogatz, S.H., 2015. Nonlinear Dynamics and Chaos with Student Solutions Manual: Nonlinear Dynamics and Chaos: With applications To Physics, Biology, Chemistry, And Engineering (Studies in Nonlinearity), 2nd ed. Westview Press, Boulder, CO.

Sueur, J., Aubin, T., Simonis, C., 2008. Seewave, a Free Modular Tool for Sound Analysis and Synthesis. Bioacoustics 18, 213–226. https://doi.org/10.1080/09524622.2008.9753600

Sulston, J.E., Schierenberg, E., White, J.G., Thomson, J.N., 1983. The embryonic cell lineage of the nematode Caenorhabditis elegans. Dev. Biol. 100, 64–119.

Tsai, T.Y.-C., Choi, Y.S., Ma, W., Pomerening, J.R., Tang, C., Ferrell, J.E., 2008. Robust, Tunable Biological Oscillations from Interlinked Positive and Negative Feedback Loops. Science 321, 126–129. https://doi.org/10.1126/science.1156951

Turek, M., Besseling, J., Bringmann, H., 2015. Agarose Microchambers for Long-term Calcium Imaging of Caenorhabditis elegans. J Vis Exp e52742. https://doi.org/10.3791/52742

Uriu, K., 2016. Genetic oscillators in development. Development, Growth & Differentiation 58, 16–30. https://doi.org/10.1111/dgd.12262

Vuong-Brender, T.T.K., Ben Amar, M., Pontabry, J., Labouesse, M., 2017. The interplay of stiffness and force anisotropies drives embryo elongation. eLife 6, e23866. https://doi.org/10.7554/eLife.23866

Webb, A.B., Lengyel, I.M., Jörg, D.J., Valentin, G., Jülicher, F., Morelli, L.G., Oates, A.C., 2016. Persistence, period and precision of autonomous cellular oscillators from the zebrafish segmentation clock. eLife 5, e08438. https://doi.org/10.7554/eLife.08438

Zhang, R., Lahens, N.F., Ballance, H.I., Hughes, M.E., Hogenesch, J.B., 2014. A circadian gene expression atlas in mammals: implications for biology and medicine. Proc. Natl. Acad. Sci. U.S.A. 111, 16219–16224. https://doi.org/10.1073/pnas.1408886111

Acknowledgements: We thank Stephane Thiry, Kirsten Jacobeit and the FMI Functional Genomics Facility for RNA sequencing, Iskra Katic for help in generating transgenic strains, Maria Olmédo and Henrik Bringmann for introducing us to the luciferase and the single animal imaging assays, respectively, Dimos Gaidatzis and Michael Stadler for advice on computational analyses, Laurent Gelman for help with imaging, and Benjamin Towbin, Lucas Morales Moya, Prisca Liberali and Luca Giorgetti for comments on the manuscript. **Funding:** M.W.M.M. is a recipient of a Boehringer Ingelheim Fonds PhD fellowship. This work is part of a project that has received funding from the European Research Council (ERC) under the European Union's Horizon 2020 research and innovation programme (Grant agreement No. 741269, to H.G.). The FMI is core-funded by the Novartis Research Foundation. **Author contributions:** Gert-Jan

Results

Hendriks and Yannick Hauser performed RNA sequencing time courses. Milou Meeuse and Yannick Hauser analyzed RNA sequencing data. Milou Meeuse performed and analyzed luciferase assays. Guy Bogaarts developed the graphical user interface for the luciferase data. Yannick Hauser acquired and analyzed single worm imaging data. Jan Eglinger wrote the KNIME workflow for the single worm imaging. Charisios Tsiairis conceived parts of the analysis. Helge Großhans, Milou Meeuse and Yannick Hauser conceived the project and wrote the manuscript. **Competing interests:** The authors declare no competing interests. **Data and materials availability:** All sequencing data generated for this study have been deposited in NCBI's Gene Expression Omnibus (Edgar et al., 2002) and are accessible through GEO SuperSeries accession number GSE133576 https://www.ncbi.nlm.nih.gov/geo/query/acc.cgi?acc=GSE133576 . A reviewer token for data access is available through the editorial office. The dauer exit time course was published previously (Hendriks et al., 2014) and is accessible through GEO Series accession number GSE52910 (http://www.ncbi.nlm.nih.gov/geo/query/acc.cgi?acc=GSE52910).
Published research reagents from the FMI are shared with the academic community under a Material Transfer Agreement (MTA) having terms and conditions corresponding to those of the UBMTA (Uniform Biological Material Transfer Agreement).
Conflict of Interests: The authors declare that they have no conflict of interest.

Figures

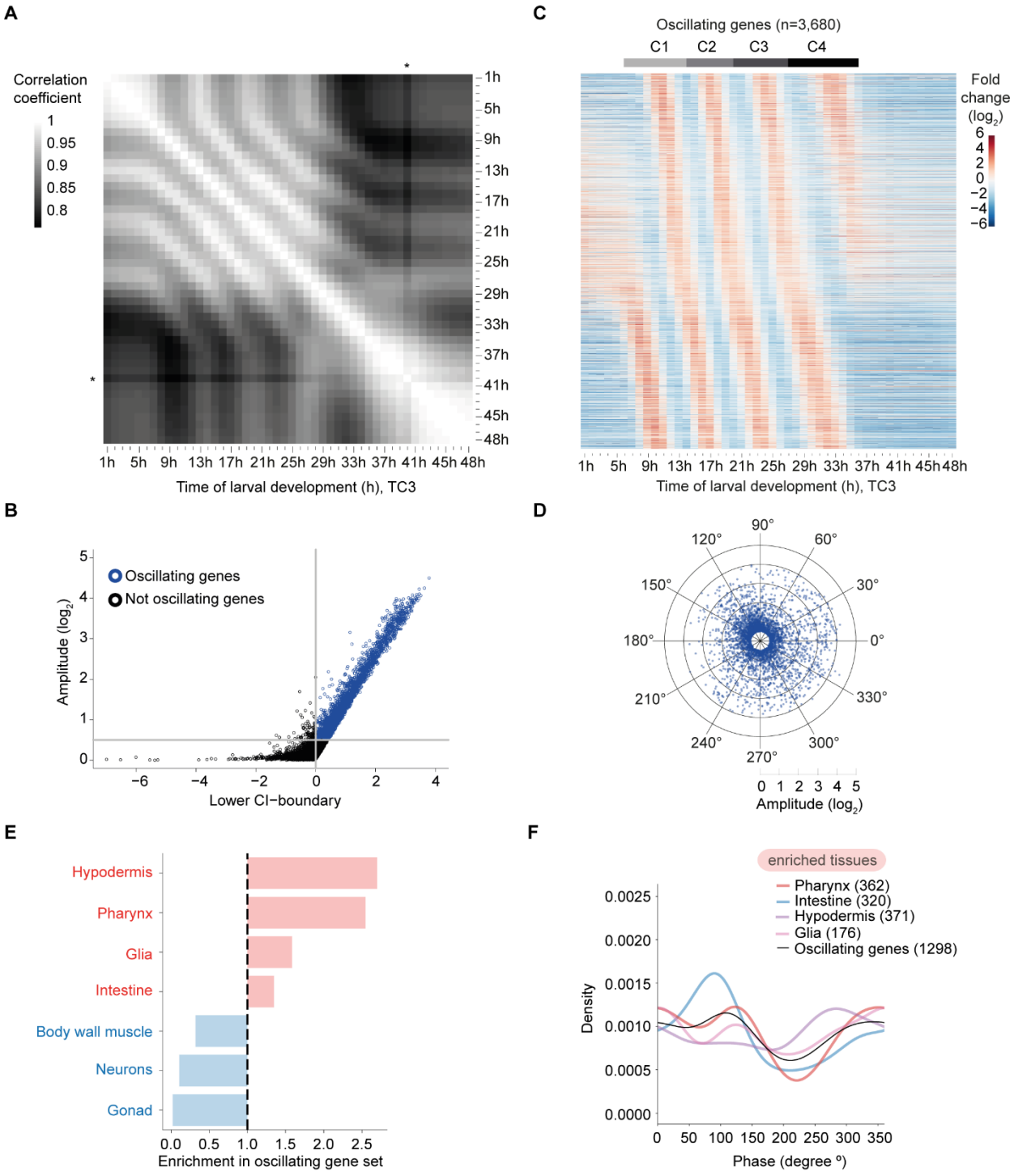

Fig 1: A massive oscillator with dispersed peak phases in several tissues

(A) Pairwise correlation plot of log_2-transformed gene expression patterns obtained from synchronized population of L1 stage larvae sampled and sequenced from t = 1 h until t = 48 h

(TC3; a fusion of the two time courses TC1 and TC2 after 13 h; Fig. S1A,B). Asterisk indicates an outlier, time point t = 40 h.

(B) Scatter plot identifying genes with oscillatory expression (henceforth termed oscillating genes, *blue*) based on amplitude and 99% confidence interval (99%-CI) of a cosine fitting of their expression quantified in TC2 (Methods). A lower CI-boundary ≥ 0, i.e. p-value ≤ 0.01, and a $\log_2$(amplitude) ≥ 0.5, which corresponds to a 2-fold change from peak to trough, were used as cut-offs. Genes below either cut-off were included in the 'not oscillating' group (*black*). Fig. S1C reveals gene distributions in a density scatter plot.

(C) Gene expression heatmaps of oscillating genes as classified in Fig. 1B and S1C. Oscillating genes were sorted by peak phase and mean expression per gene from t = 7 h to t = 36 h (when oscillations occur) was subtracted. n=3,680 as not all genes from the long time course (TC2) were detected in the early time course (TC1). Gray horizontal bars indicate the individual oscillation cycles, C1 through C4 as later determined in Fig. S8.

(D) Radar chart plotting amplitude (radial axis, in $\log_2$) over peak phase (circular axis, in degrees) as determined by cosine fitting in Fig. 1B.

(E) Enrichment (*red*) or depletion (*blue*) of tissues detected among oscillating genes expressed tissue-specifically relative to all tissue-specific genes using annotations derived from (Cao et al., 2017). Significance was tested using one-sided binomial tests which resulted in p-values < 0.001 for all tissues.

(F) Density plot of the observed peak phases of tissue-specifically expressed oscillating genes for all enriched tissues.

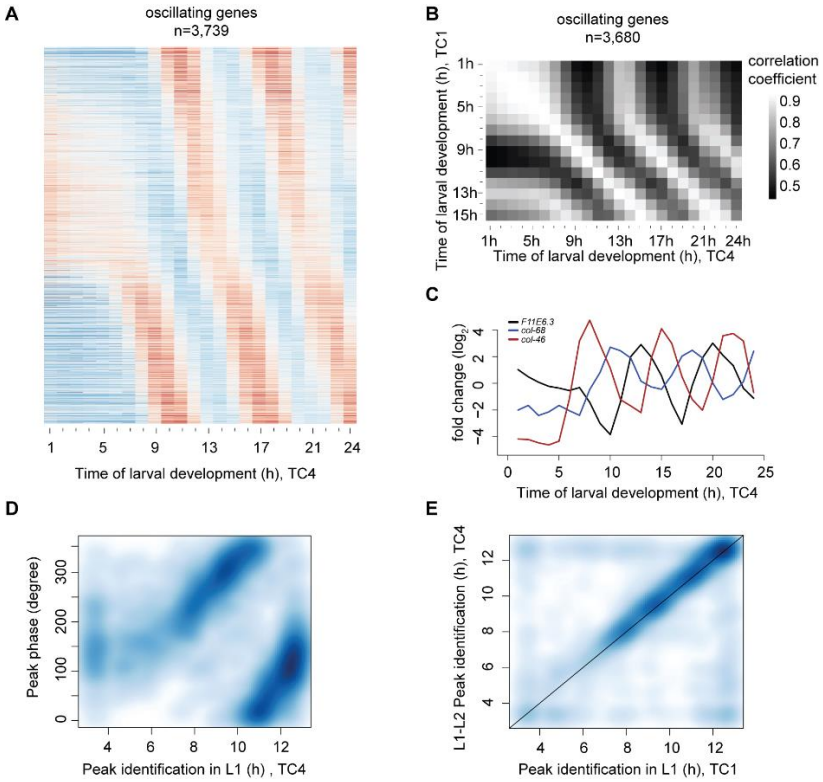

Fig 2: Oscillations start with a time lag in L1

(A) Gene expression heatmap of detectably expressed oscillating genes sampled from a separate early developmental time course (TC4; t = 1 h to t = 24 h). Genes were ranked according to their peak phase as determined in Fig. 1.

(B) Pairwise correlation plot of log_2-transformed oscillating gene expression data obtained from both early larval development time courses, TC1 and TC4.

(C) Gene expression traces of representative genes *F11E6.3*, *col-68* and *col-46*.

(D) Scatter plot of calculated oscillating gene peak phase (Fig. 1) over the time of occurrence of the first expression peak in L1 larvae, observed in TC4. Peak detection was performed using a spline analysis. As visual inspection did not reveal peaks in the heatmap during the first three hours, and as the first cycle ends at 13 h, we performed this analysis for t = 3 h to t = 13 h to reduce noise.

(E) Scatterplot comparing experimentally identified first peaks of gene expression (as in D) of the two early time course replicates, TC1 and TC4.

All analyses for oscillating genes identified in Fig. 1 with detectable expression (n=3,680).

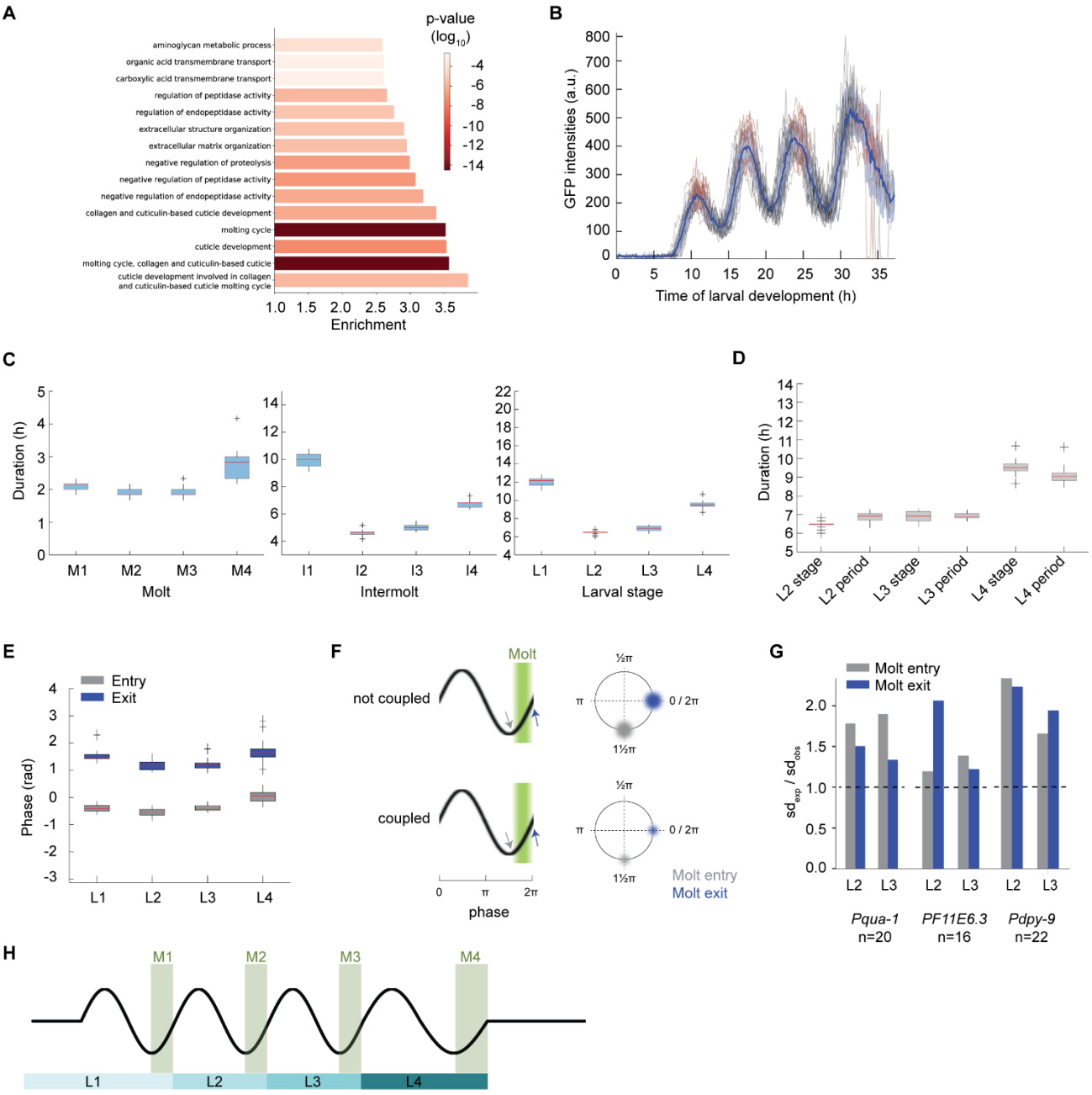

Fig 3: Oscillatory gene expression is coupled to molting

(A) GO-term enrichments for oscillating genes as classified in Fig. 1C. The top 15 enriched terms are displayed.

(B) GFP signal quantification for *qua-1p::gfp::pest::h2b::unc-54*$_{3'UTR}$ expressing single animals (HW2523, n=20) over larval development, starting from hatch (t = 0 h). Molts (*red*), mean intensity (*blue line*) and standard deviation across population (*shading*) are indicated.
(C), (D) Boxplots of molt, intermolt and larval stage durations (C) and of larval stage durations and period times of oscillations (D) of single animals (HW2523) developing in microchambers (n=20). In (D), L1 was excluded because of the time lag before oscillations manifest after hatching.
(E) Boxplot of phase at molt entry (start of lethargus) and molt exit (end of lethargus) separated by larval stages for single animals (HW2523) developing in microchambers (n=20)

(F) Schematic models of size of expected phase variation (radius of colored blur) at molt entry (*gray*) and molt exit (*blue*) depending on the coupling status between oscillations and molting.

(G) Barplots displaying the ratio of expected standard deviation over observed standard deviation for phase calling at either molt entry or molt exit for the indicated reporters. A dashed line indicates parity.

(H) Schematic depiction of coordination between oscillatory gene expression and development.

Boxplots in (C) – (E) extend from first to third quartile with a line at the median, outliers are indicated with a cross, whiskers show 1.5*IQR.

Results

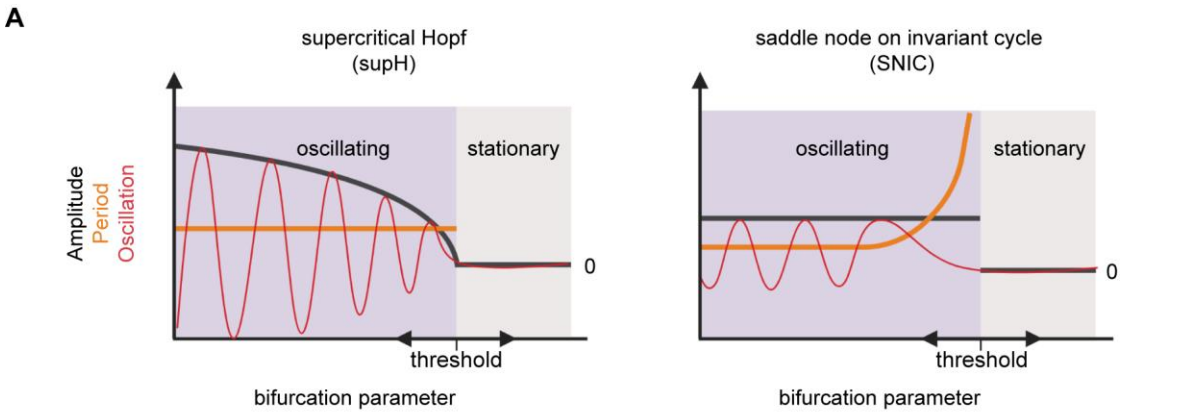
A
supercritical Hopf
(supH)
saddle node on invariant cycle
(SNIC)
oscillating
stationary
Amplitude
Period
Oscillation
0
threshold
bifurcation parameter

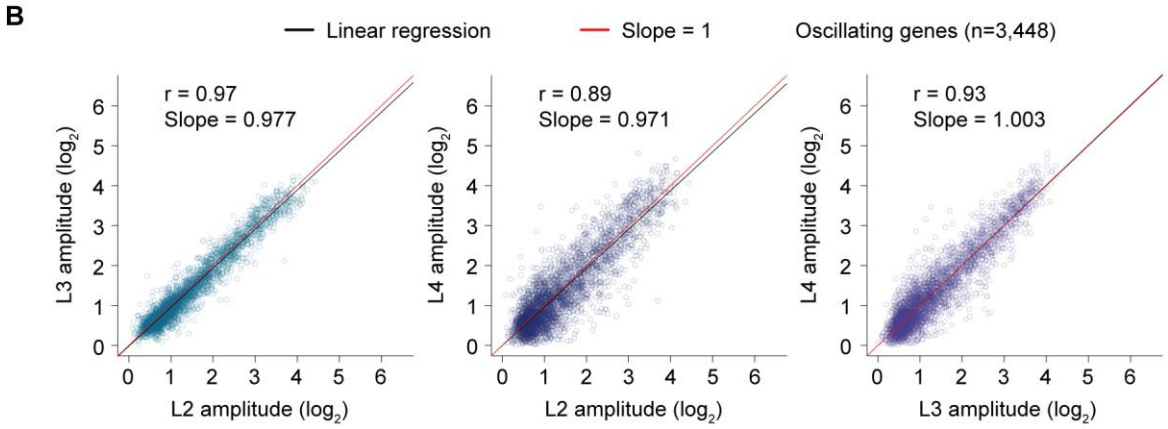
B
Linear regression
Slope = 1
Oscillating genes (n=3,448)
r = 0.97
Slope = 0.977
r = 0.89
Slope = 0.971
r = 0.93
Slope = 1.003
L3 amplitude (log2)
L4 amplitude (log2)
L2 amplitude (log2)
L3 amplitude (log2)

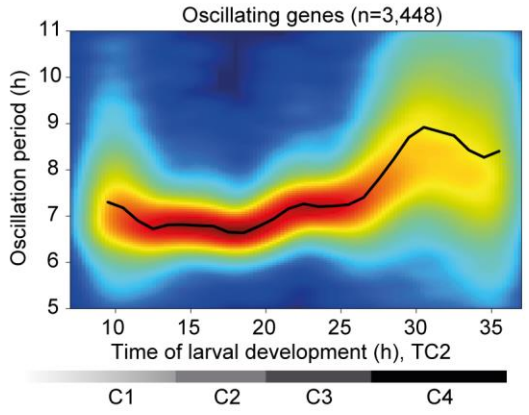
C
Oscillating genes (n=3,448)
Oscillation period (h)
Time of larval development (h), TC2
C1
C2
C3
C4

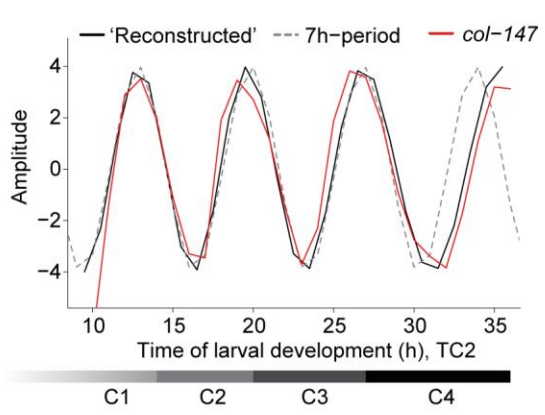
D
'Reconstructed'
7h-period
col-147
Amplitude
Time of larval development (h), TC2
C1
C2
C3
C4

Fig 4: Change in period without noticeable change in amplitude

(A) Schematic depiction of amplitude and period behaviors in response to a control parameter change for an oscillatory system transitioning between a quiescent (stationary) and an oscillatory state through the indicated bifurcations (created with BioRender.com). Note that transitions can occur in either direction.

(B) Amplitudes derived from cosine fitting to the individual oscillations of L2, L3 and L4 stage (TC2) plotted against each other. Pearson correlation coefficient r, slope of the linear regression (*black*) and the diagonals (slope=1; *red*) are indicated. 291 genes were excluded from oscillating genes due to altered mean expression in L4, see Fig. S4, i.e., n=3,448.

(C) Density plot showing oscillation period at every time point for each of the oscillating genes (n=3,448) as quantified by Hilbert transform. Mean oscillation period over all oscillating genes is shown by the black line. Horizontal gray bars indicate oscillation cycles C1 through C4 as in Fig. 1C.

(D) Expression changes for an oscillation with a constant 7h period (*dotted line*), and an oscillation reconstructed from the mean oscillation period in (C) (*black line*), both amplitudes set to four. The expression of a representative gene, *col-147* (mean normalized) is shown (*red line*). Horizontal gray bars indicate oscillation cycles C1 through C4 as in Fig. 1C.

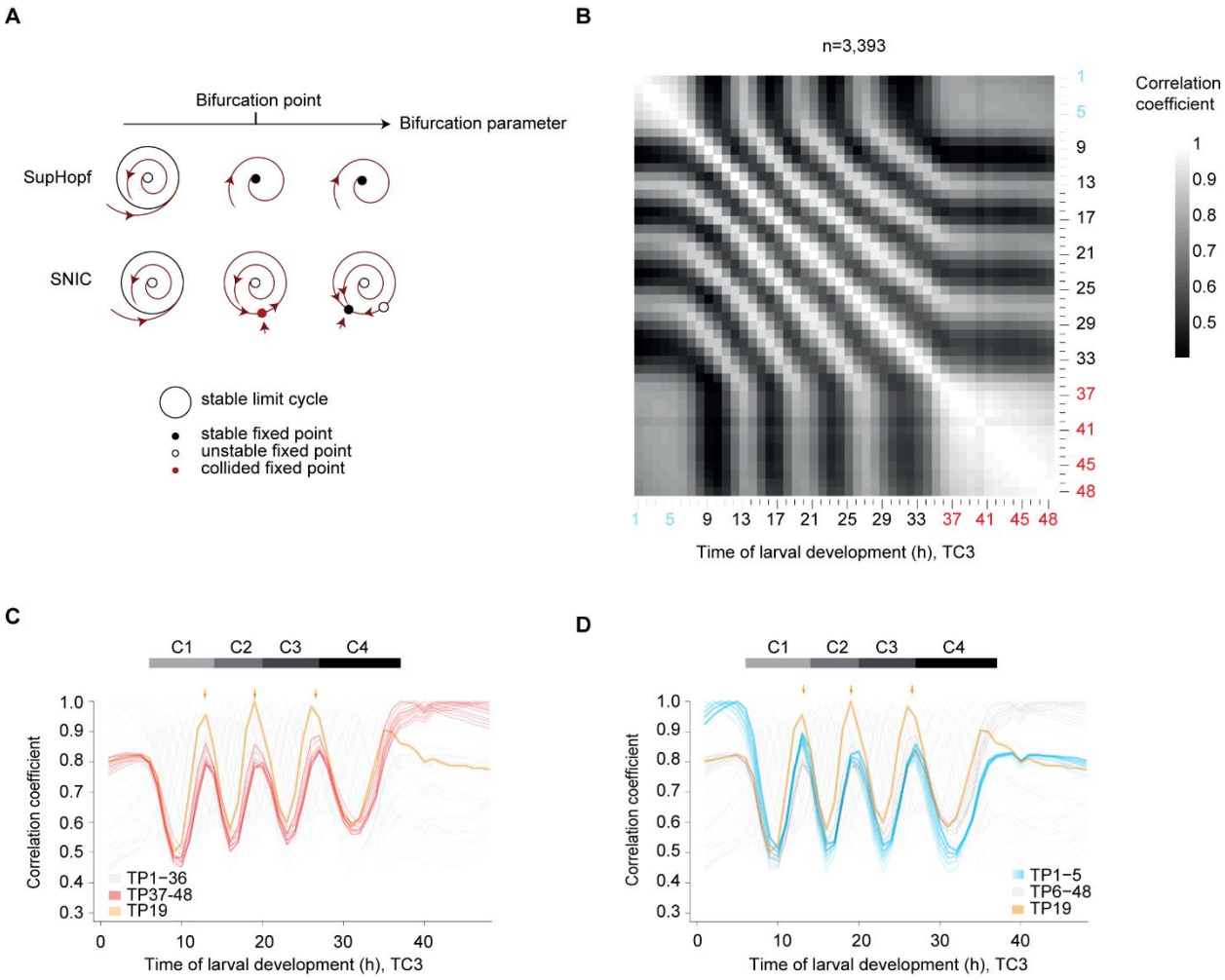

Fig 5: The oscillator is phase arrested in early L1 and adults

(A) Phase plane diagrams depicting supH and SNIC bifurcations, respectively, showing the change in qualitative behavior as the bifurcation parameter value changes (arrow). The bifurcation point, i.e. the parameter value at which the bifurcation occurs, is indicated.

(B) Pairwise correlation plot of $\log_2$-transformed oscillating gene expression data obtained from TC3, i.e., the fusion of TC1 (*blue labels*) and TC2 (*black*). Genes which deviated in mean expression in L4 were excluded (Fig. S4), resulting in n=3,393 genes.

(C) Lines of correlation for TP37–48 (*red*) to all time points in the fused larval time course. Arrows indicate local correlation maxima at TP13, 19 and 26/27. Correlation traces for TP ≤ 36 h are shown in light gray, except for TP19 (*orange*). Fig. S5 illustrates how correlation lines were generated.

(D) Lines of correlation for TP1–5 (*blue*) and TP19 (*orange*) to all time points in the fused larval time course. Arrows indicate local correlation maxima at TP13, 19 and 26/27.

All correlations were determined by Pearson correlation. Correlation values were obtained from Fig. 5B.

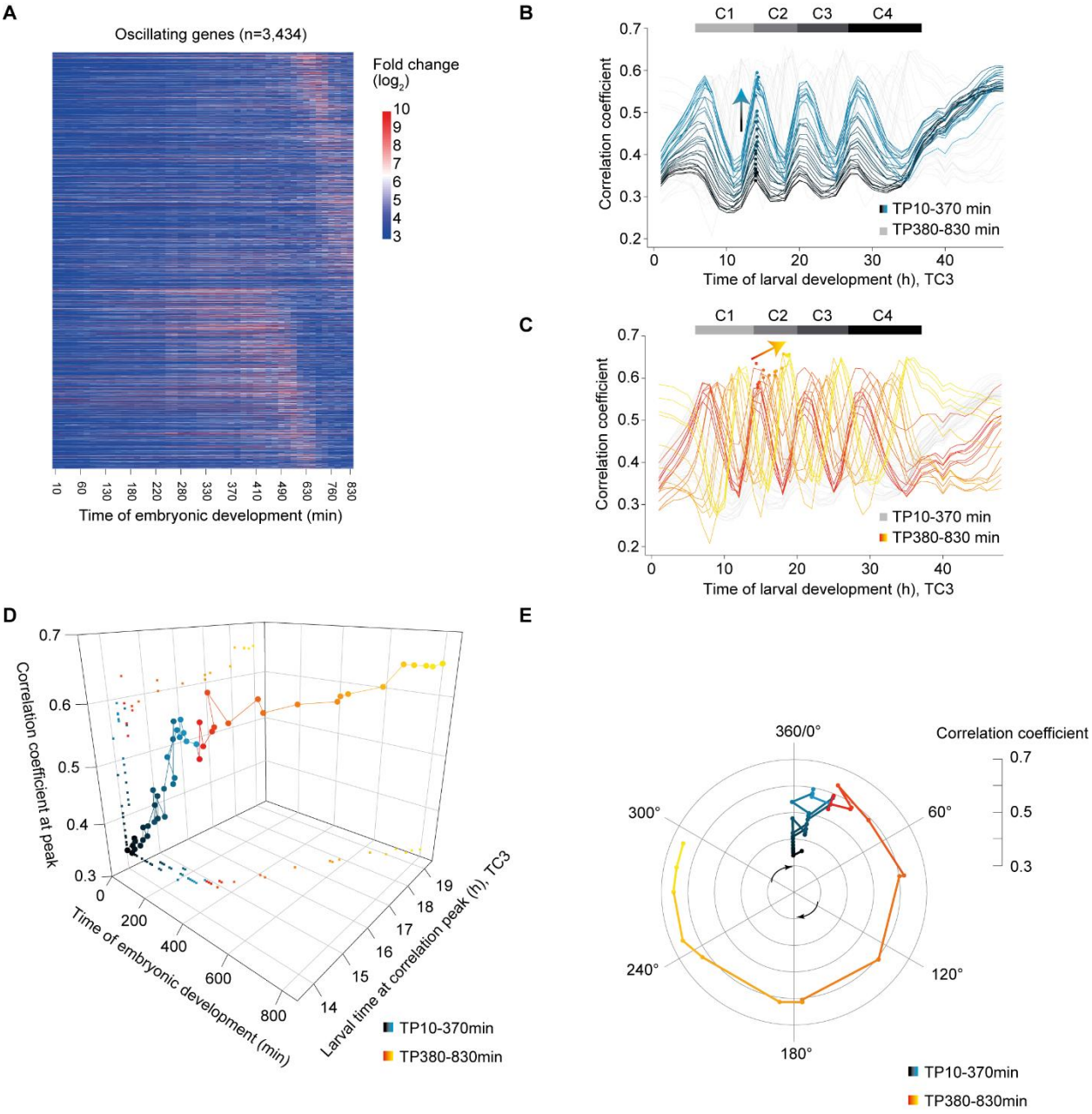

Fig 6: Transition to an oscillatory state during embryogenesis

(A) Heatmap of log_2-transformed embryonic expression of oscillating genes, excluding L4 deviating genes, sorted by larval peak phase (defined as in Fig. 1).

(B, C) Pairwise correlation coefficients between embryonic and larval time points (Fig. S7) plotted over larval time for embryonic TP10-370 min (B, *black-blue gradient*) and TP380-830 min (C, *red-yellow gradient*), respectively. Dots represent peaks of the correlation lines after spline analysis in the second oscillation cycle (C2), arrows indicate trends. Horizontal gray bars indicate oscillation cycles C1 through C4 as in Fig. 1C.

(D) 3D-scatter plot of the correlation coefficient peak for each embryonic time point to the time of larval development at the second oscillation cycle (C2). Embryonic time is determined by time of sample collection, larval time by spline interpolation. Color scheme as in B and C.

(E) Polar plot of correlation coefficient peak over the time point in the second larval oscillation cycle (C2) at which the correlation peak is detected. TP14 is defined as 0° and correlates most highly to TP20, thus defined as 360°. Values are as in D; color scheme as in B and C.

All correlations were determined by Pearson correlation.

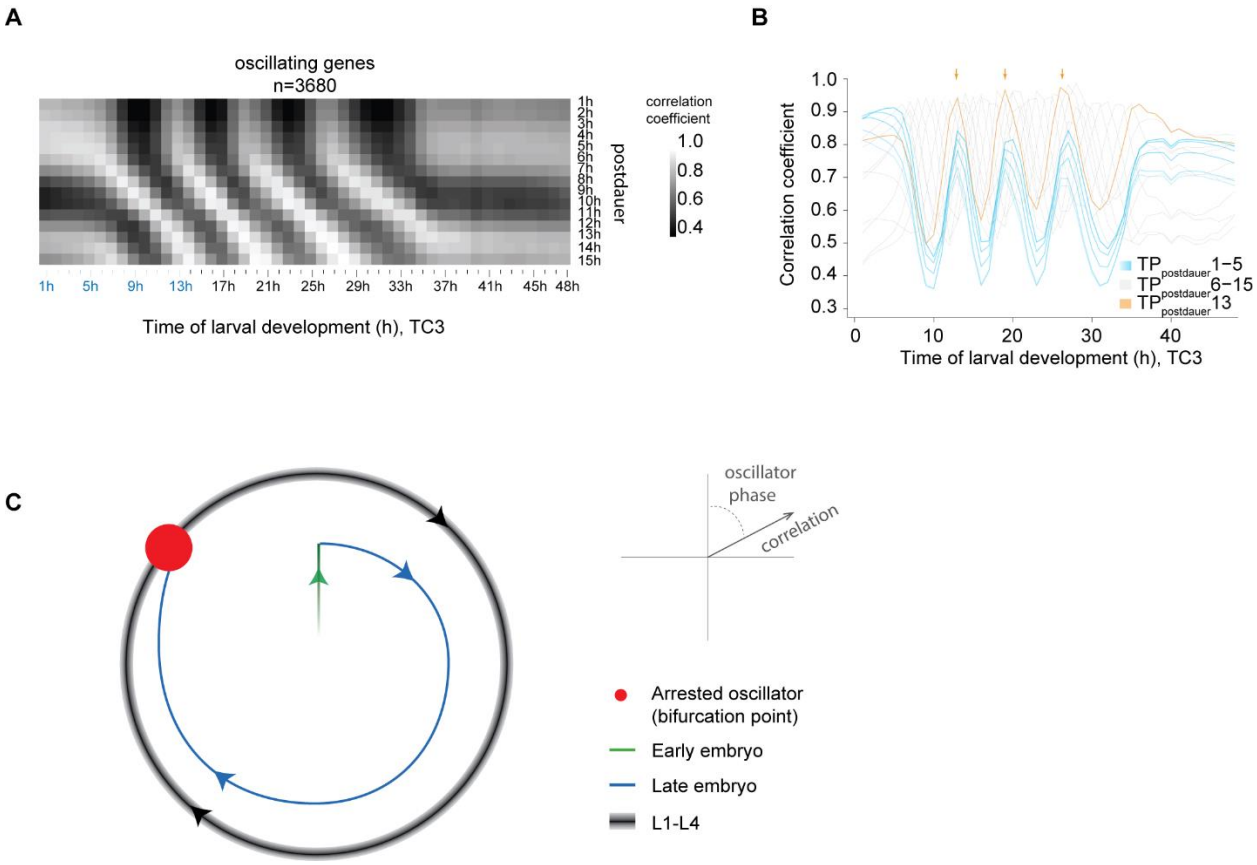

Fig 7: Re-initiation of oscillations after dauer from an arrested oscillator phase

(A) Pairwise-correlation map of log_2-transformed oscillatory gene expression of dauer exit samples ("postdauer") and fused larval time course (TC3) samples.

(B) Correlation of the indicated time points after plating dauer-arrested animals on food (TPpostdauer) to the fused larval time course, TC3. Arrows indicate peaks of correlation to TP13/19/26.5 (300°) of TC3.

(C) Schematic depiction of behavior of the *C. elegans* oscillator from embryo to adult. A phase-specific arrest (*red dot*) is observed in hatch, early L1, young adults, and dauer-arrested animals. See Fig. S8 for additional data supporting four similar oscillation cycles during L1 through L4.

Results

Methods

C. elegans strains

The Bristol N2 strain was used as wild type. The following transgenic strains were used:
HW1370: *EG6699; xeSi136 [F11E6.3p::gfp::h2b::pest::unc-54 3'UTR; unc-119 +] II* (this study)
HW1939: *EG6699, xeSi296 [eft-3p::luc::gfp::unc-54 3'UTR, unc-119(+)] II* (this study)
HW2523: *EG6699*: *xeSi437 [qua-1p::gfp::h2b::pest::unc-54 3'UTR; unc-119 +] II* (this study)
HW2526: *EG6699: xeSi440 [dpy-9p::gfp::h2b::pest::unc-54 3'UTR; unc-119 +] II* (this study)
PE254: *feIs5 [sur-5p::luc::gfp; rol-6(su1006)] V* (Lagido et al., 2008)
PE255: *feIs5 [sur-5p::luc::gfp; rol-6(su1006)] X* (Lagido et al., 2008)

All transcriptional reporters and luciferase constructs produced for this study were generated using Gibson assembly (Gibson et al., 2009) and the destination vector pCFJ150 (Frøkjaer-Jensen et al., 2008). First a starting plasmid was generated by combining *Not*I digested pCFJ150, with either *Nhe-1::GFP-Pest-H2B* or *Nhe-1::luciferase::GFP* (adapted from pSLGCV (Lagido et al., 2008)) and ordered as codon optimized, intron containing gBlocks® Gene Fragment (Integrated DNA Technologies), and *unc-54 3'UTR* (amplified from genomic DNA) to yield pYPH0.14 and pMM001 respectively. Second, promoters consisting of either 2kb upstream of the ATG or up to the next gene were amplified from *C. elegans* genomic DNA before inserting them into *Nhe*I-digested pYPH0.14 or pMM001. PCR primers and resulting plasmids are listed in the Table S3. Third, we obtained transgenic worms by single-copy integration into EG8079 worms, containing the universal *ttTi5605* locus on chromosome II by following the published protocol for injection with low DNA concentration (Frøkjær-Jensen et al., 2012). All MosSCI strains were backcrossed at least twice.

Methods luciferase assay

Gravid adults were bleached and single embryos were transferred by pipetting into a well of a white, flat-bottom, 384-well plate (Berthold Technologies, 32505). Embryos hatched and developed in 90 µL volume containing *E. coli* OP50 (OD_{600} = 0.9) diluted in S-Basal medium (Stiernagle, Theresa, n.d.), and 100 µM Firefly D-Luciferin (p.j.k., 102111). Plates were sealed

with Breathe Easier sealing membrane (Diversified Biotech, BERM-2000). Luminescence was measured using a Luminometer (Berthold Technologies, Centro XS3 LB 960) for 0.5 seconds every 10 minutes for 72 hours at 20°C in a temperature-controlled incubator and is given in arbitrary units.

Luminescence data was analyzed using an automated algorithm for molt detection on trend-corrected data as described previously (Olmedo et al., 2015), but implemented in MATLAB, and with the option to manually annotate molts in a Graphical User Interface. The hatch was identified as the first data point (starting from time point 4 to avoid edge effects) that exceeds the following value: the mean + 5*stdev of the raw luminescence of the first 20 time points.

To quantify the duration of the molts, we subtracted the time point at molt entry from the time point at molt exit. To quantify the duration of larval stages, we subtracted the time point at molt exit of the previous stage (or time point at hatch for L1) from the time point at molt exit of the current stage. The duration of the intermolt was quantified as duration of the molt subtracted from duration of the larval stage. For statistical analysis, we assumed the durations to be normally distributed and used Welch two-sample and two-sided t-test, i.e. the function ‘t.test’ of the package ‘stats’ (version 3.5.1) (R Core Team, n.d.) in R.

RNA sequencing

For RNA sequencing, synchronized L1 worms, obtained by hatching eggs in the absence of food, were cultured at 25°C and collected hourly from 1 hour until 15 hours of larval development, or 5 hours until 48 hours of larval development, for L1–L2 time course (TC1) and L1–YA time course (TC2) respectively. A replicate experiment was performed at room temperature from 1 hours until 24 hours (TC4). RNA was extracted in Tri Reagent and DNase-treated as described previously (Hendriks et al., 2014). For the TC2 and TC4, libraries were prepared using the TruSeq Illumina mRNA-seq (stranded – high input), followed by the Hiseq50 Cycle Single-end reads protocol on HiSeq2500. For the TC1, libraries were prepared using the Illumina TruSeq mRNA-Seq Sample Prep Kit (Strand-sequenced: any), followed by the Hiseq50 Cycle Single-end reads protocol on HiSeq2500.

Results

Processing of RNA-seq data

RNA-seq data were mapped to the *C. elegans* genome using the qAlign function (splicedAlignment=TRUE) from the QuasR package (Au et al., 2010; Gaidatzis et al., 2015) in R. Gene expression was quantified using qCount function from the QuasR package in R. For TC2 and Dauer exit (Hendriks et al., 2014) time course, QuasR version 1.8.4 was used, and data was aligned to the ce10 genome using Rbowtie aligner version 1.8.0. For TC1, QuasR version 1.2.2 was used, and data was aligned to the ce6 genome using Rbowtie aligner version 1.2.0. For TC4 (Fig. 2), RNA-seq data were mapped to the *C. elegans* ce10 genome using STAR with default parameters (version 2.7.0f) and reads were counted using htseq-count (version = 0.11.2). Counts were scaled by total mapped library size for each sample. A pseudocount of 8 was added and counts were $\log_2$-transformed. For the TC2, lowly expressed genes were excluded (maximum $\log_2$-transformed gene expression - ($\log_2$(gene width)-mean($\log_2$(gene width))) ≤ 6). This step was omitted in the early time courses because many genes start robust expressing only after 5-6 hours. Expression data of the dauer exit time course was obtained from (Hendriks et al., 2014).

Classification of genes

To classify genes, we applied cosine fitting to the $\log_2$-transformed gene expression levels from t=10 hours until t=25 hours of developmental time (mid L1 until late L3) of TC2, when the oscillation period is most stable (Fig. 4C). During this time the oscillation period is approximately 7 hours, which we used as fixed period for the cosine fitting. We built a linear model as described (Hendriks et al., 2014) using cos(ωt) and –sin(ωt) as regressors (with 13 degrees of freedom). In short, a cosine curve can be represented as:

$C * \cos(\omega t + \varphi) = A * \cos(\omega t) - B * \sin(\omega t)$

With $A = C * \cos(\varphi)$

and $B = C * \sin(\varphi)$

From the linear regression ('lm' function of the package 'stats' in R) we obtained the coefficients A and B, and their standard errors. A and B represent the phase and the amplitude of the oscillation:

$phase = \arctan(A, B)$

$amplitude = \sqrt{A^2 + B^2}$

Results

As the density of the genes strongly decreased around 0.5 (Fig. S1C) we used amplitude ≥ 0.5 as a first classifier. We propagated the standard error of the coefficients A and B to the amplitude using Taylor expansion in the 'propagate' function (expr=expression(sqrt(((A^2)+(B^2))), ntype = 'stat', do.sim=FALSE, alpha=0.01) from the package 'propagate' (version 1.0-6) (Spiess, 2018) in R. We obtained a 99% confidence interval (99%-CI) for each gene. As 99%-CI that does not include 0 is significant (p-value=0.01), we used the lower boundary (0.5%) of the CI as a second classifier. Thus, we classified genes with an amplitude ≥ 0.5 and lower CI-boundary ≥ 0 as 'oscillating' and genes with an amplitude < 0.5 or a lower CI-boundary < 0 were classified as 'not oscillating' (Fig. 1B, S1C). Every gene thus has an amplitude and a peak phase. A peak phase of 0° is arbitrarily chosen, and thus current peak phases are expected to differ systematically from the previously assigned peak phases (Hendriks et al., 2014). To compare the peak phases of TC2 with those of the previously published L3-YA time course (TC6), we calculated the phase difference (TC2 – TC6) (Fig. S1D, E). We added 360° to the difference and used the modulus operator (%%360), to maintain the circularity within the data. The coefficient of determination, R^2, was calculated by 1-(SSres/SStot), in which the SStot (total sum of squares) is the sum of squares in peak phase of the L1-YA time course. SSres (response sum of squares) is the sum of squares of the phase difference.

Time course fusion

In order to obtain an RNAseq time course spanning the complete larval development, we fused the L1–L2 time course (TC1, TP1 – TP15) with the L1–YA course (TC2, TP5 – TP48). To decide which time points to choose from the individual time courses, we correlated the gene expression of all genes (n = 19,934) of both time courses against each other using the $\log_2$ transformed data with a pseudocount of 8 with pearson correlation. In general, we saw good correlation between the two time courses, e.g. $TP1_{(TC1,\ L1–L2)}$ correlated well with $TP1_{(TC2,\ L1–YA)}$ etc. (Fig. S1B). Additionally, we could see comparable correlation values of $TP13_{(TC2,\ L1–YA)}$ and $TP13_{(TC1,\ L1\text{-}L2)}$ with $TP1–5_{(TC1,\ L1–L2)}$ (not shown). We concluded that $TP13_{(TC1,\ L1–L2)}$ and $TP13_{(TC2,\ L1–YA)}$ are highly similar and thus fused at this time point, i.e., combined $TP1–TP13_{(TC1,\ L1–L2)}$ with $TP14–TP48_{(TC2,\ L1–YA)}$.

Exclusion of genes based on L4 mean expression

Given that oscillating genes were identified based on gene expression in TP10-TP25, when oscillation period is most stable, some genes showed deviating behavior in the last oscillation cycle, C4. Hence, for quantification of oscillation amplitude, period and correlation, we excluded those genes. We determined the mean expression levels for each gene over time in oscillation cycles C2 (TP14-TP20), C3 (TP20-TP27) and C4 (TP27-TP36). Genes (n=291) were excluded if the absolute value of the difference in mean expression between L2 and L4 normalized by their mean difference exceeded 0.25, i.e. abs((L2meanExpr-L4meanExpr)/(0.5*(L2meanExpr-L4meanExpr)))>0.25.

Quantification of oscillation amplitude

To quantify the oscillation amplitude for each larval stage, we split the TC2 in 4 separate cycles, roughly corresponding to the developmental stages, i.e. C1: TP6-TP14, C2: TP14-TP20, C3: TP20-TP27 and C4: TP27-TP36 developmental time. We applied cosine fitting to C2, C3 and C4 as described above to the expression of oscillating genes in TC2, excluding genes with deviating mean expression in L4 as described above. We excluded C1, because amplitudes were sometimes difficult to call reliably. We used a fixed period of 7 h for C2-C3 and 8.5 h for C4 as determined by quantification of the oscillation period (Fig. 4C). We applied a linear regression using the function ‘lm’ of the package ‘stats’ in R to find the relationship between the amplitudes across different stages, i.e. the slope. The correlation coefficient, r, was determined using the ‘cor’ function (method=pearson) of the package ‘stats’ in R.

Quantification of oscillation period

For a temporally resolved quantification of the oscillation period, we filtered the mean-normalized $\log_2$ transformed gene expression levels of oscillating genes, excluding L4 deviating genes (we selected TP5-TP39, because oscillations cease at ~TP36 and the inclusion of 3 additional time points avoided edge effects) using a Butterworth filter (‘bwfilter’ function of the package ‘seewave’ (version 2.1.0) (Sueur et al., 2008) in R, to remove noise and trend-correct the data. The following command was used to perform the filtering: bwfilter(data, f = 1 , n = 1, from = 0.1, to = 0.2, bandpass = TRUE, listen = FALSE, output = "matrix"). The bandpass frequency from 0.1 to 0.2 (corresponding to 10 hour and 5 hour period respectively) was selected

based on the Fourier spectrum obtained after Fourier transform ('fft' function with standard parameters of the package 'stats'). As an input for the Hilbert transform we used the butterworth-filtered gene expression. The 'ifreq' function (with standard parameters from the package 'seewave') was used to calculate the instantaneous phase and frequency based on the Hilbert transform. To determine the phase progression over time we unwrapped the instantaneous phase (ranging from 0 to 2π for each oscillation) using the 'unwrap' function of the package 'EMD' (version 1.5.7) (Kim and Oh, 2018) in R. To avoid edge effects, we removed the first 4 data points (TP5-TP8) and last 3 data points (TPTP37-TP39) of the unwrapped phase (retaining TP9-TP36). The angular velocity is defined as the rate of phase change, which we calculated by taking the derivative of the unwrapped phase. The instantaneous period was determined by 2π/angular velocity and was plotted for each gene individually and as mean in a density plot. The mean of the instantaneous period over all oscillating genes was used to reconstruct a 'global' oscillation by taking the following command: sin(cumsum(mean angular velocity)) and plotted together with a 7h-period oscillation and the mean normalized expression of a representative gene, *col-147*.

Correlation analyses of RNAseq data

Log_2-transformed data was filtered for oscillating genes and then plotted in a correlation matrix using the R command cor(data, method="pearson"). The correlation line plots represent the correlations of selected time points to the fused full developmental time course (Fig. S5) and are specified in the line plot.

To reveal the highest correlations for a selected time point, we analyzed the correlation line of this time point between TP7 and TP36 (the time in which oscillations occur) using a spline analysis from Scipy (Jones et al., 2001) in python ("from scipy.interpolate import InterpolatedUnivariateSpline" with k=4) and stored the spline as variable "spline". We identified peaks of the correlation line by finding the zeros of the derivative of the spline (cr_points = spline.derivative().roots()). The highest correlations of the respective correlation line were thus the value of the spline at the time point where the spline derivative was zero and the value was above the mean of the correlation line (cr_vals = spline(cr_pts) followed by pos_index = np.argwhere(cr_vals>np.mean(data.iloc[i])) and peak_val = cr_vals[pos_index]). Thus, we identified the correlation of particular time points (e.g. TP14–TP19) with their corresponding

time points in the next oscillation cycle. Thereby, we were able to identify cycle time points as described in the results section. We defined the first cycle time point, e.g. TP14 of cycle 2, as 0°, and the last unique one, TP19, as 300°. TP14 (0° of cycle 2) is also 360° of cycle 1. Note that a sampling interval of 1 hour means that a TP in one cycle may correlate equally well to two adjacent TPs in another cycle, as seen for instance in the correlation of TP13 to TP26 and TP27. The spline interpolation places the peak of correlation in the middle of these time points at ~TP26.5. The spline analysis thus annotates cycle points correctly even in C4 which has an extended period.

We performed correlation analyses without mean normalization of expression data, hence correlation values cannot be negative but remain between 0 and 1. We made this decision because a correlation analysis using mean-centered data, where correlations can vary between -1 and +1, requires specific assumptions on which time points to include or exclude for mean normalization, and because it is sensitive to gene expression trends. However, we confirmed, as a proof of principle, the expected negative correlation of time points that are in antiphase when using mean-centered data (Fig. S9) using all oscillating genes in TC3 (n = 3680).

GO-term analysis

GO-term analysis was performed using the GO biological process complete option (GO ontology database, release 2019-02-02) from the online tool PANTHER ("PANTHER Classification System," n.d.) (overrepresentation test, release 2019-03-08, standard settings).

Tissue specific analysis

In order to reveal if particular tissues are enriched in oscillating genes, we used single cell sequencing data from (Cao et al., 2017). In particular, we used Supplementary "Table S6: Differential expression test results for the identification of tissue-enriched genes" where each gene's highest and second highest tissue expression and the ratio of is reported. We selected tissue specific genes based on a ratio > 5 and a qvalue < 0.05 (these criteria reduced the number of genes to investigate). Using this list of genes we calculated the percentage of tissues present in both, all genes and oscillating genes using the function "Counter" from "collections" in python (*labels, values = zip(*Counter(tissue_info_thr["max.tissue"]).items())*). In order to obtain the enrichment of tissues, we divided the percentage of tissue X among oscillating genes in the tissue

enriched dataset by the percentage of tissue X among all genes in the tissue enriched data set and plotted the resulting values. The list of tissue specific oscillating genes was further used to investigate the peak phases within one tissue by plotting a density plot of the peak phase (from Fig. 1) for every tissue. As we lack data below 0 degree and above 360 degree, density values at these borders are distorted as the density is calculated over a moving window. Since we are confronted with cyclical data and thus 0 degree corresponds to 360 degree, we added and subtracted 360 degree to each phase value, thus creating data that ranged from -360 degree to 720 degree which allowed us to plot the correct density at the borders 0 and 360 degree. We used python (pandas) to plot this data using the following command:
data_tissue ["Phase"].plot(kind="kde", linewidth=5, alpha=0.5, bw=0.1)

Identification of first gene expression peaks in L1 larvae

To identify the first peak of oscillating genes, we used a spline analysis in Python ("from scipy.interpolate import InterpolatedUnivariateSpline") from TP3 – TP13. We chose these time points to remove false positives in the beginning due to slightly higher noise for the first 2 time points as well as not to identify the second peak which occurred at ≥TP14 for some very early genes. The function used was "InterpolatedUnivariateSpline" with k=4. After constructing the spline, we identified the zeros of the derivative and chose the time point value with the highest expression value and a zero derivative as the first peak time point.

Embryonic gene expression time course

Embryonic gene expression data was obtained from (Hashimshony et al., 2015), and represented precisely staged single embryos at 10 min intervals from the 4-cell stage up to muscle movement and every 10-70 min thereafter until 830 minutes. We obtained the gene count data from the Gene Expression Omnibus data base under the accession number GSE50548, for which sequencing reads were mapped to WBCel215 genome and counted against WS230 annotation. We normalized the gene counts to the total mapped library size per sample, added a pseudocount of 8, and $\log_2$-transformed the data. We selected genes according to the larval oscillating gene annotation, with L4 deviating genes excluded, and plotted their embryonic expression patterns according to peak phase in larvae. The embryonic time course was correlated to the fused larval time course (TC3) using the 'cor' function (method='pearson') of the package 'stats' in R (Fig.

S7A). Correlation line plots were generated by plotting the correlation coefficients for each embryonic time point over larval time. To identify the peaks of the correlation lines with a resolution higher than the sampling frequency, we interpolated the correlation lines using the 'spline' function (n=240, method='fmm') of the package 'stats' in R. To call the peaks of the interpolated correlation lines, we applied the 'findpeaks' function (with nups=5, ndowns=5) of the package 'pracma' on the time points on the interpolated time points 10-185, that cover the four cycles. To find the embryonic time point at which oscillations initiate, we plotted the larval TP in cycle 2 at which the correlation peak occurred over embryonic time (Fig. S7B) and determined the intersection of the two linear fits, using the 'solve' function of the package 'Matrix' (version 1.2-15) (Bates and Maechler, 2018) and the 'lm' function of the package 'stats' in R respectively. To determine the 95%-CI of the x-coordinate of the intersect, the standard error of the slope a and the intercept b of the two linear fits was propagated using Taylor expansion in the 'propagate' function (expr = expression((b1-b2)/(a2-a1)), ntype = "stat",do.sim = FALSE, alpha=0.05) from the package 'propagate' in R. The pairwise correlation map was generated with the 'aheatmap' function of the package 'NMF' (version 0.21.0) (Gaujoux and Seoighe, 2010) and the 3D plot was generated with the '3Dscatter' function of the package 'plot3D' (version 1.1.1) (Soetaert, 2017) in R.

Time-lapse imaging of single animals

Single worm imaging was done by adapting a previous protocol (Turek et al., 2015), and is similar to the method reported in (Gritti et al., 2016). Specifically, we replaced the previous 3.5-cm dishes with a "sandwich-like" system: The bottom consisted of a glass cover slip onto which two silicone isolators (GRACE Bio-Labs, SKU: 666103) with a hole in the middle were placed on top of each other and glued onto the glass cover slip. We then placed single eggs inside the single OP50 containing chambers, which were made of 4.5% agarose in S-basal. The chambers including worms were then flipped 180 degree and placed onto the glass cover slip with the silicone isolators, so that worms faced the cover slip. Low melt agarose (3% in S-basal) was used to seal the agarose with the chambers to prevent drying out or drifts of the agarose chambers during imaging. The sandwich-like system was then covered with a glass slide on the top of the silicone isolators to close the system.

Results

We used a 2x sCMOS camera model (T2) CSU_W1 Yokogawa microscope with 20x air objective, NA = 0.8 in combination with a 50µm disk unit to obtain images of single worms. For a high throughput, we motorized the stage positioning and the exchange between confocal and brightfield. We used a red LED light to combine brightfield with fluorescence without closing the shutter. Additionally, we used a motorized z-drive with 2 µm step size and 23 images per z-stack. The 488nm laser power for GFP imaging was set to 70% and a binning of 2 was used.

To facilitate detection of transgene expression and oscillation, we generated reporters using the promoters of genes that exhibited high transcript levels and amplitudes, and where GFP was concentrated in the nucleus and destabilized through fusion to PEST::H2B (see strain list above). We placed embryos into chambers containing food (concentrated bacteria HT115 with L4440 vector) and imaged every worm with a z-stack in time intervals of 10 min during larval development in a room kept at ~21°C, using a double camera setting to acquire brightfield images in parallel with the fluorescent images. We exploited the availability of matching fluorescent and brightfield images to identify worms by machine learning. After identification, we flattened the worm at each time point to a single pixel line and stacked all time points from left to right, resulting in one kymograph image per worm. We then plotted background-subtracted GFP intensity values from the time of hatch (t = 0 h), which we identified by visual inspection of the brightfield images as the first time point when the worm exited the egg shell.

Time lapse images were analyzed using a customized KNIME workflow (Supplemental File 1). We analyzed every worm over time using the same algorithm. First, we identified the brightest focal planes per time point by calculating the mean intensity from all focal planes per time point and selecting the focal planes that had a higher intensity than the mean. Then we maximum-projected the GFP images over Z per time point and blurred the brightfield image and also max projected over Z (blurring the brightfield improved the machine learning process later on). All images per worm over time were analyzed by Ilastik machine learning in order to identify the worm in the image. The probability map from Ilastik was used to select a threshold that selected worms of a particular experiment best. (The threshold might change slightly as brightfield images can look slightly different due to differences in the sample prep amongst experiments.) Using a customized ImageJ plugin, we straightened the worm. The straightened GFP worm image was then max projected over Y which resulted in a single pixel line representing the GFP intensities in a worm and after stacking up all the single pixel lines in Y

direction, we obtained the kymographs. In order to remove noise coming from the head and tail regions of the worm due to inaccuracy of the machine learning, we measured mean GFP intensities per time point ranging from 20% until 80% of the worms anterior – posterior axis. For background subtraction we exploited the fact that only the nuclei were GFP positive and thus subtracted the minimum intensity value between GFP nuclei from their intensity values.

After the KNIME workflow, we imported the measured GFP intensities into Python and analyzed the traces using a butterworth filter and Hilbert transform analysis (both from Scipy (Jones et al., 2001)). We used the butterworth bandpass filter using b, a = butter(order =1, [low,high], btype=”band”) with low=1/14 and high=1/5, corresponding to 14 hour and 5 hour periods respectively. We then filtered using filtfilt(b, a, data, padtype='constant') to linearly filter backwards and forwards.

For individual time points where the worm could not be identified by the Ilastik machine learning algorithm, we linearly interpolated (using interpolation from pandas (McKinney, 2010)) using “pandas.series.interpolate(method = 'linear', axis =0, limit = 60, limit_direction = 'backward'”, between the neighboring time points to obtain a continuous time series needed for the Hilbert transform analysis. Using Hilbert transform, we extracted the phase of the oscillating traces for each time point and specifically investigated the phase at molt entry and molt exit for our different reporter strains.

In order to determine time points in which worms are in lethargus, we investigated pumping behavior. As the z-stack of an individual time point gives a short representation of a moving worm, it is possible to determine whether animals pump (feeding, corresponds to intermolt) or not (lethargus / molt). Additionally to the pumping behavior, we used two further requirements that needed to be true in order to assign the lethargus time span: First, worms needed to be quiescent (not moving, and straight line) and second, a cuticle needed to be shed at the end of lethargus. Usually worms start pumping one to two time points before they shed the cuticle. This analysis was done manually with the software ImageJ, and results were recorded in an excel file, where for every time point, the worms’ behavior was denoted as 1 for pumping and as 0 for non-pumping.

To determine a possible connection between oscillations and development, we applied error propagation, assuming normal distribution of the measured phases and larval stage durations. Thereby, we exploited the inherent variation of the oscillation periods and

developmental rates among worms, rather than experimental perturbation, to probe for such a connection. We define the phase θ at either molt exit or entry as $\theta \equiv \frac{2\pi}{T_o} * T_d \sim (\mu, \sigma^2)$ with $T_o \sim (\mu_o, \sigma_o^2)$ being the period of oscillation and $T_d \sim (\mu_d, \sigma_d^2)$ the intermolt duration (for phase at molt entry) or larval stage duration (for phase at molt exit), resulting in a phase with mean μ and a standard deviation σ. Should the two processes be coupled as in scenario 2, we would expect

$\sigma_{observed} < \sigma_{calculated}$.

To calculate the phase at molt entry and molt exit with error propagation we used the "uncertainties" package (Lebigot, n.d.) in python. The larval stage duration as well as intermolt duration and period were treated as ufloat numbers, representing the distributions coming from our measurement (e.g. 7.5 +/- 0.2). These distributions were then used to calculate the expected phase at molt entry (using the intermolt duration) and molt exit (using the larval stage duration) using: $phase(err.prop) = \frac{2*pi}{period} * larval\ stage$. This resulted in the phase being represented by an ufloat number and thus a distribution which we used for plotting after normalizing for the mean to compare the variation of the data.

Supplementary Figures and Materials

Developmental function and state transitions of a gene expression oscillator in *C. elegans*

Authors: Milou W.M. Meeuse, Yannick P. Hauser, Gert-Jan Hendriks, Jan Eglinger, Guy Bogaarts, Charisios Tsiairis, Helge Großhans*

*Correspondence to: helge.grosshans@fmi.ch.

This PDF file includes:

Figs. S1 to S9
Tables S2 to S3

Other Supplementary Materials for this manuscript include the following:

Table S1
File S1

A

	Description	TP	Figure	# osc genes	# osc w/o deviating L4 genes
TC1	early larval time course, replicate 1	1-15	2	3680	NA
TC2	long developmental time course	5-48	4, S1, S4	3739	3448
TC3	TC1 (TP1-13) + TC2 (TP14-48)	1-48	1, 2, 5, 6, 7, S1, S5, S8, S9	3680	3393
TC4	early larval time course, replicate 2	1-24	2	3739	NA
TC5	TC4 (TP1-13) + TC2 (TP14-48)	1-48	S2	3739	NA
TC6	L3-YA TC from Hendriks et al, 2014	21-36	S1	2718	NA
embryo	Hashimshony et al, 2015	10-830	6, S7	3723	3434
dauer	Hendriks et al, 2014	1-15	7	3680	3393

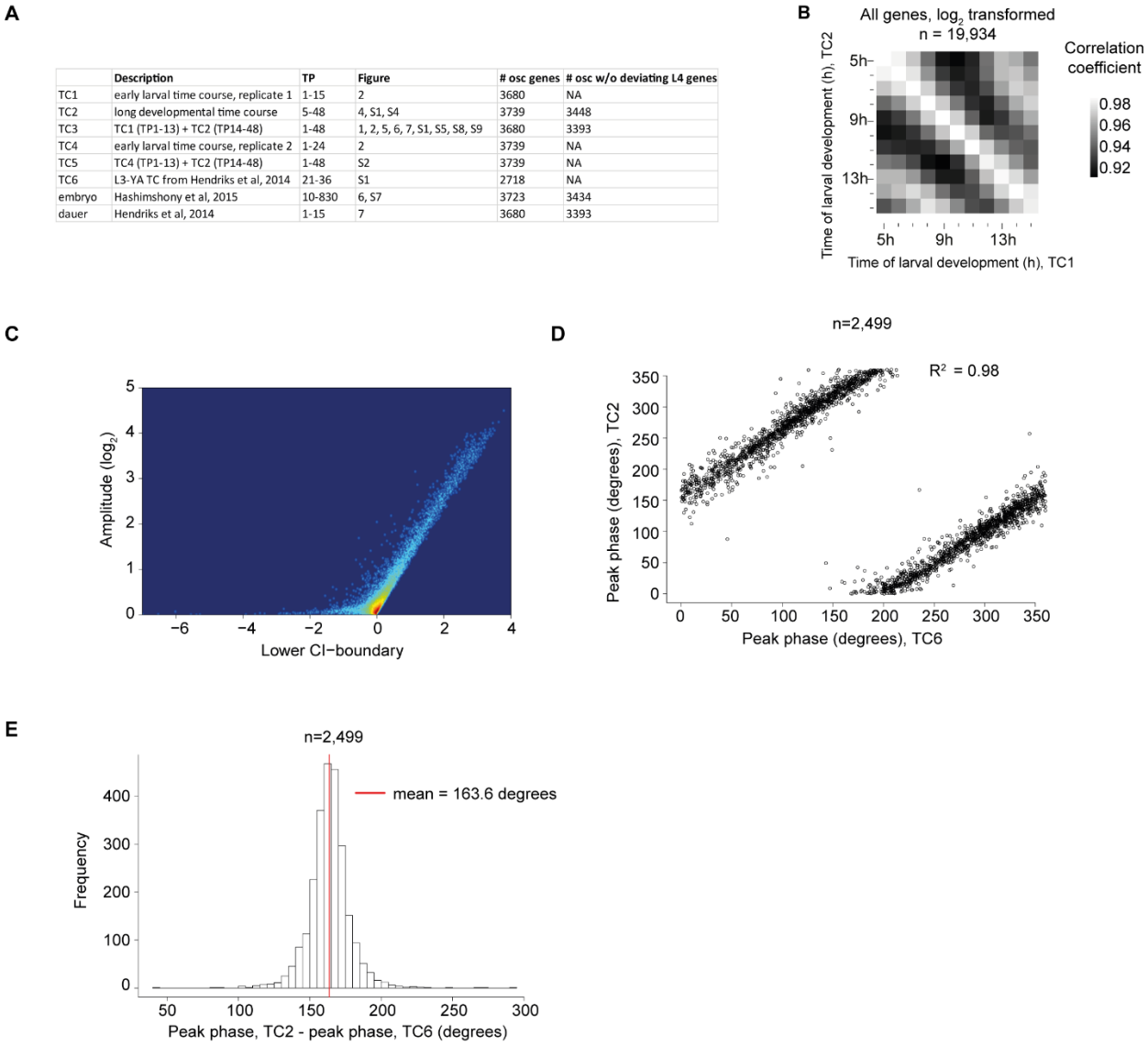

Fig. S1. Identification of 3,739 'oscillating' genes

(A) Overview of time courses in this study

(B) Pairwise-correlation of log_2 transformed count data (n=19,934) of the early time course (TC1) with the long developmental time course (TC2). High correlation is detected for samples that correspond to the same time points, justifying a fusion of these time courses to one continuous full developmental time course (TC3).

(C) Smooth scatter of amplitude over lower boundary of 99% confidence interval of the amplitude as determined by cosine fitting and error propagation (see methods, related to Fig. 1B).

(D, E) Scatterplot (D) of the peak phase of the long developmental time course (TC2) described here over the previously published L3-YA time course (TC6) (Hendriks et al., 2014). Genes that were identified as 'oscillating' in both time courses (n = 2,499) are shown. Peak phases correlate well as confirmed by the coefficient of determination, R^2, as indicated. However, they differ systematically (E) because a peak phase of 0° is arbitrarily chosen. A red vertical line indicates the mean phase difference (TC2 – TC6; corrected for circularity as described in Methods). Note

that the gene-specific peak phase calculated here and previously both also differ from the arbitrarily assigned cycle phases in Fig. S8 and their discussion.

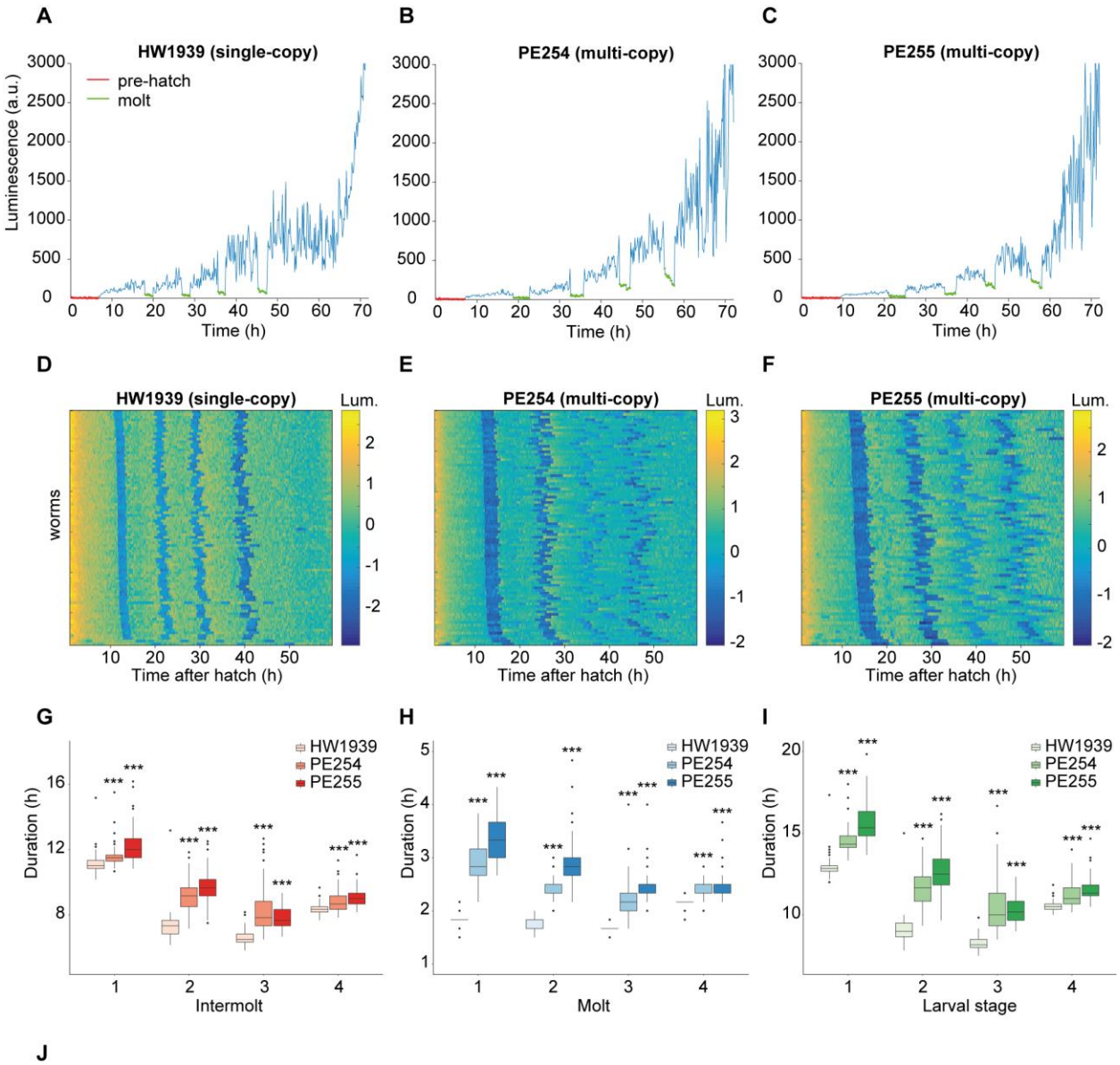

J

	stage 1	stage 2	stage 3	stage 4
Intermolt PE254	1.04 (p=3.28E-03)	1.26 (p=4.51E-31)	1.26 (p=3.07E-19)	1.05 (p=1.94E-08)
Intermolt PE255	1.10 (p=1.98E-10)	1.32 (p=1.39E-35)	1.19 (p=3.72E-30)	1.08 (p=2.10E-16)
Molt PE254	1.60 (p=4.92E-51)	1.40 (p=9.60E-54)	1.33 (p=2.11E-29)	1.11 (p=8.68E-23)
Molt PE255	1.84 (p=2.49E-50)	1.65 (p=3.53E-37)	1.46 (p=2.33E-38)	1.15 (p=9.74E-21)
Larval stage PE254	1.11 (p=5.20E-20)	1.28 (p=2.35E-40)	1.27 (p=1.99E-22)	1.07 (p=4.32E-14)
Larval stage PE255	1.20 (p=6.93E-31)	1.38 (p=2.97E-42)	1.25 (p=3.97E-40)	1.10 (p=8.24E-22)

Fig. S2. A strain with single-copy integrated luciferase transgene develops rapidly and synchronously

(A-C) Representative raw luminescence traces of individual animals grown at 20°C. As the egg-shell is impenetrable to luciferin, a sudden increase in luminescence at the beginning of the time course indicates hatch (pre-hatch in red). Abrupt drops and subsequent rises in luminescence specify molts (in green). The previously published strains (B, PE254; C, PE255) (Olmedo et al., 2015) express luciferase from randomly integrated multi-copy transgene arrays that carry a semi-dominant version of the cuticular collagen *rol-6* as a marker (Lagido et al., 2008). To exclude that this genetic make-up could interfere with our quantification, we integrated a luciferase

transgene, driven by the strong, ubiquitous and constitutive *eft-3* promoter, into the genome through Mos1-mediated single copy integration (MosSCI) (A, HW1939).
(D-F) Heatmap per strain showing trend-corrected luminescence (Lum.) trace for one animal per horizontal line (D, Single-copy integrated HW1939 (n=86). E, Multi-copy integrated PE254 (n=88). F, Multi-copy integrated PE255 (n=79)). Hatch is set to t = 0 h and traces are sorted by time of entry into first molt. Blue indicates low luminescence and corresponds to the molts.
(G-I) Quantification of the duration of each intermolt (G), molt (H), larval stage I) for indicated strains in hours. The newly generated strain developed more rapidly and with less variability with regard to the duration of individual stages. Although the general trend in larval stage durations was shared between the different strains, i.e. L1>L4>L2&L3 (I), animals carrying the *rol-6*-marked multi-copy luciferase arrays also exhibited an extended M1 molt (H) as reported previously (Olmedo et al., 2015). This effect disappeared when using the single-copy transgene strain. Hence, the duration of molt M1 became comparable to that of M2 and M3 and lengthening of L1 is explained by lengthening of intermolt 1. Significant differences between single-copy integrated (n=86) and multi-copy integrated strains (PE254 (n=88) and PE255 (n=79)) is indicated (*** P<<0.001, Welch two sample, two-sided t-test). Boxplots extend from first to third quartile with a line at the median, outliers are indicated with a cross, whiskers show 1.5*IQR.
(J) Table showing fold changes of mean durations of indicated stages for PE254 and PE255 compared to HW1939 for data shown in G-I. P-values are indicated in brackets (Welch two-sample, two-sided t-test).

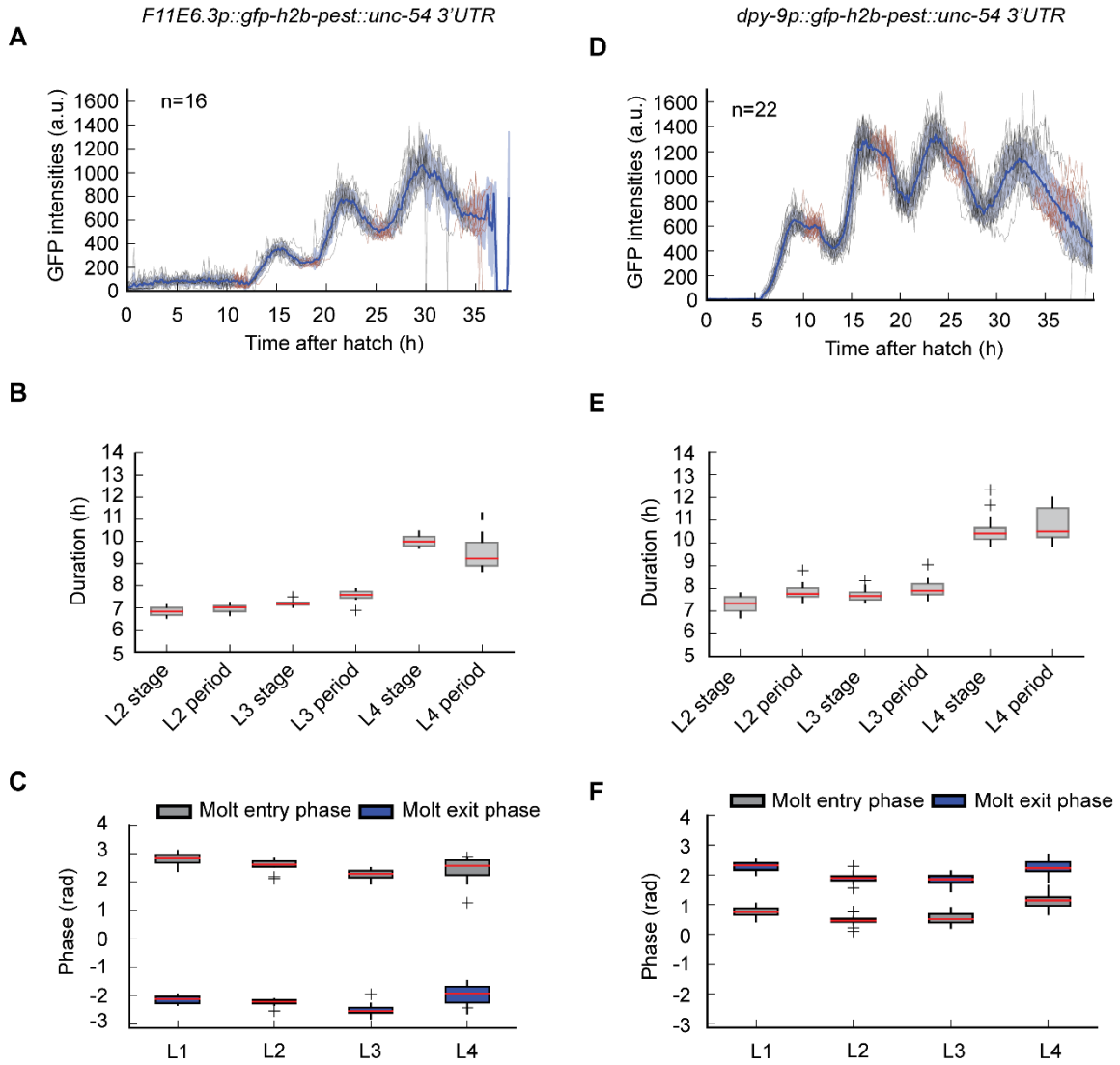

Fig. S3. Single worm imaging with two additional reporter strains confirms phase-locking of oscillations to molts independently of peak phases

(A, D) GFP quantification of single worm kymographs for the *F11E6.3* (HW1370, n=16) and the *dpy-9* (HW2526, n=22) transcriptional reporters respectively. All traces were aligned to the time of hatching, which was set to t = 0 h. Segments in red indicate lethargus while the blue shading indicates the standard deviation at each time point with the blue line representing the mean across worm. Only three peaks are visible for the *F11E6.3* reporter, because the assay terminated before the final rise in expression seen with RNA sequencing.

(B, E) Comparison of larval stage duration and period times of oscillations in hours for L2-L4 larval stages for *F11E6.3* and *dpy-9* transcriptional reporters respectively.

(C, F) Boxplot of expression phases at molt entry (start of lethargus) and molt exit (end of lethargus) separated by larval stages; n = 16 for *F11E6.3* (D) and n = 22 for *dpy-9* (I) transcriptional reporters.

Boxplots extend from first to third quartile with a line at the median, outliers are indicated with a cross, whiskers show 1.5*IQR.

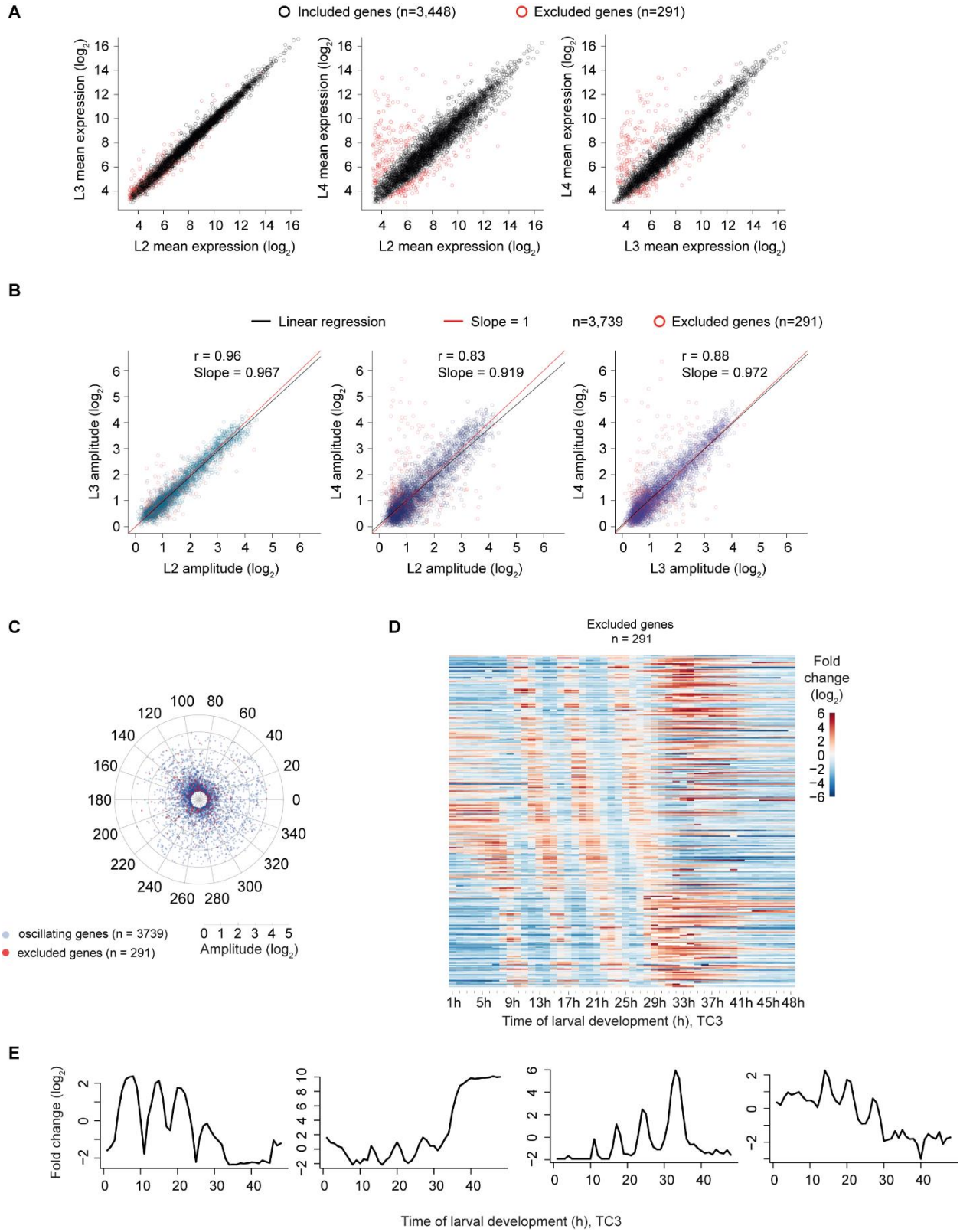

Fig. S4: Exclusion of genes based on deviating behavior in L4 stage

(A) Scatter plot showing mean expression over time in L2, L3 or L4 for each oscillating gene. Genes indicated in red were excluded based on the L2-L4 scatter plot (Methods).

(B) Scatter plot showing the amplitude in L2, L3 or L4 for each oscillating gene. Genes indicated in red correspond to red genes in A and were excluded from amplitude analysis in Fig. 4.
(C) Polar Scatterplot visualizing the amplitude and peak phase of all oscillating genes (n = 3739) in blue and the excluded oscillating genes (n = 291) in red. The excluded genes do not show a particular peak phase or amplitude preference.
(D) Gene expression heatmap of log_2 transformed mean normalized data of the excluded oscillating genes in the fused time course TC3 (n = 291).
(E) Example gene expression of four excluded oscillatory genes that were excluded based on the L2-L4 scatter plot in (A).

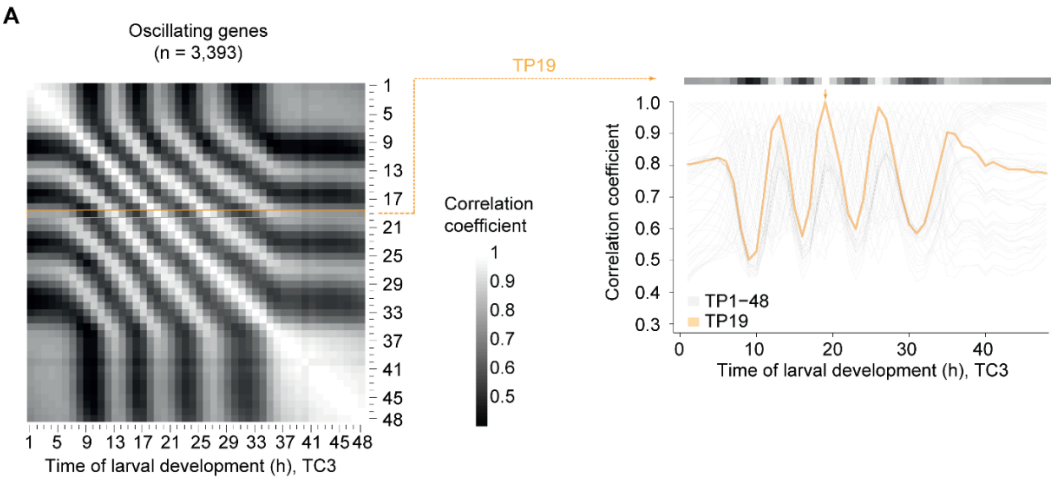

Fig. S5. Correlation line explanation

(A) Left: Pairwise-correlation plot of log_2-transformed oscillatory gene expression patterns without L4 deviating genes obtained from synchronized population of L1 stage larvae at 25°C (TC1, TP1 – 13) combined time points from the long developmental time course (TC2, TP14 – 48), as in Fig. 5B (n = 3,393). Right: The correlation of TP19 versus all other time points is plotted as a line (orange), correlation with itself at 19 hours is 1.0 (orange arrow).

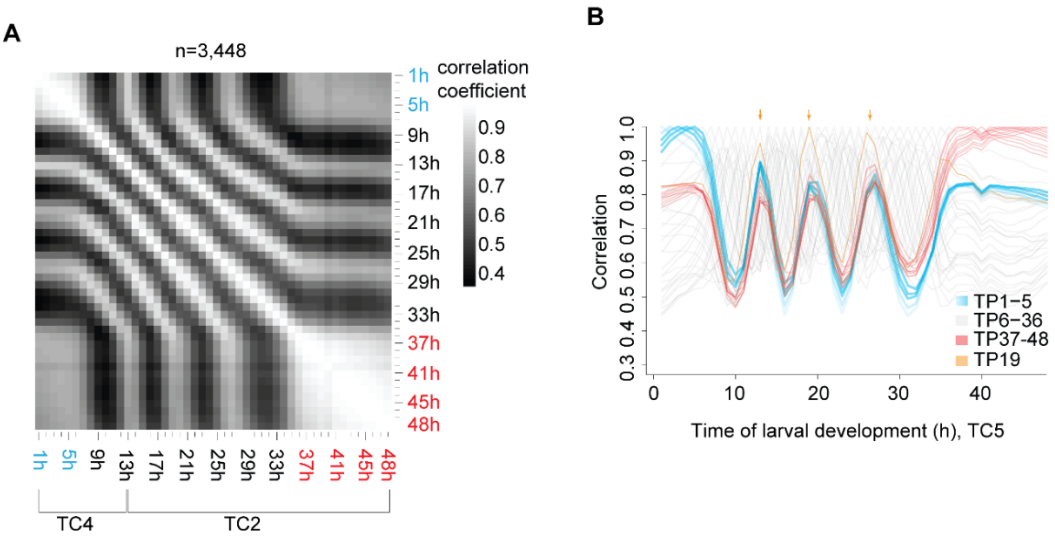

Fig. S6: Arrested phase of the oscillator is reproduced in a second RNA sequencing experiment

(A) Pairwise correlation plot of log_2-transformed oscillatory gene expression patterns without L4 deviating genes (n=3,448) from the replicate time course TC4 (TP1 – 13) fused with TP14 – 48 of the long RNA seq time course TC2 (TP14 – 48).
(B) Correlations of expression patterns for the indicated time points to all other time points of the fused time course from A. TP1 – 5 (blue) as well as the adult time points (red) correlate highly with TP13, TP19 and TP26/27 (arrows). Hence, oscillations are arrested in the same phase at the beginning and the end of the time course.

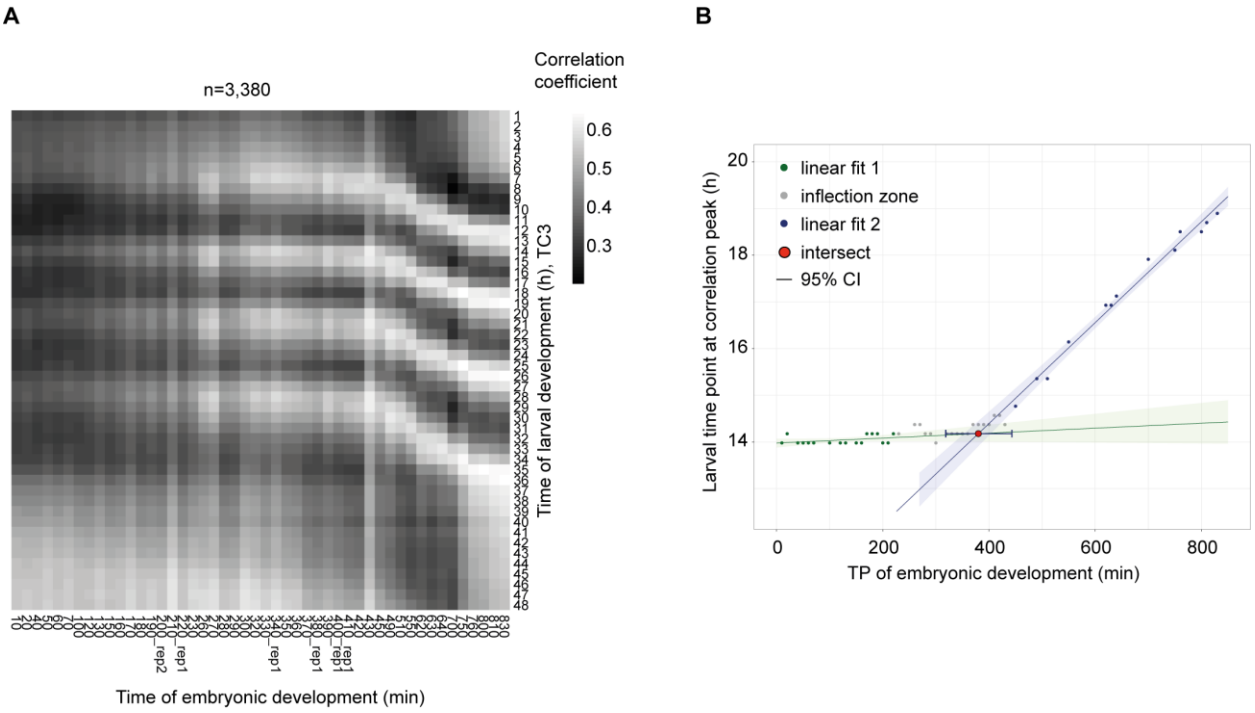

Fig. S7. Initiation of oscillations during mid-embryogenesis

(A) Pairwise correlation map of log_2-transformed oscillating gene counts of fused larval time course to embryonic time course (Hashimshony et al., 2015).

(B) Scatter plot showing the larval time point of the larval oscillation cycle 2 (Fig. 6) for each embryonic time point. The larval time point of the peak was determined after spline interpolation (*9*). Linear model 1 (y = 5.312e-04*x + 13.98, p=0.098, R^2 = 0.162, 16 degrees of freedom) was fitted to the data of embryonic TP10-TP230 min (in green) and linear model 2 (y = 0.0108*x + 10.07, p=2.08e-11, R^2 = 0.985, 11 degrees of freedom) was fitted to the data of embryonic TP450-TP830min (in blue). The embryonic time at the intersection (in red, 380.0 min (95%-CI 317.6 min – 444.2 min)) of the linear models was determined in the inflection zone, i.e. points (in grey) not used for model 1 or model 2 fit, and the 95% CI was determined by propagating the standard errors of the coefficients of the linear models (Methods).

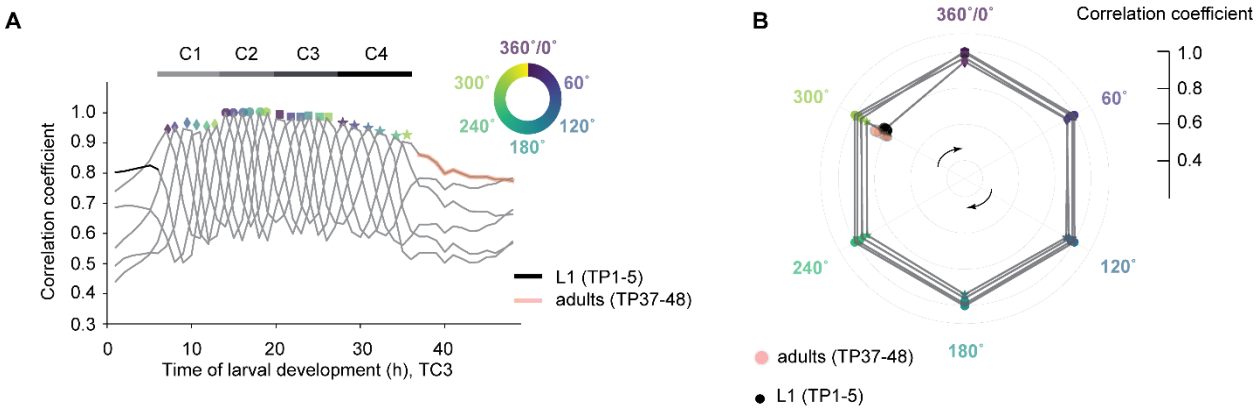

Fig. S8: Oscillations are invariant over time

The correlation analysis revealed a stably arrested oscillator state in early L1 and young adults. To explore how the oscillating state changes over time, we investigated the similarity among the four oscillation cycles, C1 through C4. Specifically, we compared oscillator states at each time point sampled during C2 to the three other cycles. By choosing C2 as a starting point, we could examine correlations to both earlier and later cycles. Because the last time point (360°) of one cycle is the first time point (0°) of the following cycle, we truncated each cycle at 300° for this analysis, to avoid an artificially inflated correlation.

Using spline interpolation and local maxima detection to determine correlation peaks (Methods) for each of the six time points TP14/0° through TP19/300° of C2 to the other cycles, we observed high and largely invariant values across each of the other three cycles. In other words, except for the extended period during L4, little variability occurs in oscillations across the four cycles.

(A) Correlation of cycle 2 time points (TP14–19; corresponding to 0° to 300°; marked by indicated colors) to all other time points of the fused larval time course (TC3). For the correlation analysis we used the $\log_2$-transformed oscillating gene expression data without the L4 deviating genes. Diamonds (cycle 1), circles (cycle 2), squares (cycle 3) and stars (cycle 4) indicate correlation peak values and peak times determined by spline interpolation.

(B) Polar plot displaying correlation of cycle 2 gene expression patterns with those of the corresponding points in the other cycles. Color scheme and symbols as in B. Adult time points (red circles) and start (0° in cycle 1; orange) are placed according to correlations in A and B, respectively.

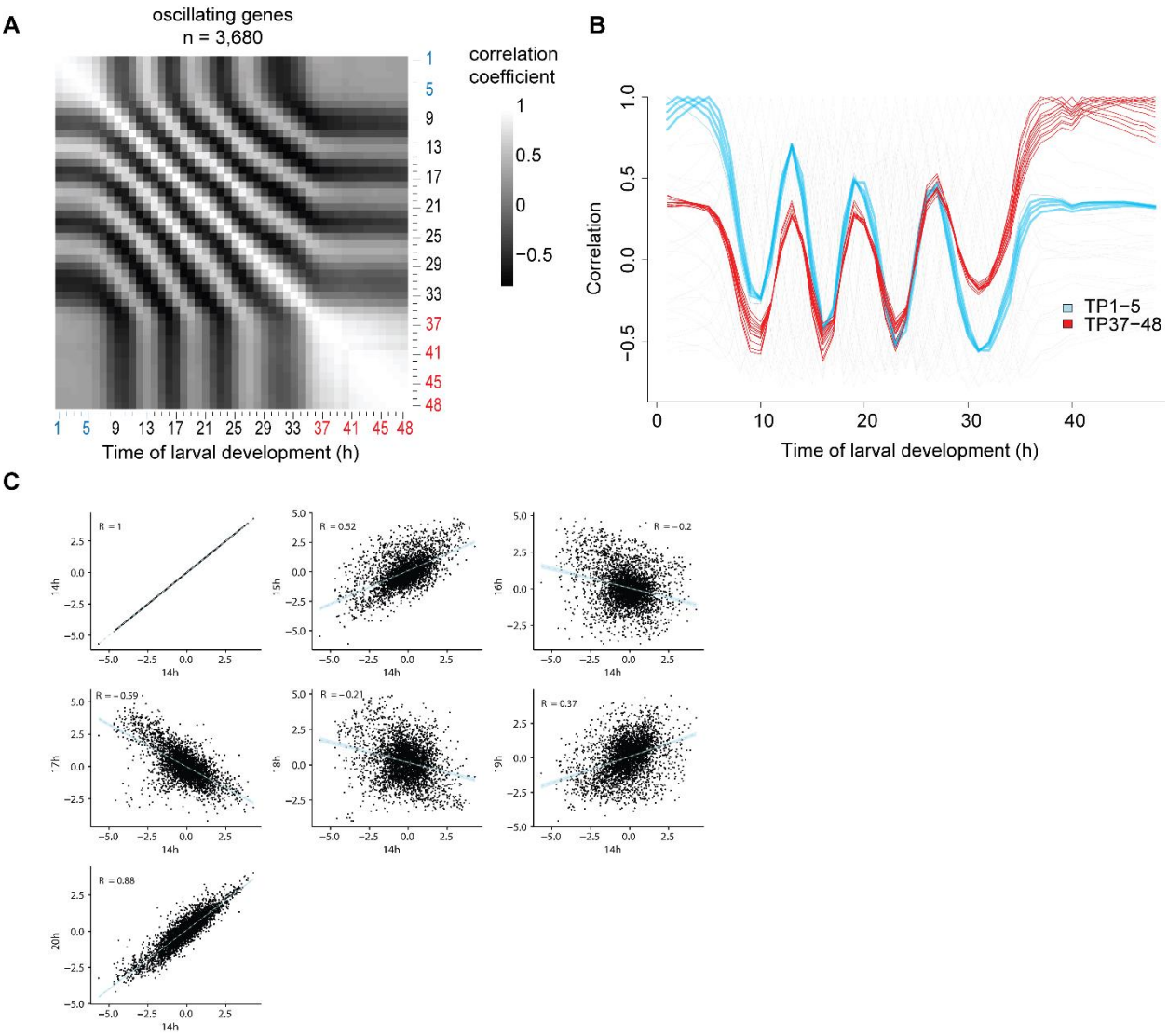

Fig. S9: Correlation analysis with mean normalized data yields qualitatively similar results to an analysis without mean normalization

(A) Pairwise correlation plot of log2-transformed, mean normalized oscillating gene expression from the fused developmental time course (Fig 1C, n = 3,680).

(B) Correlation line plots reveal repetitive similarity of TP1 – 5 to TP13, TP19 and TP26/27. Due to mean normalization, the correlation lines oscillates around 0.

(C) Scatter plot comparing log_2-transformed, mean-normalized oscillating gene expression data of individual time points.

The Spearman correlation coefficient is indicated on the left corner and can range from anti-correlation (-1) to full correlation (+1).

Table S1. Related to Fig. 1 – Similar GO terms are enriched for the L1–YA developmental time course and the L3-YA time course (Separate File)
GO term enrichment for ‘GO biological process complete’ for the L1–YA developmental time course described here and the previously published L3–YA time course (Hendriks et al., 2014). Similar GO terms were enriched for both time courses.

Table S2. Related to Figure 3 - Larval developmental duration in single worm imaging experiments

Median durations of molts, intermolts and larval stage durations determined for single worm imaging reporter strains grown in microchambers at ~21°C ambient temperature.

Reporter	Larval stage	Median duration (h)
qua-1	I1	10
qua-1	I2	4.7
qua-1	I3	5
qua-1	I4	6.8
qua-1	M1	2.2
qua-1	M2	1.8
qua-1	M3	1.8
qua-1	M4	2.8
qua-1	L1	12.2
qua-1	L2	6.5
qua-1	L3	6.9
qua-1	L4	9.5
dpy-9	I1	10.2
dpy-9	I2	5.5
dpy-9	I3	5.6
dpy-9	I4	7.8
dpy-9	M1	2
dpy-9	M2	1.8
dpy-9	M3	2
dpy-9	M4	2.7
dpy-9	L1	12
dpy-9	L2	7.3
dpy-9	L3	7.7
dpy-9	L4	10.4
F11E6.3	I1	10.5
F11E6.3	I2	5
F11E6.3	I3	5.3
F11E6.3	I4	7.5
F11E6.3	M1	1.8
F11E6.3	M2	1.7
F11E6.3	M3	1.8
F11E6.3	M4	2.5
F11E6.3	L1	12.5
F11E6.3	L2	6.8
F11E6.3	L3	7.2
F11E6.3	L4	10

Table S3. Plasmids and primers used

Vector name	Backbone	Inserts	Primers	Primer sequence
pYPH0.14	pCFJ150	GFP::H2B::Pest	GFP-pest-H2B FW1 + Overhang	gcgtgtcaataatatcactcGCTAGCATGTCTAGACTTAGCCATGGC
			GFP-pest-H2B RV1 + Overhang	gccgatgcggagctcttatcTTACTTGCTGGAAGTGTACTTG
		Unc-54 3'UTR	Unc-54 3'UTR FW1 + Overhang	AGTACACTTCCAGCAAGTAAgataagagctccgcatcg
			Unc-54 3'UTR RV1 + Overhang	Aacatatccagtcactatggaaacagttatgtttggtatattggga
pYPH5	pYPH0.14	F11E6.3 promoter	F11E6.3 FW1 + Overhang	gcgtgtcaataatatcactcaggaaaacctcaaattttgttaacact
			F11E6.3 RV + Overhang	GCTAAGTCTAGACATcatggttacctaaaaatataaagctct
pYPH69	pYPH0.14	dpy-9 promoter	dpy-9 promoter FW +OH to pYPH0.14	gcgtgtcaataatatcactcgtacaatagaaaaaagcagcaat
			dpy-9 promoter RV +OH to pYPH0.14	CCATGGCTAAGTCTAGACATtctgcaataataagtattgaaaacaaga
pYPH70	pYPH0.14	qua-1 promoter	qua-1 promoter FW +OH to pYPH0.14	gcgtgtcaataatatcactcatacttttgcactacacggag
			qua-1 promoter RV +OH to pYPH0.14	CCATGGCTAAGTCTAGACATcttaaatataggttaagcatgataggat
pMM001	pCFJ150	luciferase::GFP	unc-54 3'UTR + overhang gfp	GCATGGATGAACTATACAAAgataagagctccgcatcg
			gfp + overhang unc-54 3'UTR	gccgatgcggagctcttatcTTTGTATAGTTCATCCATGCC
			luc, piece2 + overhang piece 1	GACTACAAGgtaagtttaaacagttcggtactaactaacca
			luc, piece1 + overhang piece 2	ccgaactgtttaaacttacCTTGTAGTCTTGGAG
			luc, piece1 + overhang NheI and backbone	tgtcaataatatcactcGCTAGCATGGAGGACGCCAAGAA
		Unc-54 3'UTR	gfp + overhang luc::spacer (piece2)	TACCGGTAGAAAAAATGAGTAAAGGAGAAGAACTTTTCACTGG
			luc::spacer (piece2) + overhang gfp	GTGAAAAGTTCTTCTCCTTTACTCATTTTTTCTACCGGTAC
pMM002	pMM001	eft-3 promoter	Peft-3 RV primer (OH to :luciferase)	ATGTTCTTGGCGTCCTCCATgagcaaagtgtttcccaac
			Peft-3 FW primer (OH to pCF150)	gcgtgtcaataatatcactcGCACCTTTGGTCTTTTATTGT

Data S1. (separate file)
KNIME workflow for analyzing GFP intensities in the single worm imaging.

References:

Hashimshony, T., Feder, M., Levin, M., Hall, B.K., Yanai, I., 2015. Spatiotemporal transcriptomics reveals the evolutionary history of the endoderm germ layer. Nature 519, 219–222. https://doi.org/10.1038/nature13996

Hendriks, G.-J., Gaidatzis, D., Aeschimann, F., Großhans, H., 2014. Extensive oscillatory gene expression during C. elegans larval development. Mol. Cell 53, 380–392. https://doi.org/10.1016/j.molcel.2013.12.013

Lagido, C., Pettitt, J., Flett, A., Glover, L.A., 2008. Bridging the phenotypic gap: Real-time assessment of mitochondrial function and metabolism of the nematode Caenorhabditis elegans. BMC Physiology 8, 7. https://doi.org/10.1186/1472-6793-8-7

Olmedo, M., Geibel, M., Artal-Sanz, M., Merrow, M., 2015. A High-Throughput Method for the Analysis of Larval Developmental Phenotypes in Caenorhabditis elegans. Genetics 201, 443–448. https://doi.org/10.1534/genetics.115.179242

End of manuscript "State transitions of a developmental oscillator"

2.2 Genes expressed in the hypodermis do not necessarily oscillate

Gert-Jan Hendriks and Yannick Hauser performed RNA sequencing time course. Yannick Hauser acquired and analyzed the worm imaging data. Jan Eglinger wrote the KNIME workflow for the worm imaging. Helge Großhans and Yannick Hauser conceived the experiment.

Intrigued by the fact that many oscillating genes are found in the hypodermis (Meeuse et al., 2019), and considering that the hypodermis is the tissue mostly responsible to renew the cuticles after molting, we wondered whether all transcripts expressed in the hypodermis are oscillating. To investigate this possibility we examined *tbb-1* which showed constitutive expression during larval development as determined by a previous mRNA sequencing time course (Fig 2.1C, Meeuse et al., 2019) and ubiquitous GFP expression from its transcriptional reporter. This reporter was particularly interesting because of the possibility that non-oscillating genes in the sequencing time course could still oscillate in individual tissues. However, due to the fact that we do not have tissue-specific sequencing and rely on the whole worm transcriptome which is a composite signal of the individual tissues, the oscillations from the individual tissues could annihilate each other. Thus, we would misinterpret and underestimate the number of oscillating genes by looking at the whole worm mRNA sequencing data. To address this issue, we quantified the GFP intensity of the ubiquitously expressed *tbb-1* transcriptional reporter specifically in the hypodermis, during the L4 stage (Fig 2.1D). This did not reveal any evidence of oscillations, but instead recapitulated the mRNA sequencing data. This supports our idea that not all genes in the hypodermis oscillate. Nonetheless, we only tested one transcriptional reporter of a housekeeping gene and thus we cannot generalize this finding as housekeeping genes might be the only exceptions.

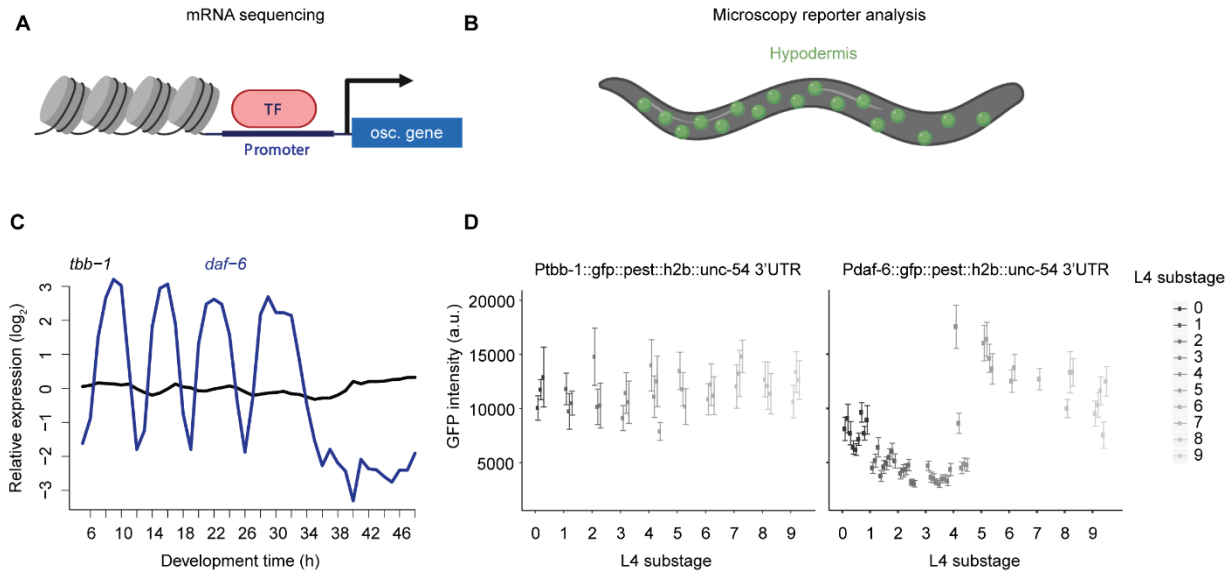

Fig 2.1: stable expression of *tbb-1* in the hypodermis

A, Design of transcriptional reporter of oscillating genes (image created with BioRender.com).

B, GFP intensities are specifically analyzed in hypodermal tissue (image created with BioRender.com).

C, mRNA abundance over time of *tbb-1* and *daf-6* as determined by sequencing in Meeuse et al., 2019.

D, GFP intensities measured by confocal microscopy of two GFP transcriptional reporters driven by the *tbb-1* and the *daf-6* promoter, respectively during the L4 stage. The L4 sub-stages were identified using vulva morphology (Mok et al., 2015).

2.3 Single worm sequencing reveals non-sinusoidal oscillations

Yannick Hauser and Sebastien Smallwood developed the single worm time course sampling strategy and Yannick Hauser performed the time course. Sebastien Smallwood performed library preps and sequencing. Yannick Hauser developed the pseudotiming algorithm and analyzed all count data. Helge Großhans and Yannick Hauser conceived the experiment.

Despite the insights obtained from the sampled time courses in Meeuse et al., 2019, we were still lacking a detailed understanding of the true shape of the oscillations. We were motivated by the idea that core oscillator genes could display non-sinusoidal oscillations, similar to bistability behavior that has been observed for relaxation oscillators (see section 1.2.2) and output genes of the oscillator could oscillate with more sinusoidal shapes. Given that in bulk samples thousands of worms are contributing to the transcript count data per time point our read-out represents a mean expression of many worms. Hence, we wondered whether the sinusoidal nature of the oscillations is merely a result of averaging out non-sinusoidal behavior on the single worm level. Additionally, sequencing bulk samples complicates the investigation of asynchronously developing worm strains as amplitude would be damped and the peak phase of the oscillations would be shifted in general. These considerations motivated us to sequence single worms over developmental time to investigate the shape of the oscillations in greater detail. To this end we sampled single worms from 16 – 31 hours after plating synchronized L1 worms using the COPAS worm sorter into single wells, before processing them then further for sequencing using SmartSeq2 (as described in the methods). Even though synchronized worms by egg prep should develop synchronously, small differences in the developmental speed can be amplified over time resulting in slightly different developmental stages at the time point of sampling. In a real-world experiment, individual worms in a synchronized population grown for X hours likely show a distribution around X hours, with most worms being close to X hours in development and some being advanced or delayed (Fig 2.2 A). Hence, upon sequencing single worms from such a population, we have to deal with the asynchrony and correct for it to align the individually sequenced worm samples according to real developmental time instead of sampled time. As we have seen in previous analyses, the principal components (PC) of bulk sequenced worms from timepoints 1 – 48 hours after plating show a rotating behavior by plotting PC 1 against PC2 of the oscillatory gene expression (Fig 2.2B). Based on this observation, we used the oscillating gene set (as identified in Meeuse et al., 2019) in the single worm gene expression dataset and performed principal component analysis on these genes

specifically. Fig 2.2C shows that PC1 and PC2 form a circle with each dot representing the oscillating gene expression of individual worms reduced to two dimensions. As we know that development should be inferable from this representation as shown in Fig 2.2B, we sought to sort worms according to their angle in the two-dimensional plot (as exemplified with α for a given worm in Fig 2.2D). However, this analysis would suffer from the fact that we sampled more than just one oscillation cycle, thus, worms from cycle 2 would be characterized by the same angle as worms from cycle 1. To overcome this drawback, we used the additional information from the sampling numbers, which correlate with the sampling time point and thus to developmental progression. Upon plotting the initial sample number against the calculated phase of the individual samples, the different cycles become apparent and can be identified using the DBScan clustering algorithm (Fig 2.2E). Only few samples could not be assigned to one cycle and were thus excluded. The cycle annotation allows us to sort the samples within one cycle as shown in Fig 2.2F according to their calculated angle from Fig 2.2D. To finally obtain the sorting of all samples, we added the samples from the individual cycles consequentially after each other as illustrated in Fig 2.2G resulting in the unwrapped angle. Finally, to combine all data information and visualize the pseudo-timing of all samples, we plotted PC1 against PC2 in XY and the unwrapped angle from Fig 2.2G in the z-dimension resulting in a spiral traveling from small to big unwrapped angles.

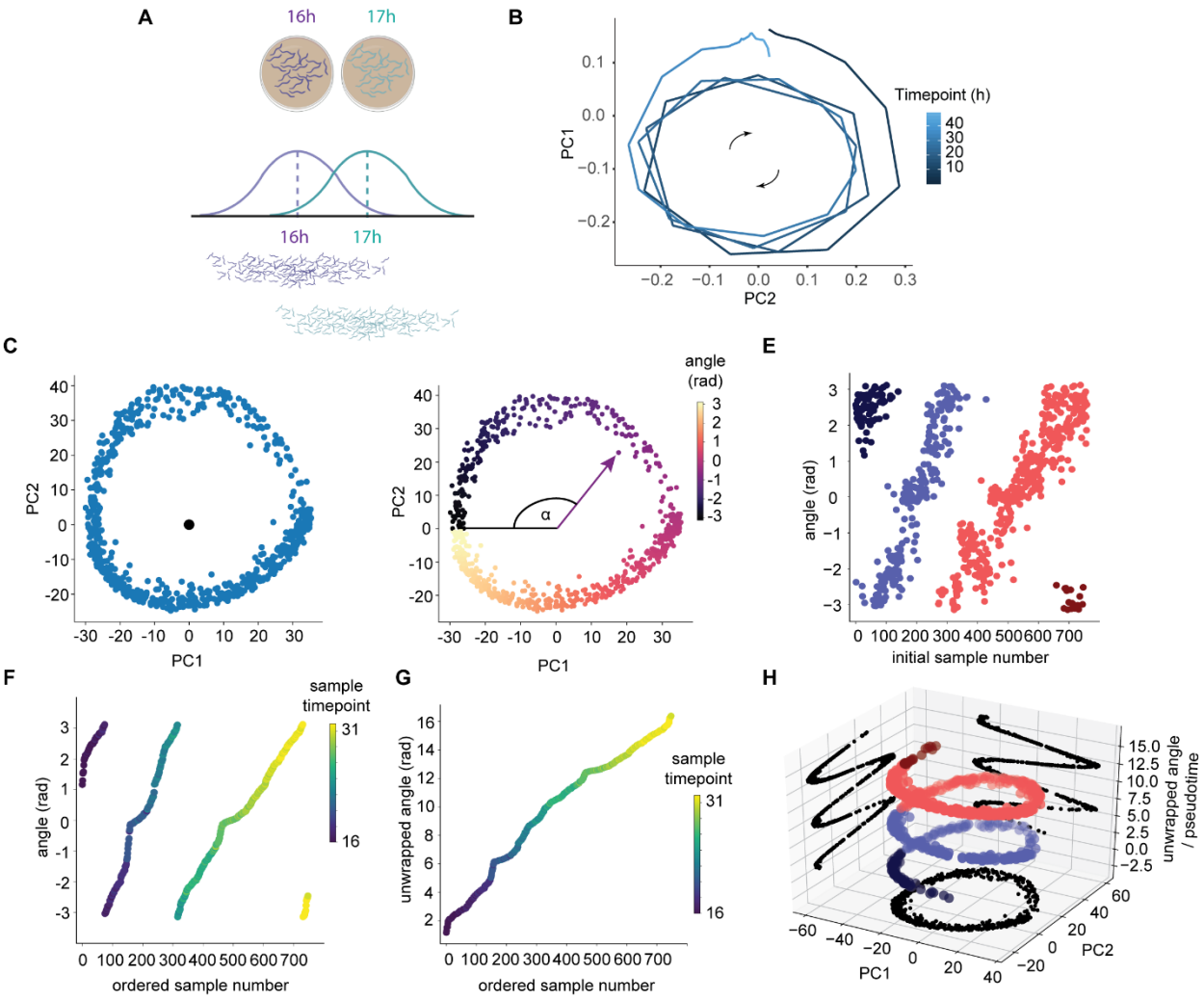

Fig 2.2: Pseudo-timing of single worm sequencing data using principal components

A, Sampling of synchronized single worms results in a distribution of real developmental time with a spread around the expected (sampled) developmental time as worms differ slightly in developmental speed (image created with BioRender.com)

B, Principal component (PC) analysis on sequenced bulk samples obtained from time course 4 in Meeuse et al., 2019 for oscillating genes (n=3,393, genes with a mean expression trend in L4 were excluded) reveal that PC1 and PC2 are represented by a sine and cosine respectively. If plotted against each other, samples follow a circle in PC1/PC2 space.

C, Principal component analysis on oscillating genes (n=3,739) from single worm samples (n=760) confirmed the circular nature in the PC1/PC2 scatterplot. The black dot indicates the origin (0,0) of the 2-dimensional coordinate system.

D, The angle of every individual sample according to its position in the 2-dimensional PC plot. One sample is indicated with its angle α.

E, Identification of the different oscillation cycles by plotting the initial sampling number against the phase calculated from D and applying the DBScan clustering algorithm. Clusters are identified by the local density of samples.

F, Sorting of samples according to their angle information for each oscillation cycle independently. The color indicates the time point at which samples were taken.

G, The sorted samples from F fused together across cycles in order to create continuous angular information. The color indicates the time point at which samples were taken.

H, A 3D plot displaying the original PC1 against PC2 on the x-y plane, whereas the z-axis represents the unwrapped angular information from G. The coloring indicates the different oscillation cycles corresponding to E.

After ordering single worms based on pseudo-time, we were interested to group oscillatory gene expression based on their shapes, potentially revealing core oscillator genes or functional groups of genes associated with certain oscillation shapes. Indeed, we were able to detect non-sinusoidal gene expression oscillations, as represented by two example genes in Fig 2.3A(I). In order to simplify downstream visualizations and analyses, we binned the gene expression of each individual transcript into 75 equally spaced angle bins and plotted the mean expression and standard deviation for every bin, exemplified with the three example genes in Fig 2.3A(II) and shown for all oscillating genes in a heatmap (Fig 2.3B). We further characterized groups of oscillating behavior using hierarchical clustering on the binned data into 20 distinct clusters (Fig 2.3C). These clusters represent different shapes of oscillating gene behavior and clear non-sinusoidal behaviors become apparent as exemplified in cluster 2 or 11. Nevertheless, other clusters such as clusters 14 or 15 still appeared rather sinusoidal. In comparison to the bulk sequencing experiment (Meeuse et al., 2019), we can readily detect differences in the oscillation shapes of the clusters with more non-sinusoidal oscillations in single worm sequencing data (Fig

2.3D). For some clusters, such as cluster 6, we failed to observe the expected increase of amplitudes in comparison to the bulk data which we expected due to the reduction of asynchrony effects. This result might, at least to a certain extent, be explained by the reduced sequencing depth resulting from the single worm sequencing protocol. The lower sequencing depth might thus result in lower sensitivity (i.e. detection limit) of lowly expressed transcripts (Svensson et al., 2017) and hence we might only capture the values around the peak for these transcripts, leading to a reduced amplitude.

At this point, we could not identify specific tissues or functions associated with different cluster behaviors. One reason might be that our clustering is still influenced by the peak phase as well as the amplitude (see discussion) and thus the identification of the true shape clusters is missing. Future clustering approaches might overcome these limitations and reveal a more meaningful clustering based on the shape of the oscillations, thus potentially allowing us to find behaviors corresponding to a functional group of genes such as collagens.

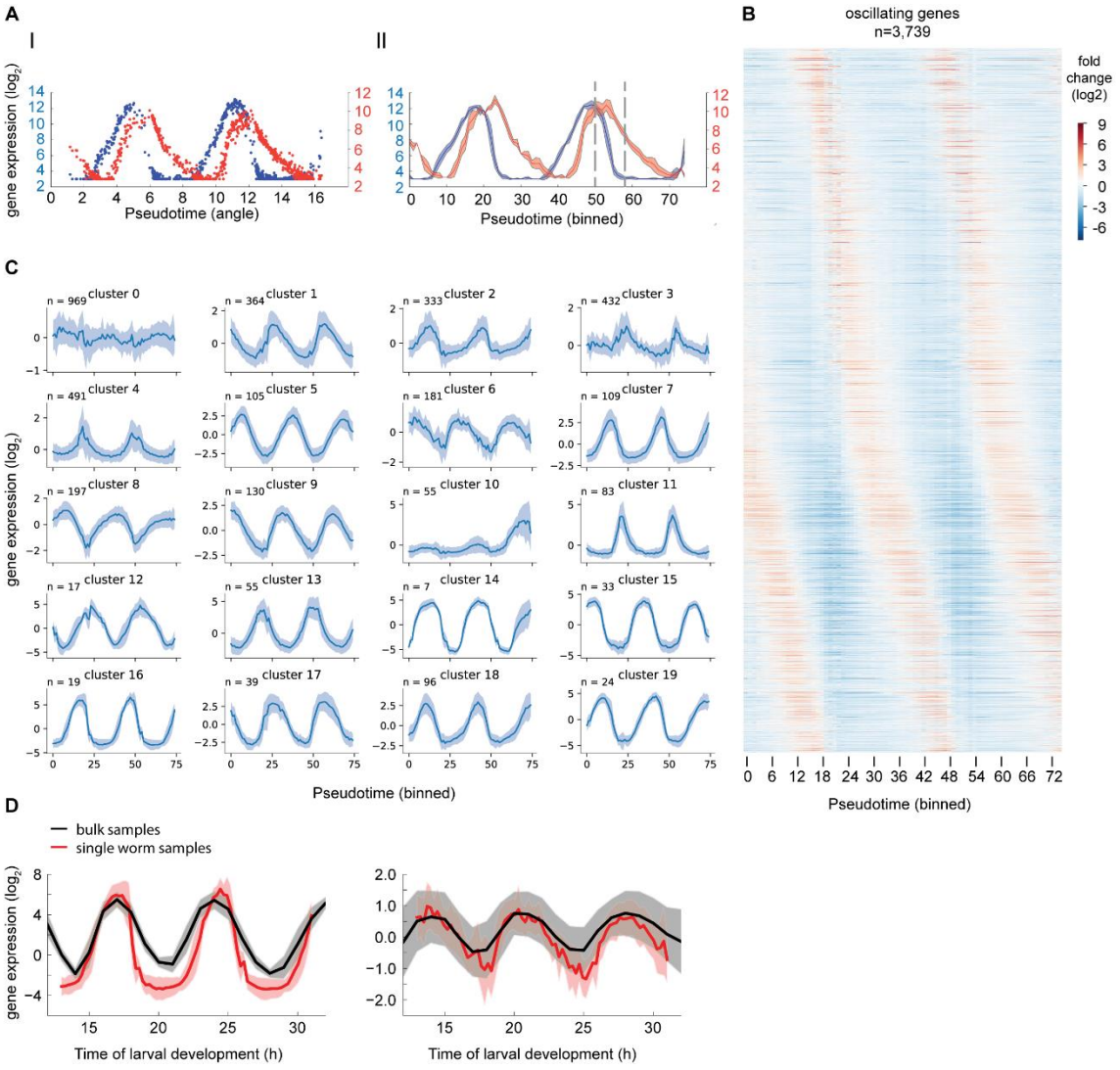

Fig 2.3: Gene expression oscillations show non-sinusoidal behavior in single worms

A, Example sorted gene expression data of two different transcripts over pseudotime. **I**: raw data, **II**: binned expression into 75 equally spaced angular bins, where the shaded region represents the standard deviation per bin over pseudotime. The dashed lines indicate a time window where the progression of the oscillation is increased for the blue example gene (fast decay) while progression stays unchanged for the red example gene (slow decay).

B, Gene expression heatmap in $\log_2$ of the mean-centered binned data (n=3,739).

C, Single worm sequencing data clustered by hierarchical clustering on the mean-centered binned expression. For each cluster, the line shows the mean expression and the shaded area represents the standard deviation over time.

D, Cluster 16 (left) and cluster 6 (right) expression from the single worm sequencing in red was compared with the corresponding gene expression from the bulk sequencing in black. The mean expression of the cluster is shown in a solid line accompanied by a shaded area, representing the standard deviation.

2.4 *blmp-1* manuscript

Milou Meeuse performed the RNAPII ChIP sequencing time course. Yannick Hauser performed all transcriptional reporter RT-qPCR time courses. Milou Meeuse and Yannick Hauser performed luciferase assays with blmp-1 RNAi and mutant animals respectively. Milou Meeuse performed the auxin inducible degron luciferase assays. Yannick Hauser performed and analyzed the blmp-1(tm548) mutant time course and acquired and analyzed single worm imaging data. Jan Eglinger wrote the KNIME workflow for the single worm imaging. Helge Großhans, Milou Meeuse and Yannick Hauser conceived the project and Yannick Hauser wrote the manuscript under supervision from Helge Großhans.

The BLMP-1 transcription factor supports coupling of oscillatory gene expression with development

Yannick P. Hauser[1,2]*, Milou W.M. Meeuse[1,2]*, Jan Eglinger[1], Helge Großhans[1,2,3]

[1] Friedrich Miescher Institute for Biomedical Research (FMI), Maulbeerstrasse 66, CH-4058 Basel.

[2] University of Basel, Petersplatz 1, CH-4001 Basel.

[3] Correspondence to: helge.grosshans@fmi.ch.

* equal contribution.

Abstract:

Molecular oscillators can organize gene expression during development both temporally and spatially. In *C. elegans*, oscillations occur for ~25% of the transcriptome to control molting and potentially other developmental processes. The underlying mechanisms and organization of the oscillator remain unknown. Here, we report that rhythmic RNA polymerase II recruitment produces rhythmic transcript levels, which we can reproduce quantitatively by promoter-fusion reporter genes. We identify the transcription factor BLMP-1, orthologous to mammalian PRDM1, as a rhythmically accumulating transcription factor that is required for robust rhythmic development, molting, and animal viability. Strikingly, its loss causes strong desynchronization of oscillatory gene expression of a small set of genes from bulk oscillatory gene expression and rhythmic development. Hence, we propose a function for BLMP-1 in coupling oscillatory gene expression and larval development.

Introduction

Genetic oscillators drive fundamental rhythmic processes in biology such as circadian rhythms (Panda et al., 2002), somitogenesis (Aulehla and Herrmann, 2004; Oates et al., 2012), or plant lateral root branching (Moreno-Risueno et al., 2010). In *C. elegans,* a particularly striking example exists with ~3,700 genes (~25% of the transcriptome) exhibiting high-level oscillations but a diversity of peak phases (Hendriks et al., 2014; Kim et al., 2013, preprint Meeuse et al., 2019). The oscillations are coupled to, and presumably drive, the molting cycle (preprint Meeuse et al., 2019), i.e. the process of new cuticle synthesis and old cuticle shedding. Oscillations may also time other developmental processes and coordinate them with the molt.

The oscillator's architecture has remained largely unknown. Although oscillations appear to occur in several tissues, it is unclear whether one or multiple oscillators exist, and if the latter, whether they are organized hierarchically, as observed for the mammalian circadian clock with its system of a master pacemaker and peripheral oscillators (Mohawk et al., 2012) (Welsh et al., 2010), or in a more distributed manner. In either scenario, and because oscillations are phase-locked during development (i.e., transcript levels peak in the same order over time; Hendriks et al., 2014; Meeuse et al., 2019), some level of coupling needs to exist among oscillations in different tissues. Indeed, even within a single tissue, coupling of oscillators appears an important principle in biology, as coupling of cell-autonomous oscillators appears necessary for robust oscillations of appropriate periods in both the circadian master pacemaker (Patke et al., 2020) and the presomitic mesoderm (PSM) (Herrgen et al., 2010; Jiang et al., 2000; Riedel-Kruse et al., 2007).

The molecular nature of the *C. elegans* oscillator has also been elusive. Rhythmic accumulation of intronic reads in RNA sequencing experiments suggested the possibility that rhythmic

transcription drive oscillatory output, but more direct validation of this, and establishment of a mechanism have been missing. However, the coupling between molting and oscillations provide an opportunity for phenotypic screens for oscillator mutants and thus might provide mechanistic insights. In analogy to observations for the circadian clock, the phenotype severity may depend on both the level at which an affected factor acts, e.g., core oscillator vs. output, and the extent of redundancy in the system (Takahashi, 2004). Thus, complete inactivation of the *C. elegans* oscillator may cause larval death, while more moderate impairments may cause greater variability, or increases or decreases of larval stage durations relative to the wild-type situation.

Performing a focused screen of 92 transcription factors, we identified BLMP-1 as important for wild-type progression through larval stages (Meeuse et al., in preparation). BLMP-1, an orthologue of the lineage-specifying mammalian transcription factor BLMP1/PRDM1 was previously shown to regulate developmental timing of *C. elegans* gonad migration (Horn et al., 2014; Huang et al., 2014). Here, we report that BLMP-1 protein accumulates rhythmically during larval development and that it functions repetitively during larval development. BLMP-1 depletion causes an extension of larval molts, with more severely affected animals also exhibiting an extended intermolt and, frequently, death. Although most genes exhibit an increased period upon BLMP-1 depletion that maintains synchronization between developmental progression and gene expression oscillation, a small group of genes defies this pattern. Hence, these genes become unsynchronized with development, characterized by a precocious upregulation relative to molts. Our results thus suggest that loss of BLMP-1 leads to internal desynchronization between groups of genes, which most prominently happens during the molt. Hence we propose that BLMP-1 is either directly or indirectly connected to the core of the *C. elegans* developmental oscillator.

Results:

Rhythmic transcription of oscillating genes is driven by rhythmic RNAPII occupancy

Previously, we showed that oscillating mRNA levels are preceded by rhythmic pre-mRNA abundance by comparing intronic with exonic reads, suggesting that rhythmic transcription could drive transcript oscillations (Hendriks et al., 2014). However, based on short, single end read sequences, one cannot readily distinguish between excised introns by splicing or introns still residing in a pre-mRNA. Hence, we sought to test the possibility of rhythmic transcription more directly by exploring the dynamics of DNA-dependent RNA polymerase II (RNAPII) binding to transcription start sites (TSSs) of genes with oscillating expression (henceforth oscillating genes for short; preprint Meeuse et al., 2019). We performed RNAPII chromatin immunoprecipitation coupled to sequencing (ChIP-seq) and mRNA sequencing (mRNA-seq) on synchronized wild-type worms collected hourly at 22 hours until 33 hours of development at 25°C. RNAPII ChIP-seq reads were quantified in a 1-kb window around the TSS as a proxy for temporal RNAPII promoter occupancy on oscillating genes. We found rhythmic binding of RNAPII at many of the promoters which were highly comparable to the mRNA-seq reads (Fig 1A, B, Fig S1). While not for all oscillating genes, the RNAP II ChIP sequencing results clearly indicated that rhythmic binding of RNAP II occurs on the promoters of oscillating genes. We detected instances where oscillating mRNA levels are not accompanied by rhythmic RNAP II promoter binding. This observation might reflect instances of post-transcriptional regulation. However, we notice a general reduction of amplitudes in the ChIP sequencing experiment, probably due to a lower dynamic range as compared to RNA sequencing.

We conclude that rhythmic transcription, and in particular rhythmic recruitment of RNAPII to genes, is a major driver of transcript level oscillations.

Results

Promoter driven gfp reporters recapitulate transcription of endogenous genes

Intrigued by the ChIP-seq results, we aimed to further confirm rhythmic transcription and to investigate amplitude and peak phase of transcript oscillations in more detail using transcriptional reporters. The reporters contained putative promoters (either 2kb upstream of the ATG or until the next upstream gene) of oscillating genes driving the expression of a destabilized nuclear *gfp*. We used the *unc-54* 3'UTR to exclude 3'UTR-mediated posttranscriptional regulation and because *unc-54* did not display transcript oscillation in our mRNA sequencing time courses (Hendriks et al., 2014; Meeuse et al., 2019). Importantly, all reporters were integrated into the *C. elegans* genome into single copy at the same defined genomic locus. Thus, we were able to directly compare dynamic changes of abundance of the endogenous transcript and its *gfp* counterpart within the same worm strain. To assess transcript levels over the course of development, we performed hourly resolved real-time quantitative PCR (RT-qPCR) time course experiments from 22 – 37 hours on a synchronously developing population for each reporter strain individually (Fig 1C). In every case examined, we observed rhythmic reporter transcript accumulation. Yet more remarkable, the patterns of the endogenous transcripts and their derived reporters were also quantitatively highly similar, i.e., in all tested cases except one, peak phases and amplitudes were comparable (Fig 1C, Fig S2). (We suspect, but have not examined further, that in the one case where we observe a deviation, Fig. S2A, the reporter may lack relevant promoter elements.). Furthermore, in the case of *F58H1.2* for which we have obtained low amplitudes in the ChIP-seq experiment we obtained high amplitudes in the reporter RT-qPCR time course (Fig S2B), further suggesting that the differences in amplitudes between ChIP-seq and mRNA-seq probably are of technical nature and do not primarily arise from post-transcriptional regulation of the transcripts.

Results

These results reveal that the promoter is important for oscillatory gene expression and sufficient to recapitulate the endogenous transcript dynamics.

A short conserved promoter element in the daf-6 promoter can induce oscillatory transcription

In *C. elegans*, promoters are usually not mapped confidently as trans-splicing occurs for a high percentage of genes, thus complicating the correct annotation of the full 5'UTR sequences and its distinction from other regulatory elements (Allen et al., 2011; Blumenthal and Steward, 1997; Hastings, 2005; Lasda and Blumenthal, 2011). Hence, our chosen promoters included the 5'UTR of oscillating genes which are considered to be neutral with regard to reporter activity. To further test this assumption and investigate promoter sequences without including their endogenous 5' UTRs, we focused on the *daf-6* promoter where we detected a short 197 bp-long promoter element with sequence conservation in nematode species (Fig S3). To determine whether this element could induce oscillatory transcription without its endogenous 5'UTR, we combined it with the Δ*pes-10* minimal promoter (Fire et al., 1990). Driving transcription of *gfp* from Δ*pes-10* alone resulted in very low expression without oscillatory dynamics (Fig 1D, left) and consistent with previous observation (Fire et al., 1990), we detected GFP expression only in one cell in the pharynx region (data not shown). However, including the *conserved element* (*ce*) from the *daf-6* promoter 5' to the Δ*pes-10* resulted in *gfp* expression in hypodermal tissue (data not shown). Oscillatory gene expression of *gfp* driven by the *ce*::Δ*pes-10* promoter was confirmed by RT-qPCR and revealed comparable dynamics to the endogenous transcript oscillation (Fig 1D, right). Thus, even small promoter elements can suffice to induce oscillatory gene expression in *C. elegans*.

Depletion of BLMP-1 increases lethargus duration

Results

Exploiting the previously observed coupling of mRNA oscillations and development (Meeuse et al., 2019) together with the reported contribution of transcription in mRNA oscillations here, we conducted a screen for relevant transcription factors in a parallel study (Meeuse et al., in preparation). Specifically, we screened transcription factors that oscillate on the mRNA level (n=92, based on Hendriks et al. 2014) for aberrant timing, duration, or otherwise abnormal occurrence of molts. We identified several hits, which included *blmp-1*. The phenotypes observed for *blmp-1* appeared unique: although molts were extended, larval stages were not, because molt extension appeared compensated by intermolt shortening (Meeuse et al., in preparation).

We sought to validate the screening data, on larger numbers of animals, using the same experimental approach, namely a luminescence-based assay that facilitates detection of molt entry and molt exit, and thus determination of molt, intermolt and larval stage duration, on single animals in high throughput. Briefly, animals expressing a luciferase transgene constitutively were cultured in a multi-well plate in a temperature-controlled luminometer in the presence of food and luciferin. Continuous light emission results, except during lethargus (molts), when animals do not feed and thus do not ingest luciferin. We performed this assay on *blmp-1* RNAi- or mock-treated animals (n>60 each). Consistent with the screen results (Meeuse et al., in preparation), *blmp-1(RNAi)* caused lengthening of molts (Fig 2A, Fig S4). We also observed in some but not all experiments largely unchanged larval stage durations, because lengthening of molts was compensated by a shortening of intermolts (Fig 2 A - C, Fig S4). Consistent with additional results presented below, we attribute this variable effect on larval stage duration to variation in BLMP-1 depletion obtained in different RNAi experiments, with greater depletion causing an increase in both molts and larval stage durations.

Results

Lack of BLMP-1 causes larval lethality and reduced developmental rates in survivors

To validate the notion that the broader defects in some experiments were characteristic of a more extensive loss of BLMP-1 activity, we investigated *blmp-1* null mutant *(tm548)* animals in a luciferase assay. We detected a high level of larval developmental arrest or death (Fig 2D), typically detected as a gradual loss of luminescence after exit from the first molt (Fig S5).

Focusing on the subset of animals that developed through all larval stages, we found that the first molt (M1) was greatly extended in *blmp-1(tm548)* mutant relative to wild-type animals, as were subsequent molts (Fig 2E). By contrast, intermolts were more variably affected, with a substantial lengthening detectable for intermolt 2 (I2), but much less so for I1 and I3, and in fact a decrease for I4 (Fig 2F). From M1 onwards, and for both molts and intermolts, durations also became more variable (Fig 2E, F).

BLMP-1 is required for cuticle integrity

Whereas luminescence is low in wild-type animals during lethargus, when luciferin is not ingested, we consistently observed elevated luminescence during M2 through M4 in both *blmp-1* RNAi-treated and *blmp-1(tm548)* mutant (Fig 3A, B, Fig S5). To examine whether this could reflect luciferin uptake via routes other than ingestion; e.g., by penetration of the cuticular barrier, we examined cuticular permeability to the DNA stain Hoechst 33258. We incubated synchronized L4 stage larvae with the dye and quantified the fraction of animals with nuclear DNA staining. While such staining was rarely observed in wild-type animals, it was highly penetrant in *blmp-1* mutant animals, comparable to the known cuticle defective strain *bus-8(e2885),* which we used as a positive control (Fig 3C, D). Hence, we conclude that BLMP-1 is required for a timely and a proper cuticle formation.

Results

BLMP-1 protein oscillates during larval development

We have shown that *blmp-1* RNA levels oscillate during development (Fig 4A; Hendriks et al., 2014; Meeuse et al., 2019) and that it is important for a rhythmic molting process (Fig 2). Hence, we wondered whether BLMP-1 protein was rhythmically active. To address this possibility, we performed a time-resolved Western Blot analysis on a strain engineered to express *3xflag::blmp-1* from the endogenous locus. We plated these animals as synchronized L1 stage larvae, grew them at 25°C, and sampled hourly between 23 – 32 hours after plating, covering the L3 and early L4 stage (Fig 4B). Given the limitations of Western Blots, namely its non-linearity, we relied on qualitative observations and did not measure protein levels quantitatively. However, even with these limitations, a highly dynamic pattern of BLMP-1 accumulation was evident.

To confirm the robustness of this result and link it more directly to developmental progression, we repeated it with the following modifications: we grew animals at 20°C, when they develop slightly slower, and sampled hourly between 17 – 27 hours after plating, to cover L2 until early L3 stages. Moreover, we used a strain that additionally expressed a luciferase transgene, enabling us to monitor developmental progression while sampling from a liquid culture (see methods). This experiment confirmed that BLMP-1 also oscillates during the earlier stages and, by using the parallel luciferase assay to approximate time of molting, revealed low levels of BLMP-1 protein during the molt and a peak during the first part of the intermolt. We thus conclude that both *blmp-1* mRNA and BLMP-1 protein accumulate rhythmically throughout larval development.

BLMP-1 has a rhythmic function in development

Results

To understand whether rhythmic BLMP-1 protein accumulation reflect rhythmic BLMP-1 activity, we tagged the endogenous protein with a degron to achieve timed and reproducible BLMP-1 protein depletion. Specifically, we tagged *blmp-1* with the *auxin-inducible degron* (*aid*) and expressed *Arabidopsis* TIR1 ubiquitously and constitutively to achieve conditional and fast degradation of AID::BLMP-1 by addition of auxin (Zhang et al., 2015). When we added different concentrations of auxin to embryos and followed their development in a luciferase reporter assay, we found that the length of the molts depended on the concentration of auxin. Molts were extended to at most 2-fold with increasing auxin concentration (Fig S7). Moreover, consistent with the results from the *blmp-1(tm548)* mutant and *blmp-1(RNAi)* luciferase analysis, intermolts were increased at high auxin concentrations, but decreased at lower auxin concentrations (Fig S7).

If rhythmic expression of *blmp-1* were relevant for its physiological function, we would expect that phenotypic outcomes differed depending on when during a larval stage BLMP-1 degradation was triggered. To test this, we plated *aid::blmp-1* embryos of various ages in a microwell plate to run the luciferase assay. After 24 h or 32 h in the luminometer, we added 250 μM final concentration auxin to all wells, and restored the plates to the luminometer. This ensures that animals will be of different ages at the time they begin to experience AID::BLMP-1 degradation because early-hatched animals will be older at this time point.

At t=24h, most animals were somewhere in larval stage 2 (Fig 5A), allowing us to quantify the effect of AID::BLMP-1 depletion on I2 and all subsequent molts and intermolts. We found that M3 was greatly, and similarly, extended for all auxin treated animals relative to vehicle treated animals, irrespective of their age in L2, when they were first exposed to auxin. By contrast, the durations of M2 and I3 correlated with the time of the onset of AID::BLMP-1 degradation in L2,

i.e., the younger the animals were at the time of auxin treatment, the more dramatic the extension relative to vehicle contol (Fig 5B). Finally, I2 did not show any obvious lengthening, even in animals that received auxin already early in I2, suggesting that the effects of intermolt lengthening only occur after worms progressed through a molt. Thus, aberrant intermolt durations might reflect a secondary effect arising from defects in molting. We observed analogous results when we repeated this experiment by applying auxin at t=32h, when animals are in L3 (Fig S8).

These results suggest that the extension of a molt is not an all-or-nothing event, but is rather time-dependent. Given that BLMP-1 levels oscillate, a parsimonious interpretation of these data is that BLMP-1 is rhythmically active. Formally, however, we cannot rule out a cumulative effect, where extended depletion of BLMP-1 over time increase phenotype severity.

A few oscillating genes are strongly uncoupled in blmp-1(tm548) mutants

To understand how BLMP-1 affected gene expression, we performed an RNA sequencing time-course on synchronized populations of *blmp-1(tm548)* mutant and wild-type animals grown at 25°C. We focused on the first 24 hours after plating synchronized L1s to observe the effects of *blmp-1* loss in situations of both normal and abnormal developmental progression. Specifically, *blmp-1* mutant animals develop synchronously and at largely normal rate through the first intermolt, but then exhibit a greatly extended, yet still relatively synchronous molt 1, followed by an extended and variable intermolt 2 (Fig 2E, F). Thus, we hypothesized that relevant effects of *blmp-1* loss might be visible at, or shortly before, the time when development is detectably impaired. Conversely, as developmental delays and asynchrony increase, and assuming that the previously observed coupling between oscillation period and larval stage duration continues to hold in *blmp-1* mutant animals, we expected to observe more global difference in oscillatory

gene expression, namely lower amplitudes, increased periods and, accordingly, a delayed peak occurrence (Fig 6A, top). In such a scenario, fold changes calculated between mutant and wild-type animals for a given time point after plating would be rhythmic (Fig 6A bottom), i.e., expression of a gene would be up in *blmp-1* mutant relative to wild-type animals at some time points, and then down at subsequent time points, in a recurring pattern.

Indeed, we observed lower amplitudes (Fig 6B) as well as increased periods in our RNA sequencing data (Fig 6C) as determined from a Hilbert transformation on the butterworth filtered gene expression traces (see methods, as in Meeuse et al., 2019). To reduce noisy gene expression traces, we excluded genes that were fitted poorly by a butterworth filter ($R^2 \leq 0.4$). In agreement with our expectation, we detected rhythmic fold changes when comparing expression patterns of wild-type and *blmp-1(tm548)* mutant for identical time points (Fig 6D). Moreover, consistent with an unaltered developmental rate of the mutant animals up to molt 1, the rhythmic fold changes became detectable on from approximately 10 hours onward. Taken together, these observations suggest that comparing equivalent time points between wild-type and mutant is generally not valid.

To address the extent to which oscillating gene expression differed between mutant and wild-type animals, we focused on determining their phases at selected time points using the Hilbert transformation. Analysis using a Hilbert transform has the advantage that we can compare the progression of oscillations directly, instead of just interpreting fold-changes. For every selected gene, we calculated the phase difference between mutant and wild-type animals at two different time points, TP16 and TP19. These were chosen because they are in the time when fold changes are clearly observable between the two strains, and because they are almost half a period (for wild-type animals) apart, thus reducing the risk of biases from peak phases. When visualized in a

scatterplot, a large majority of genes (2,124, corresponding to 93.9 %) displayed phase shifts in the mutant relative to the wild-type at both time points, some (132, 5.8%) massively (Fig 6E). However, a few genes clearly defied this general trend and revealed comparable phases in mutant and wild-type worms at a given time point despite the strong developmental delay. In other words, with the observation that *blmp-1(tm548)* mutants develop slower than wild-type, the expression of these genes had substantially uncoupled from development in the *blmp-1* mutant animals. Furthermore, we see a spread of phase differences, suggesting that the level of desynchronization of gene expression and development in *blmp-1* mutant animals can vary for each individual gene and is not a binary separation into uncoupled or coupled. Thus we suspect that *blmp-1* mutant animals display a more global uncoupling of gene expression with development with few genes showing a severe uncoupling.

We hypothesized that this finding could result from loss of BLMP-1 regulation on these genes, leading to a precocious upregulation relative to other oscillating genes that are still closely coupled with the development of the worm. In order to investigate the severely uncoupled genes, we compared their gene expression in wild-type and *blmp-1(tm548)* mutants by plotting their mean expression and standard deviation over time (Fig 6F(I)). We selected genes with similar peak phases in order to make the summary plot meaningful as otherwise means of gene expression would be affected by the different peak times. The identified genes are enriched in peak phases between 75 and 175 degree and depleted otherwise (Fig 6G). Importantly, the effects we observe seem to be specific to a particular set of genes and do not arise primarily from the peak phase of these genes, as a reference set of oscillating genes in the same peak phase do not show these effects (Fig 6 F(II)). On the other hand, genes with a strong phase shift (n = 132)

(Fig 6E, green), that are potentially still coupled to development, showed opposite peak phase enrichment compared to the uncoupled genes (Fig 6F(III), green).

BLMP-1 couples gene expression with development

As we were missing exact information about the timing of developmental events in the *blmp-1(tm548)* mutant RNA sequencing experiment, we could only hypothesize that genes with similar peak times in *blmp-1(tm548)* mutants and wild-type were severely uncoupled from development in *blmp-1(tm548)* mutants. We thus wondered whether and to which extent the suspected strong uncoupled genes identified in Fig 6E indeed show uncoupling to developmental progression. We employed a single worm imaging technique (Meeuse et al., 2019) to investigate the expression of appropriate transcriptional GFP reporters in parallel with developmental progression in single worms. This allows us to directly relate gene expression changes to developmental progression (Fig 7A), and thereby circumvent any changes on amplitudes and phases arising from population asynchrony. We created a transcriptional reporter for *F11E6.3*, a gene that belonged to the group showing a shift in peak time (Fig 7B) and for *F16B4.4*, a gene that did not change in the peak time in the *blmp-1* mutant time course (Fig 7C). Since *blmp-1(tm548)* embryos were not sufficiently robust for the assay, with many of them dying before hatching, we compared animals exposed to mock or *blmp-1* RNAi. Due to variable larval stage durations in *blmp-1* RNAi, the traces were separately scaled to the average length of each individual larval stage to make direct comparison between mock and *blmp-1* RNAi possible. The solid line represent the mean of all individual traces with the standard deviation indicated with the shaded area. The mean of the molt entry and exit is indicated in vertical lines for both mock RNAi (black) and *blmp-1* RNAi (red). Due to increased escapers from the chambers in L4, we focused on L1 – L3 stages.

Results

We found that the *F11E6.3* reporter oscillation remained synchronized with the molts (i.e., the trough happens always around the molt entry and the peak occurs in the middle of the intermolt) in both mock and *blmp-1* RNAi (Fig 7D, Fig S10). In contrast, the *F16B4.4* reporter showed a strong shift in peak time relative to the molt timing, peaking precociously during the molt in *blmp-1* RNAi whereas its normal peak happened during the intermolt in mock RNAi treated worms (Fig 7E, Fig S10).

Results

Discussion / Conclusion

In this study, we have further characterized the *C. elegans* oscillator and shed light on the transcriptional regulation of oscillatory gene expression with a particular focus on the transcription factor BLMP-1 in oscillatory mRNA abundance and rhythmic development. We have shown that BLMP-1 is expressed rhythmically and functions in a periodic fashion. Furthermore we have provided evidence that loss of BLMP-1 leads to internal desynchronization among groups of oscillating genes and between gene expression oscillations and developmental events. Using the present knowledge we propose a coupling function of BLMP-1, synchronizing oscillatory gene expression and development.

Transcription is the main driver of oscillatory gene expression

With our time resolved ChIP sequencing experiment we have provided evidence that transcription is the main driver for the rhythmic mRNA output of the *C. elegans* oscillator since ChIP-seq and mRNA-seq reads globally showed a strikingly similar pattern. Some oscillating transcripts were not accompanied by rhythmic RNAPII occupancy and conversely, some genes with rhythmic RNAPII occupancy did not display oscillating mRNA abundance. Although this might reflect a different mode of their regulation, we note that the amplitudes of RNAPII occupancy were generally lower than those of the corresponding transcripts. Hence, the dynamic range of RNAPII ChIP-seq appears to be lower than that of mRNA sequencing, possibly due to lower coverage in ChIP sequencing, and thereby contribute to false negative results. Nevertheless, we cannot exclude that additional post-transcriptional regulatory mechanisms exist to either generate or damp oscillations, such as post-transcriptional regulation by microRNAs (Kim et al., 2013). However, given the fact that we confirmed oscillatory transcriptional regulation on promoters by reporters with the supposedly unregulated *unc-54* 3'UTR, we

consider transcriptional regulation as the abundant mechanism. It is of note that our promoters contained the 5' UTR sequence and even though some of these annotated sequences were extremely short, it remains possible that they can modulate rhythmic gene expression. However, using the conserved *daf-6* promoter element (*ce*) in combination with the Δ*pes-10* minimal promoter reveals that the endogenous 5' UTR is not necessary to induce oscillatory gene expression and that amplitude and peak phase might be encoded in relatively small promoter elements.

Further (conserved) promoter elements should be tested in the future to investigate this possibility. Characterization of additional small promoter elements driving oscillatory gene expression with similar peak phases might enable us to reveal common sequence motifs regulating these peak phases.

Phase and relative amplitude are both recapitulated by the promoter reporter constructs

We can recapitulate both the relative amplitude as well as the peak phase with our transcriptional reporters driving *gfp::pest::h2b::unc-54* 3'UTR for almost all reporters tested. In line with the ChIPseq results, this strongly indicates that transcription regulated on the chosen promoter sequences is the main driver for oscillatory gene expression. However, apart from rhythmic production, oscillatory gene expression can also be shaped by degradation rates. Mathematical models have shown that the relative amplitudes and the peak phase are dependent on the stability of the component, leading to lower relative amplitudes and later peak times upon increased stability (Korenčič et al., 2012; Lück et al., 2014). Hence either not only the production but also the degradation dynamics are recapitulated by our reporters, or degradation rates are high enough in general so that a small difference in degradation rate between our *gfp* and the endogenous transcript do not lead to an observable difference in the peak phase.

Results

BLMP-1 as a candidate transcription factor in the regulation of the C. elegans developmental clock

In the circadian field, primary clock components are defined by a set of characteristics, with arrhythmicity and strong period increase (or decrease) of the circadian rhythm being strong indicators for primary clock components (reviewed in Takahashi 2004). Based on our luciferase assay results the *blmp-1(tm548)* null mutant satisfies these criteria on the phenotypic level and thus make *blmp-1* an attractive candidate for a clock component. Nevertheless, as we investigate a developmental oscillator, primary clock components might also be lethal or lead to larval arrest. Indeed, we observe a high degree of larval arrest or death after the first molt in the luciferase assay with *blmp-1* mutants. Furthermore, the oscillating protein abundance, though not a prerequisite for rhythmic activity, is an indication for BLMP-1 being rhythmically active. Consistent with reports from *Drosophila,* where dBlimp-1 seems to be unstable (Agawa et al., 2007), and together with the fact that we observe oscillating BLMP-1 levels, we suspect a relatively high degradation rate for *C. elegans* BLMP-1 protein as well.

BLMP-1 is timely needed in multiple larval stages to regulate molt durations

Previous studies have shown that BLMP-1 is involved in timing developmental events by preventing precocious *unc-5* expression and turn of the distal tip cell (DTC) during L3/L4 (Horn et al., 2014; Huang et al., 2014). Here we report BLMP-1 to be rhythmically expressed on both mRNA and protein levels throughout larval development which suggested functions beyond the DTC turn. Using conditional depletion with the auxin inducible degron system, we have provided evidence for a repetitive function of BLMP-1 in regulating the timing of molts since conditional reduction in every larval stage resulted in a time dependent lengthening of the molt directly following depletion. Interestingly, lengthening of intermolts was not observed during the

same intermolt in which BLMP-1 depletion occurred, further indicating a specific role for BLMP-1 in the regulation of molt durations. Intermolt lengthening occurred only in the following larval stage(s) when worms developed through a molt in BLMP-1 depleted conditions suggesting that intermolt lengthening could be a secondary effect arising from an increased molt length. Molts of later larval stages did not further increase in their duration, but rather plateaued at the maximum duration obtained in the molt before, possibly due to the fact that BLMP-1 depletion reached the maximum. We speculate that specific amounts of BLMP-1 are needed at each molt to regulate their durations. The earlier BLMP-1 depletion is induced, the lower the levels at the molts, when BLMP-1 is needed, which leads to increased molts lengths depending on the time of BLMP-1 depletion.

Furthermore, the developmental phenotypes in *blmp-1(tm548)* mutants such as asynchronous development arising after the first molt are indicative for a mis-regulation in the molting process that induces subsequent developmental phenotypes. We can only speculate about the exact process that is affected in *blmp-1* mutants, a disrupted formation of the cuticle would result in defects before hatching, when the first cuticle is synthesized. The fact that we see worms developing synchronously through the first intermolt however suggests that *blmp-1* is involved in other processes, as for example apolysis. Also, in line with this hypothesis is the observation that *blmp-1(tm548)* mutants do not show increased luciferase signals during the first molt (an indication of an impaired L1 cuticle). However, after the first molt and ecdysis, the subsequent molts are all characterized by elevated luciferase signal during the molts. Impaired or incomplete apolysis would not manifest in M1 as observable effects through luciferase assays might only arise after worms shed the old cuticle and due to incomplete apolysis rupture the new cuticle.

BLMP-1 prevents precocious expression of oscillating genes to synchronize oscillations

The general delay and drop in amplitude in oscillatory gene expression we detect in our sequencing data might be at least partially explained by the slow and asynchronous development of the mutant. We further thought about two scenarios that could explain this result. First, BLMP-1 could positively regulate almost all oscillating genes and thus the mutation causes a delay in global oscillatory gene expression and development with a few genes defying this pattern. Second, BLMP-1 negatively regulates a few oscillatory genes which will lead to a precocious peak in the mutant eventually resulting in a delayed development as phase coupling between oscillatory genes is lost. In this case, the precocious peaking genes coincide now again with the peak time of the wild-type whereas all non-regulated genes would be delayed in their peak. For both scenarios it is obvious that the oscillator's output is not completely synchronized anymore, e.g. the phase locking of genes that did not change their peak time in *blmp-1(tm548)* mutants to all other genes is lost and potentially not synchronized to the development of the worm anymore.

Consistent with BLMP-1's suggested function in preventing precocious expression of *unc-5* (Huang et al., 2014), we report here that BLMP-1 affects timing of oscillating gene expression globally with a few genes being strongly affected and thus precociously expressed relative to the molts and other oscillating genes in the *blmp-1(tm548)* mutant. We could further confirm these results with a reporter by single worm imaging where we observe a precocious upregulation of our transcriptional reporter *F16B4.4* during every molt (Fig 6 D). This suggests a repetitive role for BLMP-1 in repressing gene expression specifically during the molt in order to prevent precocious expression. We did, however, not detect the previously reported *unc-5* gene to be precociously expressed in our sequencing data which might be due to a precocious *unc-5* expression in only the DTC whereas *unc-5* expression in VNC motor neurons (Killeen et al.,

2002) might not be affected and thus the effect might be too small to detect in whole worm sequencing.

Given that molts and development were observed to be asynchronous and delayed in the *blmp-1(tm548)* mutant animals in luciferase assays we were initially surprised to observe precocious expression. However, even though groups of oscillating genes might peak earlier, this does not necessarily imply faster development. The resulting unsynchronized oscillatory gene expression might be deleterious for proper succession of developmental events as gene expression of sub-groups of oscillating mRNAs is not delivered at the right time relative to others and development.

It seems remarkable that only a small set of genes severely uncoupled can already lead to a strong phenotype. However, we can imagine the milder global uncoupling that we observed in the *blmp-1(tm548)* mutant time course to contribute to the phenotypes. Unfortunately due to the low number of genes showing a strong peak shift, we could not find GO terms nor promoter elements shared between them. Nevertheless, the identified genes responding in the *blmp-1(tm548)* mutant show a clear phase preference and peak almost opposite of *blmp-1*. This would further suggest a repressing role for BLMP-1, preventing precocious peaking of its downstream targets and favor a function of BLMP-1 in synchronizing outputs of oscillating gene expression with each other. A repressing function of BLMP-1 also seems equivalent to *Drosophila's* dBlimp-1 where loss of dBLIMP-1 leads to a precocious peak in dFTZ-F1 (Agawa et al., 2007), which is involved in timing of ecdysone-induced developmental pathway, responsible for essential developmental processes such as molting or metamorphosis. Hence, BLMP-1 might be responsible to prevent precocious gene expression in a rhythmic manner in *C. elegans* to

synchronize groups of gene expression oscillations among each other and with developmental events.

BLMP-1 as a putative coupling factor

With the present data, we propose BLMP-1 as a coupling agent, either synchronizing different oscillators among each other or synchronizing the outputs of oscillatory gene expression. Hence, BLMP-1 ensures that groups of oscillating genes with different physiological functions are synchronized with each other, an important feature for proper rhythmic development that depends on execution of multiple rhythmic processes. Coupling was previously studied mainly among oscillators in different cells (Herrgen et al., 2010; Kim et al., 2010; Riedel-Kruse et al., 2007), and we propose these studies to further inspire future experiments and interpretations regarding the coupling in the *C. elegans* oscillator. The studies in the segmentation clock have shown that reduced of Notch-Delta coupling between cells using the inhibitor DAPT leads to unsynchronized, yet sustained oscillations, among neighboring cells (Riedel-Kruse et al., 2007). Synchronization was observed to be dependent on the coupling strength between cells and was completely lost below a coupling strength threshold. Analogous to these observations, we imagine BLMP-1 as a coupling agent synchronizing multiple oscillators during *C. elegans* larval development. Reduced BLMP-1 protein levels might result in lower coupling strength up to a (bifurcation) point where oscillations are completely uncoupled. Given our results that only strong reduction of BLMP-1 levels lead to severe asynchrony in larval development, such a mechanism seems appealing.

References

Agawa, Y., Sarhan, M., Kageyama, Y., Akagi, K., Takai, M., Hashiyama, K., Wada, T., Handa, H., Iwamatsu, A., Hirose, S., et al. (2007). Drosophila Blimp-1 Is a Transient Transcriptional Repressor That Controls Timing of the Ecdysone-Induced Developmental Pathway. Mol. Cell. Biol. *27*, 8739–8747.

Allen, M.A., Hillier, L.W., Waterston, R.H., and Blumenthal, T. (2011). A global analysis of C. elegans trans-splicing. Genome Res. *21*, 255–264.

Arribere, J.A., Bell, R.T., Fu, B.X.H., Artiles, K.L., Hartman, P.S., and Fire, A.Z. (2014). Efficient marker-free recovery of custom genetic modifications with CRISPR/Cas9 in caenorhabditis elegans. Genetics *198*, 837–846.

Aulehla, A., and Herrmann, B.G. (2004). Segmentation in vertebrates: Clock and gradient finally joined. Genes Dev. *18*, 2060–2067.

Bethke, A., Fielenbach, N., Wang, Z., Mangelsdorf, D.J., and Adam, A. (2009). Nuclear hormone receptor regulation of microRNAs controls developmental progression. Science (80-.). *324*, 95–98.

Blumenthal, T., and Steward, K. (1997). RNA Processing and Gene Structure (Cold Spring Harbor Laboratory Press).

Edgar, R. (2002). Gene Expression Omnibus: NCBI gene expression and hybridization array data repository. Nucleic Acids Res. *30*, 207–210.

Fire, A., Harrison, S.W., and Dixon, D. (1990). A modular set of lacZ fusion vectors for studying gene expression in Caenorhabditis elegans. Gene *93*, 189–198.

Fraser, A.G., Kamath, R.S., Zipperlen, P., Martinez-Campos, M., Sohrmann, M., and Ahringer, J. (2000). Functional genomic analysis of C. elegans chromosome I by systematic RNA interference. Nature *408*, 325–330.

Frøkjær-Jensen, C., Davis, M.W., Ailion, M., and Jorgensen, E.M. (2012). Improved Mos1-mediated transgenesis in C. elegans. Nat. Methods *9*, 117–118.

Gibson, D.G., Young, L., Chuang, R.-Y., Venter, J.C., Hutchison, C.A., and Smith, H.O. (2009). Enzymatic assembly of DNA molecules up to several hundred kilobases. Nat. Methods *6*, 343–345.

Hastings, K.E.M. (2005). SL trans-splicing: Easy come or easy go? Trends Genet. *21*, 240–247.

Hendriks, G.J., Gaidatzis, D., Aeschimann, F., and Großhans, H. (2014). Extensive Oscillatory Gene Expression during C.elegans Larval Development. Mol. Cell *53*, 380–392.

Herrgen, L., Ares, S., Morelli, L.G., Schröter, C., Jülicher, F., and Oates, A.C. (2010). Intercellular coupling regulates the period of the segmentation clock. Curr. Biol. *20*, 1244–1253.

Horn, M., Geisen, C., Cermak, L., Becker, B., Nakamura, S., Klein, C., Pagano, M., and Antebi, A. (2014). DRE-1/FBXO11-dependent degradation of BLMP-1/BLIMP-1 governs C. elegans developmental timing and maturation. Dev. Cell *28*, 697–710.

Huang, T.F., Cho, C.Y., Cheng, Y.T., Huang, J.W., Wu, Y.Z., Yeh, A.Y.C., Nishiwaki, K., Chang, S.C., and Wu, Y.C. (2014). BLMP-1/Blimp-1 Regulates the Spatiotemporal Cell Migration Pattern in C. elegans. PLoS Genet. *10*.

Jiang, Y.J., Aerne, B.L., Smithers, L., Haddon, C., Ish-Horowicz, D., and Lewis, J. (2000). Notch signalling and the synchronization of the somite segmentation clock. Nature *408*, 475–479.

Kamath, R.S., and Ahringer, J. (2003). Genome-wide RNAi screening in Caenorhabditis elegans. Methods *30*, 313–321.

Katic, I., Xu, L., and Ciosk, R. (2015). CRISPR/Cas9 genome editing in Caenorhabditis elegans: Evaluation of templates for homology-mediated repair and knock-ins by homology-independent DNA repair. G3 Genes, Genomes, Genet. *5*, 1649–1656.

Killeen, M., Tong, J., Krizus, A., Steven, R., Scott, I., Pawson, T., and Culotti, J. (2002). UNC-5 function requires phosphorylation of cytoplasmic tyrosine 482, but its UNC-40-independent functions also require a region between the ZU-5 and death domains. Dev. Biol. *251*, 348–366.

Kim, Grün, D., and Van Oudenaarden, A. (2013). Dampening of expression oscillations by synchronous regulation of a microRNA and its target. Nat. Genet. *45*, 1337–1345.

Kim, J.R., Shin, D., Jung, S.H., Heslop-Harrison, P., and Cho, K.H. (2010). A design principle underlying the synchronization of oscillations in cellular systems. J. Cell Sci. *123*, 537–543.

Korenčič, A., Bordyugov, G., Košir, R., Rozman, D., Goličnik, M., and Herzel, H. (2012). The Interplay of cis-Regulatory Elements Rules Circadian Rhythms in Mouse Liver. PLoS One *7*.

Lasda, E.L., and Blumenthal, T. (2011). Trans-splicing. Wiley Interdiscip. Rev. RNA *2*, 417–434.

Lück, S., Thurley, K., Thaben, P.F., and Westermark, P.O. (2014). Rhythmic degradation explains and unifies circadian transcriptome and proteome data. Cell Rep. *9*, 741–751.

Meeuse, M.W.M., Hauser, Y.P., Hendriks, G.-J., Eglinger, J., Bogaarts, G., Tsiairis, C., and Großhans, H. (2019). State transitions of a developmental oscillator. BioRxiv 755421.

Miki, T.S., Carl, S.H., and Großhans, H. (2017). Two distinct transcription termination modes dictated by promoters. Genes Dev. *31*, 1870–1879.

Mohawk, J.A., Green, C.B., and Takahashi, J.S. (2012). Central and Peripheral Circadian Clocks in Mammals. Annu. Rev. Neurosci. *35*, 445–462.

Moreno-Risueno, M.A., Norman, J.M. Van, Moreno, A., Zhang, J., Ahnert, S.E., and Benfey, P.N. (2010). Oscillating Gene Expression Arabidopsis Root Branching. Science (80-.). *329*, 1306–1312.

Oates, A.C., Morelli, L.G., and Ares, S. (2012). Patterning embryos with oscillations: Structure, function and dynamics of the vertebrate segmentation clock. Development *139*, 625–639.

Olmedo, M., Geibel, M., Artal-Sanz, M., and Merrow, M. (2015). A high-throughput method for the analysis of larval developmental phenotypes in Caenorhabditis elegans. Genetics *201*, 443–448.

Panda, S., Hogenesch, J.B., and Kay, S.A. (2002). Circadian rhythms from flies to humans. Nature *417*, 329–335.

Patke, A., Young, M.W., and Axelrod, S. (2020). Molecular mechanisms and physiological importance of circadian rhythms. Nat. Rev. Mol. Cell Biol. *21*, 67–84.

Riedel-Kruse, I.H., Müller, C., and Oates, A.C. (2007). Synchrony dynamics during initiation, failure, and rescue of the segmentation clock. Science (80-.). *317*, 1911–1915.

Takahashi, J.S. (2004). Introduction: Finding new clock components; past and future. *19*, 339–347.

Virtanen, P., Gommers, R., Oliphant, T.E., Haberland, M., Reddy, T., Cournapeau, D., Burovski, E., Peterson, P., Weckesser, W., Bright, J., et al. (2020). SciPy 1.0: fundamental algorithms for scientific computing in Python. Nat. Methods 1–12.

Welsh, D.K., Takahashi, J.S., and Kay, S.A. (2010). Suprachiasmatic Nucleus: Cell Autonomy and Network Properties. Annu. Rev. Physiol. *72*, 551–577.

Zhang, L., Ward, J.D., Cheng, Z., and Dernburg, A.F. (2015). The auxin-inducible degradation (AID) system enables versatile conditional protein depletion in C. elegans. Development *142*, 4374–4384.

Acknowledgements: We thank Stephane Thiry, Kirsten Jacobeit and the FMI Functional Genomics Facility for RNA sequencing, Iskra Katic for help in generating transgenic strains, and Laurent Gelman for help with imaging. **Funding:** The FMI is core-funded by the Novartis Research Foundation. This work has received funding from the European Research Council (ERC) under the European Union's Horizon 2020 research and innovation programme (grant agreement No [741269]). **Author contributions:** Milou Meeuse performed the RNAPII ChIP sequencing time course. Yannick Hauser performed all transcriptional reporter RT-qPCR time courses. Milou Meeuse and Yannick Hauser performed luciferase assays with *blmp-1* RNAi and mutant animals respectively. Milou Meeuse performed the auxin inducible degron luciferase assays. Yannick Hauser performed and analyzed the *blmp-1(tm548)* mutant time course and acquired and analyzed single worm imaging data. Jan Eglinger wrote the KNIME workflow for the single worm imaging. Helge Großhans, Milou Meeuse and Yannick Hauser conceived the project and Yannick Hauser wrote the manuscript under supervision from Helge Großhans. **Competing interests:** The authors declare no competing interests. **Data and materials availability:** All sequencing data generated for this study will be deposited in NCBI's Gene Expression Omnibus (Edgar, 2002) and will be accessible through GEO Series accession number XXX .

Published research reagents from the FMI are shared with the academic community under a Material Transfer Agreement (MTA) having terms and conditions corresponding to those of the UBMTA (Uniform Biological Material Transfer Agreement).

Figures

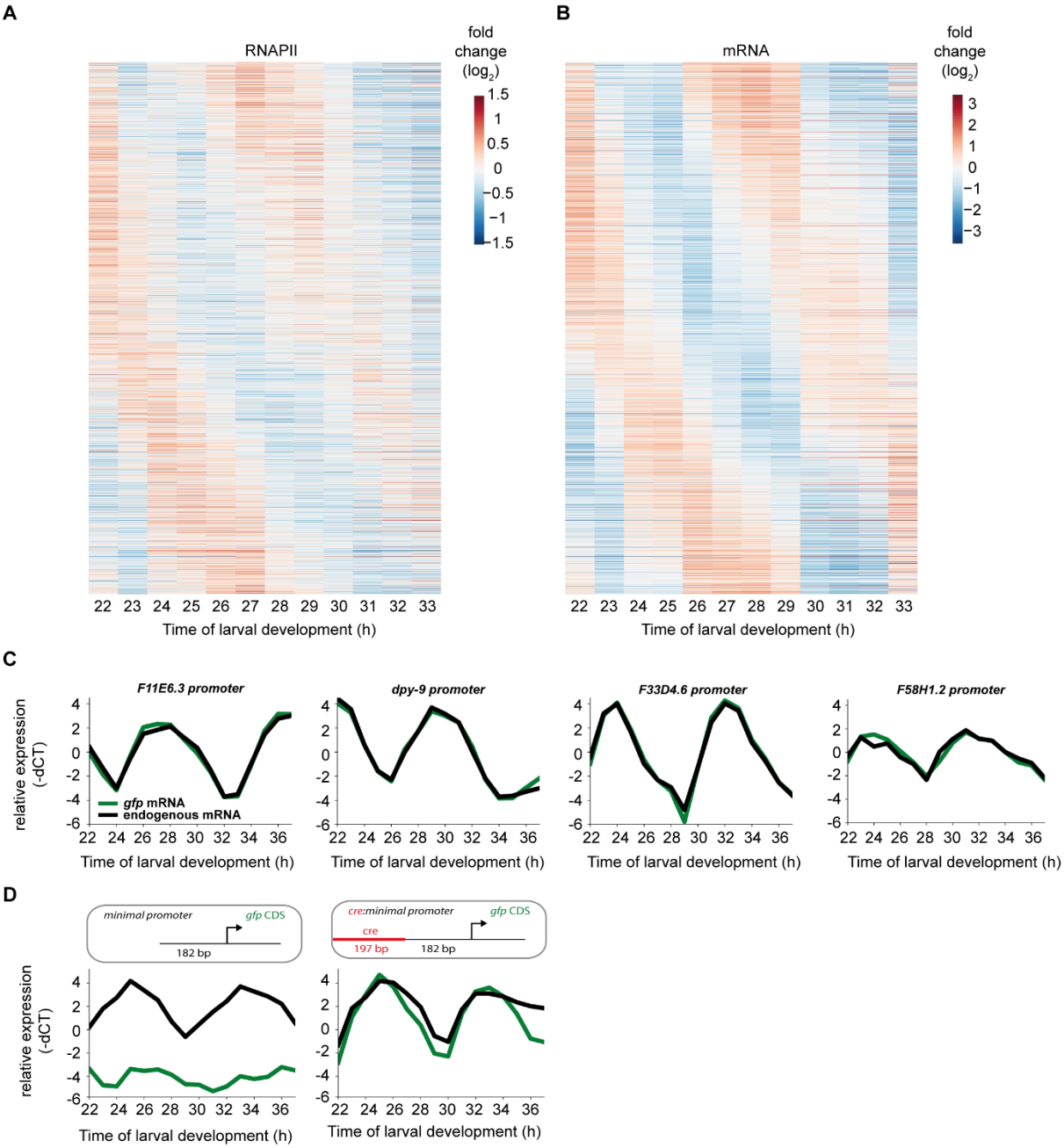

Fig 1: Oscillatory gene expression arises from promoter-driven rhythmic transcription

A, Log_2-transformed, mean-normalized RNA polymerase II ChIP sequencing reads of oscillating genes revealed transcription to be the main driver for oscillatory gene expression (n=2,106). Reads are ordered according to peak phase obtained from Meeuse et al., 2019.

B, Log_2-transformed, mean normalized RNA sequencing data, ordered by peak phase according to A (n=2,106).

C, D, RT-qPCR time courses of *gfp* and endogenous transcripts. Promoters of oscillating genes driving a destabilized, nuclear gfp can recapitulate the peak phase and amplitude of endogenous transcript oscillation on the mRNA level (C). A small conserved element in the *daf-6* promoter can induce oscillatory gene expression. (D).

Relative expression was plotted as (target Ct values – actin Ct values) * (-1) and then mean normalized for each trace individually (C) or mean normalized to the *daf-6* mean expression to compare expression levels (D).

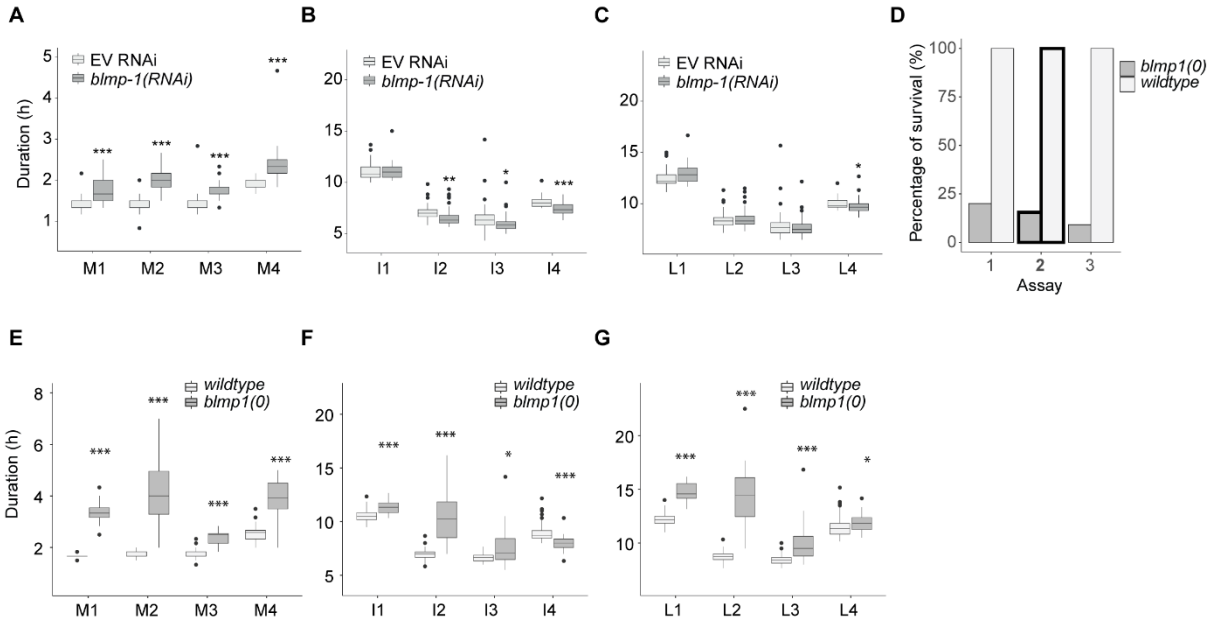

Fig 2: BLMP-1 loss of function leads to developmental defects and a cuticle defect

A – C, Boxplots of the quantification of single animal larval stage, intermolt and molt durations in mock and *blmp-1* RNAi. In general we observe longer molts (A), accompanied by shorter intermolts (B), leading to similar larval stage durations (C) in *blmp-1* RNAi compared to mock RNAi (n>60). Significantly different durations are indicated (* P<0.05, ** P<0.01, *** P<0.001, Welch two-sample and two-sided t-test)

D, Manual quantification of detected lethality or arrest in *wild-type* and *tm548(tm548)* worms for three replicate assays with 20%, 15.5% and 9% of survival for assay 1, 2 and 3 respectively. The assay used in E – G is indicated in bold.

E – G, Quantification of larval stage, intermolt and molt durations of *wild-type* (n=76) and *blmp-1(tm548)* (n=20). The *blmp-1* mutant shows increased durations and higher variability for larval stages, intermolts and molts after the first intermolt. Significantly different durations are indicated (* P<0.05, ** P<0.01, *** P<0.001, Welch two-sample and two-sided t-test)

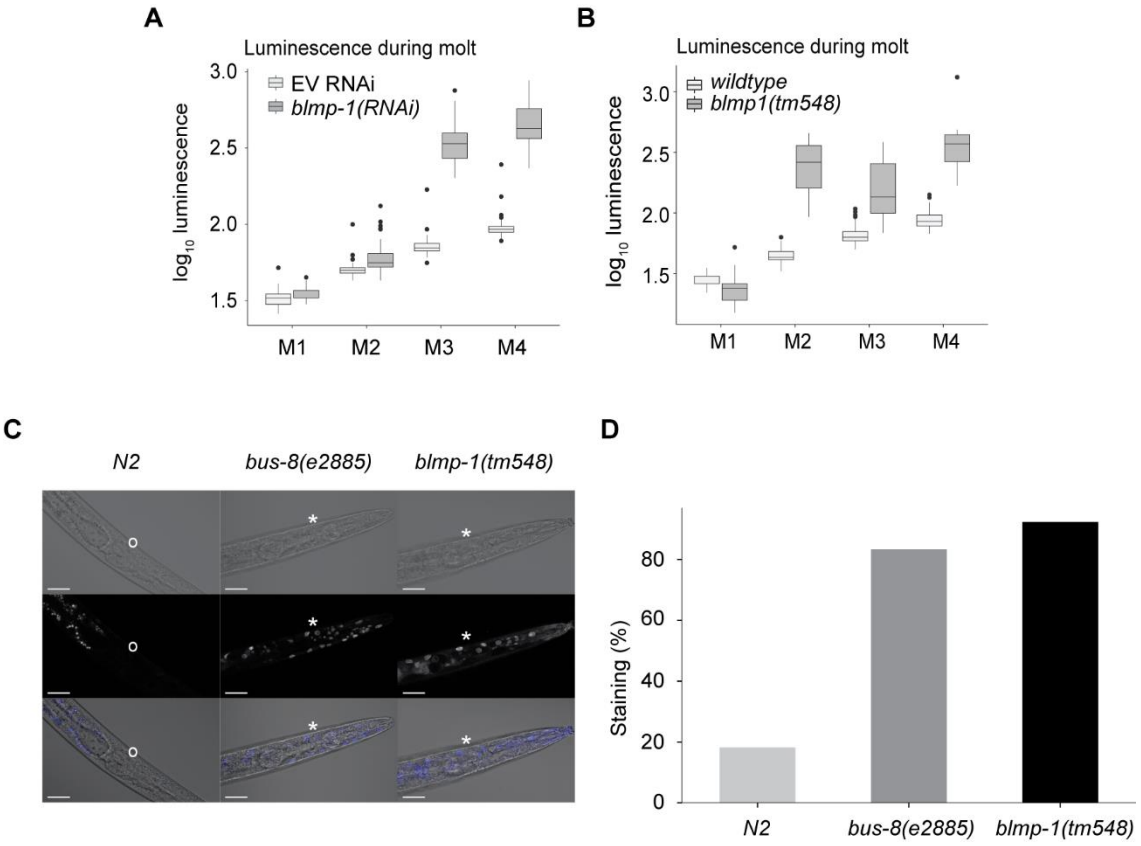

Fig 3: BLMP-1 is required for cuticle integrity

A, B, Luminescence intensities during the molts in mock (EV) and *blmp-1* RNAi (A) and in wild-type and *blmp-1(tm548)* mutants (B) in $\log_{10}$. Intensities were $\log_{10}$-transformed as otherwise the differences in M1 and M2 would be invisible.

C, Representative images from staining N2, *bus-8(e2885)* and *blmp-1(tm548)* in Hoechst 33258 to test for cuticle permeability. The scale bar in the left lower corner represents 20µm.

D, Quantitative analysis showing the percentage of stained worms after incubation in Hoechst. *bus-8(e2885)* and *blmp-1*(*tm548)* show higher percentage of staining (>80%), n≥11.

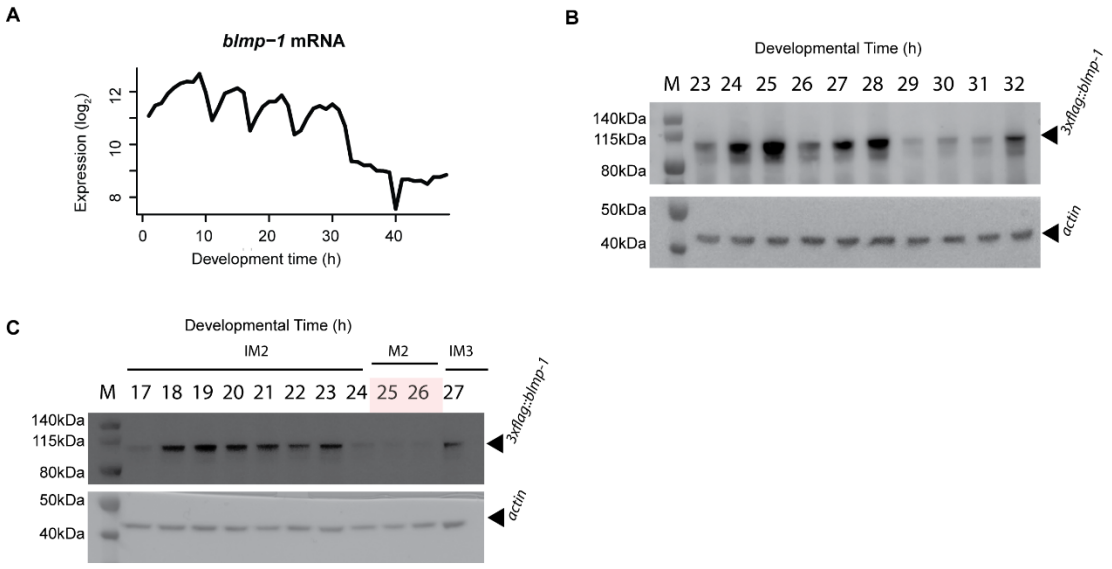

Fig 4: The transcription factor BLMP-1 is oscillating at the mRNA and protein level

A, The mRNA abundance of the transcription factor *blmp-1* oscillates (*blmp-1* mRNA levels during larval development from (Meeuse et al., 2019).

B, **C**, 3xFLAG::BLMP-1 protein detected by Western Blot. Protein abundance covering roughly L3 to early L4 (25°C) using HW2639 (B) and from early L2 to early L3 stage (20°C) using HW2802 (C). The molt in C is determined by luciferase assays that were performed in parallel (Fig S6) and indicated in salmon.

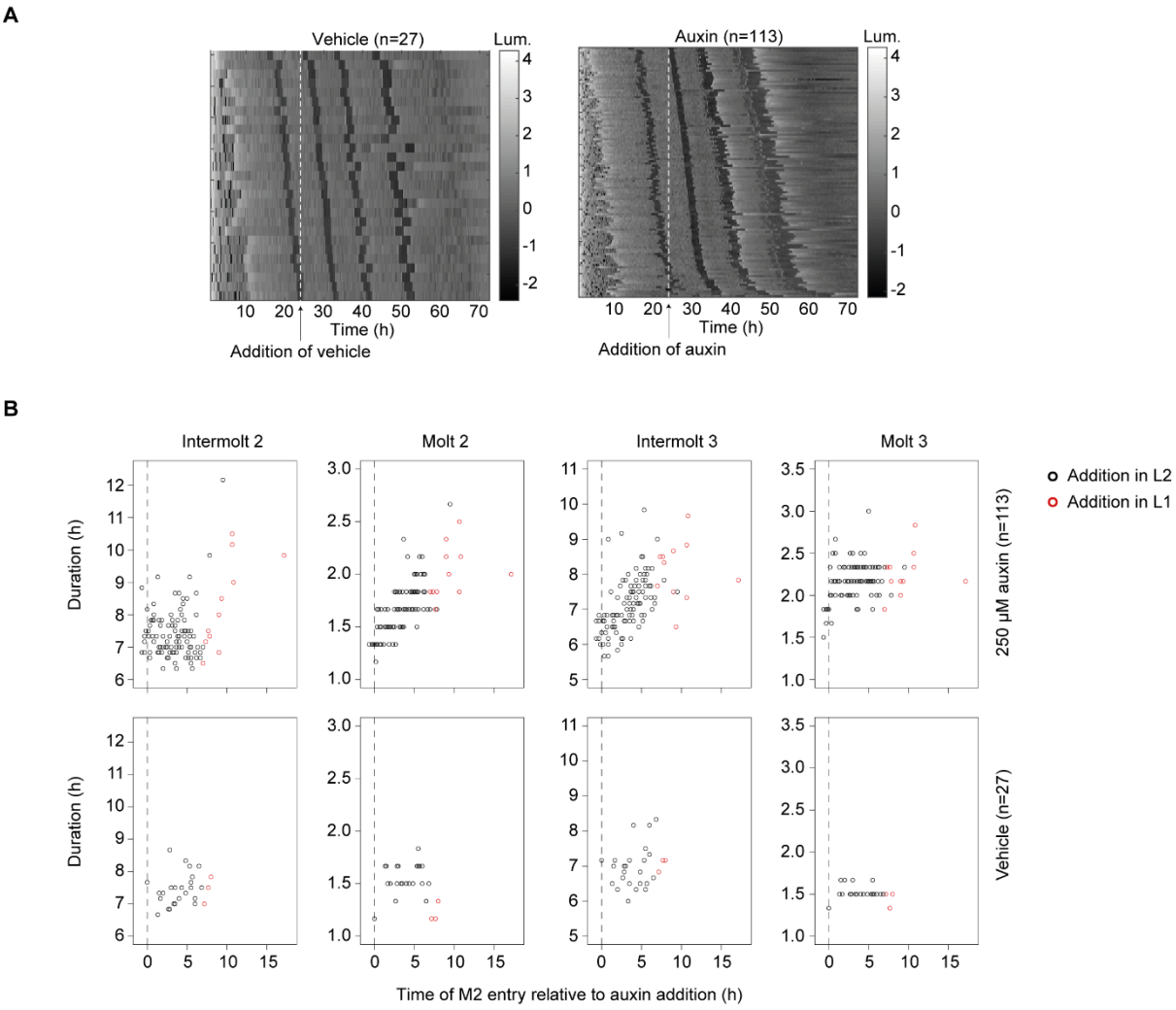

Fig 5: Molt lengthening is dependent on the onset of BLMP-1 degradation

A, Heatmaps showing trend-corrected luminescence (Lum.) traces; one animal per horizontal line. Vehicle (0.25% ethanol; left) or 250 µM auxin (right) were added at t=24h. t=0 h corresponds to the start of the assay. Embryos hatch at different time points and traces are sorted by entry into second molt. Dark grey indicates low luminescence and corresponds to the molts.

B, Duration of intermolt 2, molt 2, intermolt 3 and molt 3 plotted over the time of molt entry 2 relative to auxin treatment in control and auxin treated animals shown in A. Few worms experience auxin already in L1 (red) probably resulting in an increased duration in intermolt 2 already.

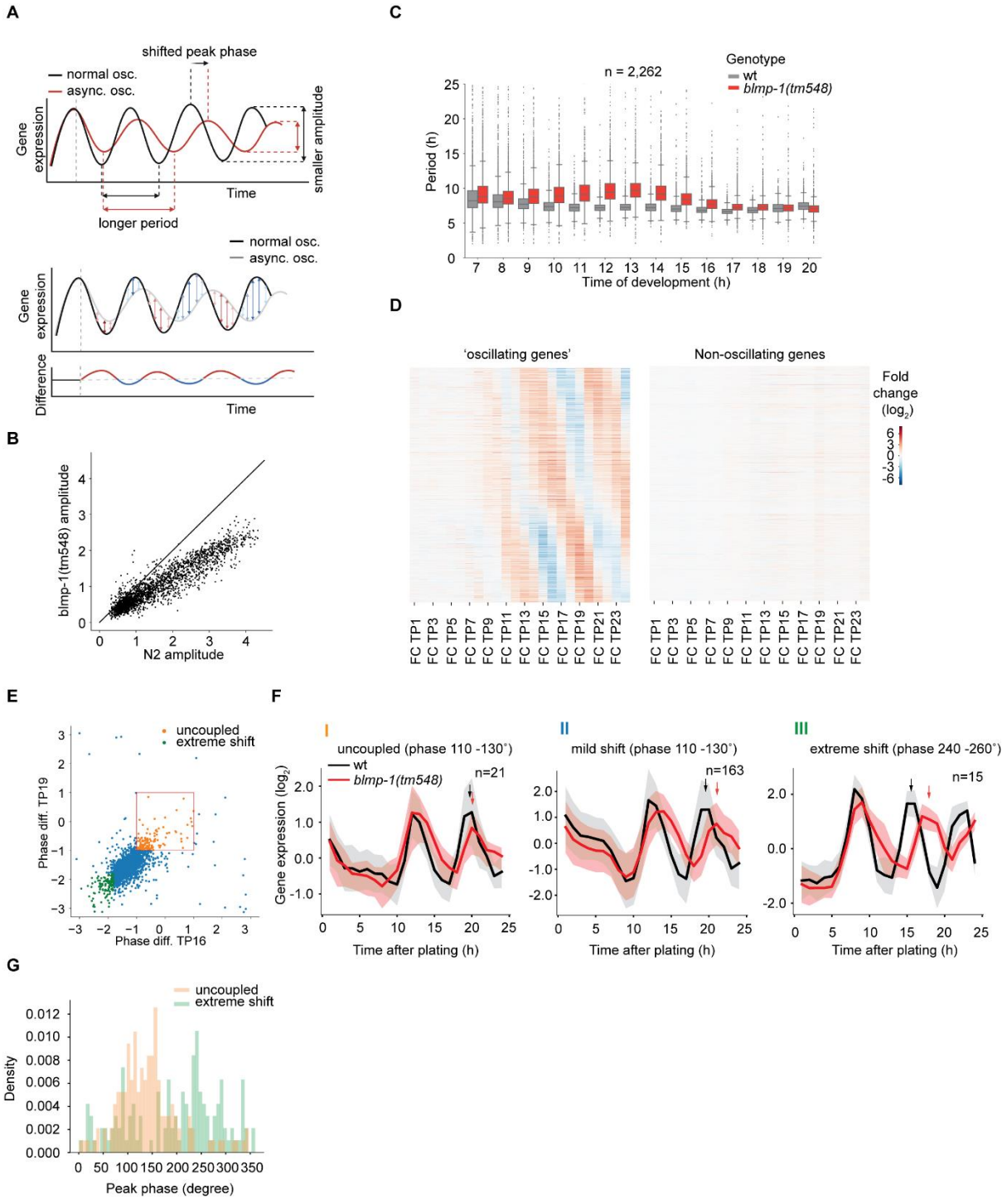

Fig 6: A few genes defy the general increase of period length of oscillation

Only oscillating genes that were reasonably well fit with the butterworth filter were analyzed.

A, Schematic of oscillating gene expression effects expected in an asynchronously, and on average more slowly developing mutant. Expected effects are: increased periods, shifted peak phases, decreased amplitudes. Due to the shifted oscillatory gene expression, calculating fold changes between a normal and an asynchronous worm strain lead to rhythmically changing fold changes (lower panel).

B, Scatterplot comparing the mean of amplitudes in $\log_2$ from oscillating genes in wild-type against *blmp-1(tm548)* mutants. Amplitudes were determined on oscillating genes (n=2,262).

C, Boxplots of periods of oscillating genes in wild-type and *blmp-1(tm548)* over time. *blmp-1(tm548)* mutant animals show increased periods from 9 to 17 hours of larval development (n=2,262).

D, Heatmap of fold differences between wild-type and *blmp-1(tm548)* of $\log_2$-transformed expression values of oscillating genes (left, n=2,262) and non-oscillating genes (right, n=6,699).

E, Scatterplot of phase differences at time points 16 and 19 of oscillating genes. A small phase differences at both time points ("uncoupled") are shown in yellow (n=138) whereas genes with a big negative phase difference, and thus peaking later in *blmp-1* mutants compared to wild-type, are shown in green (n=132).

F, I: Example gene expression of a subset of peak phases (110 – 130°, n=21) of "uncoupled" genes with small phase difference as identified in E (yellow). Gene expression peaks occur roughly at the same time in wild-type and *blmp-1(tm548)*. **II:** Reference gene expression of genes with identical peak phase distribution as in I (110 – 130°, n=163). The reference genes do not show premature upregulation and show a shifted peak in comparison to *blmp-1(tm548)*. **III**: Example gene expression of extremely shifted genes as in E (green) of a subset of peak phases (240 – 260°, n=15). Genes do not show premature upregulation in the beginning of the time course and show a strong shift, peaking almost antiphase in *blmp-1(tm548)* in comparison to wild-type. Arrows indicate peak times for genes in wild-type (black) and *blmp-1(tm548)* mutant animals.

G, Peak phase distribution of oscillating genes of both, extremely shifted genes and "uncoupled" genes, as determined in E.

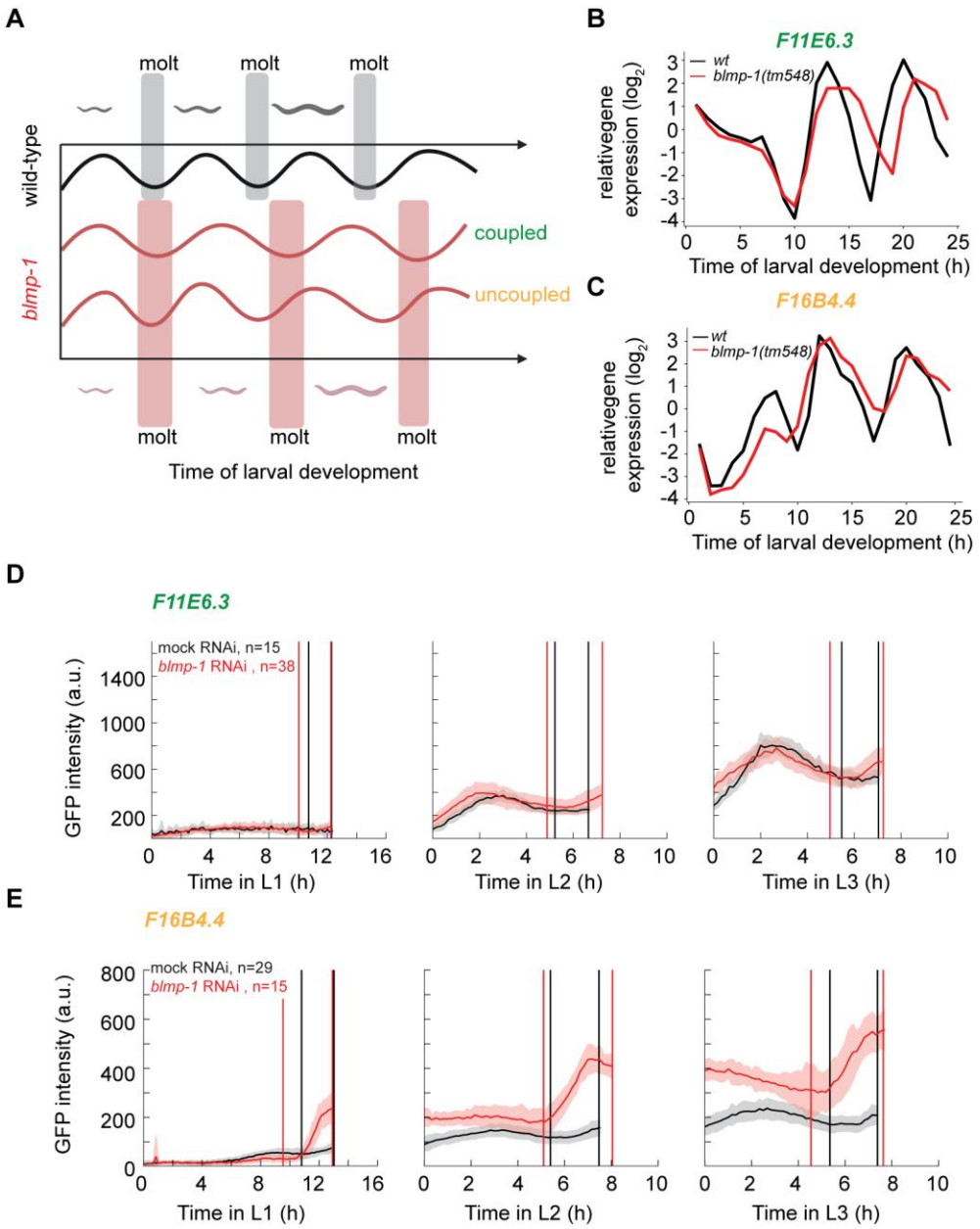

Fig 7: *blmp-1* downregulation leads to internal desynchronization

A, Model of uncoupled gene expression in *blmp-1* depleted conditions. The behavior of uncoupled and coupled genes in *blmp-1* depleted conditions (red) is compared to a reference gene in the wild-type condition (black). In *blmp-1* depleted conditions, genes still coupled to development (green) will slow down together with slower development. Relative to the molt, coupled genes thus peak at similar times while uncoupled genes (yellow) will oscillate

unsynchronized relative to development and thus change peak relative to molts. Created with Biorender.com

B, C, Example of a supposedly to development uncoupled gene, *F16B4.4*, and a coupled gene, *F11E6.3*, in the *blmp-1(tm548)* mutant RNA sequencing time course.

D, E, GFP intensities of the transcriptional reporters in B and C respectively, observed in single worms over time in both mock (black) and *blmp-1* RNAi (red). The strongly uncoupled gene *F16B4.4* shows a shift of peak time relative to the molts and is peaking during the molt in *blmp-1* RNAi while peaking during the intermolt in mock RNAi, revealing a strong uncoupled oscillation with developmental events such as the molt.

Results

Methods

ChIP-sequencing

For RNA polymerase II ChIP-sequencing, synchronized L1 wild-type worms were grown at 25°C. Worms were collected hourly from 22 hours (90.000 worms) until 33 hours (46.000 worms) developmental time. RNA polymerase II ChIP was performed as previously described (Miki et al., 2017). In short, worms were incubated in M9 with 2% Formaldehyde for 30 minutes at room temperature with gentle agitation to allow protein-DNA crosslinking. Worms were lysed with beads using the FastPrep-24 5G machine (MP Biomedicals, settings: 8 m/sec, 30 sec on, 90 sec off, 5 cycles). Lysates were sonicated using the Bioruptor Plus Sonication system (Diagenode, settings: 30 sec on, 30 sec off, 20 cycles). 250 µg sonicated chromatin was incubated with 10 µg mouse anti-RNA polymerase II CTD antibody (8WG16, Abcam) at 4°C for 2 hours with gentle agitation and subsequently with 45 µL Dynabeads Protein G (Thermo Fisher Scientific) at 4°C overnight with gentle agitation. Elute was treated with 0.13 ug/uL RNase and 1 ug/uL Proteinase K. ChIP-seq libraries were prepared using NEBNext Ultra DNA Library Prep Kit for Illumina (New England Biolabs) and sequenced using the HiSeq 50 cycle single-end reads protocol on the HiSeq 2500 system.

Sequencing reads were aligned to the ce10 *C. elegans* genome using the qAlign function (default parameters) from the QuasR package in R. ChIP-seq counts within 1-kb windows, i.e. -500 bp to +500 bp around the annotated TSS (using WS220/ce10 annotations), were scaled by total mapped library size per sample and log2-transformed after adding a pseudocount of 8. Genes with a mean scaled TSS window count of less than 8 across all samples were excluded. Log2-transformed counts were then quantile-normalized using the normalize.quantiles function from the preprocessCore library in R (Bolstad, B. M., Irizarry R. A., Astrand, M, and Speed, T.

P. (2003) *A Comparison of Normalization Methods for High Density Oligonucleotide Array Data Based on Bias and Variance.* Bioinformatics 19(2) ,pp 185-193). Finally, quantile-normalized values were row-centered.

RT-qPCR reporters

Gravid adult worms were bleached to specifically obtain eggs which were incubated in M9 buffer overnight (12 to 16 hours) on a rotating wheel. After incubation, hatched worms will be synchronized in L1 arrest due to starvation. The synchronized L1 population was plated onto agar plates with food (*E. coli, OP50*) to initiate synchronous larval development. The concentration of worms per plate can vary between 1,000 and 4,000 worms per plate. In total, 2,000 – 8,000 worms were sampled each time point with fewer worms for the last time points.

Worms were collected hourly between 22 and 37 hours at 25 degree (for *gfp* reporter data) after plating synchronized L1. Worms were washed off the plate(s) and washed 3 times in M9 buffer. After washing, 1ml Tri Reagent (MRC) was added, frozen in liquid nitrogen and stored overnight at -80°C. Conventional RNA isolation using phenol chloroform extraction (adapted from (Bethke et al., 2009) was used to extract RNA which was then diluted to the same concentration for each sample and used as input for the Promega Protocol: "ImProm-II™ Reverse Transcription System" to convert RNA to cDNA. The resulting cDNA was diluted 1:1000 for testing actin transcript levels and 1:20 for endogenous transcripts. qPCR was then performed on the Step one Realtime PCR machine using primer pairs of which one was exon-exon spanning to detect mature mRNA levels.

RT-qPCR analysis:

Results

Actin Ct values were subtracted from the target Ct values to obtain a relative quantification, represented by delta Ct (dCt). To obtain the mean normalized mRNA levels, the dCt mean of the time series was subtracted from from each time point value first and then multiplied by -1. These values were then plotted to compare endogenous versus gfp mRNA levels. In the case of the minimal promoter Δ*pes-10* experiments, all dCt values were mean normalized according to the *daf-6* dCt mean value.

Luciferase assays

Embryos were obtained by bleaching gravid adults that express the xeSi296 transgene [*Peft-3::luc::gfp::unc-54 3'UTR, unc-119(+)*] II obtained by single-copy integration into the oxTi185 locus on chromosome II. Single embryos were placed into a well of a white, flat-bottom, 384-well plate (Berthold Technologies, 32505) by pipetting where they hatched in 90 uL liquid culture. For RNAi experiments, the feeding method was used. *E. coli* HT115 bacteria carrying empty plasmids (L4440, mock RNAi) or an RNAi plasmid with an insert targeting *blmp-1* (Fraser et al., 2000; Kamath and Ahringer, 2003) were induced with 1 mM IPTG for 1 hour at 37 degrees. For blmp-1 mutant luciferase assays, OP50 was used instead of HT115 bacteria. Bacteria were diluted in S-Basal medium (OD600 = 0.9), with 100 μM Firefly D-Luciferin, 100 μg/mL Ampicillin and 1 mM IPTG in the case of RNAi. For Auxin Inducible Degradation (AID) experiments, *E. coli* OP50 were diluted in S-Basal medium (OD_{600} = 0.9) and 100 μM Firefly D-Luciferin (p.j.k., 102111). 3-Indoleacetic acid (Auxin, Sigma-Aldrich, I2886) was dissolved in 100% ethanol and diluted 400 times in the culture medium obtaining concentrations as indicated. Vehicle control condition is 0.25% ethanol. Auxin or vehicle control was included in the culture medium at the start of the assay or was pipetted into single wells during the assay at time points indicated. Plates were covered with a Breathe Easier sealing membrane (Diversified Biotech,

BERM-2000). Luminescence was measured using a Luminometer (Berthold Technologies, Centro XS3 LB 960) for 0.5 seconds every 10 minutes for 72 hours at 20 degrees in a temperature controlled incubator.

Luminescence data was used for molt detection using an automated algorithm in MATLAB, including an option to manually annotate molts in a Graphical User Interface. In short, the hatch was detected by the first data point that exceeds the mean + 5*stdev of the raw luminescence of the first 20 time points and also exceeds the raw luminescence by 3. The molts were detected according to the method previously described (Olmedo et al., 2015) implemented in MATLAB.

Spearman's correlation coefficients were calculated using the function cor in R with default parameters. 95% confidence intervals were determined by bootstrapping using the function boot (R=10000) and boot.ci (basic bootstrap method) of the package boot in R.

Hoechst 33258 staining

Synchronized L1 worms by egg prep were plated and grown up to the L4 stage at 25 degree. Worms were then washed 3 times in 10ml of M9 buffer. After washing, Hoechst 33258 was added to 10ml to a final concentration of 1µg/ml and incubated for 15min on a rotating wheel. Incubation with Hoechst 33258 was then followed by 3 washes in M9 after which worms were concentrated in 1ml of M9 of which a few µl were mounted on a 2% (w/v) agarose slide with 3µl of Levamisole (10mM) before a z-stack (z-stack interval 0.7) was acquired using a LSM700 confocal microscope (Axio Imager Z2 (upright microscope) + LSM 700 scanning head, 40x/1.3 oil immersion objective, 6% laser power, 378ms exposure time, 512x300 pixels). The z-stack was mean projected and grey values were adjusted the same intensity range for all images (0-

8000) in Fiji. Staining was quantified manually by assigning worms as being stained if blue signal in the nuclei was obvious.

Western Blots

Worms were synchronized by egg prep and grown on NG2% plates at 25 degree (Fig 4B) or in liquid culture with OP50 (OD_{600}~3.5) at 20 degree with a concentration of 1worm/µl to the indicated developmental time points and 10,000 – 12,000 worms per time point were harvested by pipetting the required amount of liquid to a 15ml falcon tube (Fig 4C). The worm samples were washed three times before the worm pellet was snap frozen in liquid nitrogen. 2x volume lysis buffer was added to 1x volume of frozen pellet and incubated at 95°C for 5 minutes. Samples were placed back on ice for 1min and sonicated subsequently (Bioruptor, Diagnode, 13 cycles, 30sec on/off at 4°C). The sonicated samples were centrifuged at 12,000 rcf for 10min at 4°C and the supernatant transferred to a new Eppendorf tube. Protein concentration in the supernatant was determined by Nanodrop (Protein function A280). Samples were diluted to 5ug/ul final concentration with lysis buffer and stored at -20°C or used for Western Blotting. For Western Blotting, 1ul of Bromophenol blue was added before incubation at 95°C for 3 minutes. 25ul of 5ug/ul were loaded and the Western was run in MOPS buffer at 95V. The protein was transferred to a PVDF membrane for 1h at 20V, followed by blocking in 5% Skim Milk in TBS-T (0.05%) for 1 hour. For 3xflag::BLMP-1 and ACTIN detection, the membrane was cut and incubated in primary antibodies for 1 hour at room temperature respectively. After primary antibody incubation, the membrane was washed 3x 15min in TBS-T (0.05%). In case of actin, secondary antibody incubation for 45min - 1hour was performed and washed again 3x 15min in TBS-T (0.01%). Detection was performed using ECL reagents (RPN2232 and RPN2209, GE Healthcare) which was added to the membrane for 1min before the signal was detected using the

ImageQuant™ LAS 4000 (GE Healthcare). Antibodies and dilutions used: anti-FLAG-HRP (Sigma Aldrich A8592, 1:1,000), mouse anti-ACTIN clone 4 (EMD Millipore MAB1501, 1:5,000), anti-mouse IgG HRP linked (GE Healthcare NXA931, 1:7,500).

blmp-1(tm548) mutant time course

L1 by egg prep and overnight incubation in M9 were plated on food and grown at 25 degree. Samples were taken hourly from 1 hour until 24 hours of development and RNA isolation was performed using conventional RNA isolation with phenol chloroform extraction (adapted from Bethke et al. 2009). Sequencing libraries were prepared using the TruSeq Illumina mRNA-seq (stranded - high input) protocol followed by sequencing using the HiSeq 50 Cycle Single end reads protocol on HiSeq 2500.

Processing of RNA sequencing results

RNA-seq data were mapped to the ce10 genome of *C. elegans* using STAR with default parameters (version 2.7.0f) and reads were counted using htseq-count (version = 0.11.2). Counts were then scaled by the mapped library size for each sample. A pseudocount of 8 was added and counts were $\log_2$-transformed. Lowly expressed genes were excluded (maximum $\log_2$-transformed gene expression - ($\log_2$(gene width)-mean($\log_2$(gene width))) ≤ 6).

Analysis to identify genes with small phase differences

Fold changes (FC) between *blmp-1(tm548)* mutant and wild-type (N2) expression was calculated by subtracting the $\log_2$-transformed N2 expression from the *blmp-1(tm548)* mutant expression using numpy (version = 1.17.4), sorted by the previously annotated peak phases of the transcripts (Meeuse et al., 2019) and plotted in heatmaps using seaborn (version = 0.9.0) using the function sns.heatmap(FC, cmap = "RdBu_r", vmin=-8, vmax=8). To calculate instantaneous phases of

oscillations, the butterworth filtered signal (order = 1, low_freq_cut = 1/14, high_freq_cut = 1/4) was transformed by a Hilbert transform (as described in Meeuse et al., 2019). The butterworth filtered signal was used to calculate the R^2 between the filtered signal and the original gene expression for each gene (

$R^2 = 1 - \frac{sum(residuals^2)}{sum(gene\ expression - mean(gene\ expression)^2)}$). Genes which were not well fitted with the butterworth filter ($R^2 < 0.4$) were not used for downstream analysis. To obtain the phase differences between *blmp-1(tm548)* and wild-type expression we subtracted the instantaneous phases of wild-type from *blmp-1(tm548)*. Due to the circular nature of the phase, we had to correct for transiently occurring big differences in the phase by subtracting 2pi from the phase difference. To identify genes that did not change tremendously in their progression between wild-type and *blmp-1(tm548)* mutants, we selected genes that showed a phase difference of < |1| (rad) at two distinct time points (time point 16 and time point 19). As a control and to select genes showing an extreme phase difference we selected genes with a large phase difference of < -1.8 (rad).

Single worm imaging

Sample preparation and analysis were performed as described in Meeuse et al., 2019.

GFP::AID imaging

Worm handling and microscopy:

Worms were synchronized by egg prep and hatching into M9 (42 mM Na2HPO4, 22 mM KH2PO4, 86 mM NaCl, 1 mM MgSO4) and cultured on Escherichia coli OP50 containing 2% NGM plates with red fluorescent beads in order to monitor feeding behavior of the worms. After 23 hours of development, feeding was monitored carefully to observe the time of the molt. One

hour after feeding stopped, worms were considered to be in the molt and were transferred onto 1mM containing auxin 2% NGM and normal 2% NGM plates and GFP intensities were monitored using the Zeiss Z1 microscope. Imaging slides were prepared a glass slide with agarose and immobilized worms by levamisole and covered with a cover glass. A z-stack was taken using a step size of 2µm and 300ms exposure time for GFP. The same procedure was repeated 4 hours after the first imaging set to obtain images of worms for which auxin was added during the intermolt.

Image analysis was performed on the z-stack after segmentation of the worm. The mean intensity of the worm was calculated and used for plotting using a customized KNIME workflow.

Model fitting and half-life calculation:

An exponential decay described by $f(x) = ae^{xk} + b$ was assumed for the degradation dynamics of AID::GFP. Thus we used Python's scipy integration of curve fitting (Virtanen et al., 2020), using "*from scipy.optimize import curve_fit*" and then fitted the curve using "*curve_fit(exponential, x_array, y_array, p0=[1400,-0.15, 1400])*", where exponential is the exponential function assumed, x_array the experimental x-values (time after auxin treatment) and y_array the observed AID::GFP intensities. p0 denotes the initial values for a, k and b. The half-life was calculated using $t_{1/2} = \frac{\ln(2)}{-k}$.

Transgenic CRISPR strains *aid::blmp-1*

Endogenous tagging of *blmp-1* with the auxin inducible degron (aid) was performed by CRISPR/Cas9 using the previously established *dpy-10(cn64)* co-conversion (Arribere et al., 2014) . The sgRNA sequence: 5' gccgaagagaacggtgccgg 3' was cloned into Not1-digested pIK198 (Katic et al., 2015) by Gibson assembly using the hybridized sequence from

5' AATTGCAAATCTAAATGTTTgccgaagagaacggtgccggGTTTAAGAGCTATGCTGGAA **3'**

and

5' TTCCAGCATAGCTCTTAAACccggcaccgttctcttcggcAAACATTTAGATTTGCAATT **3'**. The aid sequence was synthesized by IDT (Integrated DNA Technologies) as a gBlocks® Gene Fragments and contained 65 bp homology to blmp-1 locus, 30 bp downstream of the ATG startcodon.

5'ttcgatctcattttaaacaaaacctgtaaaaaatgGGTCAAGGAAGTGGGGATGACGGTGTTCCGatgcctaa agatccagccaaacctccggccaaggcacaagttgtgggatggccaccggtgagatcataccggaagaacgtgatggtttcctgccaaaa atcaagcggtggcccggaggcggcggcgttcgtgaagCCGGCACCGTTCTCTTCGGCTGCTGCGGCAGCT CACTCACCACCTCATTCTCCCCTTTCTGTCGG **3'**.

The injection was performed in wild-type animals which were injected with 10 ng/µL gBlock, 100 ng/µL sgRNA plasmid, 20 ng/µL AF-ZF-827 (Arribere et al., 2014), 50 ng/µL pIK155 (Katic et al., 2015) and 100 ng/µL pIK208 (Katic et al., 2015).

Transgenic CRISPR strain *3xflag::blmp-1*

N-terminal tagging endogenous *blmp-1* with 3xFLAG was performed using the same *dpy-10(cn64)* co-conversion CRISPR/Cas9 strategy as used for the *blmp-1::aid* strain (see above, Arribere et al. 2014). The sgRNA with the sequence

5' aaaaatgggtcaaggaagtg **3'**

was used to cleave genomic DNA followed by rescue with the 4nmole Ultramer oligo sequence from IDT

5'cttctcttttccttcgatctcattttaaacaaaacctgtaaaaaatgGATTATAAAGACGATGACGATAAGCGTGACTACA AGGACGACGACGACAAGCGTGATTACAAGGATGACGATGACAAGAGAGGAGCCGGATCTggt caaggttcaggggatgacggtgttccgccggcaccgttctcttcggctgctgcggc **3'**

Where yellow capital letters indicate the 3xFLAG with a spacer sequence in blue. The overlap to the genomic locus is indicated in small letters, comprising 47bp and 59bp overhang.

The injection was performed in wild-type animals which were injected with 20 ng/µL gBlock, 100 ng/µL sgRNA plasmid, 20 ng/µL AF-ZF-827(Arribere et al., 2014) , 50 ng/µL pIK155 (Katic et al., 2015) and 100 ng/µL pIK208 (Katic et al., 2015).

Transgenic reporter strain generation

Results

GFP reporters were cloned by Gibson (Gibson et al., 2009) with amplified the promoters from genomic DNA using the primers listed below which were inserted into Nhe1-digested pYPH0.14 as previously described Meeuse et al., 2019. Transgenic animals were obtained by single copy-integration of the transgene into the ttTi5605 locus (MosSCI site) on chromosome II into EG6699 animals, with the published MosSCI protocol (Frøkjær-Jensen et al., 2012).

Worm strains:

HW1360: EG6699, xeSi131[F58H1.2p::GFP::H2B::Pest::unc-54 3', unc-119+] II

HW1361: EG6699, xeSi132[R12E2.7p::GFP::H2B::Pest::unc-54 3', unc-119+] II

HW1370: EG6699; xeSi136[F11E6.3p::GFP-H2B-Pest::unc-54 3'UTR; unc-119 +] II

HW1371: EG6699; xeSi137[F33D4.6p::GFP-H2B-Pest::unc-54 3'UTR; unc-119 +] II

HW1372: EG6699; xeSi138[C05C10.3p::GFP-H2B-Pest::unc-54 3'UTR; unc-119 +] II

HW1431: EG6699, xeSi160[daf-6Δ4p::GFP::H2B::Pest::unc-54 3'UTR; unc-119 +] II

HW1435: EG6699, xeSi164[daf-6Δconsp::GFP::H2B::Pest::unc-54 3'UTR; unc-119 +] II

HW1436: EG6699, xeSi165[daf-6 1xcons:: Δpes-10p::GFP::H2B::Pest::unc-54 3'UTR; unc-119 +] II

HW1437: EG6699, xeSi166[Δpes-10p::GFP::H2B::Pest::unc-54 3'UTR;unc-119 +] II

HW1939: EG8079, xeSi296[eft-3p::luc::gfp::unc-54 3'UTR] II

HW2521: EG6699,xeSi131[F58H1.2p::GFP::H2B::Pest::unc-54 3', unc-119+] II ;blmp-1 (tm548) (I)

HW2526: EG6699, xeSi440[dpy-9p::GFP::H2B::Pest::unc-54 3'UTR; unc-119 +] II

Results

HW2523: EG6699, xeSi437[qua-1p::GFP::H2B::Pest::unc-54 3’UTR; unc-119 +] II

HW2529: unc-119(ed3) III; ieSi59 [eft-3p::aid::GFP::unc-54 3'UTR + Cbr-unc-119(+)] III ; ieSi57 [eft-3p::TIR1::mRuby::unc-54 3’UTR, cb-unc-119(+)] II

HW2532: EG8079, xeSi296[eft-3p::Luciferase::gfp::unc-54 3’UTR; unc-119 +] II ; blmp-1(tm548) (I)

HW2639: blmp-1 (xe180[3xFlag::blmp-1]) I

HW2120: xe80 blmp-1(blmp-1::aid) I; EG8079, xeSi296 [eft-3p::luc::gfp::unc-54 3'UTR, unc-119(+)] II; EG8080, xeSi376 [eft-3p::TIR1::mRuby::unc-54 3’UTR, cb-unc-119(+)] III

HW2033: *bus-8 (e2885)* X

HW2802: blmp-1 (xe180[3xFlag::blmp-1]) I ; xeSi296[eft-3p::Luciferase::gfp::unc-54 3’UTR; unc-119 +] II

HW3028: EG6699,xeSi517[F16B4.4p::GFP::H2B::Pest::unc-54 3', unc-119+] II

Supplementary Figures

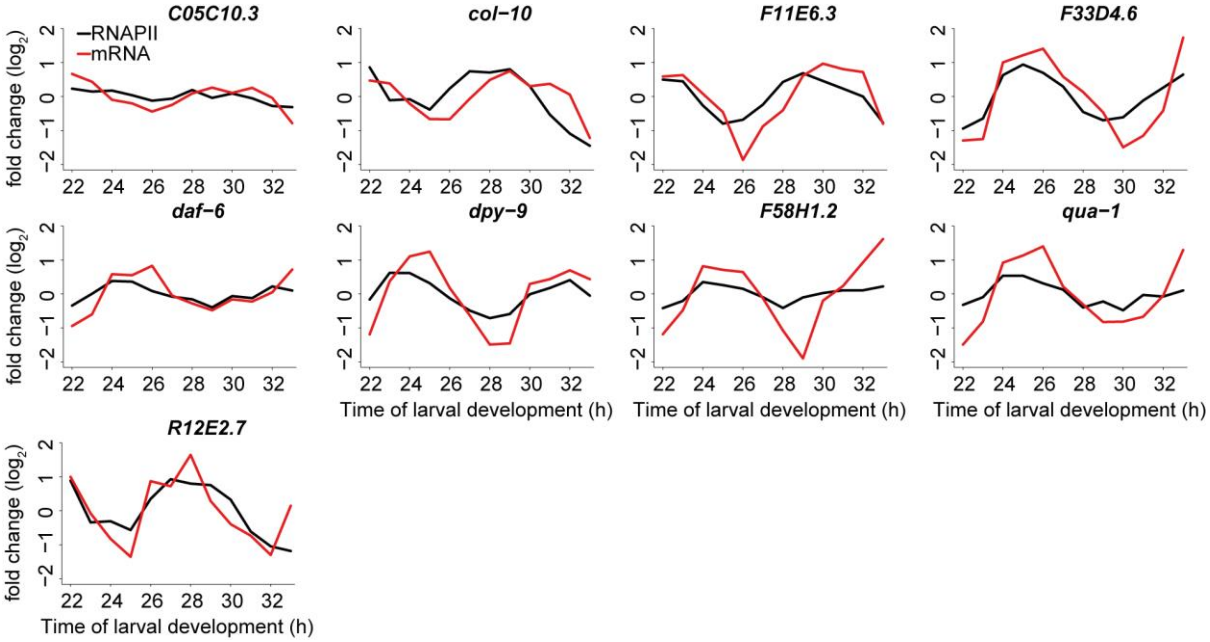

Fig S1: Most genes used for reporters show oscillations on RNAPII ChIPseq and transcript level

With the exception of *C05C10.3* and *F58H1.2*, we can observe oscillatory RNAPII ChIPseq oscillations, mostly preceding the mRNA transcript oscillation.

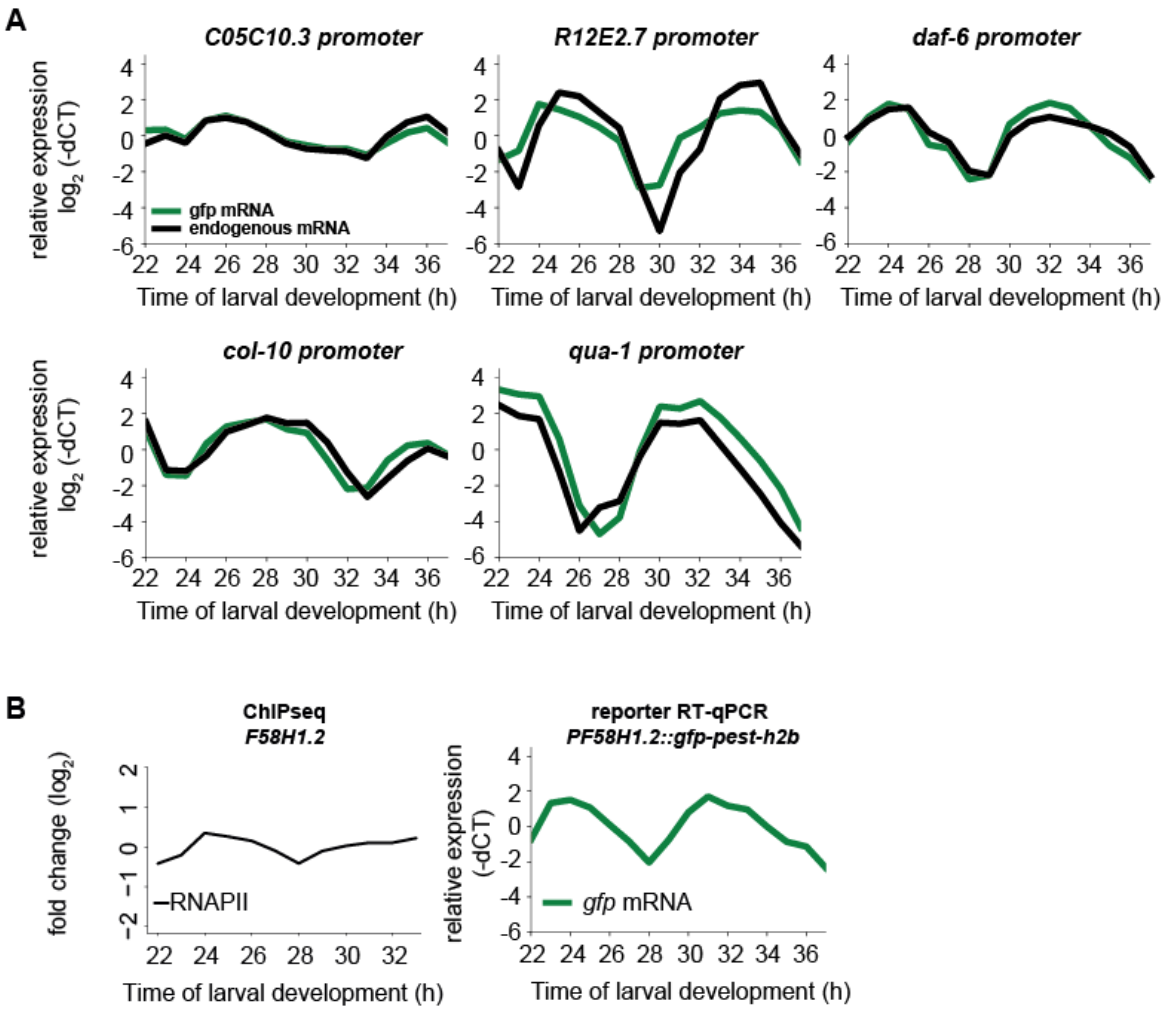

Fig S2: Additional transcriptional reporters investigated by RT-qPCR time courses

A, Five additional transcriptional reporters were tested by RT-qPCR time courses. All except the reporter for *R12E2.7* recapitulated the amplitude and the peak phase. In the *R12E2.7* case, we assume that we did not capture the entire promoter sequence or we that miss a distant regulatory element.

B, Comparison of ChIP-seq reads (left) and RT-qPCR reporter gfp levels of *F58H1.2*. We detect a big amplitude in the RT-qPCR experiment even though the amplitude is low in the ChIP-seq experiment.

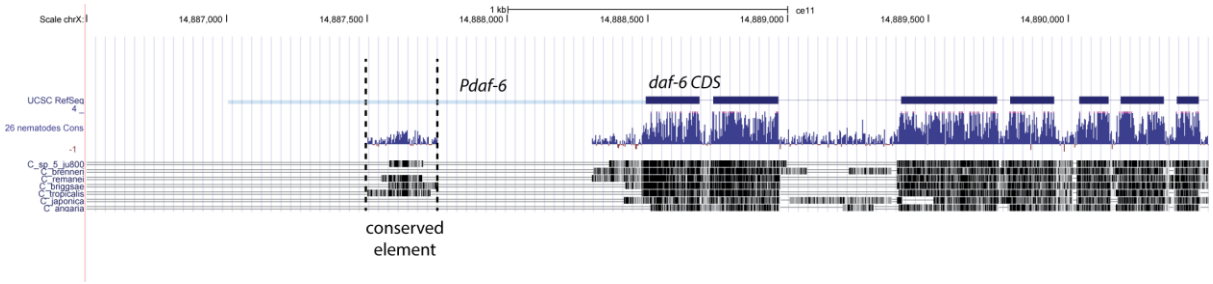

Fig S3: The *daf-6* promoter contains a short conserved promoter element

Visual representation of the chosen *daf-6* promoter with the conserved element indicated.

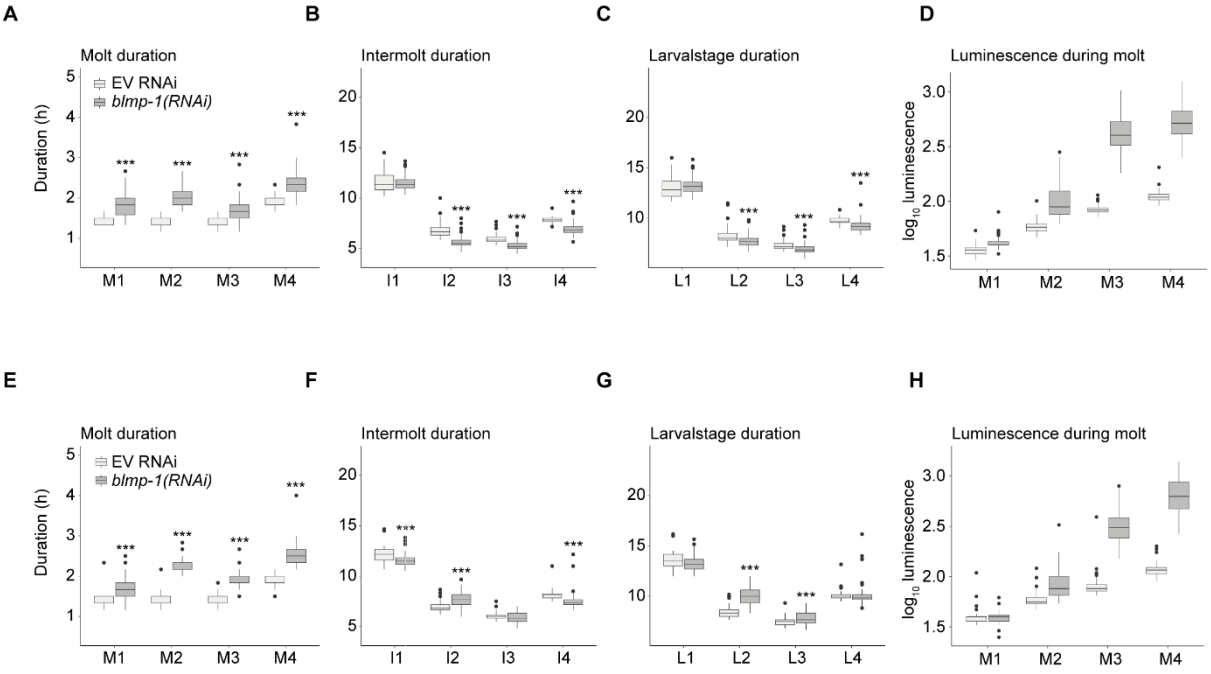

Fig S4: Replicates of developmental phenotypes arising from *blmp-1* knockdown.

Boxplots of the quantification of single animal larval stage, intermolt and molt durations in mock and *blmp-1* RNAi. Both replicates confirm the longer molts (A, D), that are accompanied by shorter intermolts (B), or similar intermolt lengths (E), leading to similar (C) or slightly longer (F) larval stage durations in *blmp-1* RNAi compared to mock RNAi. Significantly different durations are indicated (* P<0.05, ** P<0.01, *** P<0.001, Welch two-sample and two-sided t-test)

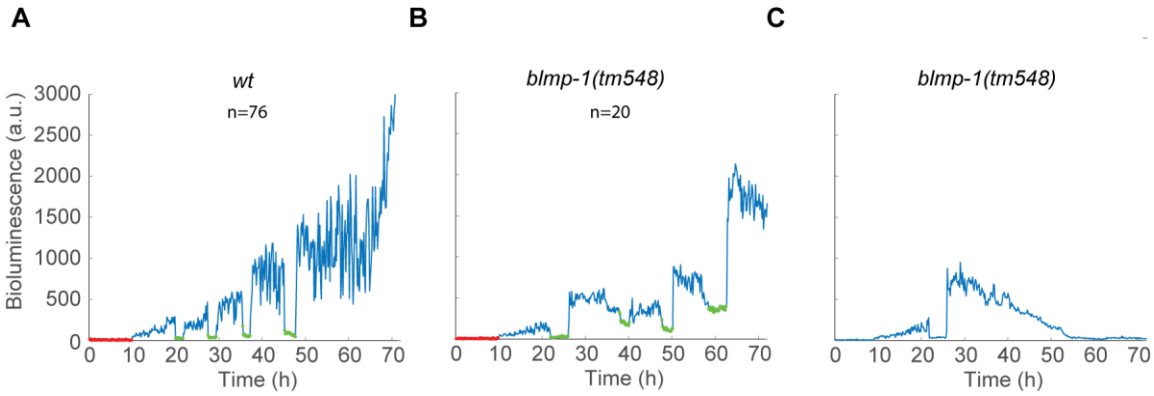

Figure S5: Luciferase assay example traces of wild-type and *blmp-1(tm548)* worms

A – C, Representative luminescence traces from a wild-type (A) and surviving *blmp-1(tm548)* mutant (B). Many *blmp-1(tm548)* mutants die after exiting molts which is represented by a gradual decrease of luminescence after the exit from the first molt (C).

Results

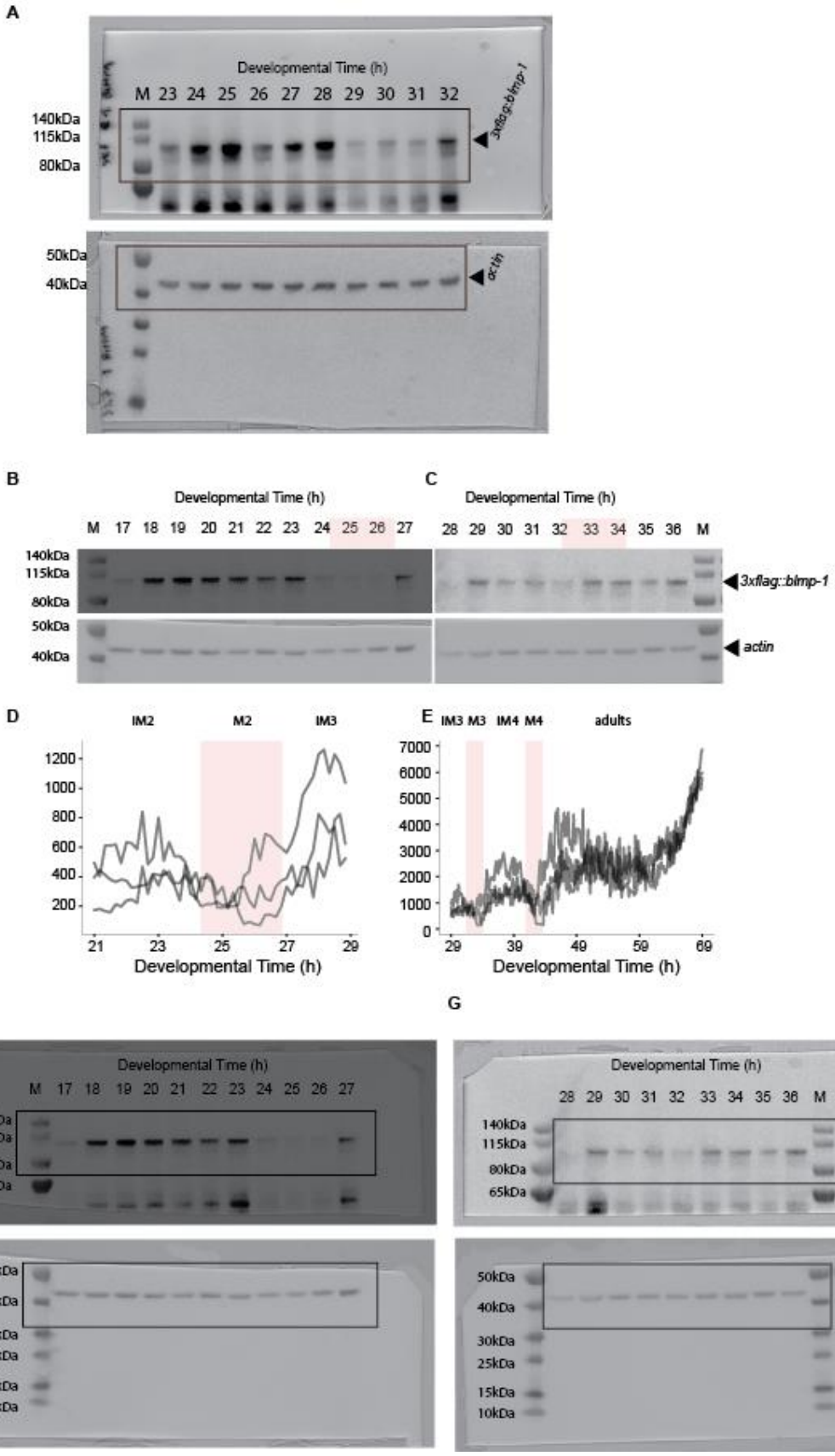
A
Developmental Time (h)
M 23 24 25 26 27 28 29 30 31 32
140kDa
115kDa
80kDa
3xflag::blmp-1
50kDa
40kDa
actin
B
Developmental Time (h)
M 17 18 19 20 21 22 23 24 25 26 27
140kDa
115kDa
80kDa
50kDa
40kDa
C
Developmental Time (h)
28 29 30 31 32 33 34 35 36 M
3xflag::blmp-1
actin
D
IM2
M2
IM3
1200
1000
800
600
400
200
21 23 25 27 29
Developmental Time (h)
E
IM3 M3 IM4 M4
adults
7000
6000
5000
4000
3000
2000
1000
0
29 39 49 59 69
Developmental Time (h)
F
Developmental Time (h)
M 17 18 19 20 21 22 23 24 25 26 27
140kDa
115kDa
80kDa
65kDa
50kDa
40kDa
30kDa
25kDa
15kDa
10kDa
G
Developmental Time (h)
28 29 30 31 32 33 34 35 36 M
140kDa
115kDa
80kDa
65kDa
3xflag::blmp-1
50kDa
40kDa
30kDa
25kDa
15kDa
10kDa
actin

Fig S6: Western Blot of *3xflag::blmp-1* worms (HW2639 and HW2802)

A, Uncropped Western Blot images of 3xFLAG::BLMP-1 protein in HW2639 worms grown on NG2% plates at 25°C.

B, C, 3xFLAG::BLMP-1 protein detected by Western Blot in HW2802 worms grown in liquid culture at 20°C. Protein abundance from early L2 to early L3 stage (B) and early L3 to late L4 stage (C) originating from the same time course. The molts, as determined by luciferase assays (D, E), are indicated in salmon.

D, E, Luminescence intensities over time of multiple HW2802 worms (n<10 for each of the 3 wells on the plate), starting from 21 hours (D) or 29 hours (E) of development. The drop in signal from 25 to 26 hours (D) and 32 to 34 hours (E) is indicative for the molt. The molt assignment in this case was performed on multiple worms cultured in one well mainly to speed up handling time. However, thus the molt assignment is less accurate than in Fig S5 resulting from slight developmental asynchrony present in the population.

F, G, Uncropped images of Western Blots shown in B and C.

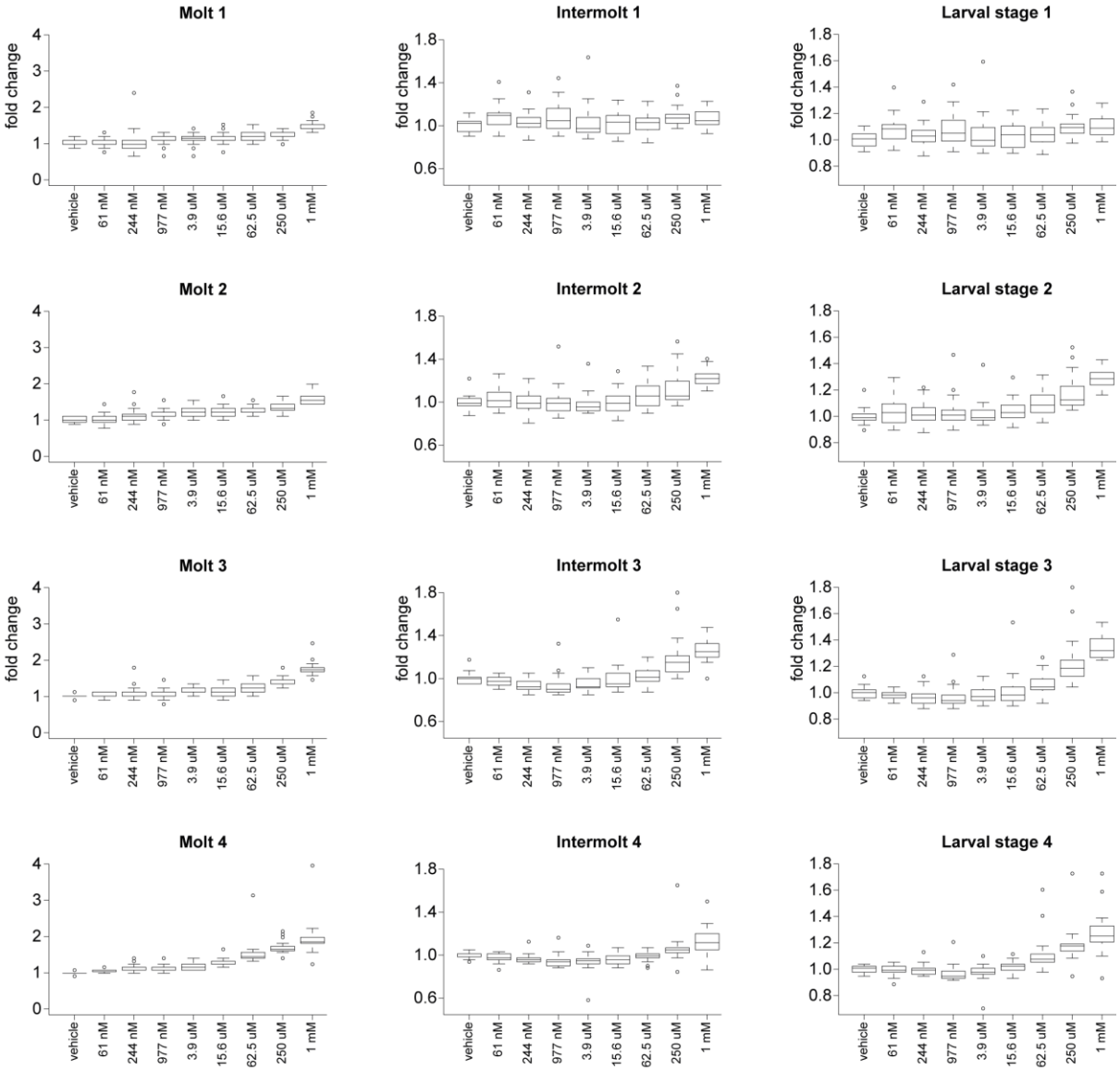

Fig S7: After intermolt 1, both molts and intermolts show an auxin dependent increase in duration compared to vehicle.

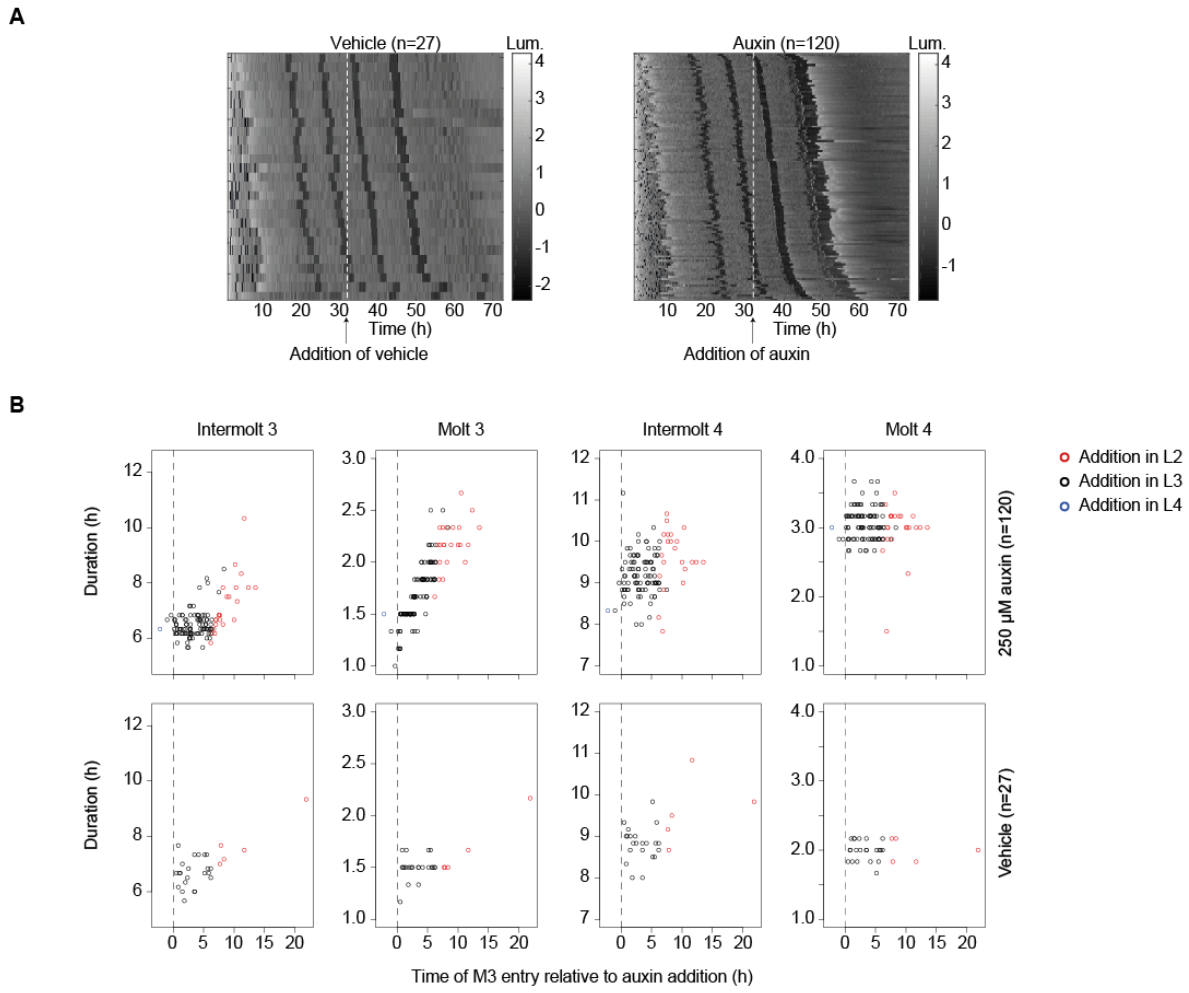

Fig S8: Molt lengthening is dependent on the onset of BLMP-1 degradation in L3

Same experimental set-up as in Fig 4 with the exception that auxin was added in L3 at 32 hours.

A,B, Heatmaps showing trend-corrected luminescence (Lum.) traces; one animal per horizontal line. Vehicle (0.25% ethanol; left) or 250 µM auxin (right) were added at t=32h. t=0 h corresponds to the start of the assay. Embryos hatch at different time points and traces are sorted by entry into second molt. Dark grey indicates low luminescence and corresponds to the molts.

B, Duration of intermolt 3, molt 3, intermolt 4 and molt 4 plotted over time of molt 3 relative to auxin treatment in control and auxin treated animals shown in A. Worms experiencing auxin earlier than desired (addition in L2) are labelled in red. One worm experienced auxin later than desired (addition in L4) which is labelled in blue.

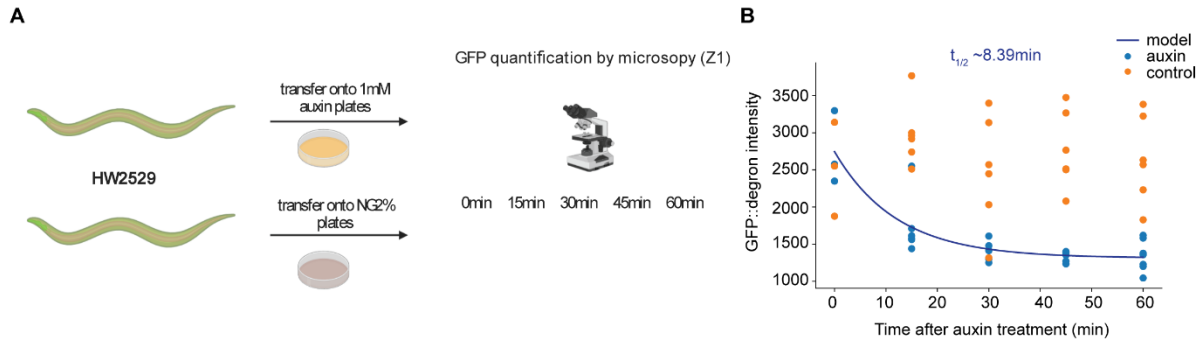

Fig S9: GFP::aid is degraded rapidly upon auxin treatment

A, Experimental design: ubiquitous *aid::gfp* expressing worms were placed on either auxin-containing plates or normal NG2% plates, followed by AID::GFP quantification at 15 minute intervals (image created with BioRender.com).

B, AID::GFP quantification in the whole worm over time for both conditions, auxin and normal NG2% plates.

To characterize the auxin inducible degradation system and to confirm the reported fast half-life of targeted proteins, we crossed the worm strain CA1205 with CA1200 (Zhang et al., 2015) to obtain HW2529 which expresses both *aid::gfp* and *tir-1* from the strong, ubiquitous and constitutive *eft-3* promoter. Culturing HW2529 worms on 1mM auxin-containing plates should result in degradation of AID::GFP which we indeed observed by microscopy. However, we opted for a more quantitative analysis of the AID::GFP degradation and decided to quantify AID::GFP fluorescence over time immediately after L3 worms were transferred to auxin containing plates. We observed a rapid reduction in fluorescence upon culturing the worms in presence of auxin (Fig S9 B). The rapid AID::GFP degradation did not depend on whether auxin was provided during the molt or during the intermolt as we observed similarly low levels after 15 minutes onwards for in either situation. Thus the data was combined. Our negative control, worms grown on normal NG2% plates, did not show any reduction of AID::GFP over time, confirming that the effect is specifically due to auxin. To calculate the half-life of AID::GFP in the presence of auxin we fitted an exponential decay to the experimentally observed data and could confirm that the observed apparent half-life at 8.39 minutes is indeed short upon treatment with auxin.

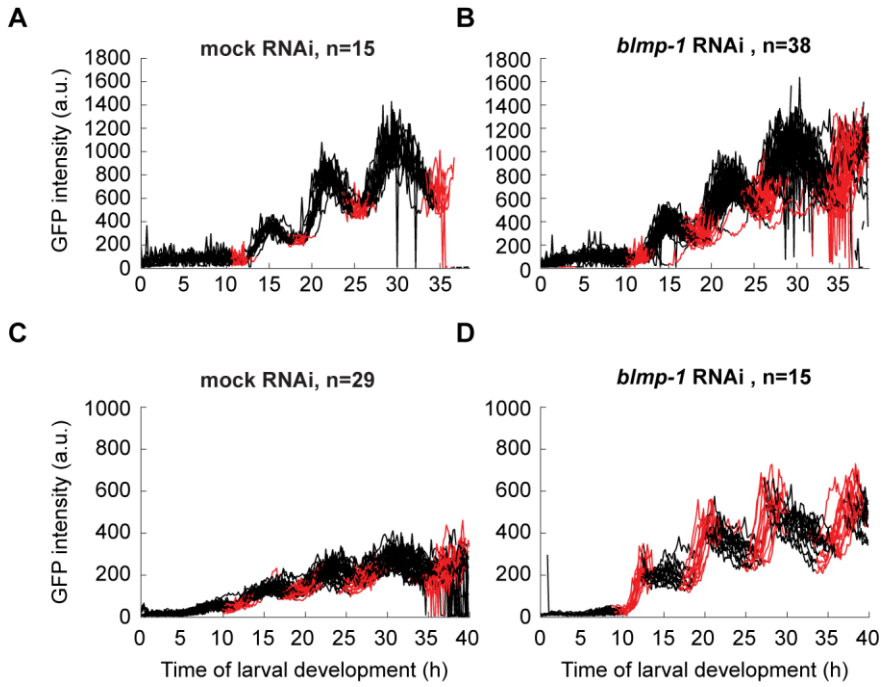

Fig S10: Unscaled single worm imaging GFP traces

Unscaled GFP intensities over larval development. Molting times are indicated in red.

A, B, Unscaled single worm imaging GFP traces of the transcriptional reporter *F11E6.3* in mock RNAi (A) and *blmp-1* RNAi (B) conditions. The GFP intensity peak occurs during intermolt for both RNAi conditions.

C, D, The unscaled single worm imaging GFP traces of the transcriptional reporter for *F16B4.4* show a striking difference in peak times between mock and *blmp-1* RNAi. In mock RNAi (C) the peak occurs during the intermolt, while in *blmp-1* RNAi (D), the peak happens precociously in the molt.

End of manuscript "The BLMP-1 transcription factor supports coupling of oscillatory gene expression with development"

2.5 5’ UTR exchange in the *F11E6.3* reporter modifies oscillatory gene expression

Yannick Hauser performed the time courses and all data analysis. Helge Großhans and Yannick Hauser conceived the experiment.

As shown in section 2.4 (*blmp-1* manuscript), the promoters of oscillating genes driving *gfp* generated mRNA oscillations that recapitulated the peak phase and amplitude of the endogenous transcripts. Promoters in *C. elegans* usually contain the 5’ UTR sequence because assigning the transcriptional start site is difficult in *C. elegans* due trans-splicing of the transcript to a splice leader sequence (see section 1.7.1). Consequently, our transcriptional reporters contained the annotated 5’ UTR in the promoter sequence which motivated us to investigate potential regulatory aspects arising from the 5’ UTR sequence. We focused on the transcriptional reporter of *F11E6.3* as a test case and replaced its 5’ UTR with the *actin-1 (act-1)* 5 ‘UTR, generating a chimeric promoter sequence. Even though expression was still observed in the expected tissues hypodermis, Pnp cells, vulva, head and tail cells (not shown), the chimeric promoter did not perfectly recapitulate the endogenous mRNA dynamics anymore. Instead, it showed a precocious peak phase compared to the endogenous transcript oscillation in two independent replicate experiments (Fig 2.4A(II) & (III)). Furthermore, the amplitude appears slightly increased in the *gfp* transcript oscillation and the mean expression *gfp* expression was consistently lower for the *act-1* 5’UTR compared to the normal 5’ UTR (Fig 2.4B). In order to quantify the peak phase shift, we fitted a cosine on both, endogenous and *gfp* transcript oscillations and calculated the phase difference between detected peaks. Confirming the visual impression, the calculated phase difference revealed that the *gfp* transcript peaks roughly 30° before the endogenous transcript in the case of the replaced 5’ UTR (Fig 2.4C).

The results obtained by exchanging the the 5’ UTR sequence of the *F11E6.3* promoter validate and further strengthen the importance of the promoter sequence in generating oscillatory gene expression. As our promoters contain the annotated 5’UTR sequences our results indicate that they need to be considered in transcriptional reporter designs. Furthermore, we could demonstrate that, at least in this instance, the untranslated regulatory regions in the 5’ UTR of transcriptional reporter constructs have the capacity to modify oscillatory gene expression. The observed phase shift was reproducibly obtained and thus we hypothesize two plausible scenarios that could explain the observed phase shift. First the 5’ UTR might indeed encode a regulatory sequence to specify the

peak phase of the resulting mRNA. Second, the transcribed mRNA with the *actin* 5' UTR could be affected in stability, thus degrading faster, which would lead to an expected phase shift depending on the extent of destabilization. Additionally correlating with increasing degradation rates, we would predict lower mean expression values. Consistent with the present data and supported by the peak shift together with higher amplitudes and lower expression levels, we speculate that indeed the mRNA with the exchanged 5' UTR is less stable.

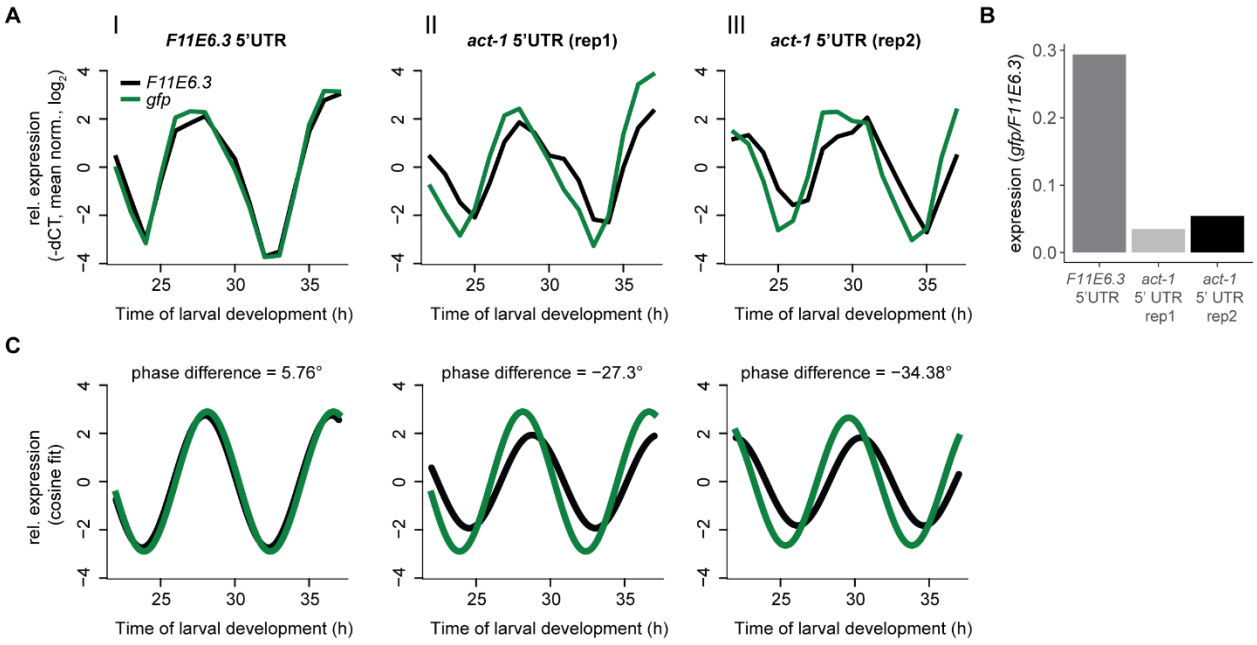

Fig 2.4: Exchanging the 5' UTR of the *F11E6.3* promoter leads to a peak phase shift

A, RT-qPCR time courses from reporter strains driving *gfp* from the endogenous *F11E6.3* promoter (I) or an *F11E6.3* promoter where the 5' UTR sequence was replaced by that of *act-1* (II & III).
B, Barplot representing the percentage of mean *gfp* expression relative to the endogenous *F11E6.3* mean expression.
C, Cosine fits for *F11E6.3* and *gfp* RT-qPCR data from A to calculate their phase difference. In both cases, the *gfp* transcript shows precocious peaks and troughs compared to *F11E6.3*, resulting in a negative phase difference.

2.6 Reduced BLMP-1 levels lead to de-synchronization of a small group of genes

Yannick Hauser and Milou Meeuse performed the time course and RNA isolation. Stéphane Thiry performed library preps and sequencing. Count normalization was performed by Dimos Gaidatzis. Yannick Hauser analyzed the count data. Helge Großhans, Yannick Hauser and Milou Meeuse conceived the experiment.

To reveal the immediate global changes on oscillatory gene expression resulting from BLMP-1 downregulation, we depleted BLMP-1 protein in a temporally controlled manner and subsequently sampled worms for RNA sequencing. To achieve fast degradation of BLMP-1, we again used the auxin-induced degron (aid) tagged BLMP-1 (Zhang et al., 2015) in liquid culture to be comparable with our luciferase assay results (see section 2.4, *blmp-1* manuscript). Due to the fact that we see phenotypes resembling *blmp-1* RNAi in low auxin concentration or *blmp-1* mutants in high auxin concentration, we decided to test both low and high auxin conditions. We cultured a synchronous population for 20 hours, split the culture and added auxin to a final concentration of 3.9µM and 250µM or the vehicle ethanol as control. After auxin treatment, we sampled all conditions every 30min and performed RNA sequencing (see methods). Following up on the observation of a desynchronized oscillator behavior in the *blmp-1(tm548)* mutant time course (see section 2.4, *blmp-1* manuscript), we were specifically interested in oscillating genes that were affected in their phase progression upon BLMP-1 downregulation. As we will see, the effects resulting from auxin treatment were mild even in the 250µM auxin concentration, thus I will focus only on the condition with 250µM auxin. Overall, oscillating genes mainly maintained their oscillation in the AID::BLMP-1 depleted samples (Fig 2.5A, B), suggesting that only subtle changes occurred. To obtain a detailed quantification of oscillatory behavior of transcripts we used a butterworth filtering (Stephen Butterworth, 1930) to reduce high-frequency noise followed by a Hilbert transform (Gabor, 1946), which enabled us to investigate instantaneous phase progression over time and per transcript. In order to reduce false-positive hits in our analysis, we selected only transcript oscillations that were reliably fitted by the butterworth filtering by selecting gene with $R^2 > 0.6$ which was calculated from the residuals between the butterworth filtered signal and the original signal (Fig 2.5C, Fig S2). To identify genes responding to reduced AID::BLMP-1 levels, we plotted the phase difference between auxin and vehicle for the time points 35.5 hours and 40.5 hours of larval development (Fig 2.5D). A general trend was observed as most genes in the auxin treatment were shifted towards earlier time points, resulting in a positive phase difference.

However, when we inspected individual examples of genes, we observed only marginal differences between vehicle- and auxin-treated animals (Fig 2.5E, G). Many genes showed a general phase shift which is represented by two example genes *daf-6* and *F11E6.3*.

We proceeded the analysis by focusing only on the strongest effects as exemplified in Fig 2.5F, H and identified 15 strongly shifted genes. The identified group of genes contained the *F16B4.4* (Fig 2.5F), a gene that was identified as desynchronized in section 2.4 (*blmp-1* manuscript) in both the *blmp-1(tm548)* mutant mRNA sequencing time course and the single worm imaging (see section 2.4, *blmp-1* manuscript). The strong phase shift of *F16B4.4* and *grsp-2* could also be reproduced in an independent separate time course, this time using RT-qPCR (Fig S3). Interestingly the identified group of genes (n=15) showed a strong phase preference during and right after the molt (Fig 2.5J) which allowed plotting the characteristic changes of the group as shown in Fig 2.5I. The identified strong changing genes peaked almost antiphase of the *blmp-1* mRNA peak phase (Fig 2.5J) which is similar to the effects we see with the *blmp-1(tm548)* mutant (*blmp-1* manuscript). While we could not observe a strong global effect on oscillatory gene expression following downregulation of AID::BLMP-1 we nevertheless identified a small group of genes that showed a dramatic phase shift in their peak expression.

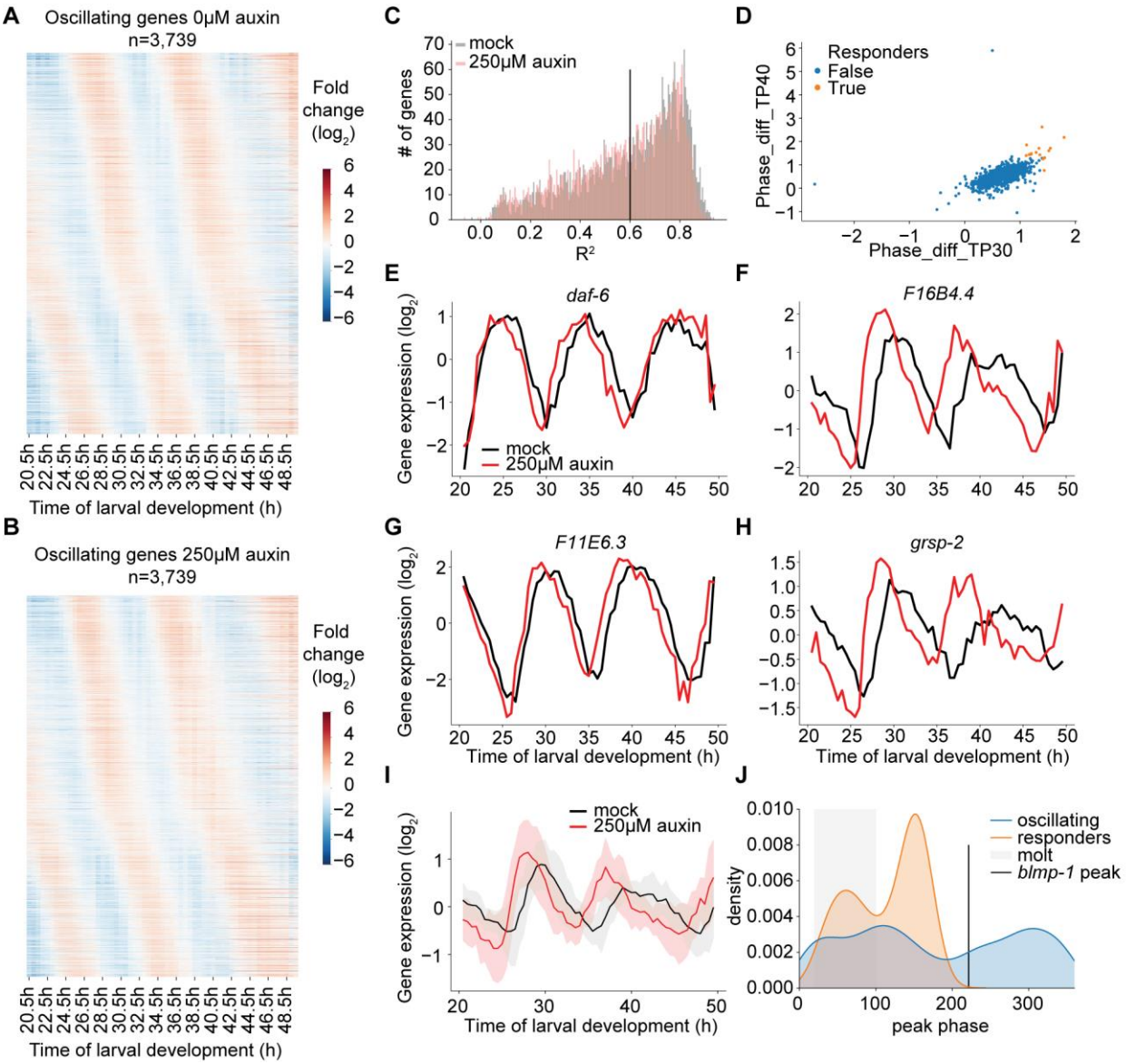

Fig 2.5: Conditional depletion of AID::BLMP-1 leads to strong precocious expression of few genes

A, B, Heatmaps of log_2-transformed, mean normalized gene expression of oscillating genes in the *aid::blmp-1* time course with vehicle (A) or 250µM auxin treatment (B).

C, Genes were filtered for genes with an $R^2 > 0.6$ (solid black line) which was calculated from butterworth filtered oscillating traces.

D, 2D scatterplot showing the phase difference at two time points between auxin and vehicle treatment for each oscillating gene that passed the threshold in C. Genes with a high phase difference of >1.4 rad at both time points were selected as strong responders to AID::BLMP-1 degradation by 250µM auxin.

E, G, Gene expression of two example genes characterized by the general small phase difference between vehicle and auxin treated samples.

F, H, Gene expression of two responding genes as selected in D.

I, Summarized mean gene expression of strong responders from D. The standard deviation is depicted in the transparent area (n=15).

J, Density plot showing the peak phase distribution of strong responding genes upon auxin treatment (orange, n=15) in comparison with the peak phase distribution of all oscillating genes passing the threshold (blue, n=1,826). The time of the molt is indicated in grey and the peak phase of *blmp-1* is shown as a solid black line. Peak phases were used from Meeuse et al., 2019.

2.7 *daf-6* promoter-driven GFP oscillations are damped in reduced BLMP-1 conditions

Yannick Hauser performed the imaging and analyzed all data. Helge Großhans and Yannick Hauser conceived the experiment.

We further investigated the transcriptional reporters that we initially created (section 2.4, *blmp-1* manuscript) by looking at BLMP-1 ChIPseq peaks from publicly available data. This revealed a potential BLMP-1 binding to the *daf-6* promoter in the proximity of the conserved element (Fig S4). To obtain an estimate on the extent of AID::BLMP-1 downregulation using the auxin-inducible degradation system, we tested the effects of downregulation of AID::BLMP-1 on the *daf-6* transcriptional reporter. Using a similar experimental strategy as in the *aid::blmp-1* sequencing experiment, confocal microscopy was performed on either *blmp-1* wild-type (wt) or *aid::blmp-1* worms, both carrying the transgenes *Peft-3::tir-1::unc-54* 3' UTR and *Pdaf-6::gfp-pest-h2b::unc-54* 3' UTR. Both strains were cultured in liquid at 20°C with 250µM auxin supplied after 20 hours of development to mimic the experimental set up as in the *aid::blmp-1* RNA sequencing time course. GFP intensities were measured specifically in hyp7 and seam cells by microscopy from 40 hours onwards when worms were in L4. As seen for the *daf-6* reporter in the vehicle treated strain Fig 2.6A, the GFP intensities oscillate in hyp7 and seam cells. Under the same conditions, a lower GFP amplitude is observed in the *aid::blmp-1* strain, i.e., upon AID::BLMP-1 degradation (Fig 2.6B). In order to quantitatively address differences of the measured GFP intensities between vehicle and auxin treatment, we performed cosine fitting on the mean summarized data. While this analysis has to be interpreted cautiously due to the non-isochronically spaced L4 substages and given our limited time resolution, we observed no obvious effect on the peak phase (Fig 2.6C) but a reduction in amplitude in the auxin condition (Fig 2.6D). Differences in the peak phase that are smaller than the assay's time resolution of roughly 1 hour are still possible though. In general, this result suggests that downregulation of AID::BLMP-1

affects the GFP oscillation driven by the *daf-6* promoter in the epidermis. This is, however, in contrast to what we have previously observed in RNA sequencing data where *daf-6* transcript oscillations showed only a minor effect.

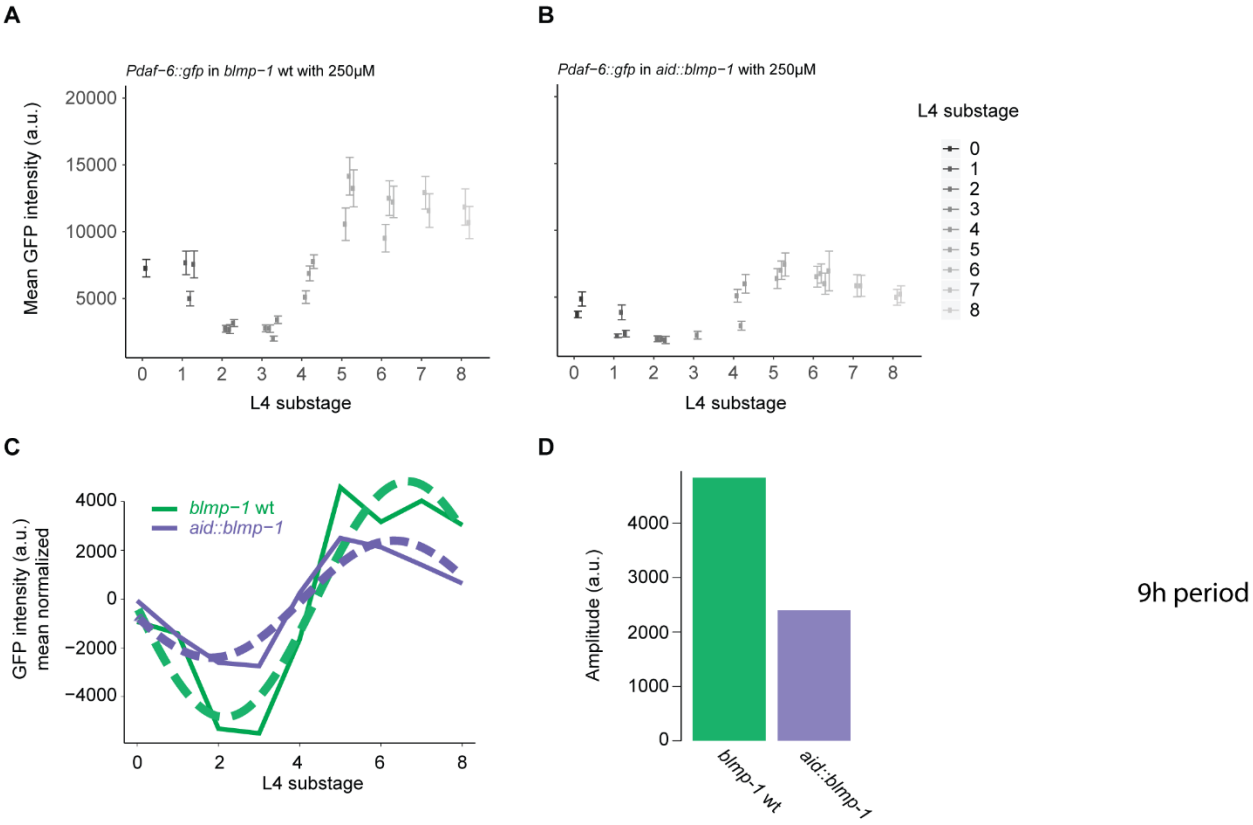

Figure 2.6: Downregulation of AID::BLMP-1 by the auxin-degradation system leads to damped GFP oscillations in the *Pdaf-6::gfp* strain.

A, GFP intensities in hypodermal cells driven by the *daf-6* promoter in worms with wild-type *blmp-1* on 250µM auxin. GFP intensity oscillations are detectable and comparable to those observed in a strain lacking TIR-1, on plates without auxin (see Fig 2.7A).

B, GFP oscillations are damped in the strain with *aid::blmp-1* on 250µM auxin. Nevertheless, low amplitude oscillations can still be detected without an obvious peak phase shift compared to the negative control in A.

C, Cosine fits for both genotypes on the mean-centered, per substage averaged data from A and B. The calculated peak phase difference of 13° between the cosine fits was minor.

D, Barplots representing the calculated amplitude from cosine fits in C for both genotypes. The GFP oscillation amplitude from the wild-type genotype was 2,434 units larger compared to the *aid::blmp-1* genotype.

2.8 BLMP-1 is inducing high amplitude oscillations of the *daf-6* reporter

Yannick Hauser performed the imaging and analyzed all data. Helge Großhans and Yannick Hauser conceived the experiment.

To test whether complete loss of function of BLMP-1 affects *daf-6* oscillations, we tested the behavior of the *daf-6* transcriptional reporter by investigating the GFP intensities during the L4 larval stage by microscopy in wild-type, *blmp-1(tm548)* mutant and *blmp-1(s71)* mutant backgrounds. We obtaining a z-stack around the region of the vulva and quantified the GFP intensity in the hypodermis by using a customized KNIME workflow (see methods). In order to temporally align the individual worms, we retrospectively staged animals according to their vulva morphology into 10 different L4 sub-stages (Mok et al., 2015). Wild type worms showed an oscillating pattern of GFP intensities over the L4 stage, whereas dramatically damped oscillating GFP intensity patterns with low basal expression were detected in *blmp-1(tm548)* and *blmp-1(s71)* mutant animals (Fig 2.7A – C). The remaining basal activity of the *daf-6* transcriptional reporter could be due to other TFs binding the *daf-6* promoter and thus activating its transcription. In contrast, the transcriptional reporter for *F58H1.2*, derived from a gene without obvious BLMP-1 ChIPseq peak in the promoter, did not show that dramatic amplitude damping in the *blmp-1(tm548)* mutant background, suggesting that not all oscillatory gene expression relies equally on BLMP-1 (Fig 2.7D, E).

It appears striking that we could detect a damped reporter oscillation of the *daf-6* transcriptional reporter in the *blmp-1(tm548)* mutant background (Fig 2.7) as well as in the conditional BLMP-1 depletion experiment (Fig 2.6) but no strong transcriptional changes in the *aid::blmp-1* sequencing time course (Fig S3) or the *blmp-1* mutant time course. While we can argue that AID::BLMP-1 was not sufficiently depleted in the RNA sequencing time course, our expectation was to observe changes of *daf-6* in the *blmp-1* mutant RNA sequencing time course at least. What could cause this discrepancy between the two experimental approaches? It could be argued that in the case of *blmp-1* mutants, retrospective staging by vulva morphology fails to account for the correct

developmental stage, similar to the aberrant timing of the DTC movement in these larvae. However, we reject this argument based on the fact that we would expect to observe mean GFP intensities throughout the L4 sub-stages with high variability within one sub-stage if staging was random. Additionally, we can also not exclude that despite the recapitulation of oscillatory gene expression by promoters, we are still missing regulatory elements in our transcriptional reporters. Hence while under normal conditions, the reporters recapitulate the endogenous situation, the possibility remains that in a perturbed system, the endogenous transcript might be more robust in comparison to the reporter. Finally, the fact that we only observe epidermal tissue in the confocal imaging experiments while *daf-6* is expressed also in head and tail cells might at least partially explain the obtained results. Oscillations of *daf-6* in head and tail might not be dependent on BLMP-1 and thus still occur normally, leading to a reduction of the effect that we can observe in RNA sequencing experiments where we sample whole worms. In the future, it will be interesting to address by confocal microscopy whether *daf-6* oscillations in head and tail cells are unaffected by BLMP-1.

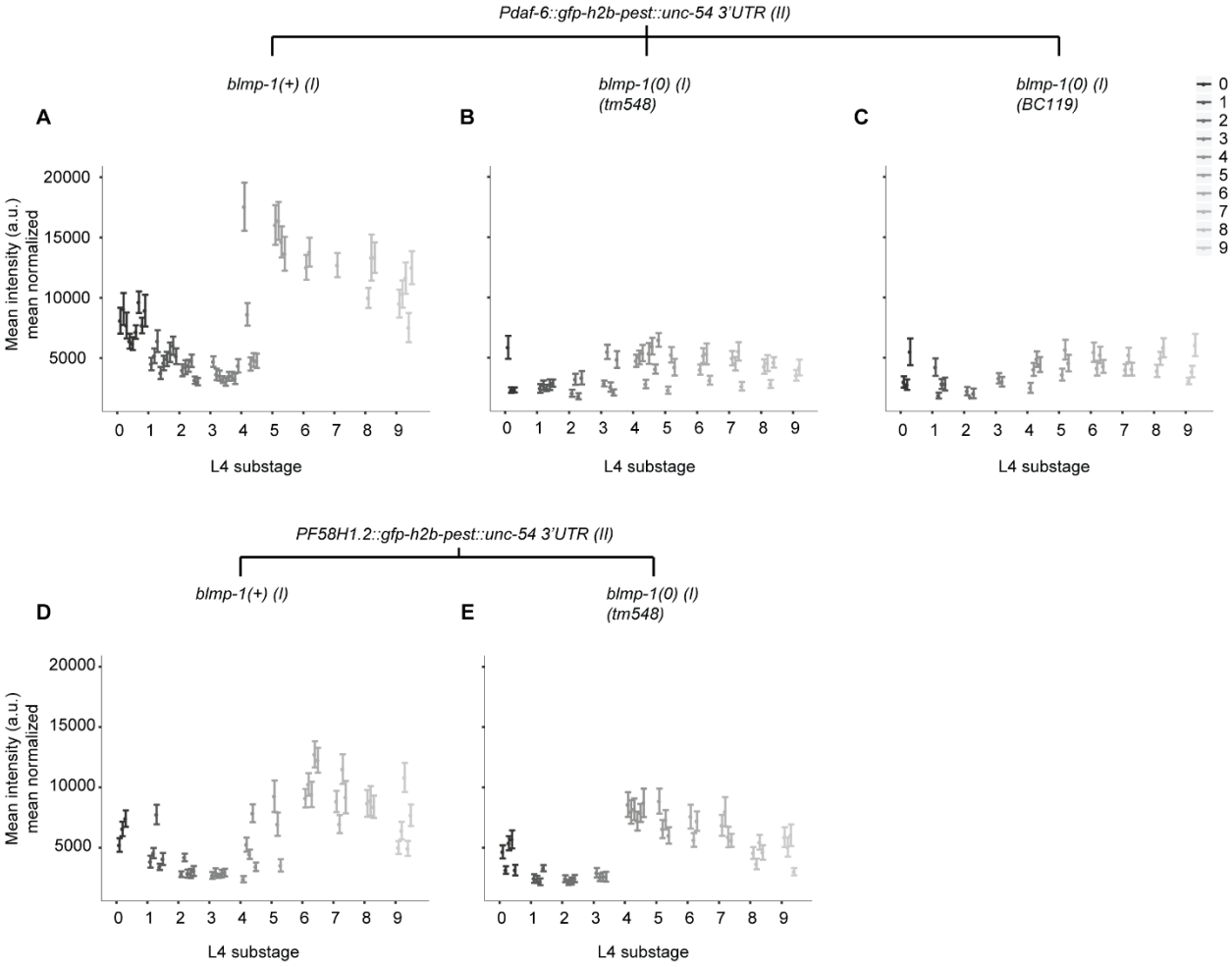

Fig 2.7: *blmp-1* mutants display damped oscillations of the *daf-6* reporter

A – C, GFP intensities measured from *Pdaf-6::gfp::pest::h2b::unc-54 3'UTR* (HW1431) in wild-type (A), *blmp-1(tm548)* mutant (B) and *blmp-1(s71)* mutant worms per nuclei in individual worms by confocal microscopy during the L4 stage. Worms were retrospectively aligned to developmental age by scoring vulva morphology (Mok et al., 2015). Each dot represents the mean of all measured nuclei per single worm with the standard deviation in whiskers. GFP, driven by the *daf-6* promoter, oscillates in wild-type background whereas oscillations are extensively reduced in two independent *blmp-1* mutants.

D, E, GFP intensities in measured as in A – C in the *F58H1.2p::gfp::pest::h2b::unc-54 3'UTR* (HW1360) in wild-type (A), *blmp-1(tm548)* mutant (B) and *blmp-1(s71)* mutant worms.

2.9 Epistatic interactions between *dre-1* and *blmp-1* mutations

Yannick Hauser performed all luciferase assays. Luciferase assays were analyzed using a customized Matlab algorithm as described in Meeuse et al., 2019. Helge Großhans and Yannick Hauser conceived the experiment.

Based on the previous observations that BLMP-1 is negatively regulated by the E3 ubiquitin ligase DRE-1 (Horn et al., 2014; Huang et al., 2014), we were curious to observe the phenotypes in *dre-1* mutants and *blmp-1(tm548); dre-1(dh99)* double mutants arising from this regulation. The *dre-1(dh99)* mutant is a hypomorph strain and we expect elevated BLMP-1 protein levels in this mutant. We wondered whether we can achieve accelerated progression through larval stages by providing higher levels of BLMP-1 in the case of *dre-1(dh99)* mutants, as opposed to the *blmp-1(tm548)* mutants. However, as evident from Fig 2.8C, we observed slightly longer larval stage durations. The *dre-1(dh99)* mutants also showed a slight increase of variability in molt, intermolt and larval stage durations which was, however, less severe than compared to the blmp-1 single mutant or the double mutant animals. In contrast and as already discussed in section 2.4 (*blmp-1* manuscript), *blmp-1(tm548)* mutants show high variability in L2 and L3 with also longer larval stage durations for L1 and L2 and the increased variability can also be detected in the intermolts and molts. Interestingly, the *blmp-1(tm548)*; *dre-1(dh99)* double mutants showed an intermediate phenotype with increased variability and larval stage duration in between the two single mutants as exemplified nicely in L2 (Fig 2.8B, C) and confirmed in an independent experiment (Fig S5).

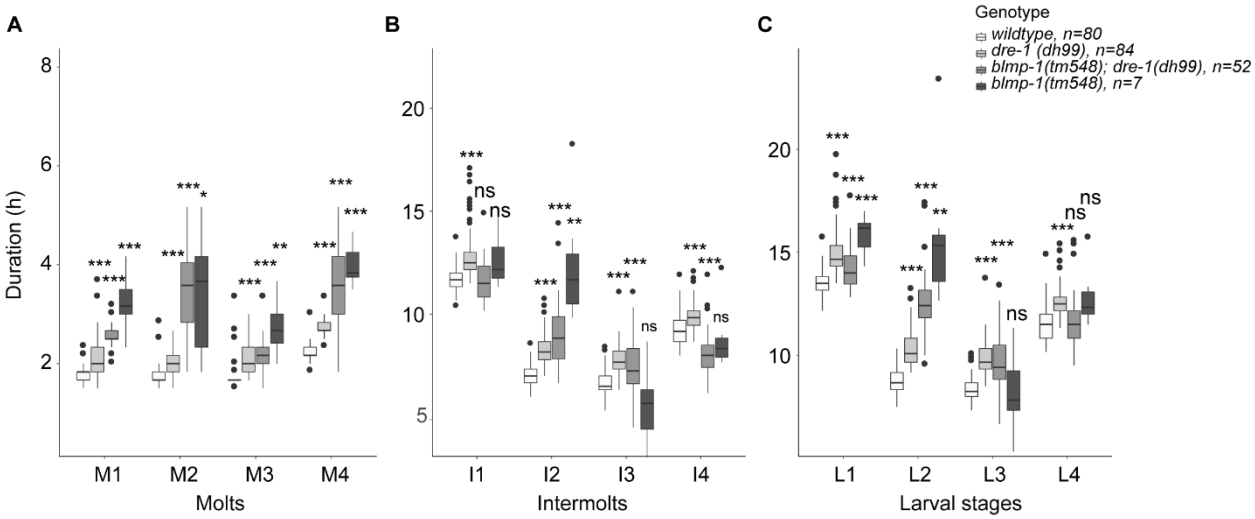

Fig 2.8: *dre-1(dh99)* mutation can partially rescue *blmp-1(tm548)* phenotypes

A – C, Boxplot analysis of molt (A), intermolt (B) and larval stage (C) durations as measured by luciferase assays in wild-type, *blmp-1(tm548) and dre-1(dh99)* single and *blmp-1(tm548); dre-1(dh99)* double mutant animals. The dramatic increase in molt, intermolt and larval stage duration and variability of *blmp-1(tm548)* can be partially rescued in the double mutant *blmp-1(tm548); dre-1(dh99)*.

Boxplots extend from the first to the third quartile with a line representing the median. Whiskers range up to 1.5*IQR and outliers are shown in dots.

Motivated by the results from *dre-1(dh99)* and *blmp-1(tm548)* single and double mutants in the luciferase assay we wanted to further confirm the intermediate phenotype. To this end, we initially created a *dre-1::aid* strain and investigated the phenotype upon depletion of DRE-1. As a negative control, we used the luciferase strain that is wild-type for *dre-1* and *blmp-1*, whereas the positive control was the luciferase strain with *aid::blmp-1*. As expected, the wild-type luciferase strain completed all larval stages synchronously while the *aid::blmp-1* strain showed increased molt durations (Fig 2.9A, B). Worms with depleted DRE-1::AID levels completed only the first molt (Fig 2.9C) and showed a strong lethality after the first molt as represented by a gradual decrease of luminescence values (Fig S6). Thus, DRE-1::AID depletion using the auxin degradation system leads to stronger phenotypes than the *dre-1(dh99)* mutation, an expected result since the *dre-1(dh99)* is only a hypomorph. The strong DRE-1::AID phenotype was rescued if we depleted both AID::BLMP-1 and DRE-1::AID simultaneously (Fig 2.9D), however, the rescued phenotype still showed more severely affected molt and intermolt durations than worms with depletion of AID::BLMP-1 only (Fig 2.9E).

Based on the above-mentioned results and analogous to Horn et al., 2014, we suggest that *blmp-1* and *dre-1* influence each other. However, based on the observation that the double mutant does not phenocopy the *blmp-1(tm548)* mutant, a more complex regulation seems likely with DRE-1 acting in a parallel pathway additionally. Given that DRE-1 is an E3 ubiquitin ligase it seems plausible that its action is not restricted to BLMP-1 only.

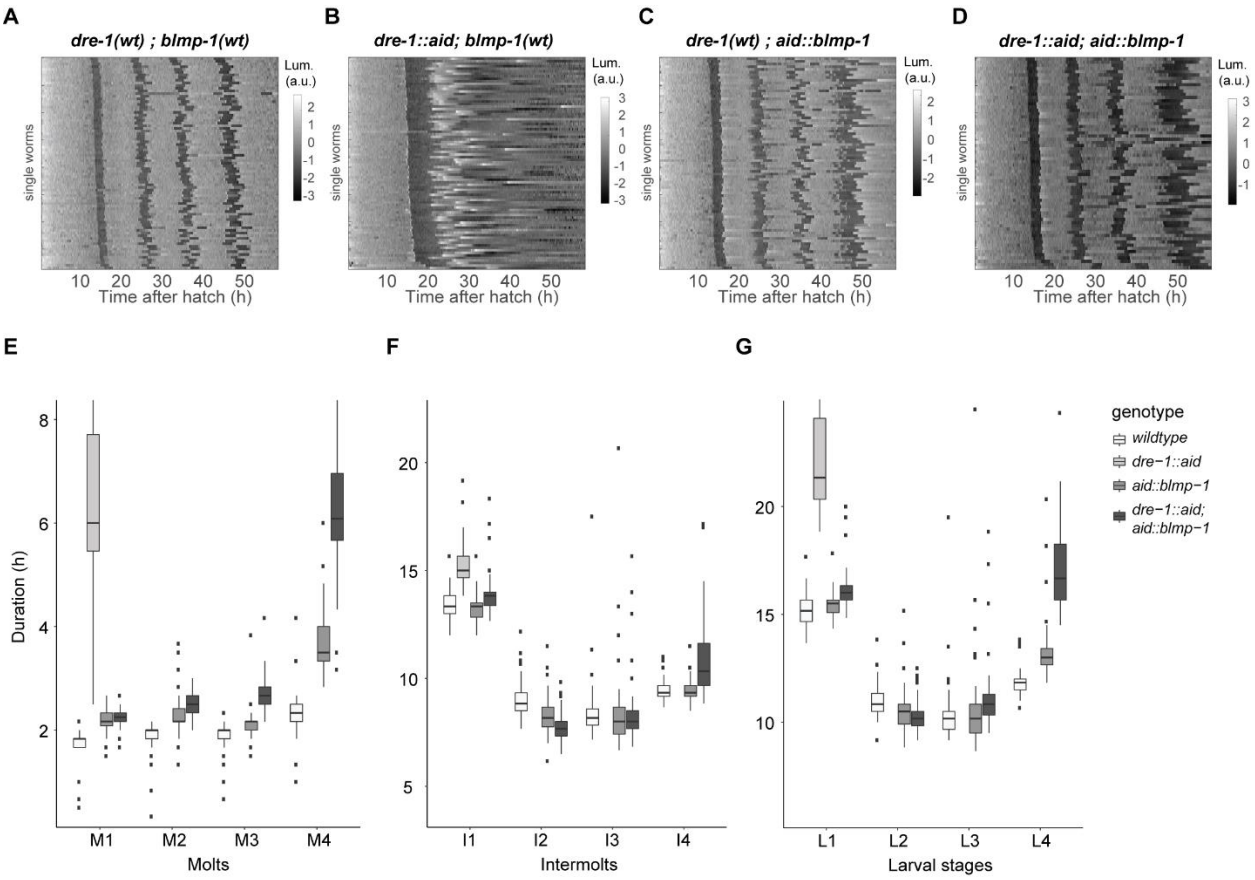

Fig 2.9: Depletion of AID::BLMP-1 and DRE-1::AID shows epistatic phenotypes

A – D, Heatmaps of trend-corrected luminescence (Lum.) traces from hatch (t=0) for the genotypes indicated in 250µM auxin (**A**: *wild-type* (n=79), **B**: *dre-1(wt); aid::blmp-1* (n=79), **C**: *dre-1::aid ; blmp-1(wt)* (n=84) and **D**: *dre-1::aid; aid::blmp-1* (n=66)).

E – G, Boxplots or molt durations (E), intermolt durations (F) and larval stage durations (G) for each genotype from in A – D.

2.10 Detailed investigations and improvements of single worm imaging data

2.10.1 Cell-based analysis of single worm imaging data results in comparable results to the whole worm-based analysis

Yannick Hauser performed all single worm imaging and analyzed the data. The cell-based KNIME workflow was developed by Yannick Hauser. Helge Großhans and Yannick Hauser conceived the experiment.

The analysis of the GFP intensities in single worms as in Meeuse et al., 2019 were measured from 20 – 80% of the anterior-posterior axis of the worm from the GFP kymograph lines which represent

the flattened worm image per time point, followed by calculation of the mean GFP intensity of kymograph line. Thus the intensity is normalized to the length of the worm, which could potentially result in undesired artifacts during the molt when the worm does not grow in length. This consideration led us to analyze the GFP intensity in cells to obtain a size-independent measure of the GFP intensities over time. For this purpose, we re-analyzed imaging data from Meeuse et al., 2019 of 22 worms containing a transcriptional reporter of *dpy-9* as a single copy integration, grown on mock RNAi in the single worm imaging. GFP intensities were obtained as explained using a customized KNIME workflow (see methods) and showed oscillatory intensities over time that were comparable to the oscillations measured in the whole worm (Fig 2.10, Fig S7). Assigning the oscillation phase at molt entry and exit showed largely comparable phases between the two analyses, with at most minimal differences between the worm-based and the cell-based analysis (Fig 2.10D). Nevertheless, the small, yet significant difference might represent an improvement of the cell-based analysis due to the reduction of artifacts coming from length normalization. The distribution of the calculated phases at molt entry and molt exit, however, were comparable in their variability.

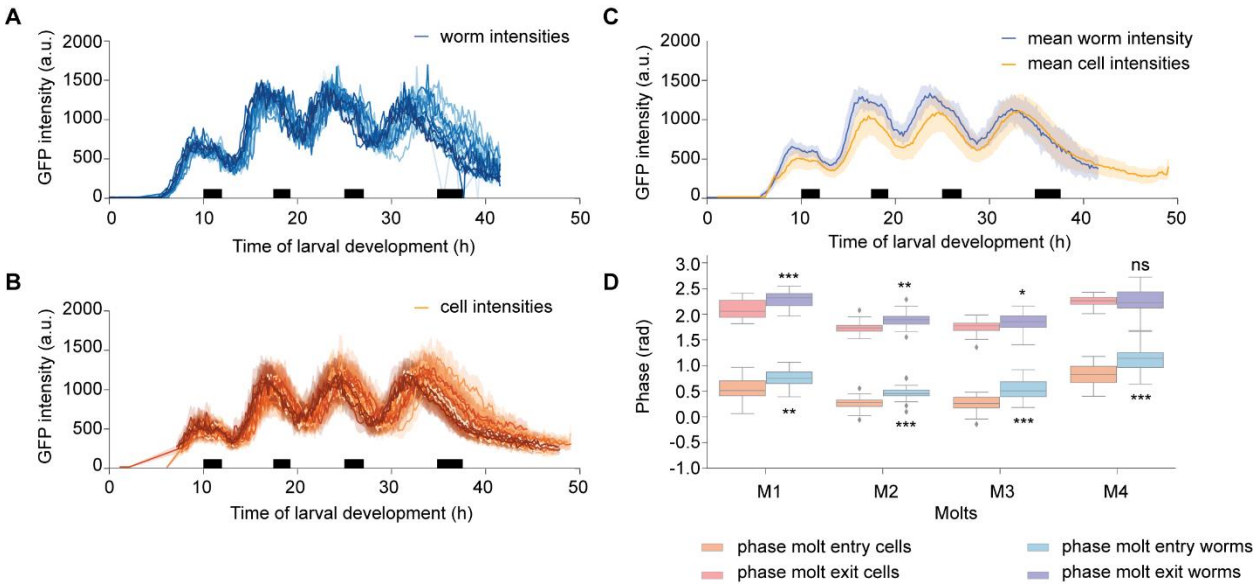

Fig 2.10: GFP intensities in cells resembles whole worm GFP intensities

A, GFP intensities as measured in Meeuse et al., 2019 per worm from 20-80% of the anterior-posterior axis (n=22).

B, Mean GFP intensities per cell in single worms. The standard deviation of cell GFP intensities per time point and worm is shown as shaded area (n=22).

C, Mean GFP intensities of all individual worms per time point from A and B in blue and orange respectively. The standard deviation is displayed in the shaded area.

D, Boxplots of the phases at molt entry and molt exit cell and worm GFP intensities. Significant differences were calculated using Welch two-sample t-test (* $p<0.05$, ** $p<0.01$, *** $p<0.001$).

Molts are indicated in black on the x-axis. Boxplots extend from the first to the third quartile with a line representing the median. Whiskers range up to 1.5*IQR and outliers are shown in dots.

The cell-based single worm imaging analysis could even avoid small artifacts arising from the fact that the worm is not growing during the molts and could provide a result with even more accuracy. Nevertheless, as the variability between the two analyses was comparable, both strategies still represent valid tools for further studies. I note that the cell-based analysis is much more time-consuming than the worm-based analysis which still argues against using the cell-specific analysis as the default approach for our further experiments. In order to further improve this method and make it applicable to not only tissue specifically expressed genes, we would require an additional tissue specifically expressed red or blue fluorescent reporter to label the cells of interest. This would enable us to analyze labeled and unlabeled cells independently and thus allow for the characterization of tissue-specific expression for reporters that are expressed in multiple tissues.

2.10.2 Oscillatory gene expression behaves similarly in different segments of the anterior-posterior axis

Yannick Hauser performed the single worm imaging. The segment analysis was performed using the KNIME workflow was developed by Jan Eglinger and is described in Meeuse et al., 2019. Helge Großhans and Yannick Hauser conceived the experiment.

We further wondered whether the oscillations occur synchronized within the hypodermis or whether they travel through the tissue as a wave as seen for example in the segmentation clock. In order to address this question, we investigated the hypodermal transcriptional reporter of *dpy-9* in detail. We divided the kymograph resulting from the GFP analysis of single worm images into three consecutive segments from 20 – 40% (anterior), 40 – 60% (middle) and 60 – 80% (posterior) of the anterior to posterior axis. The resulting GFP analysis per segment revealed a high similarity across segments with highly similar peaks and troughs (Fig 2.11) and led us to conclude that within

our temporal resolution, we cannot detect differences between anterior and posterior oscillations within the hypodermis.

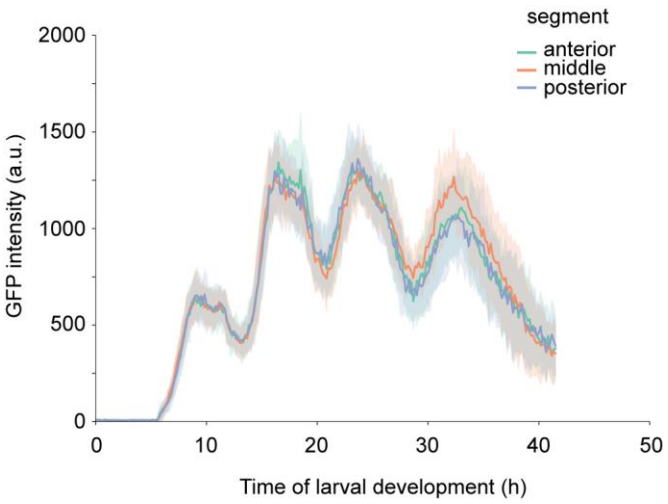

Fig 2.11: The hypodermis oscillates as a syncytium.

The hypodermal expressed transcriptional reporter of *dpy-9* analyzed in three consecutive segments across the anterior-posterior axis.

2.10.3 A convolutional neural network improves single worm imaging segmentation

Yannick Hauser performed the single worm imaging. The convolutional neural network was developed by Markus Rempfler and tested by Yannick Hauser. Helge Großhans and Yannick Hauser conceived the experiment.

Analysis of the GFP intensities from single worm imaging data required segmentation of worms to separate “worm” from “background” and to accurately quantify the GFP driven by (oscillating) promoters. We previously used Ilastik to segment the worms based on both channels, GFP and brightfield. While this strategy increased the robustness of the Ilastik segmentation, it was accompanied by the fact that we faced difficulties upon analyzing GFP intensities in worms with weak GFP signal. Not only were we unable to analyze certain worm strains with low GFP expression, we also lacked an accurate analysis of L1 worms for many of the investigated transcriptional reporters as GFP intensities were usually low in L1. In order to overcome these challenges, we trained a convolutional neural network (CNN) to recognize and segment the worm based on the brightfield images only by using 268 manually segmented images from two single

worm imaging datasets including HW2526 and HW2524 worms. The manual segmentation was especially important for cases where L1 worms were in contact with one of the chamber walls and thus the wall was risked being segmented together with the worm, a difficulty we also realized using the Ilastik segmentation. The CNN was tested on HW2524 worms, carrying a *gfp::pest::h2b::unc-54 3'UTR* reporter transgene driven by the *R07E3.6* promoter. The resulting probabilities were thresholded to yield binary masks that were used to replace the binary images in the original KNIME workflow to analyze the GFP intensities. As shown in Fig 2.12C for a single worm, the segmentation using the CNN resulted in highly similar GFP intensity values for most of the time-lapse, but performed better for early L1 worms and especially also for eggs. The CNN outperformed the Ilastik segmentation in multiple worms in L1 and eggs as demonstrated by the smaller standard deviation in the first peak after hatching in Fig 2.12E and revealed a robust segmentation in eggs. Apart from the improved egg and L1 quantification using the CNN, we could additionally observe an improved segmentation of the CNN segmentation in older adults towards the end of the time-lapse imaging (Fig 2.12E). Future datasets will show how generally applicable to slightly different time lapse microscopy images the CNN is. We foresee that we might incorporate additional images in order to apply the CNN to all time lapse microscopy data obtained at different microscopes or with slightly different acquisition settings.

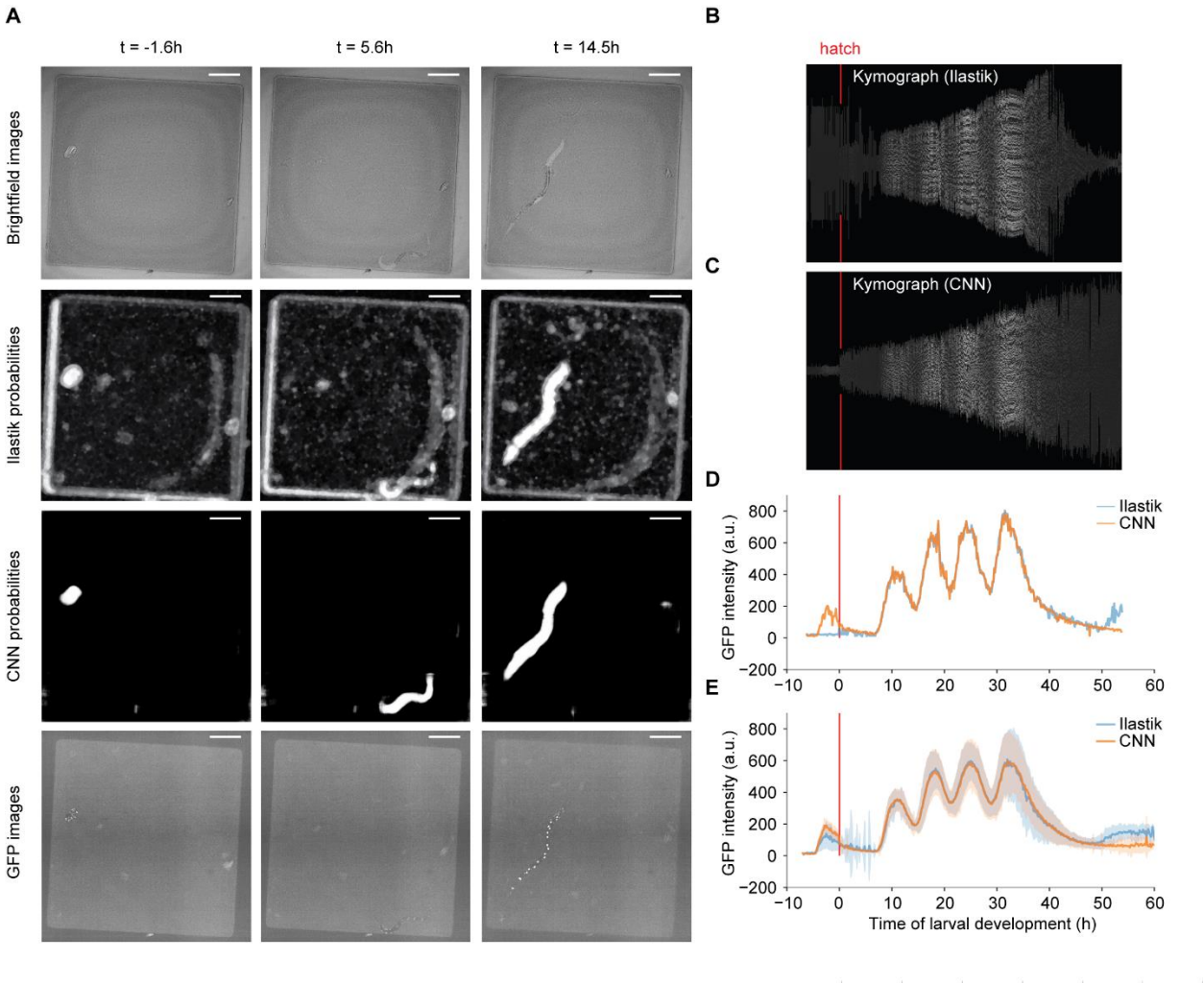

Fig 2.12: Segmentation using a convolutional neural network improves the GFP analysis in early single worms

A, Representative images of the worm analyzed in D for three different time points, as indicated. The white bar in the right upper corner corresponds to 100µm.

B, C, Kymograph of segmented GFP images over the worm development using the Ilastik segmentation mask (B) and the CNN segmentation mask (C). The hatching time is indicated in red. Due to scaling in the y-direction to the longest vertical line, the scales in y-direction differ between B and C.

D, Comparison of the GFP intensities in a single worm using either Ilastik or the CNN to segment the worm shown in A and B. GFP intensities are related to the hatch time point (t = 0).

E, Comparison as in D using all imaged worms (n=40) illustrates the differences in the GFP intensities using the CNN in L1 larvae and eggs. Solid lines represent the mean GFP intensity with the standard deviation displayed in the shaded area. GFP intensities are related to the hatch time point (t = 0).

3 Discussion

Biological oscillators have been discovered in multiple organisms to synchronize behavior with external rhythmic processes, regulate rhythmic developmental processes or regulate cell fate transitions. Hitherto, we lack a complete understanding of their mechanism, functional relevance and system behaviors. Studying various biological oscillators has improved our understanding of the general principles and idiosyncrasies between them. Here, we have presented a genetic oscillator in *C. elegans* which we study to further dissect the mechanism, functional relevance and systems behaviors in a multicellular organism. In the following, I will discuss the results obtained in these studies.

3.1 Regulation of rhythmic gene expression

Previous data has only been able to suggest transcription as a key driver for oscillatory gene expression in *C. elegans*. Here we have provided further evidence for this hypothesis by using RNA polymerase II ChIP-sequencing and transcriptional reporter studies. I will discuss these findings below.

3.1.1 Rhythmic transcription is the main driver for oscillatory gene expression

A thorough understanding of a genetic system and its characteristic behavior is impossible without the knowledge of its regulation. As the possibility remains that transcript oscillations can arise even in the presence of constant mRNA production from post-transcriptional mechanisms (Koike et al., 2012), we wanted to obtain a better understanding of the transcriptional and post-transcriptional contributions to the ~3,700 oscillating mRNA levels. The RNAPII ChIP-sequencing data and the promoter-driven *gfp* reporters further suggested transcription to be the key driver for oscillating mRNA levels. In particular, the transcriptional reporters contained the *unc-54* 3' UTR which is not predicted to be targeted by miRNAs and thus, at least for the tested reporters, the main regulation arises from promoter sequences. While we cannot exclude, and in fact might even expect that for specific cases post-transcriptional mechanism may influence (oscillatory) behavior of mRNA levels (Kim et al., 2013a), we propose the majority of transcript oscillations to be regulated by transcription on the promoter sequence.

3.1.2 The 5’ UTR can modify oscillatory gene expression

In general, we propose the observed modification of peak phase and amplitude induced by different 5’UTR sequences to primarily arise from differences in the stability of the resulting transcript as illustrated by the fact that we see dramatically reduced expression upon replacing the 5’UTR. Using theory, we can deduce an estimate of the stability of the 5’ UTR exchanged transcript by taking the peak phase shift as well as the amplitude into account for a mathematical model. If we assume that the phase shift primarily arises due to changes in the mRNA stability and that production of the mRNA molecule is oscillating, we reach the conclusion that the 5’ UTR exchanged mRNA should be less stable than the normal mRNA molecule. To further investigate the 5’ UTR effects on the stability and the peak phase of oscillating transcripts, it would be useful to test the effect of exchanging the *F11E6.3* 5’ UTR with a 5’ UTR of another oscillating gene and investigate the resulting peak phases, amplitudes and expression levels for the additional oscillating reporter with the *actin-1* 5’ UTR. To identify whether the destabilization is a general effect independent of oscillations it will be important to generate a transcriptional reporter for *actin-1*. We can then compare the *gfp* transcript levels of this reporter with the gfp levels of reporters where we replace the endogenous *actin-1* 5’ UTR with the 5’ UTR of *F11E6.3* and a non-oscillating gene.

3.2 System properties of the *C. elegans* oscillator

The RNA sequencing experiments performed here allowed us to characterize the system properties of the *C. elegans* oscillator in detail. In particular, the observed transitions between an arrested and an active oscillator state in newly hatched L1 larvae, dauer arrested animals and adults improved our understanding of the system. Advanced analysis methods such as the Hilbert transform allowed us to quantify the dynamics of amplitude and period during these transitions, two important oscillation features that are extensively analyzed in bifurcation theory. In the following, I will discuss the insights obtained from this analysis and highlight general properties of the *C. elegans* oscillator.

3.2.1 The oscillation does not travel as a wave through the hypodermis

In order to find similarities between the segmentation clock and the *C. elegans* oscillator, we wondered whether oscillations travel as a wave through tissues. Based on the experimental results

obtained from the time-lapse imaging experiments (Fig 2.11), we conclude that, at least for the investigated hypodermally expressed reporter and given our time resolution, the oscillations appear to be coordinated on the tissue level as they arise in a spatially homogenous manner and do not to travel as a wave through the tissue. This contrasts with the segmentation clock where traveling waves throughout the presomitic mesoderm are observed. Nevertheless, we cannot exclude the possibility that oscillation waves with faster dynamics than our sampling frequency of 10-minute intervals (i.e. time resolution) might exist. Considering that in a syncytium a molecular agent could travel fast through the tissue, this might represent a plausible scenario. Nevertheless, the biological relevance of such fast dynamics in comparison with a ~7 hour period seems unclear. It will be important to understand whether the hypodermal syncytium represents an exception and whether other non-syncytial tissues (e.g. intestine, muscle) differ in the behavior of oscillations. Consequently, if such a traveling wave existed, this would raise the possibility that the new oscillation cycle could be started from a master regulator potentially located at a specific location of the worm, i.e. the anterior end. While representing an important question to address the molecular regulation of the oscillator in greater detail in the future we did not further investigate this possibility, given the fact that all our other assays use either the same or lower sampling frequency and our transcriptional reporters were mainly expressed in the hypodermis.

3.2.2 Tissue-specific characterization of oscillatory gene expression

Based on the broad peak phase distribution we observed in the RNA sequencing results (Hendriks et al., 2014; Meeuse et al., 2019) we wondered how this broad distribution emerged. We imagined two different possibilities to explain this observation. First, a complex regulatory network exists in individual tissues and cells to regulate oscillating transcripts differently and thus leads to an individual peak phase for each gene. Second, each tissue only expresses genes with the same peak phase among them. The peak phase distribution would then primarily be the cause of multiple tissues expressing oscillating genes and oscillating genes that are expressing in multiple tissues for which the shared peak phases differ. Analysis of previously annotated tissue-specific expression data revealed that the hypodermis is strongly enriched in oscillating genes with a wide range of peak phases (Hendriks et al., 2014; Meeuse et al., 2019) and thus I will focus the discussion on this particular tissue.

Discussion

The RNA sequencing data did not provide further insights into tissue-specific regulation of oscillatory gene expression as we sampled whole worms where all tissues are combined thus potentially leading to misinterpretation of observed peak phases. Considering these drawbacks we focused on the imaging data that we have collected. The *dpy-9*, *qua-1* and the *F16B4.4* transcriptional reporters are all specifically expressed in the hypodermis (consistent with Cao et al. 2017, not shown) and show distinct peak phases. *dpy-9* peaks slightly before the molt, *qua-1* peaks during the molt (Meeuse et al., 2019) and *F16B4.4* peaks during the intermolt (section 2.4, *blmp-1* manuscript), thus we favor the idea of a complex regulatory network within each tissue to result in multiple peak phases possible within one tissue. Nonetheless not all oscillating genes are tissue-specifically expressed and thus may oscillate in multiple tissues with varying peak phases among these tissues. And finally, not all genes expressed in the hypodermis necessarily oscillate as we could demonstrate with the *tbb-1* promoter-driven *gfp* reporter.

The above-mentioned observations favor a complex regulatory network within individual tissues and illustrate the necessity of tissue-specific analysis for further investigations in order to characterize oscillatory gene expression in detail. Tissue-specific analyses will enable us to characterize peak phases of oscillating genes within individual tissues and reveal whether these peak phases are shared among tissues or whether they can differ. Additionally, by using tissue-specific cell cultures we can test whether the oscillations are cell-autonomous, i.e. whether cells remain oscillations after dissociation. Furthermore, in the case of a cell-autonomous oscillator, being able to perturb the oscillator at the cellular level represents one important approach to understand the network of the oscillator(s) in detail. Unfortunately however, so far, experimental approaches to establish a *C. elegans* tissue-specific cell culture have shown limited success.

In order to at least obtain tissue-specific expression data, our lab is working on establishing a single-cell sequencing method with temporal resolution. With the help of tissue specifically expressed marker genes we plan to assign each cell to a specific tissue and hence obtain a tissue-specific data set at a single-cell resolution over time to greatly improve the characterization of the oscillator.

In addition to the single-cell sequencing approach, a realistic approach for the near future is to obtain tissue-specific expression of transcriptional *gfp*-based reporters using the single worm imaging. Co-expression of tissue-specific transcriptional markers using a second fluorophore that

allows identifying the particular tissue of interest and hence analyzing the GFP intensity intensity will be of particular interest. In the future, single worm imaging will hence be a useful tool to validate these tissue-specific single-cell sequencing results. As a proof of principle, we could already demonstrate that we can successfully measure GFP intensities over time in single cells and that measuring GFP intensities in cells leads to a similar result as the analysis per worm from 20 – 80% (Fig 2.10).

3.2.3 Transcript oscillations in *C. elegans* are not necessarily sinusoidal

To investigate oscillations in single worms to reveal potentially non-sinusoidal oscillations, the development of the pseudotiming algorithm specifically designed for single worm sequencing experiments was particularly important. Without the pseudo-timing, non-sinusoidal oscillations could not have been identified as the true developmental time is not reflected in the sampling time due to slight variations in developmental progression among individual worms. This fact would lead to a similar distribution as if we would have sampled bulk samples as shown in Fig 2.2A and thus smoothen out the true oscillatory signal. Hence, even if non-sinusoidal oscillations were present, they would appear rather sinusoidal without pseudo-timing. One important consideration in the algorithm, however, is that the pseudo-timing depends heavily on the calculation of the angle from the principal components. This analysis only works reliably if the center of the circle (Fig 2.2C) is localized in proximity to 0. If the circle and its center would be extremely shifted, a meaningful calculation of the angle would be impossible. In such cases, the angular speed for all samples and clusters would be faster on one side of the circle and slower on the opposite side. This would result in increased and decreased progression through the oscillations in general for all genes and clusters at the same time of development. In such a case, we would need to correct the data by shifting all data points so that the center of the circle is at 0 in order to continue with the analysis. Our results, however, clearly indicate that individual genes and clusters show increased or decreased progression at independent times of larval development and thus we exclude the hypothesis that all non-sinusoidal traces arise from stretching and compressing of the worm development. This is particularly obvious in Fig 2.3A(II), where only the ‘blue’ gene shows a fast progression through the oscillation while the ‘red’ gene progresses slower. Hence, we conclude that the single worm sequencing data shows non-sinusoidal for many genes . We could confirm our hypothesis that for certain genes, the non-sinusoidal nature of oscillating genes is only

detectable in single worm studies by comparing the gene expression of single worms with bulk sequencing data. Using the high temporal resolution in the single worm sequencing dataset, we could identify different behaviors of oscillating genes using hierarchical clustering.

Nevertheless, the analysis would profit from further improvements as the current clustering is heavily biased by the peak phase and the amplitude of oscillating genes, e.g. genes with similar peak phases are more likely to cluster together. This drawback is inevitable and inherently arising from the clustering. In this regard further downstream analysis such as promoter motif analysis, tissue specificity analysis or Gene Ontology (GO) term analysis is complicated. In the future, more sophisticated clustering strategies, specifically designed for oscillating genes will potentially lead to less biased clusters and could reveal even stronger non-sinusoidal oscillations of clusters.

With our single worm sequencing analysis, we further plan to sequence asynchronous mutant strains and retrospectively align the individual samples according to pseudo-time. The pseudo-timing thus would enable us for the first time to sequence the transcriptome of asynchronous mutants and align these samples to generate a synchronous gene expression time series. Obviously, the asynchrony cannot be arbitrarily large as otherwise, the cycle annotation would fail if worms sampled at individual time points would show an angular distribution of $2pi$. In the case of moderate asynchrony, however, we could identify genes that peak precociously or delayed in comparison to other oscillating genes. Thus in comparison with bulk sequencing of transcription factor depleted worm populations, single worm sequencing of mutant animals might represent a superior strategy since we can retrospectively reduce moderate asynchrony. The single worm sequencing is most probably well suited to investigate mutants where a relatively small subset of oscillatory gene expression is unsynchronized from the majority of oscillating genes. In this case, the pseudotiming should allow an accurate assignment of the developmental pseudotime since many genes are behaviong normally. Mutants that affect all genes have to be investigated carefully. While a general increase in period of all oscillating genes should be a suitable case for the pseudotiming algorithm presented here, a complete unsynchronized behavior of all oscillating genes might not be correctly analyzed by the pseudotiming algorithm and carefull investigations of the specific mutant is advised. The algorithm might still result in a circular structure after the principal component analysis but the followed pseudotiming of individual samples and the resulting oscillations needs to be carefully investigated and compared to bulk sequencing results.

3.2.4 Constraining oscillator architecture from its characteristic behavior

Even though we are still lacking detailed knowledge of the molecular architecture of the oscillator, its global behavior allows us to rule out certain network topologies and favor others. The observed stable amplitudes despite a change in period length in L4 larvae (Meeuse et al., 2019) represents an important feature of so-called rigid oscillators (Abraham et al., 2010) and allows us to constrain the wiring of the core oscillator. It has been shown that negative-only feedback systems cannot display varying periods with stable amplitudes while the incorporation of interlinked negative and positive feedback loops allow for this characteristic behavior (Tsai et al., 2008). Additionally, the abrupt appearance of an oscillatory regime as observed in L1 larvae is a collective characteristic for negative-positive feedback systems and incompatible with negative-only feedback systems (Izhikevich, 2000; Mönke et al., 2017; Strogatz, 2015). The rigidity of oscillator behavior was shown to be increased in coupled oscillators and might serve developmental oscillators particularly well due to the fact that rigid oscillators likely filter noise (Abraham et al., 2010). Taken together, we propose our oscillator behavior to be in agreement with an (amplified) negative-positive feedback system such as in Fig 1.5E (Abraham et al., 2010; Mönke et al., 2017) and a rigid oscillator.

3.2.5 State transition behavior is in agreement with a SNIC bifurcation

Since we were able to constrain possible network topologies underlying the *C. elegans* oscillator, the speculation on the type of bifurcation from non-oscillatory to oscillatory is important as it can inspire and improve mathematical descriptions of the oscillator. Designing targeted experiments to validate predictions from mathematical models will be crucial in the future to understand the *C. elegans* oscillator in detail. However, it was shown that mathematical models can lead to different types of bifurcations, depending on the parameter choices (Conrad et al., 2008) and the same bifurcations can arise from different mathematical models (Purcell et al., 2010). Most of the negative-positive feedback systems were shown to bifurcate via Hopf bifurcations for many parameter choices, while only a certain parameter space leads to SNIC bifurcations. Stable amplitudes and increased periods together with sustained stable amplitudes and the possibility to arrest the oscillator at a specific phase of the oscillations are features which we observe in the *C.*

elegans oscillator that are compatible with a SNIC bifurcation (Figure 1.7, Meeuse et al., 2019). Combined with the fact that we propose the oscillator to be composed of an (amplified) negative-positive feedback system, this provides a starting point for model choices including limitations in the parameter space in future mathematical modeling approaches.

3.3 Functional relevance of the *C. elegans* oscillator

Despite detailed characterization of the *C. elegans* oscillator, a complete understanding of the functional relevance of gene expression oscillations is still missing. In the following, I will discuss the plausible developmental functions of the *C. elegans* oscillator.

3.3.1 Oscillations are coupled to molting

The observations of an arrested oscillator in the first 5 hours of L1, an increased period length in the longer L4 larval stage and the fact that the top enriched Gene Ontology terms of oscillating genes were all linked to molting pointed towards a functional relevance of the oscillations with regard to molting. However, the possibility remained that both molting and gene expression oscillation could be regulated by independent processed and do not necessarily need to be coupled. Revealing a potential functional coupling required simultaneous monitoring of oscillatory gene expression and developmental progression. Using single worm imaging we were able to obtain such data and the combination with error propagation analysis allowed us to favor the coupling of gene expression oscillations with the molts (Meeuse et al., 2019). While the exact coupling mechanism still needs to be uncovered, single worm imaging and RNA sequencing results suggest BLMP-1 to be potentially involved in this process as we could observe a strong shift in peak expression relative to the molts for a small group of genes (section 2.4, *blmp-1* manuscript).

3.3.2 Developmental functions beyond molting

Beyond a mere coupling of molting with gene expression oscillations, the phase of the arrested oscillator corresponds to the phase seen at molt exit. Given the observation that worms can arrest development after each molt (Schindler et al., 2014) in response to starvation, we speculate about a developmental checkpoint function of the oscillator (Meeuse et al., 2019). Hence, the presence of food might act as a trigger to (re-)initiate the oscillator during larval development, which is genetically encoded as mutations in the insulin signaling pathway were shown to bypass these checkpoints even in the absence of nutritional signals (Schindler et al., 2014). Even though

members of the insulin signaling like *daf-2* or *daf-16* did not reach the thresholds to be classified as oscillating in our new classification, visual inspection of their gene expression pattern looks rhythmic (Fig S9), further suggesting a connection between oscillatory gene expression and nutrition.

We further speculate the observed transition of the oscillator in early L1 and dauer exit larvae to represent a SNIC bifurcation, potentially integrating nutritional signals until oscillations initiate (see sections 1.3 and 2.1). Recent data from short-term starvation followed by release into food conditions revealed an arrest of development right after the hatch and no delay in subsequent larval stage durations when worms were re-fed (not shown). This data fits well with the checkpoint hypothesis (Schindler et al., 2014) and reveals that the delay upon release from L1 and dauer arrested larvae might be regulated differently from release from transient starvation. Given that the transiently starved larvae still arrest development argues for a strong and biologically relevant perturbation of development and possibly the oscillator, which we plan to investigate further in an RNA sequencing time course using transiently starved and re-fed larvae.

Finally, the fact that we observed slightly more oscillating genes in the intestine than expected by chance might also indicate a potential link between the oscillator and nutrition. Beyond just receiving nutritional information as an input, the oscillator might additionally serve to prepare for the short–term starvation that is induced by lethargus.

3.4 Characterization of the putative coupling agent BLMP-1

As demonstrated in section 2.4 (*blmp-1* manuscript), BLMP-1 leads to unsynchronized oscillation of a small group of genes with respect to other oscillating genes and to development (i.e. the molts). Thus we propose BLMP-1 as a putative coupling agent between either multiple oscillators or their outputs.

In both cases, BLMP-1 requires a connection from and to either both oscillators that it synchronizes (Fig 3.1A). Alternatively, BLMP-1 could also be connected to only one core oscillator and synchronize it with the output of another core oscillator (Fig 3.1B). Depending on the requirements (see section 1.5), the connections to and from BLMP-1 can represent either double-positive or double-negative regulation of BLMP-1 with the oscillators to be synchronized. In this scenario we

would favor a double-negative regulation as it increases the robustness of amplitudes of coupled oscillators with short time delays.

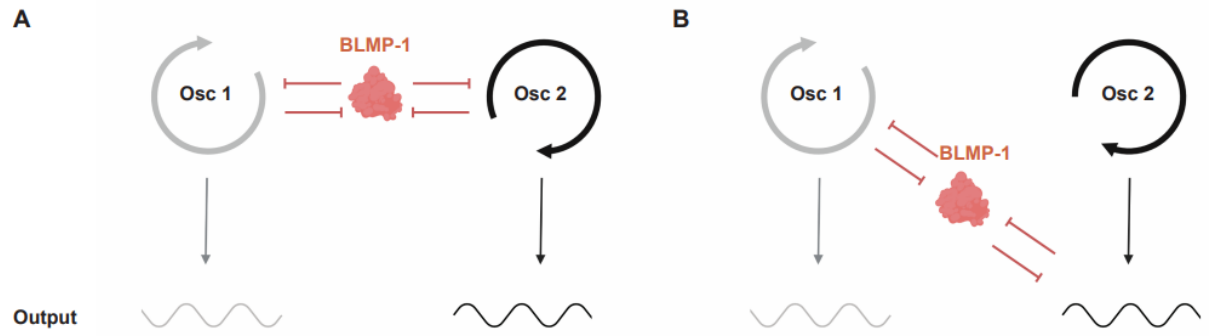

Fig 3.1: BLMP-1 as a coupling factor

We propose BLMP-1 to couple oscillations and thus synchronize their generated rhythmic output. Since we could detect precocious expression of oscillating genes in *blmp-1* loss-of-function conditions, we favor a repressive interaction from BLMP-1 towards its targets ("Osc" = oscillator). (Figure created with BioRender.com)

A, Model of BLMP-1 directly coupling two oscillators and thus synchronizing their output gene expression.

B, Alternative model in which BLMP-1 interacts only with one oscillator and synchronizes it with the output of a small subgroup of output genes of another oscillator.

BLMP-1 was previously suggested to be a heterochronic gene involved in the regulation of timing the seam cell divisions and the distal tip cell turn (Horn et al., 2014; Huang et al., 2014). Hence, BLMP-1 might, beyond synchronizing distinct rhythmic events, also be involved in synchronizing oscillatory gene expression with the linear, heterochronic pathway. The mechanism of this hypothetical synchronization remains to be elucidated, however.

3.4.1 BLMP-1 and DRE-1 are involved in a complex pathway and regulate molting

BLMP-1 and DRE-1 have been shown previously to interact. The E3 ubiquitin ligase DRE-1 targets BLMP-1 for degradation and since both *blmp-1* and *dre-1* are oscillating, we were wondering whether this regulation influences the regulation of rhythmic development. We have addressed this question using luciferase assays using *blmp-1* and *dre-1* single and double mutants and additionally used conditional depletion of either BLMP-1, DRE-1 or both using the auxin degradation system. Remarkably and in line with previous reports, reduced BLMP-1 and DRE-1

levels resulted in an intermediate phenotype and thus rescued the lethality phenotype in worms with depleted DRE-1 using auxin. One hypothesis to explain this result is that too low (BLMP-1 depletion) or too high BLMP-1 levels (DRE-1 depletion) have tremendous effects on molting due to the resulting unsynchronized oscillatory gene expression. In the case of combined BLMP-1 and DRE-1 depletion, both proteins might be expressed at low levels with the timing of their peak expression still resembling the wild-type situation and thus this might lead to an intermediate phenotype. An important aspect in the interpretation of these results is that we could not measure the exact extent of downregulation of these proteins. Thus, we do not know whether both proteins are degraded to similar amounts or whether one of the two proteins is degraded more efficiently. The strong phenotype observed in the DRE-1 depleted animals suggests a functionally relevant degree of degradation, however.

Additionally, in the mutant strains the observed *blmp-1; dre-1* double mutant phenotype does not fully resemble the *blmp-1* mutant phenotype which argues for additional pathways that are regulated by DRE-1. Otherwise, if BLMP-1 would be the sole DRE-1 target, we would expect to see the same phenotype in *blmp-1* single and *blmp-1; dre-1* double mutants. Since the *dre-1(dh99)* mutation is only a hypomorph, we have to be careful in interpreting these results and suggest to use the auxin degradation system for future studies due to the possibility of adjusting the level of degradation, depending on the supplied amount of auxin.

While these results are only the beginning of revealing the mechanism of this regulation, we wondered whether BLMP-1 and DRE-1 might represent an amplified negative feedback loop. The following additional, yet hypothetical, regulations would complete this feedback loop: i) Positive transcriptional regulation of *dre-1* by BLMP-1, ii) Positive autoregulation of BLMP-1. Thus with the previously suggested negative regulation of BLMP-1 protein by DRE-1 through targeting for degradation, these combined features would represent an amplified negative feedback loop that can lead to oscillations. However, the fact that BLMP-1 was not reported to bind to the *dre-1* promoter (Huang et al., 2014; Niu et al., 2011) argues against our hypothesis and asks for a more complex regulation. However, the absent binding of BLMP-1 to the *dre-1* promoters was drawn from ChIP seq results using GFP tagged BLMP-1, which might not reveal weak binding or contain false positives, false negatives or indirect regulation through an intermediate factor. The regulation of *blmp-1* to generate the amplification in the negative feedback might also be more complex than

just positive autoregulation as we do not observe changed *blmp-1* levels in the *aid::blmp-1* time course which would be an expected result for positive autoregulation. Finally, BLMP-1 is redundantly regulated by DRE-1, LIN-29 and DAF-12 as suggested by (Huang et al., 2014), further increasing the complexity of the BLMP-1's regulation. Together with our own observation that DRE-1 might regulate parallel pathways, we propose that the regulation revolving around BLMP-1 and DRE-1 might be more complex than just an isolated amplified negative feedback loop and further studies are needed to reveal this complex regulatory network.

4 Outlook

4.1 Elaborating on the molecular architecture

Despite our investigations on the transcriptional regulation of the *C. elegans* oscillator, a clear understanding of the molecular architecture of the oscillator remains obscure. It seems likely that a developmental oscillator might have evolved backup mechanisms in order to be more robust against mutation events. Hence, if redundancy in the regulation of oscillations exists, approaches such as the luciferase RNAi screen on transcription factors might not have identified the complete spectrum of candidate transcription factors. Assuming that transcription factors act in concert or redundantly at the core of the oscillator and that a compromised core oscillator leads to larval lethality or arrest, we might examine interesting transcription factors in a synthetic lethality screen. A synthetic RNAi screen with all oscillating transcription factors is beyond feasibility at the moment, however, testing synthetic lethality or increased phenotypes for transcription factors that are potential core oscillator components (as identified in a previous screen, Meeuse et al., in preparation) with all other oscillating transcription factors remains a possible strategy. This strategy, however, assumes that the oscillator is regulated mainly by rhythmic mRNA abundance of transcription factors and cannot reveal post-translational regulations such as protein degradation or post-translational modifications of regulatory proteins that might be important for the oscillator. Induced random mutagenesis experiments might reveal such regulation by modifying the amino acid sequence of these proteins that are relevant for post-translational regulation. However, the identification of potentially interesting mutants from random mutagenesis may be difficult as their phenotypes might be mild and thus, identification probably requires monitoring of the developmental progression. On the other hand, mutants with strong developmental phenotypes such as larval arrest could be easily identified. In both cases, mild and strong phenotypes, where and how these genes act in the oscillator architecture requires detailed follow-up analyses.

4.2 Is BLMP-1 rhythmically active?

The timed depletion of BLMP-1 in the luciferase assay resulted in an increase of molt duration depending on the time of BLMP-1 degradation (section 2.4, *blmp-1* manuscript). While this result further implies BLMP-1 as a regulator of molts durations, it does not necessarily prove a rhythmic

function of BLMP-1 per se. Earlier downregulation potentially leads to lower levels of BLMP-1 at the time when it is needed and thus results in a longer molt duration. To clearly show a rhythmic function of BLMP-1, an elegant experiment would encompass providing sufficient amounts of BLMP-1 in a defined narrow window in a *blmp-1* null background and achieve a rescue of the mutant phenotypes.

4.3 Is BLMP-1 a coupling factor and do multiple oscillators exist?

In order to validate our observation that loss of blmp-1 uncouples groups of oscillating genes, we plan to repeat the *blmp-1* mutant RNA sequencing time course followed by statistical analysis on fold changes. Hence we will be able to confidently state that the observed differences and the uncoupling can be reproduced. Furthermore, the uncoupling of gene expression and development as we see it in the single worm imaging for *F16B4.4* should be confirmed with an additional transcriptional reporter of similarly behaving transcript as *F16B4.4* in *blmp-1* RNAi condition. Upon validation of gene expression uncoupling to development we can further investigate relevant promoter sequences that are involved in the coupling / uncoupling. Promoter dissections of reporters followed by single worm imaging of their expression will reveal whether a particular promoter sequence abolishes the coupling without affecting (oscillatory) gene expression in general. We might however also face the caveat that coupling and gene expression are regulated within the same 500bp sequence and are aware of the fact that we might not immediately reveal the sequence that is responsible for the coupling alone.

Further validation of our hypothesis that multiple coupled oscillators might exist would benefit from additional investigations. Our initial attempts to investigate gene expression changes in the *blmp-1* mutant probably suffered from extreme effects arising from the asynchrony of the worm population while in the *aid::blmp-1* time course we probably did not degrade BLMP-1 sufficiently to reveal all targets. We propose to apply single worm sequencing to solve these issues by sequencing *blmp-1* (and additional) mutants in a time-course experiment. If only a subgroup of gene expression oscillations is affected in the *blmp-1* mutant we can still apply pseudotiming to order mutant worms according to developmental time. Hence we hope to acquire a synchronized time course by pseudotiming individual *blmp-1* mutants (similar to single worm imaging), allowing us to observe misregulated oscillating genes relative to genes that are not under the control of BLMP-1. If all oscillating genes are uncoupled with to slightly different extents as the

blmp-1 mutant time course suggests we might profit from additional single worm imaging results where we image two transcriptional reporters with different fluorophores in parallel, one for a severely uncoupled gene and the other for a coupled gene.

Furthermore, we hope to eventually achieve an accurate shifting of *blmp-1* peak expression, as for example by optogenetics (Krueger et al., 2019). Such a system is under development in our lab and would ideally allow us to temporally control *blmp-1* mRNA levels with fast responses and therefore, in combination with RNA sequencing we hope to further unravel gene expression changes induced by BLMP-1.

The epistatic behavior of DRE-1 with BLMP-1 might inspire further experimental approaches to obtain insights into how BLMP-1 and DRE-1 are integrated in the architecture of the oscillator. Under the assumption that the lethality of DRE-1-depleted larvae mainly arises from elevated BLMP-1 protein levels, RNA sequencing of these animals in a time course will reveal the resulting transcriptional changes. Comparing these results with the *blmp-1(tm548)* mutant time course, we expect to observe delayed peak expression of the BLMP-1 targets, as opposed to the precocious expression detected in *blmp-1(tm548)* mutant animals.

Finally, the coupled oscillators also need to be synchronized with the linear development which is regulated by the heterochronic pathway. The exact mechanism of how BLMP-1 is involved in the coupling between linear and rhythmic development and what other factors might contribute to such a coupling remains to be determined but previous studies indicated that BLMP-1 regulates LIN-29, a factor regulating the larval to adult transition (Horn et al., 2014).

4.4 Oscillator initiation from checkpoints

The observations that the oscillator arrests at a specific oscillator phase that corresponds to the phase at molt exit (ecdysis) and that worms can arrest development after the molts (Schindler et al., 2014) is indicative of the presence of a checkpoint function which might connected to nutrient input or sensing. It was shown that short-term feeding for roughly 30 – 60 minutes after the molt can overcome or prevent an arrest (Schindler et al., 2014). Therefore the question arises whether the oscillator can be initialized through a short pulse of feeding to complete another cycle, hence acting similar to a forced oscillator. While we can only speculate about such a scenario so far, it poses interesting questions to be addressed. For example, is the initiation mechanism to start the

oscillator shared between L1 / dauer arrested worms and L2, L3, L4 arrested animals, or are there distinct mechanisms at work?

A first entry point to address this question is to investigate the release of L1 arrested worms in further detail, potentially by feeding L1 arrested worms for increasing durations until we can induce the oscillator to progress to L2. Hence we can speculate to see the initiation of the oscillator only after 5 hours of feeding, the time when worms are able to pass the first checkpoint. Further investigations into the initiation of the oscillator in L1 might involve a screen for either delayed or precocious initiation of the oscillator to find factors involved in the initiation process. The results of such a screen need to be interpreted with caution however, as it might contain false positive hits arising from additional factors involved in general growth pathways.

Since the checkpoint decision was proposed to be genetically encoded (Schindler et al., 2014), targeted mutations in the insulin signaling pathway components combined with RNA sequencing might provide insights into the nutrient-dependent checkpoint decision and its connection to the oscillator.

In general, investigations into the response of the oscillator in regard to starvation will further reveal characteristic behavior indicative of the underlying regulation. As an entry point to address this point, observations of the oscillator behavior during the arrest and the release from the checkpoint followed by a comparison to the gene expression that we see in in adults and the L1 and dauer release will be informative.

5 Materials and Methods

5.1 5’ UTR exchange

Cloning

The annotated 5’ UTR from Wormbase for the *F11E6.3* promoter (http://www.wormbase.org/db/get?name=F11E6.3.2#06--10;class=transcript) with the sequence

5’acaaacataaattcttctgcaaattcatttcttcttctttacagttttcttagtccttgcatttcttctcttcgttacaatcatatcagagctttatattttt aggtaacc **3’** was replaced with the long *actin-1* (*act-1*) 5’ UTR with the sequence

5’tttaatttttcaggtacattaaaaactaatcaaa **3’** as annotated by Wormbase using the transcript *T04C12.6.10* (http://www.wormbase.org/db/get?name= T04C12.6.10#06--10;class=transcript). The *F11E6.3* promoter lacking its endogenous 5’ UTR as well as the *act-1* 5’ UTR were amplified by PCR and cloned into pYPH0.14 by Gibson cloning. This construct was named “pYPH5_exUTR1*”* and injected into ChrII MosSCI worms to obtain HW2520.

Calculation of gfp mean expression percentage

We calculated the fold difference in $\log_2$ between *gfp* and *F11E6.3* by subtracting the mean Ct value of *F11E6.3* from the Ct value of *gfp*. Since low Ct values represent high expression, we multiplied by -1. (I)

$$FC = -1 * mean(Ct_{gfp}) - mean(Ct_{F11E6.3}). \quad \text{I}$$

Since the fold change is in $\log_2$, we obtain the percentage of expression of *gfp* relative to *F11E6.3* by calculating 2 to the power of the fold change (II)

$$rel_{expr} = 2^{FC}. \quad \text{II}$$

5.2 Confocal imaging of transcriptional reporters

Imaging:

Worms were placed on a glass slide with 3ul levamisole (10mM) and covered with a coverslip in order to image them using a confocal microscope (Axio Imager Z2 + LSM 700 scanning head) with a 40x oil objective. In order to obtain consistent results, the region around the vulva was imaged using a z-stack to cover the layer of hypodermal cells. Before image acquisition, laser power was measured and adjusted to around 190uW with a power meter (THORLABS, PM100D) connected to a Microscope Slide Photodiode Power Sensor (THORLABS, S170C) and additionally controlled with an argolight slide (Argo-HM slide, ARGOLIGHT, a Precision Company) to ensure that we obtain similar fluorescence values across measurements. Laser power was usually set between 5.5 and 6%. In addition to the fluorescent images, a brightfield image was recorded, showing the vulva of the respective worms that was later used for retrospective staging.

Data analysis

To quantify GFP intensities in each nucleus per worm, a customized KNIME (*KNIME Analytics Platform 3.3.0*) workflow was used

(see:https://nodepit.com/workflow/com.nodepit.space%2Fyannickhauser%2Fpublic%2Fhausyann3_Pdaf-6_WT_BG.knwf) in which all the worms were manually classified in 10 L4 larval sub-stages based on vulva morphology, followed by a 3D segmentation and GFP intensity measurement of the individual nuclei. To do so, the GFP images were first background subtracted using the node "*ImageJ Macro*" (*run("Subtract Background...", "rolling=50 stack");*), followed by a "*Gaussian Convolution*" (sigma = 2). The cells were first segmented in 2D using Otsu thresholding with the "Global Thresholder" node followed by a "*Connected Component Analysis*" (*Connection Type = "FOUR-CONNECTED"*). Cell clumps were then separated using the "*Waehlby Cell Clump Splitter*" and a 3D segmentation was performed by first eroding the current segmentations using "*Morphological Image Operations*" (*Connection Type = FOUR-CONNECTED*) followed by connecting the segments in 3D using the "Connected Component Analysis" node in three dimension and a "Voronoi Segmentation" using the segments as seeds. In order to remove undesired segments due to auto fluorescence, these segments were removed manually by highlighting the auto fluorescent objects and removing them from the analysis using the "Interactive Segmentation View". Finally, the remaining 3-dimensional segmented cells were

analyzed using the "Feature Calculator (BETA)" node to calculate the mean intensity of each cell. The software *R* (*R version 3.6.1 (2019-07-05)*) was used to analyze and plot the cell intensities using the packages *dplyr* (*dplyr_0.8.3*) and *ggplot2* (*ggplot2_3.2.0*).

Auxin treatment:

Liquid cultures were prepared according to the *aid::blmp-1* RNA sequencing experiment.

Cosine fitting:

Cosine fitting was performed on the mean normalized GFP intensities and as described in (Meeuse et al., 2019).

5.3 *aid::blmp-1* time course

Liquid growth and sampling:

Synchronized L1 by bleaching and overnight M9 (42 mM Na2HPO4, 22 mM KH2PO4, 86 mM NaCl, 1 mM MgSO4) incubation were added to 300ml S-Medium with OP50 at OD_{600} = 3.5 to a concentration of 1worm/ul medium. The culture was incubated at 20°C on a platform shaker at 240 rpm. Worms were grown for 20 hours before auxin was added to a final concentration of 250 µM and 3.9µM followed by sampling. For the mock condition, vector (ethanol) was added to a final concentration of 0.25%. From 20.5 – 49.5 hours of development, following procedure was repeated for every condition in 30min intervals: Worms were harvested by pipetting 400-500ul of medium into 15ml falcon tubes and centrifuged at 500g for 1 minute, followed by three washes in M9. After removal of supernatant, 200ul of Norgen lysis buffer (Single Cell RNA Purification Kit, Cat. 51800) were added and 100ul were transferred each into two different 1.5ml Eppendorf tube (one for experiment, one for backup). Both tubes were snap frozen in liquid nitrogen and stored at -80°C for further processing.

RNA isolation:

Before RNA isolation, 5 cycles of freeze-thaw were performed. Then ethanol was added and RNA was isolated using the Norgen RNA isolation kit (Single Cell RNA Purification Kit, Cat. 51800, starting from step 2). DNase treatment was performed on columns (according to Norgen kit protocols) and RNA was eluted in 12ul RNase free water. RNA quality was assessed with an

Agilent Bioanalyzer prior to library preparation using the TruSeq Illumina mRNA-seq (stranded – high input) protocol, followed by the Hiseq50 Cycle Single-end reads protocol on HiSeq2500.

Processing of RNA seq data for the aid::blmp-1 time course:

The RNA-seq samples were mapped to the *C.elegans* genome (ce10) using the R package QuasR (www.bioconductor.org/packages/2.12/bioc/html/QuasR.html) with the spliced alignment algorithm SpliceMap (Au et al., 2010) as following:

"proj <- qAlign("samples.txt","BSgenome.Celegans.UCSC.ce10",splicedAlignment=TRUE)". The expression count table was created with qCount(proj,exons,orientation="opposite"). For gene quantification, gene annotation from WormBase was used (WS220). To normalize for sequencing depth, each sample was divided by the total number of reads and multiplied by 1/4th of the average library size. This reduction by 1/4 was done to account for over-amplification observed in the data. The data was produced in two batches, the first one containing time points 20h-35.5h and the second one containing time points 34h-49.5h. The time points 34h, 34.5h, 35h and 35.5h were profiled in both batches and were used to fuse the two datasets into a single one. To do so, we first calculated the average log2 expression level of those common timepoints in the three conditions as well as for the two batches separately. Comparing the results from the two batches (from common timepoints) allowed us to calculate gene specific fold-changes, representing the differences between the batches caused by technical biases. We then corrected the original expression levels by adding half or the correction amount on the first batch and the other half on the second batch. This resulted in a configuration where the average expression level for each gene of the common timepoints in the first batch was identical to average expression level for each gene in the second batch. This correction was performed for the three conditions separately. This resulted in a batch-corrected expression count table that was further log2 transformed after the addition of a pseudocount of 8 in order to minimize large changes in expression caused by low count numbers.

Validation of the aid::blmp-1 sequencing TC by RT-qPCR

Liquid growth, sampling and RNA isolation were performed in the same way as the *aid::blmp-1* sequencing time course samples with the exception that only time points 30h – 41h were sampled. RNA was diluted to the same concentration and equal amounts were used for cDNA synthesis as

described in the section 2.4 (*blmp-1* manuscript). We obtained mean normalized –dCT values as described in the section 2.4 (*blmp-1* manuscript).

Transgenic aid::blmp-1 strain generation by CRISPR

As described in the section 2.4 (*blmp-1* manuscript).

5.4 Single worm sequencing

Synchronized worms by egg prep were grown at 25°C on OP50 containing 2% NGM plates with 3,000 worms per plate. Samples were then hourly taken from 16 – 31 hours after plating by washing off three plates followed by three washing steps with M9 in a 15ml falcon tube. After washing, worms were sorted into fully skirted 96-well plates using the COPAS FP worm sorter (Union Biometrica). Each well contained 5µl of lysis buffer which consisted of 4.75µl RLT plus buffer (Qiagen, Cat No./ID: 1053393) and 0.25µl Superase-In (ThermoFisher Scientific, Cat. No. AM2694). The plates were quickly checked for successful sorting by microscopy, sealed with a PCR film (558/MJ) and then immediately transferred to -80°C. After sampling, the worms were lysed completely by freeze-thaw cycles, switching plates 5 times from a metallic rack on dry ice to a PCR block at 42°C and back. It usually took 15 seconds for the liquid to thaw. Plates were then stored at -80°C before further processing. Before proceeding with mRNA capture, the plate to be processed was incubated at 72°C for 3 minutes to further increase lysis efficiency.

RNA isolation and amplification

Adapted from Macaulay et al., 2015. The mRNA was captured using prepared Oligo-dT beads, washed 2X and prepared for reverse transcription using the BRAVO NGS workstation (Agilent). After adding RT buffer by the BRAVO robot, reverse transcription was performed on two PCR cyclers using 42°C for 60min, followed by 50°C for 10min and 70°C for 15min. Following reverse transcription, the PCR pre-amplification was performed by adding the PCR preamp mix to the wells using the BRAVO robot followed by purification of the pre-amplified reaction. In order to

reduce rRNA amplification and contamination, we used LNA modified oligos ("blocking oligos") in the PCR pre-amplification mix.

For a detailed protocol, please refer to the Appendix.

RNA sequencing

Libraries were prepared using the "Single worm mRNA-seq" library protocol followed by the Hiseq50 Cycle Single-end reads protocol on HiSeq2500.

Processing of RNA seq data

Adapters were trimmed using cutadapt (version 2.3), with an error-rate of 0.1, minimum-length of 15 and and overlap of 3. RNA-seq data were mapped to the *C. elegans* ce10 genome using STAR (version 2.7.0f) using the parameter "twopassMode Basic", followed by counting the reads using HTSeq (version 0.11.2) with the following settings: "--format bam; --stranded no; --type exon; --idattr gene_id; --mode union; --nonunique none; --secondary-alignments ignore; --supplementary-alignments ignore".

Only samples with at least 1 million reads were taken into account for further processing, resulting in 760 good quality single worm samples out of 1,317 sequenced samples (~60%). Counts were normalized to library size, $\log_2$-transformed expression values of oscillating genes (as in Meeuse et al., 2019) were selected (n=3,739) and time points were combined using pandas (version 0.25.1). The expression values were standardized using the StandardScaler from scikit-learn (version 0.21.3) and principal component analysis was performed using the PCA algorithm from scikit-learn. The angle of each worm was then calculated using "*PCs = complex(PC1, -PC2)*" followed by "*angle = numpy.angle(PCs)*" using numpy (version 1.17.4). The identification of the individual cycles was performed using the clustering algorithm DBScan (Ester et al., 1996; Schubert et al., 2017) from scikit-learn which clusters based on the density of datapoints with the command "*clustering = sklearn.cluster.DBSCAN(eps=0.3, min_samples=10).fit(angular_data)*". Datapoints that could not confidently be assigned to one cycle were excluded from the downstream analysis. Sorting of datapoints within cycles was performed using pandas' *DataFrame.sort_values()*. In order to stack the individual cycles on top of each other, we added $2 * \pi * cycle\_number$ to each datapoint. Since our cycle numbers range from 0 to 3, this did not change the angle of the earliest samples. After pseudotiming, the angular information was merged

with the gene expression data and plotted. For the binned data plots, we used scipy's binned_statistic (version 1.3.1).

The code used for sample processing and for pseudotiming single worm sequencing data can be accessed on Github:

https://github.com/fmi-basel/ggrosshans_single_worm_time_series/tree/SWS_script_from_yannick/process_single_worm_RNAseq

5.5 Cell-based single worm imaging analysis

The cell-based intensity measurement was performed in KNIME using the workflow "*Worm images_cell_Quantif_final.knwf*"

(see:https://nodepit.com/workflow/com.nodepit.space%2Fyannickhauser%2Fpublic%2FWorm%20images_cell_Quantif_final.knwf). GFP images from the single worm imaging experiment were loaded and background subtracted using the imageJ Macro node with the setting "*run("Subtract Background...", "rolling=50 stack");*" followed by a "Gaussian convolution" (*sigma = 1*) in x and y dimensions. GFP images were then thresholded using a manual threshold of 40. The resulting segmented objects were filtered based on segment area using an allowed segment area between 0 – 40,000 to remove larger objects that are not cells. We then performed a "*Connected Component Analysis*" to label segments followed by the "*Waehlby Cell Clump Splitter*" to separate individual cells touching each other (with parameters: "*distance merge threshold = 2, size merge threshold = 50*") in x and y dimension. Following the segment labelling in 2D, we performed the "*Morphological Image Operations*" to erode the segments using the two-dimensional structuring element "*sphere*" (*radius = 1.0*). After erosion of the segment, we connected the segments in 3D using the "*Connected Component Analysis*" node over x, y and z and filtered segments based on size ranging from 30 – 5,000 which removed rare cases of potentially remaining big cell clusters. The resulting small round segments were used as seeds for a "*Voronoi Segmentation*" further improving the segmentation. Based on this segmentation, we calculated the mean intensity and standard deviation of each segmented cell in 3D using the "*Feature Calculation (BETA)*" node.

The GFP mean intensities and standard deviations were plotted in python using the packages matplotlib (*matplotlib==3.1.1*), pandas (*pandas==0.25.1*) and seaborn (*seaborn==0.9.0*). To

indicate the times of molts and calculate the phase at molt entry and exit, we used the same analysis as described in Meeuse et al., 2019. The calculation of significant differences between the cell-based and worm-based phases at molte exit and entry was performed using Welch two-sample t-test using "*scipy.stats.ttest_ind(cell-based_data, worm-based_data, equal_var = False*)" from the scipy package (*scipy==1.3.1*).

5.6 Segmentation of worms using a convolutional neural network

The segmentation of worms in SWI chambers was obtained using a convolutional network (CNN). We manually curated the previously existing segmentation resulting from Ilastik for 268 SWI images obtained from two SWI datasets (159 from SWI on HW2524, 20180601 and 119 from SWI on HW2526, 20190719). 41 of these images were randomly sampled for the validation set. During training, the images were augmented using random noise and flips in order to increase robustness of the CNN against potential image quality fluctuations in future datasets. The images were preprocessed using a minimum projection over the image stack consisting of 23 images per time point and worm, resulting in a single 2D image per time point for each worm and generating the input for the CNN training. We decided to use a UNet-like CNN (Ronneberger et al., 2015) architecture with residual connections and trained it using the binary cross entropy loss with Adam (Kingma and Ba, 2015) as optimizer. The CNN's output was generated using a sigmoid activation function resulting in a probability map for foreground which in our case represented the worm. These probability maps ranging from 0 – 255 for each pixel were then thresholded at value 20 to obtain binary segmentation maps used as masks in the KNIME workflow to analyze GFP intensities in the segmented worms from the GFP images. The CNN was developed in Python and can be accessed from Github (https://github.com/fmi-basel/faim-worm-segmentation).

5.7 Segment analysis of single worm imaging data

As described in Meeuse et al., 2019 with the exception that the GFP intensities were analyzed in sections from anterior to posterior, which can be adjusted in the node 270 "Table Creator" in the KNIME workflow

(see:https://nodepit.com/workflow/com.nodepit.space%2Fyannickhauser%2Fpublic%2FWorm%20images_final_with%20workaround.knwf).

5.8 CRISPR tagging of *dre-1* with *aid:3xFLAG*

Tagging of *dre-1* with the auxin inducible degron (aid) and 3xFLAG was performed using the same *dpy-10(cn64)* co-conversion CRISPR/Cas9 strategy as used for the *aid::blmp-1* strain (see section 2.4, *blmp-1* manuscript, Arribere et al. 2014). Two sgRNAs with the sequences

5' ACGCCGATCTCAACGGAAAC **3'** (sgRNA1, YK12_YK13) and

5' GAATGATATATTTGTGGAGA **3'** (sgRNA2, YK3_YK4)

were used to cleave genomic DNA around the *dre-1* stop codon, followed by rescue with the gBlock sequence from IDT

5'tgagaagaacttttgttgctccgctgttcggatttcgctacaaaaattaaaattgtaaattcaaattcaaagtttctagtacaaagcgactcca
aaaaaagagaaaaatcgtttattatttttctttttttcaataaaaataatttcagattcttctgcgactgtggtgctggaactctcgaacggcactgtc
acctgcaaaatgtgccacgtgacaacgacactgtctatgactcagcgacgccgatctcaacggaaacaggcaccgaaattatgcctaaaga
tccagccaaacctccggccaaggcacaagttgtgggatggccaccggtgagatcataccggaagaacgtgatggtttcctgccaaaaatc
aagcggtggcccggaggcggcggcgttcgtgaaggactacaaagaccatgacggtgattataaagatcatgacatcgattacaaggatga
cgatgacaagtaaggacgaaaaactttcagcttctccacaaatatatcattcacttcttctctcatgttcgtgttttgtattcattatcacatcacac
tacccatttcgcagtctttcataccgatttgagatctctttctctttcctcccaattattttcttcgaacttttttggtgtaatttaacactctagctttttttt
tcgttcacgtttttccgcattgcttatcacttttatctttcaacctttttaaagtgcaaactttctgtgatatagttga **3'**

to insert the *aid::3xFLAG* tag 5' of the *dre-1* stop codon (*aid*: blue, *3xFLAG*, yellow, stop codon: red, overlap to genomic locus: black).

The injection was performed in wild-type animals which were injected with 20 ng/µL gBlock, 100 ng/µL sgRNA plasmid, 20 ng/µL AF-ZF-827 (Arribere et al., 2014), 50 ng/µL pIK155 (Katic et al., 2015) and 100 ng/µL pIK208 (Katic et al., 2015).

5.9 Worm strains used in this thesis

Genotype	HW number
xeSi114[tbb-1p::GFP(PEST)-H2B::unc-54 3'UTR, unc-119 (+)] II;	1190
EG6699,xeSi131[*F58H1.2p::GFP::H2B::Pest::unc-54 3', unc-119*+] II	1360
EG6699,xeSi132*[R12E2.7p::GFP::H2B::Pest::unc-54 3', unc-119*+] II	1361
EG6699, xeSi136[*F11E6.3p::GFP-H2B-Pest::unc-54 3'UTR; unc-119* +] II	1370
EG6699, xeSi137[*F33D4.6p::GFP-H2B-Pest::unc-54 3'UTR; unc-119* +] II	1371
EG6699, xeSi138[*C05C10.3p*::GFP-H2B-Pest::unc-54 3'UTR; unc-119 +] II	1372
EG6699, xeSi159[*daf-6p::GFP::H2B::Pest::unc-54 3'UTR; unc-119* +] II	1429
EG6699, xeSi160[*daf-6Δ4p::GFP::H2B::Pest::unc-54 3'UTR; unc-119* +] II	1431
EG6699, xeSi165[*daf-6 1xcons:: Δpes-1p0::GFP::H2B::Pest::unc-54 3'UTR; unc-119* +] II	1436
EG6699, xeSi166[*Δpes-10p::GFP::H2B::Pest::unc-54 3'UTR;unc-119* +] II	1437
EG8079, xeSi296[eft-3p::luc::gfp::unc-54 3'UTR] II	1939
EG8082,xeSi311 [eft-3p::luc::gfp::unc-54 3'UTR, unc-119(+)] V	1992
xe80 blmp-1(aid::blmp-1) I; EG8079, xeSi296 [eft-3p::luc::gfp::unc-54 3'UTR, unc-119(+)] II; EG8080, xeSi376 [eft-3p::TIR1::mRuby::unc-54 3'UTR, cb-unc-119(+)] III	2120
EG6699, xeSi160[daf-6Δ4p::GFP::H2B::Pest::unc-54 3'UTR; unc-119 +] II ; blmp-1(tm548) I	2510
EG6699, xeSi433[col-10p::blmp-1::gfp::blmp-1 3'UTR; unc-119 +] II	2511
EG6699, xeSi433[col-10p::blmp-1::gfp::blmp-1 3'UTR; unc-119 +] II ; EG8082, xeSi311[eft-3p::Luciferase::gfp::unc-54 3'UTR; unc-119 +] V	2514
EG6699, xeSi296[eft-3p::Luciferase::gfp::unc-54 3'UTR; unc-119 +] II ; blmp-1(tm548) I ; dre-1(dh99) V	2517
EG6699, xeSi436[F11E6.3p_act-1 5'UTR::GFP::H2B::Pest::unc-54 3'UTR; unc-119 +] II	2520
EG6699,xeSi131[F58H1.2p::GFP::H2B::Pest::unc-54 3', unc-119+] II ; blmp-1(tm548) (I)	2521
EG6699, xeSi438[R07E3.6p::GFP::H2B::Pest::unc-54 3'UTR; unc-119 +] II	2524
EG6699: xeSi440 [dpy-9p::gfp::h2b::pest::unc-54 3'UTR; unc-119 +] II	2526
EG8079, xeSi296[eft-3p::Luciferase::gfp::unc-54 3'UTR; unc-119 +] II ; blmp-1(tm548) (I)	2532
EG8079, xeSi296[eft-3p::Luciferase::gfp::unc-54 3'UTR; unc-119 +] II ; dre-1(dh99) V	2534
EG6699, xeSi160[daf-6Δ4p::GFP::H2B::Pest::unc-54 3'UTR; unc-119 +] II ; blmp-1(s71) I	2535
EG6699, xeSi434[eft-3p::blmp-1::gfp::blmp-1 3'UTR; unc-119 +] II ; EG8082, xeSi311[eft-3p::Luciferase::gfp::unc-54 3'UTR; unc-119 +] V	2538
blmp-1 (xe180[3xFlag::blmp-1]) I ; xeSi296[eft-3p::Luciferase::gfp::unc-54 3'UTR; unc-119 +] II	2802
blmp-1 (xe180[3xFlag::blmp-1]) I ; xeSi296[eft-3p::Luciferase::gfp::unc-54 3'UTR; unc-119 +] II ; dre-1(dh99) V	2830
xe80 blmp-1(aid::blmp-1) I; EG8080, xeSi376 [eft-3p::TIR1::mRuby::unc-54 3'UTR, cb-unc-119(+)] III ; EG6699, xeSi160[daf-6Δ4p::GFP::H2B::Pest::unc-54 3'UTR; unc-119 +] II	3079
EG6699, xeSi296 [eft-3p::luc::gfp::unc-54 3'UTR, unc-119(+)] II; EG8080, xeSi376 [eft-3p::TIR1::mRuby::unc-54 3'UTR, cb-unc-119(+)] III	3076

5.10 Plasmids used in this thesis

Vector name	Backbone	Inserts	Primers	Primer sequence
in Meeuse & Hauser et al., in submission				
pYPH0.14	pCFJ150	GFP::H2B::Pest	GFP-pest-H2B FW1 + Overhang	gcgtgtcaataatatcactcGCTAGCATGTCTAGACTTAGCCATGGC
			GFP-pest-H2B RV1 + Overhang	gccgatgcggagctcttatcTTACTTGCTGGAAGTGTACTTG
		Unc-54 3'UTR	Unc-54 3'UTR FW1 + Overhang	AGTACACTTCCAGCAAGTAAgataagagctccgcatcg
			Unc-54 3'UTR RV1 + Overhang	Aacatatccagtcactatggaaacagttatgtttggtatattggga
pYPH5	pYPH0.14	F11E6.3 promoter	F11E6.3 FW1 + Overhang	gcgtgtcaataatatcactcaggaaaacctcaaattttgttaacact
			F11E6.3 RV + Overhang	GCTAAGTCTAGACATcatggttacctaaaaatataaagctct
pYPH69	pYPH0.14	dpy-9 promoter	dpy-9 promoter FW +OH to pYPH0.14	gcgtgtcaataatatcactcgtacaatagaaaaaaagcagcaat
			dpy-9 promoter RV +OH to pYPH0.14	CCATGGCTAAGTCTAGACATctgcaataataagtattgaaaacaaga
pYPH70	pYPH0.14	qua-1 promoter	qua-1 promoter FW +OH to pYPH0.14	gcgtgtcaataatatcactcatacttttgcactacacggag
			qua-1 promoter RV +OH to pYPH0.14	CCATGGCTAAGTCTAGACATctaaatataggttaagcatgataggat
pMM001	pCFJ150	luciferase::GFP	unc-54 3'UTR + overhang gfp	GCATGGATGAACTATACAAAgataagagctccgcatcg
			gfp + overhang unc-54 3'UTR	gccgatgcggagctcttatcTTTGTATAGTTCATCCATGCC
			luc, piece2 + overhang piece 1	GACTACAAGgtaagtttaaacagttcggtactaactaacca
			luc, piece1 + overhang piece 2	ccgaactgtttaaacttacCTTGTAGTCTTGGAG
			luc, piece1 + overhang NheI and backbone	tgtcaataatatcactcGCTAGCATGGAGGACGCCAAGAA
		Unc-54 3'UTR	gfp + overhang luc::spacer (piece2)	TACCGGTAGAAAAAATGAGTAAAGGAGAAGAACTTTTCACTGG
			luc::spacer (piece2) + overhang gfp	GTGAAAAGTTCTTCTCCTTTACTCATTTTTTCTACCGGTAC
pMM002	pMM001	eft-3 promoter	Peft-3 RV primer (OH to :luciferase)	ATGTTCTTGGCGTCCTCCATtgagcaaagtgtttcccaac
			Peft-3 FW primer (OH to pCF150)	gcgtgtcaataatatcactcGCACCTTTGGTCTTTTATTGT

In *blmp-1* manuscript or Thesis				
pYPH3	pYPH0.14	F58H1.2 promoter	*F58H1.2* promoter FW 1 + OH	gcgtgtcaataatatcactcatagatgtatactaatgaaggtaatagc
			F58H1.2 promoter RV1 + OH	GCTAAGTCTAGACATcattcctgcgtagaagcg
pYPH4	pYPH0.14	R12E2.7 promoter	*R12E2.7* promoter FW 1 + OH	gcgtgtcaataatatcactcaaatttttaaaatatcttttatttgaaaatt
			R12E2.7 promoter RV1 + OH	GCTAAGTCTAGACATcatgatgattgagatgtgttgaaa
pYPH8	pYPH0.14	F33D4.6 promoter	*F33D4.6* promoter FW + OH	gcgtgtcaataatatcactctgtgaaacggaaaaaccatgc
			F33D4.6 promoter RV + OH	GCTAAGTCTAGACATctgaaacatacatttaattctaattagt

pYPH9	pYPH0.14	C05C10.3 promoter	*C05C10.3* promoter FW + OH	gcgtgtcaataatatcactcaagttatcttttaaatcttgaataaaaa
			C05C10.3 promoter RV + OH	GCTAAGTCTAGACATtttatctgaatgaaaatttttttaattt
pYPH38	pYPH0.14	Pdaf-6Δ4 promoter (Δ-1500 to -2000)	*daf-6* promoter RV + OH	GCTAAGTCTAGACATAGAAAACCTGTAAAATACAGAAAC
			daf-6 promoter FW + OH	GCGTGTCAATAATATCACTCCGCCAATGGGGATTTTGT
pYPH39	pYPH0.14	daf-6Δ3 promoter (Δ-1000 to -1500) piece1	*daf-6* promoter FW0 + OH (to pCFJ150)	GCGTGTCAATAATATCACTCTGTTAGTTGCAATCACCTC
			daf-6Δ3 promoter RV2 + OH	GAAAACAAGGAGTGATGGTAAAATTTTCACACAAAAA
		daf-6Δ3 promoter (Δ-1000 to -1500) piece2	*6Δ3 promoter* FW2 + OH	TTTTTGTGTGAAAATTTTACCATCACTCCTTGTTTTC
			daf-6 promoter RV + OH	GCTAAGTCTAGACATAGAAAACCTGTAAAATACAGAAAC
pYPH40	pYPH0.14	daf-6Δ2 promoter (Δ-500 to -1000) piece1	*daf-6* promoter FW0 + OH (to pCFJ150)	GCGTGTCAATAATATCACTCTGTTAGTTGCAATCACCTC
			daf-6Δ2 promoter RV3 + OH	AGAGGCTGGAAAAAAGCTGTTAGAAATCAACAAGATAGAGAGA
		daf-6Δ2 promoter (Δ-500 to -1000) piece2	*daf-6Δ2* promoter FW3 + OH	ATCTTGTTGATTTCTAACAGCTTTTTTCCAGCCTCT
			daf-6 promoter RV + OH	GCTAAGTCTAGACATAGAAAACCTGTAAAATACAGAAAC
pYPH41	pYPH0.14	daf-6Δ2 promoter (Δ0 to -500)	*daf-6* promoter FW0 + OH (to pCFJ150)	GCGTGTCAATAATATCACTCTGTTAGTTGCAATCACCTC
			daf-6Δ1 promoter RV + OH	GCTAAGTCTAGACATCATTTCAATATTTGGTAATTTGCC
pYPH42	pYPH0.14	daf-6Δcons promoter piece1	*daf-6* promoter FW0 + OH (to pCFJ150)	GCGTGTCAATAATATCACTCTGTTAGTTGCAATCACCTC
			daf-6Δcons promoter RV + OH	ACGGTTAAAATTACTTTTTGGATAGTCAGTTCAATGAGGAA
		daf-6Δcons promoter piece2	*daf-6Δcons* promoter FW + OH	CCTCATTGAACTGACTATCCAAAAAGTAATTTTAACCGTCT
			daf-6 promoter RV + OH	GCTAAGTCTAGACATAGAAAACCTGTAAAATACAGAAAC
pYPH50	pYPH0.14	cons_element	*daf-6* conserved promoter element FW primer + OH (to pCFJ150)	gcgtgtcaataatatcactccatatcttcccatca
			daf-6 conserved promoter element RV primer + OH (to Δpes-10 minimal promoter)	AATTTGCAAAAAATCGATaaaccaacttgaacaaatattg
		Δ*pes-10* minimal promoter	Δ*pes-10* minimal promoter FW primer + OH (to conserved element Pdaf-6)	tatttgttcaagttggtttATCGATTTTTTGCAAATTACG
			Δ*pes-10* minimal promoter RV primer + OH (to *gfp::pest::h2b*)	GCTAAGTCTAGACATCTGAAAGTTAAAAATTACAG
pYPH51	pYPH0.14	Δ*pes-10* minimal promoter	Δ*pes-10* minimal promoter FW primer + OH (to pCFJ150)	gcgtgtcaataatatcactcGCTAGCATCGATTTTTTGCAA
			Δ*pes-10* minimal promoter RV primer + OH (to *gfp::pest::h2b*)	GCTAAGTCTAGACATCTGAAAGTTAAAAATTACAG
pYPH61	pYPH0.14	*col-10* promoter	*col-10* promoter FW + OH (to pCFJ150)	gggcgtgtcaataatatcactcatcttcttttttcatttcaatct
			col-10 promoter RV + OH (to *gfp::pest::h2b*)	CCATGGCTAAGTCTAGACATgactgaaagccaggtac
pYPH71	pYPH0.14	*R07E6.3* promoter	*R07E6.3* promoter FW + OH (to pCFJ150)	gcgtgtcaataatatcactcgaaataatcattgatgataaaattaaataa
			R07E6.3 promoter RV + OH (to *gfp::pest::h2b*)	CCATGGCTAAGTCTAGACATtttgtaggacgctctg

pYPH78	pYPH0.14	*F16B4.4* promoter	*F64B4.4* promoter FW + OH	gcgtgtcaataatatcactcatctattatcgttaaatgataactgtagt
			F64B4.4 promoter RV + OH	CCATGGCTAAGTCTAGACATgattgaacaaaatcggaatgatg
pYPH5_exUTR1	pYPH0.14	*F11E6.3* promoter + act-1 5'UTR	*F11E6.3* promoter FW + OH	gcgtgtcaataatatcactcaggaaaacctcaaattttgtt
			F11E6.3 promoter RV + OH1	ttgattagtttttaatgtacctgaaaaattaaagccgattcaaccatgac
			F11E6.3 promoter RV + OH2 (adds full overhang after OH1)	CCATGGCTAAGTCTAGACATtttgattagtttttaatgtacctgaaaaa
pYPH_BLMP1_GFP	pCFJ150	*blmp-1*	*blmp-1* FW primer + OH (to pCFJ150)	gcgtgtcaataatatcactcGCTAGCATGGGTCAAGGAAGTGGG
			blmp-1 RV primer + OH (to 2xTY1w::EGFP)	TCCTGATTGGTATGCACTTCTGGATAATGCGGCAATCC
		2xTY1w::EGFP::blmp-1 3'UTR (from OP109)	*2xTY1w::EGFP::blmp-1 3'UTR* (from OP109) FW primer + OH to *blmp-1* CDS	TCGGATTGCCGCATTATCCAGAAGTGCATACCAATCAGG
			2xTY1w::EGFP::blmp-1 3'UTR (from OP109) RV primer + OH to pCFJ150	aacatatccagtcactatggAAAATAGAAACAACTTCTAGAAAGAAA
pYPH_Pcol-10::blmp1	pYPH_BLMP1_GFP	*col-10* promoter	*col-10* promoter RV + OH (to blmp-1)	TCCCCACTTCCTTGACCCATgactgaaagccaggtac
			col-10 promoter FW + OH (to pCFJ150)	gggcgtgtcaataatatcactcatcttcttttttcatttcaatct
pYPH_Peft-3::blmp1	pYPH_BLMP1_GFP	*eft-3* promoter	*eft-3* promoter RV + OH (to blmp-1)	TCCCCACTTCCTTGACCCATTGAGCAAAGTGTTTCCCA
			eft-3 promoter FW + OH (to pCFJ150)	gcgtgtcaataatatcactcGCACCTTTGGTCTTTTATTGT

6 Supplementary Figures

6.1 Single worm sequencing

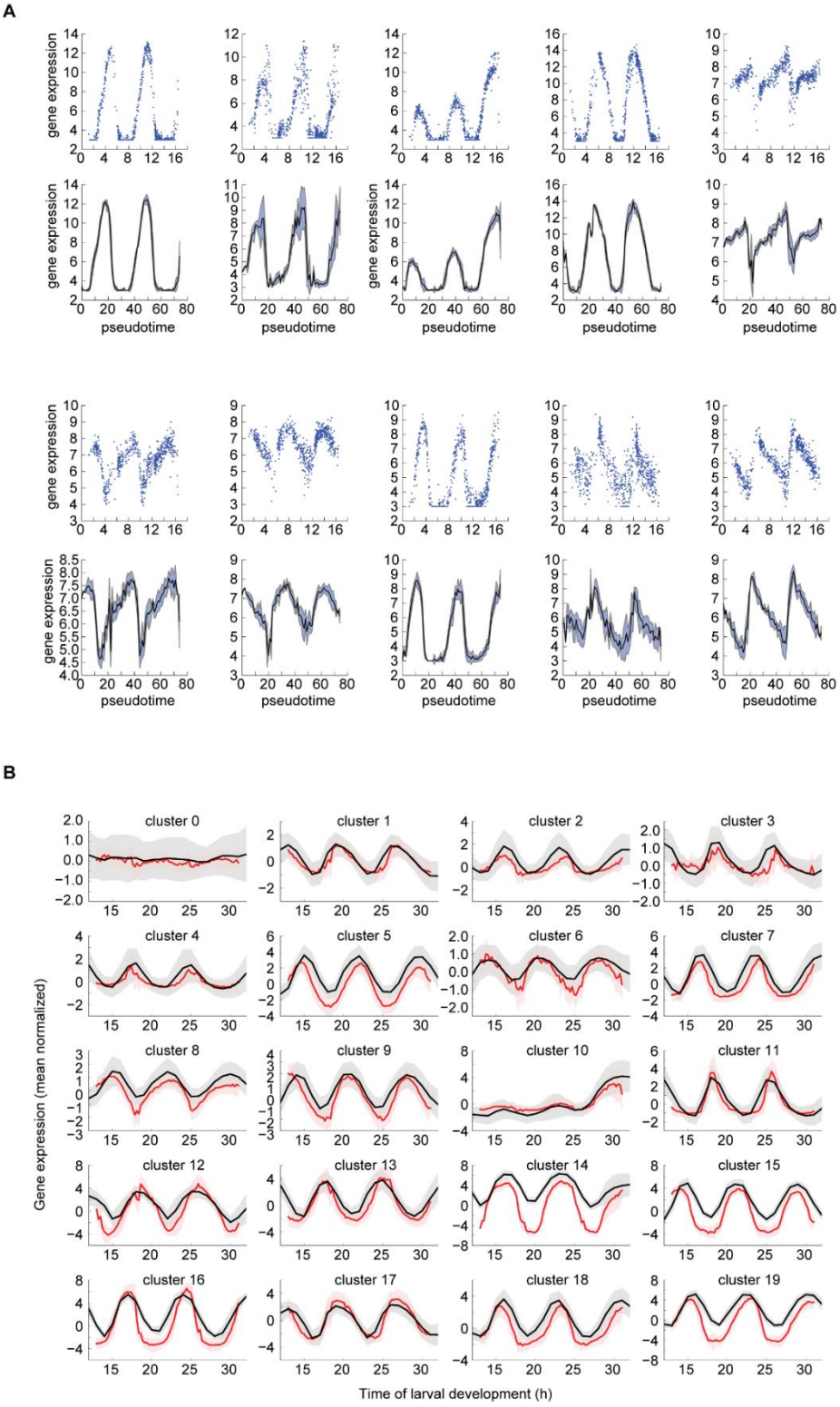

Fig S1: Additional example gene expression and all cluster comparisons to the bulk sequencing

A, Log_2-transformed gene expression traces for 10 genes with clear oscillatory behavior. Top: Pseudo-timed expression showing every individual sample, bottom: binned gene expression into equal pseudo-time bins.

B, Comparison of log_2-transformed, mean normalized gene expression clusters from single worm sequencing with to corresponding gene expression data from bulk sequencing.

6.2 *aid::blmp-1* sequencing time course

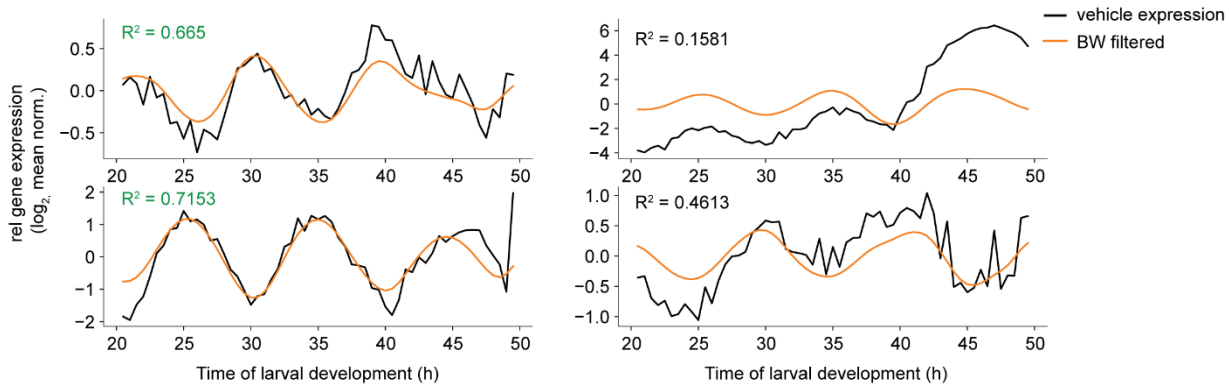

Fig S2: R^2 based thresholding to select robustly oscillating genes

A – D, Examples of oscillating genes (black) with their respective butterworth filtered signal (orange). The residuals between the butterworth filtered signal and the original signal were used to calculate the R^2. Genes with an $R^2 > 0.6$ (indicated in green) for both vehicle and auxin treatment were used for further analysis.

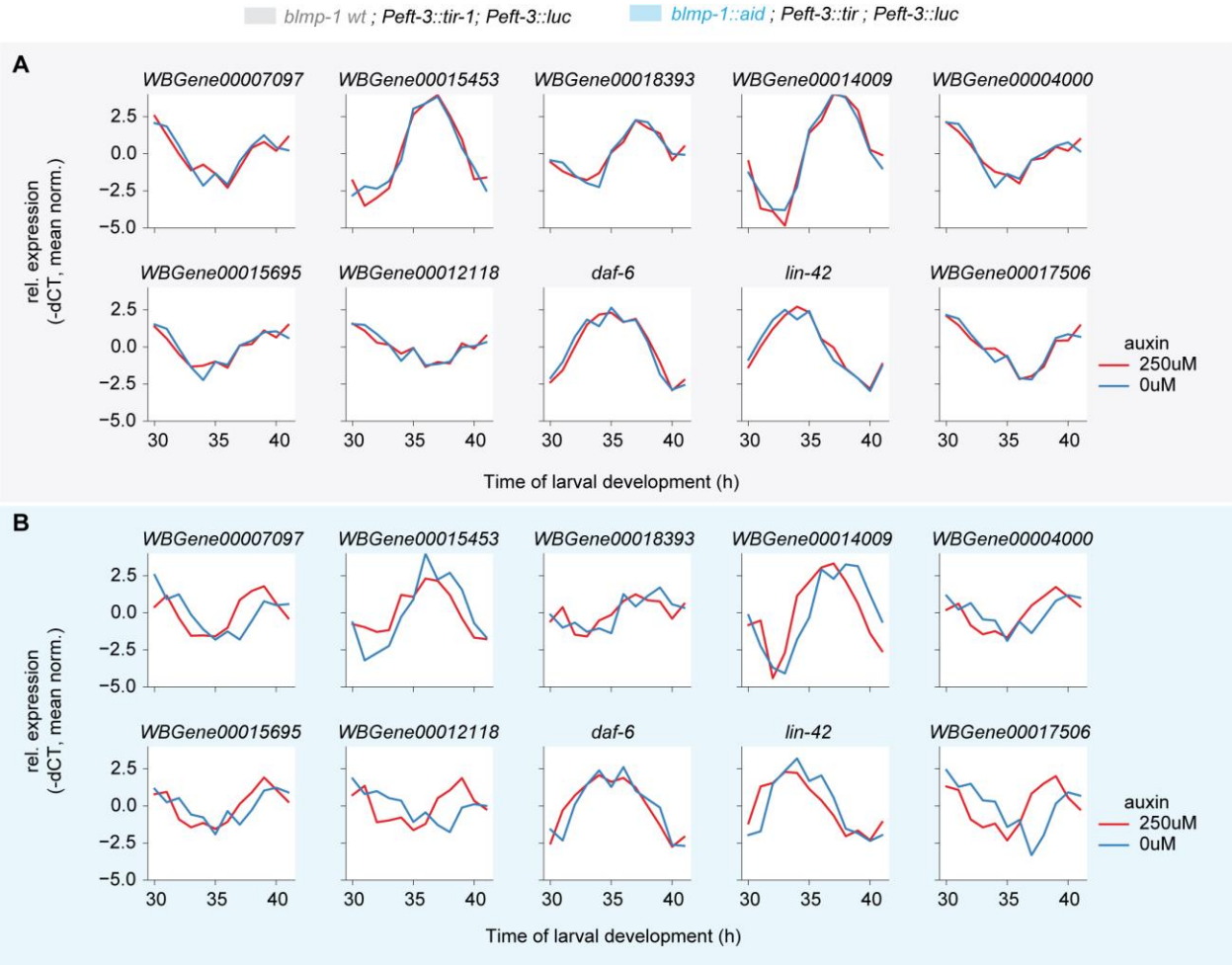

Fig S3: RT-qPCR validation of the *aid::blmp-1* time course experiment

A, RT-qPCR time course using a strain with wild-type *blmp-1* which ubiquitously expressed *tir-1* and *luciferin* in presence or absence of auxin. None of the genes responded to auxin treatment as expected due to the *blmp-1* wild-type allele.

B, RT-qPCR time course using the *aid::blmp-1* worm strain with ubiquitously expressing *tir-1* and *luciferin* in presence or absence of auxin. Genes selected from the *aid::blmp-1* sequencing time course showed reproducible behavior in the repeated RT-qPCR time course. *daf-6* did not respond in both, sequencing and RT-qPCR time courses.

6.3 BLMP-1 binding on promoter sequences

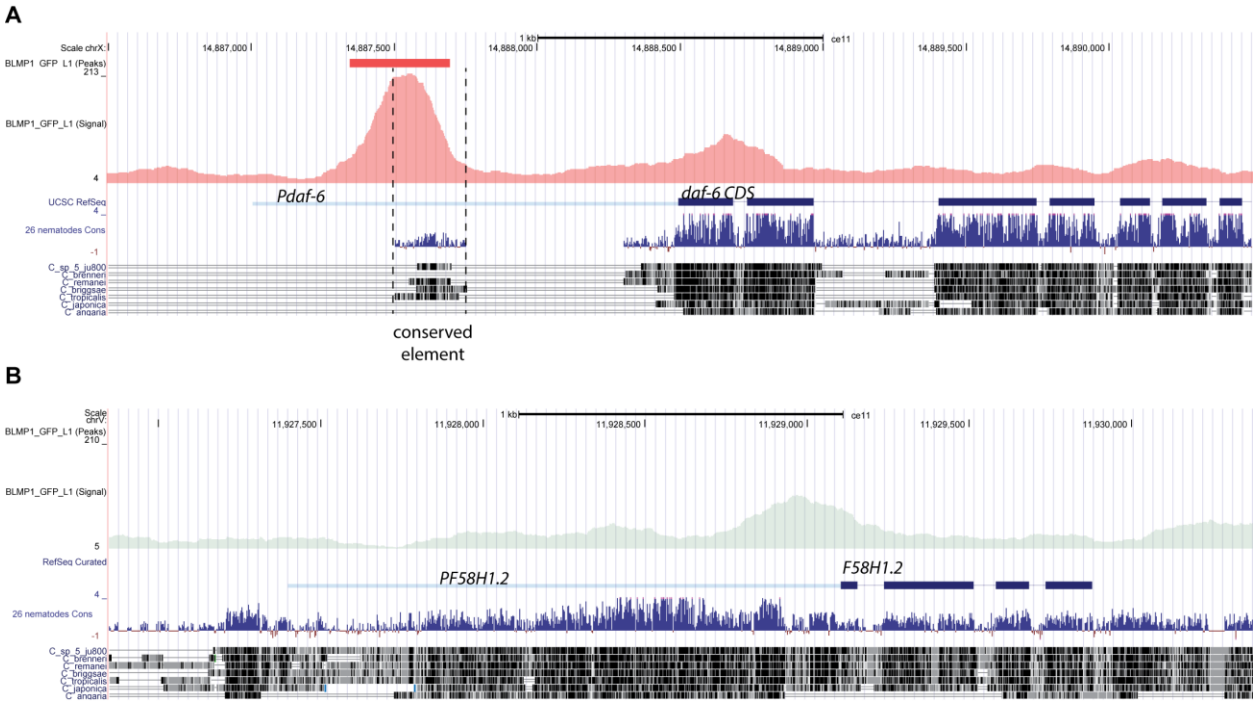

Fig S4: BLMP-1 ChIPseq analysis of publicly available data around the *daf-6* and *F58H1.2* promoters

A, BLMP-1 shows increased signal in the *daf-6* promoter in the region of a conserved promoter element.

B, The *F58H1.2* promoter does not show strong binding in the BLMP-1 ChIP sequencing data.

6.4 Epistatic behavior of *blmp-1* with *dre-1*

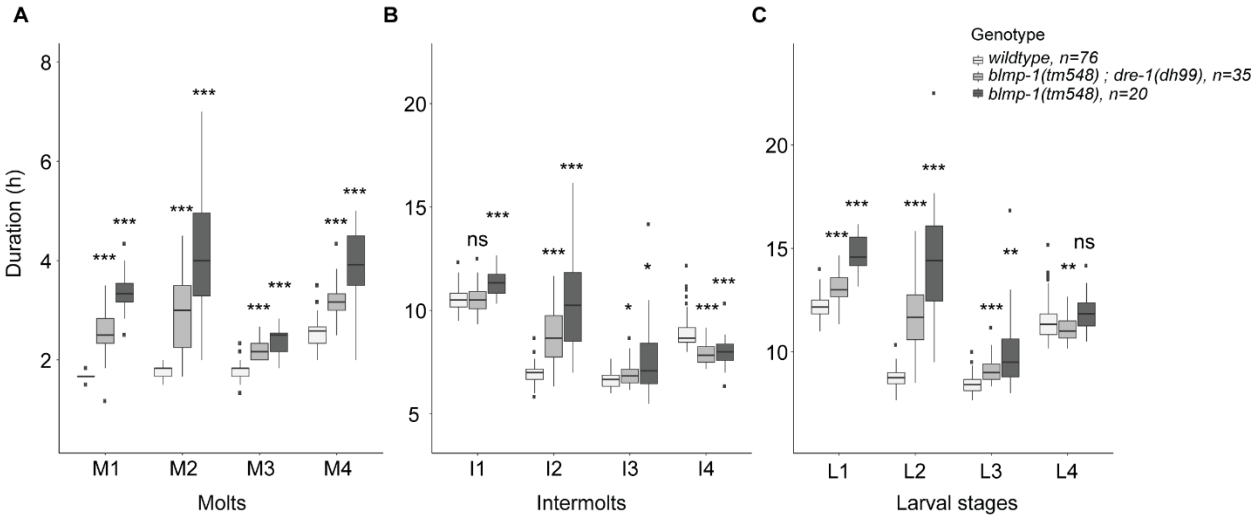

Fig S5: Replicate luciferase assay comparing the *blmp-1(tm548) (V)* mutant with *blmp-1(tm548) (I); dre-1(dh99) V* double mutant

A – C, Molt (A), intermolt (B) and larval stage (C) durations of indicated strains measured in the luciferase assay. The double mutant partially rescues the increased duration and variation of molt and intermolt durations of the *blmp-1(tm548)* mutant.

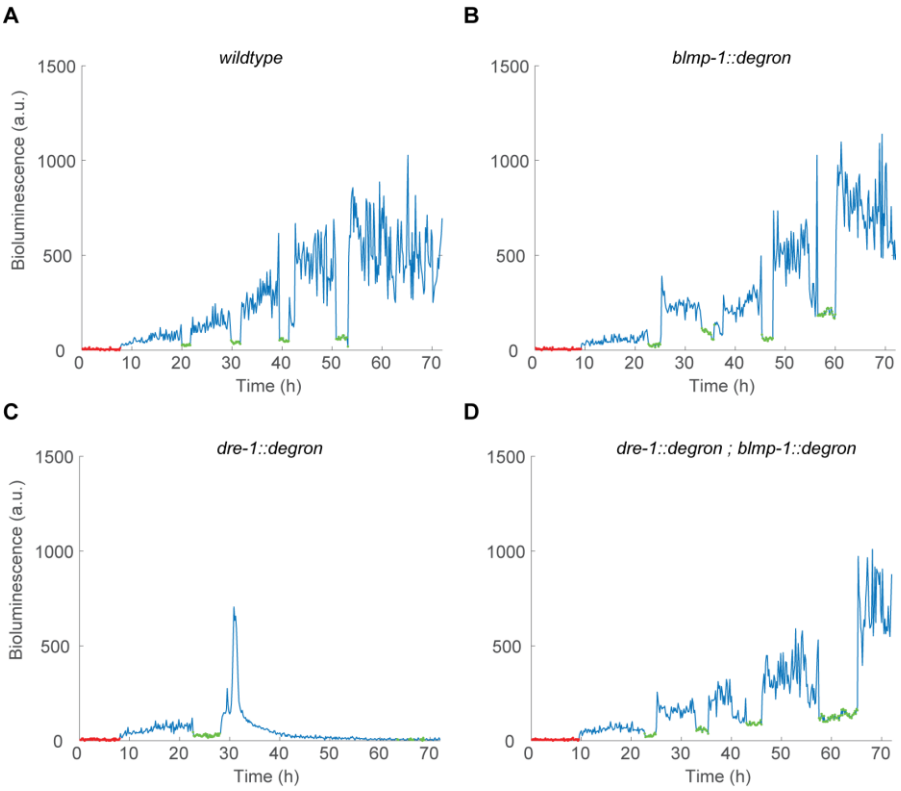

Fig S6: Example luminescence traces of single worms with BLMP-1 and DRE-1 depletion using the auxin inducible system

All strains were cultured in 250µM auxin.

A, After hatching (red), wild-type worms show normal progression through all larval stages with clear molts (green).

B, In reduced BLMP-1 levels, worms show slightly longer molts with higher luminescence intensities during the molts.

C, Reduced DRE-1 levels lead to lethality after the first molt, indicated by a progressive decrease of luminescence levels.

D, Parallel degradation of BLMP-1 and DRE-1 reduced in a partial rescue of the DRE-1 phenotype (C), with worms progressing through all larval stages while showing increased molt durations and increased luminescence during the molts.

6.5 Single worm imaging - Cell-based analysis

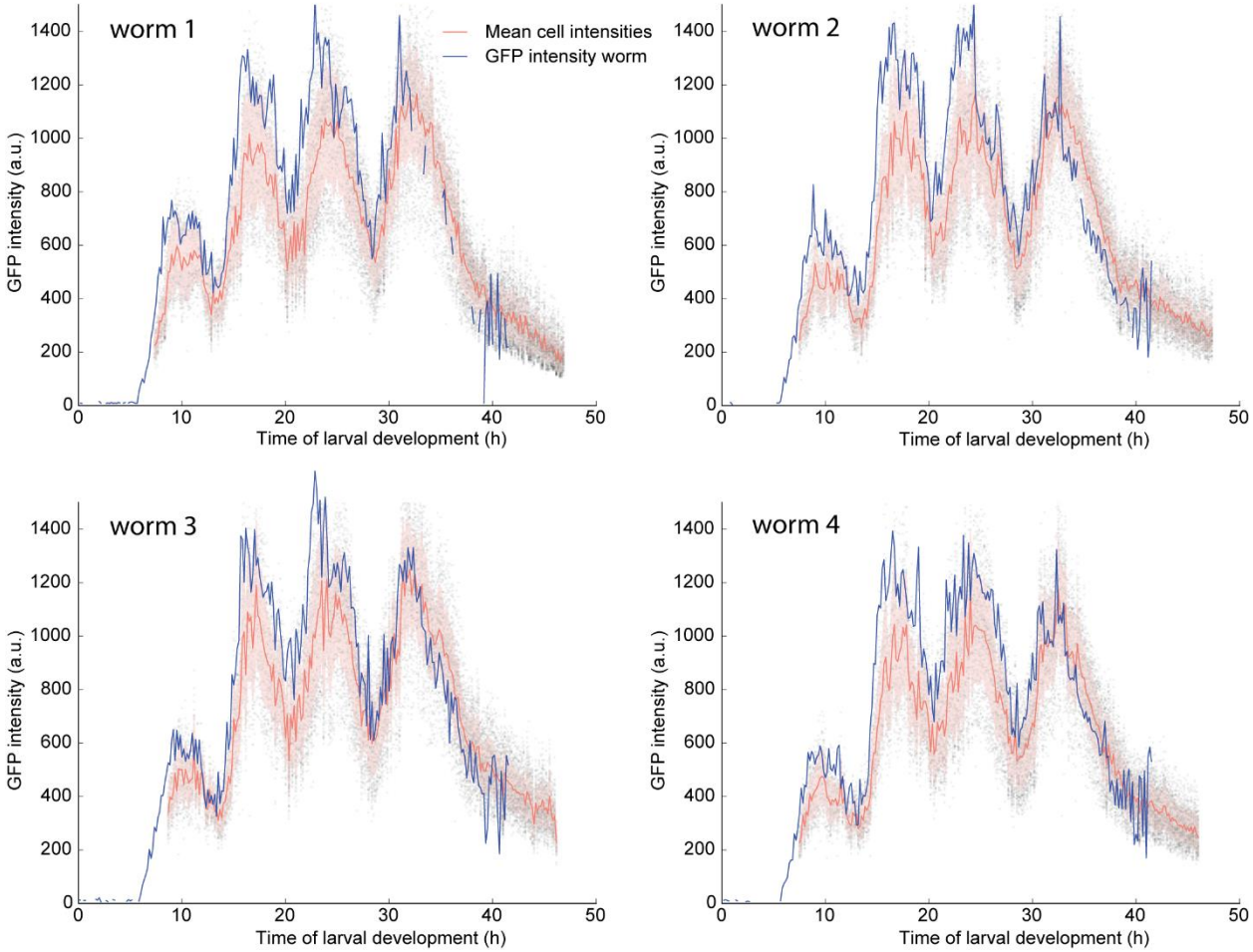

Figure S7: Measured GFP intensities in cells and whole worms are comparable

Comparison of GFP intensities in quantified in individual cells or the whole worm in four randomly chosen representative single worms. The mean intensity per cell is plotted as dots with the mean over all cells plotted in a solid line and the standard deviation in shaded area.

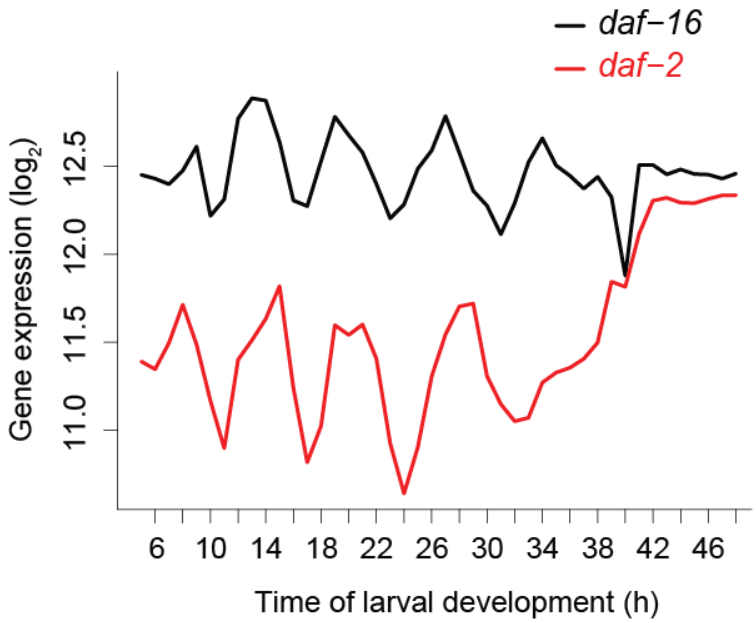

Fig S8: Log_2-transformed gene expression of *daf-16* and *daf-2*

Gene expression from (Meeuse et al., 2019) (unfused long developmental time course).

7 References

Abraham, U., Granada, A.E., Westermark, P.O., Heine, M., Kramer, A., and Herzel, H. (2010). Coupling governs entrainment range of circadian clocks. Mol. Syst. Biol. *6*, 1–13.

Agawa, Y., Sarhan, M., Kageyama, Y., Akagi, K., Takai, M., Hashiyama, K., Wada, T., Handa, H., Iwamatsu, A., Hirose, S., et al. (2007). Drosophila Blimp-1 Is a Transient Transcriptional Repressor That Controls Timing of the Ecdysone-Induced Developmental Pathway. Mol. Cell. Biol. *27*, 8739–8747.

Alberts, B., Johnson, A., Lewis, J., Raff, M., Roberts, K., and Walter, P. (2011). Molekularbiologie der Zelle, 5.Auflage.

Allen, M.A., Hillier, L.W., Waterston, R.H., and Blumenthal, T. (2011). A global analysis of C. elegans trans-splicing. Genome Res. *21*, 255–264.

Alon, U. (2007). Network motifs: theory and experimental approaches. Nat. Rev. Genet. *8*, 450–461.

Ambros, V., and Horvitz, H.R. (1984). Heterochronic mutants of the nematode Caenorhabditis elegans. Science (80-.). *226*, 409–416.

Arribere, J.A., Bell, R.T., Fu, B.X.H., Artiles, K.L., Hartman, P.S., and Fire, A.Z. (2014). Efficient marker-free recovery of custom genetic modifications with CRISPR/Cas9 in caenorhabditis elegans. Genetics *198*, 837–846.

Aschoff, J. (1960). Exogenous and endogenous components in circadian rhythms. Cold Spring Harb. Symp. Quant. Biol. *25*, 11–28.

Au, K.F., Jiang, H., Lin, L., Xing, Y., and Wong, W.H. (2010). Detection of splice junctions from paired-end RNA-seq data by SpliceMap. Nucleic Acids Res. *38*, 4570–4578.

Bae, K., Jin, X., Maywood, E.S., Hastings, M.H., Reppert, S.M., and Weaver, D.R. (2001). Differential functions of mPer1, mPer2, and mPer3 in the SCN circadian clock. Neuron *30*, 525–536.

Becskei, A., and Serrano, L. (2000). Engineering stability in gene networks by autoregulation. Nature *405*, 590–593.

Bélanger, V., Picard, N., and Cermakian, N. (2006). The Circadian Regulation of *Presenilin-2* Gene Expression. Chronobiol. Int. *23*, 747–766.

Blumenthal, T. (2005). Trans-splicing and operons. WormBook 1–9.

Bringmann, H. (2011). Agarose hydrogel microcompartments for imaging sleep- and wake-like behavior and nervous system development in Caenorhabditis elegans larvae. J. Neurosci. Methods *201*, 78–88.

Broadus, J., McCabe, J.R., Endrizzi, B., Thummel, C.S., and Woodard, C.T. (1999). The Drosophila βFTZ-F1 orphan nuclear receptor provides competence for stage-specific responses to the steroid hormone ecdysone. Mol. Cell *3*, 143–149.

Bruns, A. (2004). Fourier-, Hilbert- and wavelet-based signal analysis: Are they really different approaches? J. Neurosci. Methods *137*, 321–332.

Bunger, M.K., Wilsbacher, L.D., Moran, S.M., Clendenin, C., Radcliffe, L.A., Hogenesch, J.B., Simon, M.C., Takahashi, J.S., and Bradfield, C.A. (2000). Mop3 is an essential component of the master circadian pacemaker in mammals. Cell *103*, 1009–1017.

Cao, J., Packer, J.S., Ramani, V., Cusanovich, D.A., Huynh, C., Daza, R., Qiu, X., Lee, C., Furlan, S.N.,

Steemers, F.J., et al. (2017). Comprehensive single cell transcriptional profiling of a multicellular organism by combinatorial indexing. BioRxiv *667*, 1–35.

Cassada, R.C., and Russell, R.L. (1975). The dauerlarva, a post-embryonic developmental variant of the nematode Caenorhabditis elegans. Dev. Biol. *46*, 326–342.

Conrad, E., Mayo, A.E., Ninfa, A.J., and Forger, D.B. (2008). Rate constants rather than biochemical mechanism determine behaviour of genetic clocks. J. R. Soc. Interface *5*.

Cooke, J., and Zeeman, E.C. (1976). A clock and wavefront model for control of the number of repeated structures during animal morphogenesis. J. Theor. Biol. *58*, 455–476.

Corsi, A.K., Wightman, B., and Chalfie, M. (2015). A Transparent window into biology: A primer on Caenorhabditis elegans. In WormBook, (WormBook), p.

Cox, G.N., Staprans, S., and Edgar, R.S. (1981). The cuticle of Caenorhabditis elegans. II. Stage-specific changes in ultrastructure and protein composition during postembryonic development. Dev. Biol. *86*, 456–470.

Cramer, P. (2019). Organization and regulation of gene transcription. Nature *573*, 45–54.

Crnko, S., Du Pré, B.C., Sluijter, J.P.G., and Van Laake, L.W. (2019). Circadian rhythms and the molecular clock in cardiovascular biology and disease. Nat. Rev. Cardiol. *16*, 437–447.

Cui, Z., Xu, Q., and Wang, X. (2014). Regulation of the circadian clock through pre-mRNA splicing in Arabidopsis. J. Exp. Bot. *65*, 1973–1980.

Cyran, S.A., Buchsbaum, A.M., Reddy, K.L., Lin, M.C., Glossop, N.R.J., Hardin, P.E., Young, M.W., Storti, R. V., and Blau, J. (2003). vrille, Pdp1, and dClock form a second feedback loop in the Drosophila circadian clock. Cell *112*, 329–341.

D'Alessandro, M., Beesley, S., Kim, J.K., Jones, Z., Chen, R., Wi, J., Kyle, K., Vera, D., Pagano, M., Nowakowski, R., et al. (2017). Stability of Wake-Sleep Cycles Requires Robust Degradation of the PERIOD Protein. Curr. Biol. *27*, 3454-3467.e8.

Davis, M.W., Birnie, A.J., Chan, A.C., Page, A.P., and Jorgensen, E.M. (2004). A conserved metalloprotease mediates ecdysis in Caenorhabditis elegans. Development *131*, 6001–6008.

Dobie, R.A., and Van Hemel, S. (2004). Hearing Loss: Determining Eligibility for Social Security Benefits (National Academies Press (US)).

Duffield, G.E. (2003). DNA microarray analyses of circadian timing: The genomic basis of biological time. J. Neuroendocrinol. *15*, 991–1002.

Ester, M., Kriegel, H.-P., Sander, J., and Xu, X. (1996). A Density-Based Algorithm for Discovering Clusters in Large Spatial Databases with Noise.

Ferrell, J.E., Tsai, T.Y.C., and Yang, Q. (2011). Modeling the cell cycle: Why do certain circuits oscillate? Cell *144*, 874–885.

Foley, L.E., Ling, J., Joshi, R., Evantal, N., Kadener, S., and Emery, P. (2019). Drosophila PSI controls circadian period and the phase of circadian behavior under temperature cycle via tim splicing. Elife *8*.

Frand, A.R., Russel, S., and Ruvkun, G. (2005). Functional genomic analysis of c. elegans molting. PLoS Biol. *3*.

Gabor, D. (1946). Theory of communication. Part 1: The analysis of information. J. Inst. Electr. Eng. -

Part III Radio Commun. Eng. *93*, 429–441.

Gallego, M., and Virshup, D.M. (2007). Post-translational modifications regulate the ticking of the circadian clock. Nat. Rev. Mol. Cell Biol. *8*, 139–148.

Gissendanner, C.R., and Sluder, A.E. (2000). nhr-25, the Caenorhabditis elegans ortholog of ftz-f1, is required for epidermal and somatic gonad development. Dev. Biol. *221*, 259–272.

Golden, J.W., and Riddle, D.L. (1984). The Caenorhabditis elegans dauer larva: Developmental effects of pheromone, food, and temperature. Dev. Biol. *102*, 368–378.

Griffith, J.S. (1968). Mathematics of cellular control processes I. Negative feedback to one gene. J. Theor. Biol. *20*, 202–208.

Grün, D., Kirchner, M., Thierfelder, N., Stoeckius, M., Selbach, M., and Rajewsky, N. (2014). Conservation of mRNA and protein expression during development of C.elegans. Cell Rep. *6*, 565–577.

Hashmi, S., Zhang, J., Oksov, Y., and Lustigman, S. (2004). The Caenorhabditis elegans Cathepsin Z-like Cysteine Protease, Ce-CPZ-1, Has a Multifunctional Role during the Worms' Development. J. Biol. Chem. *279*, 6035–6045.

Hastings, K.E.M. (2005). SL trans-splicing: Easy come or easy go? Trends Genet. *21*, 240–247.

Hattar, S., Liao, H.W., Takao, M., Berson, D.M., and Yau, K.W. (2002). Melanopsin-containing retinal ganglion cells: Architecture, projections, and intrinsic photosensitivity. Science (80-.). *295*, 1065–1070.

Hedgecock, E.M., and White, J.G. (1985). Polyploid tissues in the nematode Caenorhabditis elegans. Dev. Biol. *107*, 128–133.

Hendriks, G.J., Gaidatzis, D., Aeschimann, F., and Großhans, H. (2014). Extensive Oscillatory Gene Expression during C.elegans Larval Development. Mol. Cell *53*, 380–392.

Herrgen, L., Ares, S., Morelli, L.G., Schröter, C., Jülicher, F., and Oates, A.C. (2010). Intercellular coupling regulates the period of the segmentation clock. Curr. Biol. *20*, 1244–1253.

Hirano, A., Braas, D., Fu, Y.H., and Ptáček, L.J. (2017). FAD Regulates CRYPTOCHROME Protein Stability and Circadian Clock in Mice. Cell Rep. *19*, 255–266.

Horn, M., Geisen, C., Cermak, L., Becker, B., Nakamura, S., Klein, C., Pagano, M., and Antebi, A. (2014). DRE-1/FBXO11-dependent degradation of BLMP-1/BLIMP-1 governs C. elegans developmental timing and maturation. Dev. Cell *28*, 697–710.

Van Der Horst, G.T.J., Muijtjens, M., Kobayashi, K., Takano, R., Kanno, S.I., Takao, M., De Wit, J., Verkerk, A., Eker, A.P.M., Van Leenen, D., et al. (1999). Mammalian Cry1 and Cry2 are essential for maintenance of circadian rhythms. Nature *398*, 627–630.

Huang, N.E., Shen, Z., Long, S.R., Wu, M.C., Snin, H.H., Zheng, Q., Yen, N.C., Tung, C.C., and Liu, H.H. (1998). The empirical mode decomposition and the Hubert spectrum for nonlinear and non-stationary time series analysis. Proc. R. Soc. A Math. Phys. Eng. Sci. *454*, 903–995.

Huang, T.F., Cho, C.Y., Cheng, Y.T., Huang, J.W., Wu, Y.Z., Yeh, A.Y.C., Nishiwaki, K., Chang, S.C., and Wu, Y.C. (2014). BLMP-1/Blimp-1 Regulates the Spatiotemporal Cell Migration Pattern in C. elegans. PLoS Genet. *10*.

Hubaud, A., and Pourquié, O. (2014). Signalling dynamics in vertebrate segmentation. Nat. Rev. Mol. Cell Biol. *15*, 709–721.

Hughes, M.E., DiTacchio, L., Hayes, K.R., Vollmers, C., Pulivarthy, S., Baggs, J.E., Panda, S., and Hogenesch, J.B. (2009). Harmonics of circadian gene transcription in mammals. PLoS Genet. *5*.

Imayoshi, I., Isomura, A., Harima, Y., Kawaguchi, K., Kori, H., Miyachi, H., Fujiwara, T., Ishidate, F., and Kageyama, R. (2013). Oscillatory control of factors determining multipotency and fate in mouse neural progenitors. Science. *342*, 1203–1208.

Iwanir, S., Tramm, N., Nagy, S., Wright, C., Ish, D., and Biron, D. (2013). The Microarchitecture of C. elegans Behavior during Lethargus: Homeostatic Bout Dynamics, a Typical Body Posture, and Regulation by a Central Neuron. Sleep *36*, 385–395.

Izhikevich, E.M. (2000). Neural excitability, spiking and bursting. Int. J. Bifurcat. Chaos *10*, 1171–1266.

Jiang, Y.J., Aerne, B.L., Smithers, L., Haddon, C., Ish-Horowicz, D., and Lewis, J. (2000). Notch signalling and the synchronization of the somite segmentation clock. Nature *408*, 475–479.

Johnson, T.E., Mitchell, D.H., Kline, S., Kemal, R., and Foy, J. (1984). Arresting development arrests aging in the nematode Caenorhabditis elegans. Mech. Ageing Dev. *28*, 23–40.

Johnstone, I.L. (2000). Cuticle collagen genesexpression in Caenorhabditis elegans. Trends Genet. *16*, 21–27.

Jouffe, C., Cretenet, G., Symul, L., Martin, E., Atger, F., Naef, F., and Gachon, F. (2013). The Circadian Clock Coordinates Ribosome Biogenesis. PLoS Biol. *11*.

Katic, I., Xu, L., and Ciosk, R. (2015). CRISPR/Cas9 genome editing in Caenorhabditis elegans: Evaluation of templates for homology-mediated repair and knock-ins by homology-independent DNA repair. G3 Genes, Genomes, Genet. *5*, 1649–1656.

Kim, Grün, D., and Van Oudenaarden, A. (2013a). Dampening of expression oscillations by synchronous regulation of a microRNA and its target. Nat. Genet. *45*, 1337–1345.

Kim, J.R., Shin, D., Jung, S.H., Heslop-Harrison, P., and Cho, K.H. (2010). A design principle underlying the synchronization of oscillations in cellular systems. J. Cell Sci. *123*, 537–543.

Kim, M.J., Lee, J.H., and Duffy, J.F. (2013b). Circadian Rhythm Sleep Disorders. J. Clin. Outcomes Manag. *20*, 513.

Kingma, D.P., and Ba, J.L. (2015). Adam: A method for stochastic optimization. In 3rd International Conference on Learning Representations, ICLR 2015 - Conference Track Proceedings, (International Conference on Learning Representations, ICLR), p.

Knight, C.G., Patel, M.N., Azevedo, R.B.R., and Leroi, A.M. (2002). A novel mode of ecdysozoan growth in Caenorhabditis elegans. Evol. Dev. *4*, 16–27.

Koike, N., Yoo, S.H., Huang, H.C., Kumar, V., Lee, C., Kim, T.K., and Takahashi, J.S. (2012). Transcriptional architecture and chromatin landscape of the core circadian clock in mammals. Science (80-.). *338*, 349–354.

Kojima, S., and Green, C.B. (2015). Circadian genomics reveal a role for post-transcriptional regulation in mammals. Biochemistry *54*, 124–133.

Kostrouchova, M., Krause, M., Kostrouch, Z., and Rall, J.E. (1998). CHR3: A Caenorhabditis elegans orphan nuclear hormone receptor required for proper epidermal development and molting. Development *125*, 1617–1626.

Krueger, D., Izquierdo, E., Viswanathan, R., Hartmann, J., Cartes, C.P., and de Renzis, S. (2019).

Principles and applications of optogenetics in developmental biology. Dev. *146*.

Kruse, K., and Jülicher, F. (2005). Oscillations in cell biology. Curr. Opin. Cell Biol. *17*, 20–26.

Lam, G., Hall, B.L., Bender, M., and Thummel, C.S. (1999). DHR3 Is Required for the Prepupal-Pupal Transition and Differentiation of Adult Structures during Drosophila Metamorphosis.

Lamont, E.W., Legault-Coutu, D., Cermakian, N., and Boivin, D.B. (2007). The role of circadian clock genes in mental disorders. Dialogues Clin. Neurosci. *9*, 333–342.

Lavorgna, G., Karim, F.D., Thummel, C.S., and Wu, C. (1993). Potential role for a FTZ-F1 steroid receptor superfamily member in the control of Drosophila metamorphosis. Proc. Natl. Acad. Sci. U. S. A. *90*, 3004–3008.

Lažetić, V., and Fay, D.S. (2017). Molting in *C. elegans*. Worm *6*, e1330246.

Lewis, J. (2003). Autoinhibition with transcriptional delay: A simple mechanism for the zebrafish somitogenesis oscillator. Curr. Biol. *13*, 1398–1408.

Li, M.D., Li, C.M., and Wang, Z. (2012). The role of circadian clocks in metabolic disease. Yale J. Biol. Med. *85*, 387–401.

Lim, C., and Allada, R. (2013). Emerging roles for post-transcriptional regulation in circadian clocks. Nat. Neurosci. *16*, 1544–1550.

Lucas, R.J., Hattar, S., Takao, M., Berson, D.M., Foster, R.G., and Yau, K.W. (2003). Diminished pupillary light reflex at high irradiances in melanopsin-knockout mice. Science (80-.). *299*, 245–247.

Luisa, M., Andreas, S., Bernard, C., and Jirsa, V.K. (2017). Fast – Slow Bursters in the Unfolding of a High Codimension Singularity and the Ultra-slow Transitions of Classes. 1–47.

Macaulay, I.C., Haerty, W., Kumar, P., Li, Y.I., Hu, T.X., Teng, M.J., Goolam, M., Saurat, N., Coupland, P., Shirley, L.M., et al. (2015). G&T-seq: Parallel sequencing of single-cell genomes and transcriptomes. Nat. Methods *12*, 519–522.

Mackey, M.C., and Glass, L. (1977). Oscillation and chaos in physiological control systems. Science (80-.). *197*, 287–289.

Magnúsdóttir, E., Kalachikov, S., Mizukoshi, K., Savitsky, D., Ishida-Yamamoto, A., Panteleyev, A.A., and Calame, K. (2007). Epidermal terminal differentiation depends on B lymphocyte-induced maturation protein-1. Proc. Natl. Acad. Sci. U. S. A. *104*, 14988–14993.

Mallat, S. (1999). A Wavelet Tour of Signal Processing. (San Diego: Academic Press), pp. 125–162.

Mavroudis, P.D., DuBois, D.C., Almon, R.R., and Jusko, W.J. (2018). Daily variation of gene expression in diverse rat tissues. PLoS One *13*, e0197258.

McCleery, W.T., Mohd-Radzman, N.A., and Grieneisen, V.A. (2017). Root branching plasticity: collective decision-making results from local and global signalling. Curr. Opin. Cell Biol. *44*, 51–58.

Meeuse, M.W.M., Hauser, Y.P., Hendriks, G.-J., Eglinger, J., Bogaarts, G., Tsiairis, C., and Großhans, H. (2019). State transitions of a developmental oscillator. BioRxiv 755421.

Menaker, M. (2003). Circadian rhythms: Circadian photoreception. Science (80-.). *299*, 213–214.

Mok, D.Z.L., Sternberg, P.W., and Inoue, T. (2015). Morphologically defined sub-stages of C. Elegans vulval development in the fourth larval stage. BMC Dev. Biol. *15*, 1–8.

Mönke, G., Cristiano, E., Finzel, A., Friedrich, D., Herzel, H., Falcke, M., and Loewer, A. (2017). Excitability in the p53 network mediates robust signaling with tunable activation thresholds in single cells. Sci. Rep. *7*, 1–14.

Muñoz, M.J., and Riddle, D.L. (2003). Positive selection of Caenorhabditis elegans mutants with increased stress resistance and longevity. Genetics *163*, 171–180.

Nelson, M.D., Trojanowski, N.F., George-Raizen, J.B., Smith, C.J., Yu, C.C., Fang-Yen, C., and Raizen, D.M. (2013). The neuropeptide NLP-22 regulates a sleep-like state in Caenorhabditis elegans. Nat. Commun. *4*.

Niederreither, K., McCaffery, P., Dräger, U.C., Chambon, P., and Dollé, P. (1997). Restricted expression and retinoic acid-induced downregulation of the retinaldehyde dehydrogenase type 2 (RALDH-2) gene during mouse development. Mech. Dev. *62*, 67–78.

Niu, W., Lu, Z.J., Zhong, M., Sarov, M., Murray, J.I., Brdlik, C.M., Janette, J., Chen, C., Alves, P., Preston, E., et al. (2011). Diverse transcription factor binding features revealed by genome-wide ChIP-seq in C. elegans. Genome Res. *21*, 245–254.

Niwa, Y., Masamizu, Y., Liu, T., Nakayama, R., Deng, C.X., and Kageyama, R. (2007). The Initiation and Propagation of Hes7 Oscillation Are Cooperatively Regulated by Fgf and Notch Signaling in the Somite Segmentation Clock. Dev. Cell *13*, 298–304.

Novák, B., and Tyson, J.J. (2008). Design principles of biochemical oscillators. Nat. Rev. Mol. Cell Biol. *9*, 981–991.

Nutt, S.L., Fairfax, K.A., and Kallies, A. (2007). BLIMP1 guides the fate of effector B and T cells. Nat. Rev. Immunol. *7*, 923–927.

Padmanabhan, K., Robles, M.S., Westerling, T., and Weitz, C.J. (2012). Feedback regulation of transcriptional termination by the mammalian circadian clock PERIOD complex. Science. *337*, 599–602.

Page, A.P. and Johnstone, I.L. The cuticle (March 19, 2007), *WormBook*, ed. The *C. elegans* Research Community, WormBook, doi/10.1895/wormbook.1.138.1, http://www.wormbook.org.

Palmeirim, I., Henrique, D., Ish-Horowicz, D., and Pourquié, O. (1997). Avian hairy gene expression identifies a molecular clock linked to vertebrate segmentation and somitogenesis. Cell *91*, 639–648.

Panda, S., Hogenesch, J.B., and Kay, S.A. (2002). Circadian rhythms from flies to humans. Nature *417*, 329–335.

Patke, A., Young, M.W., and Axelrod, S. (2020). Molecular mechanisms and physiological importance of circadian rhythms. Nat. Rev. Mol. Cell Biol. *21*, 67–84.

Peng, Y., and Zhang, Y. (2018). Enhancer and super-enhancer: Positive regulators in gene transcription. Anim. Model. Exp. Med. *1*, 169–179.

Pittendrigh, C.S. (1960). Circadian Rhythms and the Circadian Organization of Living Systems. Cold Spring Harb. Symp. Quant. Biol. *25*, 159–184.

Purcell, O., Savery, N.J., Grierson, C.S., and di Bernardo, M. (2010). A comparative analysis of synthetic genetic oscillators. J. R. Soc. Interface *7*, 1503–1524.

Purvis, J.E., and Lahav, G. (2013). Encoding and decoding cellular information through signaling dynamics. Cell *152*, 945–956.

Purvis, J.E., Karhohs, K.W., Mock, C., Batchelor, E., Loewer, A., and Lahav, G. (2012). p53 dynamics

control cell fate. Science *336*, 1440–1444.

Raizen, D.M., Zimmerman, J.E., Maycock, M.H., Ta, U.D., You, Y.J., Sundaram, M. V., and Pack, A.I. (2008). Lethargus is a Caenorhabditis elegans sleep-like state. Nature *451*, 569–572.

Raskin, D., and De Boer, P. (1999). Rapid pole-to-pole oscillation of a protein required for directing division to the middle of Escherichia coli. Proc. Natl. Acad. Sci. USA *96*.

Reddy, A.B., Karp, N.A., Maywood, E.S., Sage, E.A., Deery, M., O'Neill, J.S., Wong, G.K.Y., Chesham, J., Odell, M., Lilley, K.S., et al. (2006). Circadian Orchestration of the Hepatic Proteome. Curr. Biol. *16*, 1107–1115.

Reiter, F., Wienerroither, S., and Stark, A. (2017). Combinatorial function of transcription factors and cofactors. Curr. Opin. Genet. Dev. *43*, 73–81.

Riedel-Kruse, I.H., Müller, C., and Oates, A.C. (2007). Synchrony dynamics during initiation, failure, and rescue of the segmentation clock. Science (80-.). *317*, 1911–1915.

Ronneberger, O., Fischer, P., and Brox, T. (2015). U-net: Convolutional networks for biomedical image segmentation. In Lecture Notes in Computer Science (Including Subseries Lecture Notes in Artificial Intelligence and Lecture Notes in Bioinformatics), (Springer Verlag), pp. 234–241.

Rossant, J., Zirngibl, R., Cado, D., Shago, M., and Giguere, V. (1991). Expression of a retinoic acid response element-hsplacZ transgene defines specific domains of transcriptional activity during mouse embryogenesis. Genes Dev. *5*, 1333–1344.

Ruaud, A.-F. (2006). Activation of nicotinic receptors uncouples a developmental timer from the molting timer in C. elegans. Development *133*, 2211–2222.

Sainsbury, S., Bernecky, C., and Cramer, P. (2015). Structural basis of transcription initiation by RNA polymerase II. Nat. Publ. Gr. *16*, 129–143.

Schindler, A.J., Baugh, L.R., and Sherwood, D.R. (2014). Identification of Late Larval Stage Developmental Checkpoints in Caenorhabditis elegans Regulated by Insulin/IGF and Steroid Hormone Signaling Pathways. PLoS Genet. *10*, 13–16.

Schubert, E., Sander, J., Ester, M., Kriegel, H.-P., Xu, X., and Kriegel, H.-P. (2017). DBSCAN Revisited, Revisited: Why and How You Should (Still) Use DBSCAN. DBSCAN Revisited, Revisit. Why How You Should Use DBSCAN. ACM Trans. Database Syst *42*.

Shaw, M., Zhan, H., Elmi, M., Pawar, V., Essmann, C., and Srinivasan, M.A. (2018). Three-dimensional behavioural phenotyping of freely moving C. elegans using quantitative light field microscopy. PLoS One *13*, e0200108.

Siggers, T., and Gordân, R. (2014). Protein-DNA binding: Complexities and multi-protein codes. Nucleic Acids Res. *42*, 2099–2111.

Siggers, T., Duyzend, M.H., Reddy, J., Khan, S., and Bulyk, M.L. (2011). Non-DNA-binding cofactors enhance DNA-binding specificity of a transcriptional regulatory complex. Mol. Syst. Biol. *7*, 555.

Singh, R.N.S.J.E. (1978). Some Observations On Moulting in Caenorhabditis Elegans. Nematologica *24*.

Slattery, M., Riley, T., Liu, P., Abe, N., Gomez-Alcala, P., Dror, I., Zhou, T., Rohs, R., Honig, B., Bussemaker, H.J., et al. (2011). Cofactor binding evokes latent differences in DNA binding specificity between hox proteins. Cell *147*, 1270–1282.

So, W.V. (1997). Post-transcriptional regulation contributes to Drosophila clock gene mRNA cycling.

EMBO J. *16*, 7146–7155.

Sperling, S. (2007). Transcriptional regulation at a glance. BMC Bioinformatics *8*.

Stenvall, J., Fierro-González, J.C., Swoboda, P., Saamarthy, K., Cheng, Q., Cacho-Valadez, B., Arnér, E.S.J., Persson, O.P., Miranda-Vizuete, A., and Tuck, S. (2011). Selenoprotein TRXR-1 and GSR-1 are essential for removal of old cuticle during molting in Caenorhabditis elegans. Proc. Natl. Acad. Sci. U. S. A. *108*, 1064–1069.

Stephen Butterworth (1930). On the Theory of Filter Amplifiers. Exp. Wirel. Wirel. Eng. *7*, 536–541.

Stricker, J., Cookson, S., Bennett, M.R., Mather, W.H., Tsimring, L.S., and Hasty, J. (2008). A fast, robust and tunable synthetic gene oscillator. Nature *456*, 516–519.

Strogatz, S.H. (2015). Nonlinear dynamics and chaos : with Applications to Physics, Biology, Chemistry, and Engineering (Westview Press).

Sulston, J.E., and Horvitz, H.R. (1977). Post-embryonic cell lineages of the nematode, Caenorhabditis elegans. Dev. Biol. *56*, 110–156.

Sulston, J.E., Schierenberg, E., White, J.G., and Thomson, J.N. (1983). The embryonic cell lineage of the nematode *Caenorhabditis elegans*. Dev. Biol. *100*, 64–119.

Svensson, V., Natarajan, K.N., Ly, L.H., Miragaia, R.J., Labalette, C., Macaulay, I.C., Cvejic, A., and Teichmann, S.A. (2017). Power analysis of single-cell rnA-sequencing experiments. Nat. Methods *14*, 381–387.

Takahashi, J.S. (2004). Introduction: Finding new clock components; past and future. *19*, 339–347.

Takahashi, J.S. (2017). Transcriptional architecture of the mammalian circadian clock. Nat. Rev. Genet. *18*, 164–179.

Thummel, C.S. (2001). Molecular mechanisms of developmental timing in C. elegans and Drosophila. Dev. Cell *1*, 453–465.

Tsai, T.Y.C., Yoon, S.C., Ma, W., Pomerening, J.R., Tang, C., and Ferrell, J.E. (2008). Robust, tunable biological oscillations from interlinked positive and negative feedback loops. Science (80-.). *321*, 126–139.

Tunyaplin, C. (2000). Characterization of the B lymphocyte-induced maturation protein-1 (Blimp-1) gene, mRNA isoforms and basal promoter. Nucleic Acids Res. *28*, 4846–4855.

Turek, M., Besseling, J., and Bringmann, H. (2015). Agarose Microchambers for Long-term Calcium Imaging of Caenorhabditis elegans. J. Vis. Exp. 1–8.

Turner, C.A., Mack, D.H., and Davis, M.M. (1994). Blimp-1, a novel zinc finger-containing protein that can drive the maturation of B lymphocytes into immunoglobulin-secreting cells. Cell *77*, 297–306.

Vitaterna, M.H., Selby, C.P., Todo, T., Niwa, H., Thompson, C., Fruechte, E.M., Hitomi, K., Thresher, R.J., Ishikawa, T., Miyazaki, J., et al. (1999). Differential regulation of mammalian period genes and circadian rhythmicity by cryptochromes 1 and 2. Proc. Natl. Acad. Sci. U. S. A. *96*, 12114–12119.

Vitaterna, M.H., Takahashi, J.S., and Turek, F.W. (2001). Overview of circadian rhythms. Alcohol Res. Heal. *25*, 85–93.

Webb, A.B., and Oates, A.C. (2016). Timing by rhythms: Daily clocks and developmental rulers. Dev. Growth Differ. *58*, 43–58.

References

Welsh, D.K., Takahashi, J.S., and Kay, S.A. (2010). Suprachiasmatic Nucleus: Cell Autonomy and Network Properties. Annu. Rev. Physiol. *72*, 551–577.

Winfree, A.T. (1967). Biological rhythms and the behavior of populations of coupled oscillators. J. Theor. Biol. *16*, 15–42.

Winfree, A.T. (1980). The geometry of biological time (Springer Verlag).

Woo, K.C., Kim, T.D., Lee, K.H., Kim, D.Y., Kim, W., Lee, K.Y., and Kim, K.T. (2009). Mouse period 2 mRNA circadian oscillation is modulated by PTB-mediated rhythmic mRNA degradation. Nucleic Acids Res. *37*, 26–37.

Yang, J., Fong, H.T., Xie, Z., Tan, J.W.H., and Inoue, T. (2015). Direct and positive regulation of Caenorhabditis elegans bed-3 by PRDM1/BLIMP1 ortholog BLMP-1. Biochim. Biophys. Acta - Gene Regul. Mech. *1849*, 1229–1236.

Yeung, J., Mermet, J., Jouffe, C., Marquis, J., Charpagne, A., Gachon, F., and Naef, F. (2018). Transcription factor activity rhythms and tissue-specific chromatin interactions explain circadian gene expression across organs. Genome Res. *28*, 182–191.

Zeng, H., Qian, Z., Myers, M.P., and Rosbash, M. (1996). A light-entrainment mechanism for the drosophila circadian clock. Nature *380*, 129–135.

Zhang, L., Ward, J.D., Cheng, Z., and Dernburg, A.F. (2015). The auxin-inducible degradation (AID) system enables versatile conditional protein depletion in C. elegans. Development *142*, 4374–4384.

Zheng, B., Albrecht, U., Kaasik, K., Sage, M., Lu, W., Vaishnav, S., Li, Q., Sun, Z.S., Eichele, G., Bradley, A., et al. (2001). Nonredundant roles of the mPer1 and mPer2 genes in the mammalian circadian clock. Cell *105*, 683–694.

Strogatz-1994-Nonlinea-Dynamics-and-Chaos.

Acknowledgments

First and foremost I would like to thank you, **Helge**, for your constant support over these many years. It was not always easy to establish new ways of analyzing our data or to even get the data in the first place but you were always motivating and constructive in many ways. Thank you for all the freedom you gave me in exploring the biology but especially also data analysis, but also for guiding me during times when I explored too much. Despite the big challenges we faced, it was very interesting to explore such a new field and developing new experimental strategies to do so. The fact that I stayed in the lab for a PhD after my Master Thesis is yet another sign that I liked working in this lab, and I wish you and the whole group all the best for the experiments wherever the projects evolve to in the future.

I would also like to express my thanks to my Thesis Committee members, **Alexander Aulehla** and **Anne Spang**. It was always inspiring to discuss science in our advisory meetings and also during occasional worm meetings and the Oscillator meetings in Heidelberg which were fantastic events.

Many thanks to the **Grosshans group**. I had the privilege to experience many versions of it with different people and would like to thank you all for a great time. **Lene** and **Flo**, probably you will never read this but I want to express my gratitude for every kindness you gave me. You brought me back to reality many times when I was worried. Of course, **Flo**, thanks for every hour we spent on the tennis court together which refreshed my mind. Thanks, **Smita**, **Chiara, Jana**, **Maike, Kathrin and Anca** for all the fun we had together. Thanks, **Foivos and Lucas** for all the bioinformatics support and for making the last Annual Meeting such a fun event. I would also like to thank **Thomas** for your constant moral support and that we had to report our weekend plans always already on Wednesday :). Specifically, I would like to thank you **Gert-Jan**, you were not only an incredible mentor scientifically but we also had a great time next to the science part. I still remember the many discussions we had (especially also the ones outside the lab). The time we spent together was always appreciated. Thank you very much, **Milou** for the collaborative time we had as our projects evolved and for all the good talks when I struggled. We kind of grew together as PhD siblings, which really helped in many, many ways. **Rajani**, thank you so much for all the fun discussions we had in and outside the lab. I always enjoyed the time with you, be it in the

mountains or on the badminton court or when you read my thoughts. In a way, you became like my big Indian brother.

Many thanks to the **Tsiairis** group in general and especially for **Charisios** for important input whenever we shared ideas about projects. **Iskra** and **Lan**, you both were fantastic and I cannot imagine our lab without all the help you provided with the ***C. elegans* facility**! The **Functional Genomics** facility deserves special thanks as they sequenced all our time courses, regardless of how long they were and I would like to specifically mention **Sébastien**. You were of tremendous help for the single worm sequencing. With your help, this project went smoothly and without you, this would not have been possible. Thanks, **Laurent** and **Steven** for being such a great help to set up the microscopy part and also thank you **Jan** for introducing me to KNIME and putting together the KNIME workflow to analyze the single worm images. Taking this a step further, I would like to specifically mention you, **Markus,** and your great support with the convolutional neural network that you built for me. This was not a given but helped us tremendously now and I am sure also in the future.

The **Basel Group!!!** There is literally not enough space here to thank you for these 14 years of friendship which I had never imagined to experience in such a way. I enjoy every single moment we spend together and would like to express my gratitude with all my heart. You became like a second family to me for which I hope to have a bit more time now :).

Most importantly, I would like to thank my family. I cannot express how thankful I am for the constant support from every single one of you because I would probably not have managed without you. Thank you, **mum**, for your time and your open ears whenever I needed to talk to someone or needed some “Ingwer und Ewig”. Not only when I struggled with experiments or other work-related issues, but especially also in difficult times not work-related during all these years. Thanks for raising me and always supporting me in my path towards where I am now. Thank you, **dad**, to spark my interest in biology already early in my life, your advice and compassion during all these years and for being the one discovering completely different worlds in the movie theaters with me when I needed some distraction. I am incredibly thankful for teaching me how to master badminton, squash and tennis without which I would probably not have survived. **Julie**, thank you so much for being such a nice sister and your kind personality whenever we embarked on a journey together. And last but not least, thank you, **Janine**, for the beautiful moments you gave everyone

who had the privilege to know you. You shaped my personality in many ways and I am thankful for every one of them.

There are many other people I should thank but this thesis needs to have an ending and I can only say that, whoever did not find him- or herself mentioned above, you all contributed to this thesis in one or the other way and I thank each and every one of you.

8 Appendix

8.1 Detailed Single worm sequencing protocol

COPAS worm sorting setting

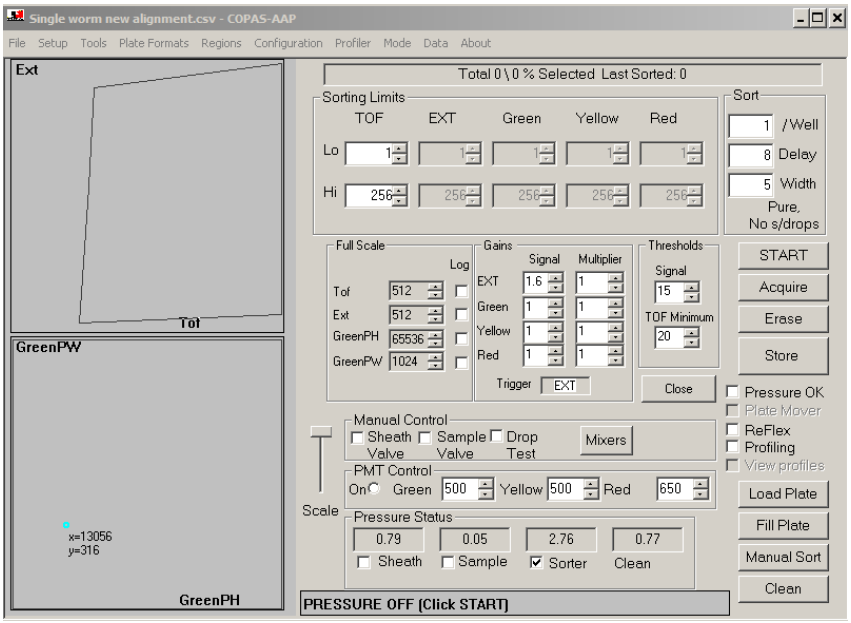

Preparation Oligo-dT beads and mRNA capture (done by genomics facility)

All mixing should be done by pipetting up and down, no vortexing!

- Prepare resuspension buffer, Wash buffer and RT buffer (add enzymes just before using the buffers)
- Use 120ul Dynabeads MyOne Streptavidin C1 (Thermofisher, Cat. No. 65001). Use a 1.5ml Eppendorf tube.
- Place on magnet and remove supernatant
- Wash 2x with 200ul of **solution A** (0.1M NaOH, 0.05M NaCl)
- Wash 2x with 200ul of **solution B** (0.1M NaOH)
- Wash 1x with 120ul of 1**X B&W buffer** (2M NaCl, 10mM Tris-HCl pH7.4, 1mM EDTA)
- Resuspend the beads in 120ul of **2X B&W buffer** + **60ul NF ddH2O** + **60ul oligo-dT*** (100uM)
- Incubate on a wheel for 20min @ RT (*now add Superase-In to resuspension buffer*)
- Wash 3x with 200ul of **1X B&W** buffer
- Resuspend in 1066ul of resuspension buffer on ice

- Add **10ul** of beads per well:
    - Use 1 PCR strip filled with **132ul of beads** per tube and pipette into plate with multichannel
- Vortex quickly (avoid drops! If drops were created, spin quickly)
- Incubate plate shaking @1200rpm on thermocycler at RT for 20min
    - NOW: finish wash buffer and RT master mix and pipette into PCR strip.
    - **Wash buffer**:
        - Prepare **4x PCR strips** with **142ul of wash buffer** in each tube. From there pipette **44ul** into wells of fully skirted plate using multichannel
    - **RT master mix**:
        - Prepare 1x PCR strip with **143ul of RT master mix** in each tube. From there pipette **11ul** into wells of semi skirted plate using multichannel
- Spin all 3 plates
- Using the BRAVO robot, wash beads 2X and add RT master mix. Follow instructions on the display.
- Immediately proceed to Reverse transcription

Reverse transcription

- Immediately glue PCR film (558/MJ) to the plate
- Vortex carefully and incubate on PCR cyclers:
    - Incubate:
        - 42°C, 60min, shaking at 1200rpm on **PCR cycler 1**
        - 50°C, 10min on **PCR cycler 2**
        - 70°C, 15min on PCR cycler
- Prepare PCR preamp master mix

PCR pre-amplification:

- Add 15ul of PCR preamp master mix directly into the RT reaction (final volume now: 25ul)
    - Prepare 1x PCR strip with **197ul** of RT master mix in each tube. From there pipette **15ul** into wells of semi skirted plate using multichannel
- Glue film (558/MJ) to plate and vortex carefully.
- Run following program:

1. 98C, 3min
2. 98C, 20sec
3. 72C, 15sec
4. 67C, 15sec
5. 72C, 6min (back to step2, **16 cycles**)
6. 72C, 5min
7. 4C, pause

(Incubations are different from standard SmarSeq2 protocol because of the blocking oligos strategy.)

Purification of Pre-amplification material

Purify only half volume in order to have backup material (if full volume is purified, double the amount of beads to obtain 1:1 ratio beads:material)

- Use the BRAVO robot for purification:
- Prepare 13ul H2O + 25ul AmPureXP homemade beads per sample in deepwell 96 well plate:
    - 1372.8ul H2O + 2640ul AmPureXP bead mixture. 334.4ul of the mixture in the first row of a deep well plate and then pipette 38ul into the deep well plate for the robot.
- Transfer 12ul from sample to the 38ul of AmPure beads in 96 deep well plate (done by the robot)
- Incubate for 10min at RT (done by robot)
- Place on magnet. Wait ~5min
- Remove supernatant.
- Add 100µl of 80% EtOH (prepare 50ml fresh every day you are doing an experiment).
- Place the plate on top of the magnet to let the beads glide to the bottom (the bottom of the wells should touch the magnetic part). This might take a few minutes depending on samples.

- Place on the magnet again and do an extra wash with 80% EtOH
- Let the beads dry for 5-10min (6min if using robot)
- Add 17µl water using the multichannel channel pipette.
- Place on magnet again and aspirate 15ul of supernatant into new tubes / plate.
- Place PCR seal
- Bioanalyser and so on.

Tagmentation.

- Prepare an index plate (dilute the primers with water) and clearly label Set A or Set B. Keep at -20C and thaw on ice.
    - _> prepared plates with 50µl total: so 5 rounds of tagmentation.
    - For 50X: take 143µl, add 163µl of water, add 25µl per well in the plate
    - For 70X: take 90µl, add 120µl of water, add 25µl per well in the plate
- Prepare a cDNA Dilution plate to a ~500pg/µl average.
- If full plate, use pure Tn5
- Prepare the Tagmentation mastermix, on ICE ALL THE TIME.
- Add 18ul of Tagmentation mix into a PCR plate semi-skirted on ice
    - Prepare 1x PCR strip with 237ul of Tagmentation mix in each tube. From there pipette 15ul into wells of semi skirted plate using multichannel
- Add 2µl of cDNA and Incubate at 55°C for 7min then pause 4°C
- Add 5µl of 0.2% SDS and incubate for 7min at 25°C then pause 4°C. Move on to step 7: PCR

Tagmention PCR.

- Prepare the Tagmentation PCR mastermix
- Add 15ul of Tagmentation PCR mix into the Tagmentation plate on ice
    - Prepare 1x PCR strip with 200ul of Tagmentation PCR mix in each tube. From there pipette 15ul into wells of semi skirted plate using multichannel
- Add 9µl of Nextera Indexes (from the plate).

- Incubate as follows:
    - 72°C for 3min
    - 95°C for 30sec
    - 10 cycles of 95°C 30sec / 55°C 30sec / 72°C 30sec
    - 72°C for 3min
    - 4°C pause.
- Purification.
- Pool samples by columns with 12.5µl for each samples. Final volume of 100µl.
- Use 100µl of AMPure XP beads.
- Elute in 16µl EB

*__oligo-dT__: **5′-bioRn-triethyleneglycol-AAGCAGTGGTATCAACGCAGAGTACT30VN-3′**,

where V is either A, C or G, and N is any base; IDT, HPLC purifed => store -20C

** **Template-Switching Oligo (5′-AAGCAGTGGTATCAACGCAGAGTACrGrG+G-3′**,

*where "r" indicates a ribonucleic acid base and "+" indicates a locked nucleic acid base; Exiqon **Aliquot** to avoid repeated freeze-thaw => Store stock at -80C*

***__ISPCR primer: 5'-AAGCAGTGGTATCAACGCAGAGT-3′; IDT, HPLC purified, store 100uM at -20C__

List of "blocking" oligos for SS2 on C.elegans

We resuspend these oligos at 100µM, and pool them equimolarly (->100µM stock)

+ = LNA: LNA modification was used to increase Tm. To my knowledge LNA modifications can be ordered only via Qiagen.
*= Phosphorothioate
/3InvdT/=3' Inverted dT

Appendix

FW1

*+A+G+CCCCGTTCTGGATAGCGGCACTGTTGGTT*C*/3InvdT/*

*RV1 +A+A+CACTGTCGGGCTAGAACGAGCAGCCAACG*C*/3InvdT/*

*FW2 +G+T+GCAGAGGTTGAGCAGTTGGCAAACGACCC*G*/3InvdT/*

*RV2 +T+G+CACGTCAGAACCGATACGGACTTCCACCAGAG*T*/3InvdT/*

*FW3 +A+C+TGGCGAACGCCTTGTATCATCGGTGGCGA*A*/3InvdT/*

*FW4 +T+G+TGCTTGCTTGCGGACGCTTTCTGGTGTGT*G*/3InvdT/*

*RV3 +G+C+GTCCGCAAGCAAGCACAATCACTAGTCCG*C*/3InvdT/*

*RV4 +A+G+CCCGTTCCCTTGGCTGTGGTTTCGCTAGA*A*/3InvdT/*

Buffers

Resuspension Buffer (for Single worm sequencing)		
Number of samples	1X	96
H2O	5.8	612.48
ERCC (1:400’000)	0.9	95.04
SuperScript II or IV 5X Buffer	2	211.2
DTT 0.1M	1	105.6
Superase-In	0.3	31.68
Total volume (µL)	10	1056

Wash Buffer (for single worm seq, this is already 2x the volume)		
Number of samples	1X	96
H2O	29.7	3136.32
SuperScript IV 5X Buffer	8.8	929.28
DTT (0.1M)	4.4	464.64
Tween 20 (10X)	0.2	21.12
Superase-In (Rnase inhibitor)	0.9	95.04
Total volume (µL)	44	4646.4

RT master mix		
Number of samples	1X	96
SuperScript IV (200U/µL)	0.55	58.08
SuperScript IV 5X Buffer	2.2	232.32
Superase-In	0.28	29.568
DTT (0.1M)	0.55	58.08
Betaine (5M)	2.2	232.32
MgCl2 (1M)	0.07	7.392
TSO **(100 µM)	0.11	11.616
dNTPs (10mM)	1.1	116.16
H2O	3.95	417.12
Total volume (µL)	11.01	1162.656

PCR preamp master mix		
Number of samples	1X	96

KAPA HiFi Ready Mix (2X)	12.5	1320.00
IS PCR primers (10 uM)	0.3	31.68
blocking oligos (10uM)	2	211.2
H2O	0.2	21.12
Total volume	15	1584.00

Tagmentation mix		
Number of samples	1X	96
5X TAPS-DMF	4.0	440.0
Pure Tn5	0.033	3.6
Water (if 2ul cDNA used)	14.0	1540.0
Total volume	18.0	1983.6

Tagmentation PCR mix		
Number of samples	1X	96
5X Phusion buffer	10.0	1100.0
Phusion Polymerase	0.5	55.5
dNTPs	1.0	110.0
Water	4.5	495.0
Total volume	16.0	1760.0